A model study of momentum-selective Mott physics

Numerical approaches and effective models for hole-doped Mott insulators

Sebastian Albert Erwin Huber

SIGILL. UNIVERSITAT. LUDOVIC. MAXIM.

Munich 2020

A model study of momentum-selective Mott physics

Numerical approaches and effective models for hole-doped Mott insulators

Sebastian Albert Erwin Huber

A dissertation submitted
to the Faculty of Physics at the
Ludwig–Maximilians–Universität München
for the degree of
Doctor rerum naturalium

Munich, February 20, 2020

First referee: Prof. Dr. Matthias Punk
Second referee: Prof. Dr. Lode Pollet
Day of submission: February 20, 2020
Day of the oral examination: May 18, 2020

Zusammenfassung (Summary in German)

Die Fermi-Flüssigkeits-Theorie ist ein zentrales Konzept in der modernen Festkörperphysik zur Beschreibung von konventionellen Metallen. Ein Zustand dieser Universalitätsklasse ist durch wohldefinierte Quasiteilchen aufgebaut, die eine endliche Anzahl an Zuständen innerhalb eines im Impulsraumes definierten Fermivolumens einnehmen. Gemäß dem Luttinger-Theorem ist das von diesem Zustand eingeschlossene Fermivolumen proportional zu der Elekronendichte modulo der gefüllten Bänder, vorausgesetzt keine Symmetrie ist gebrochen. In den vergangenen Dekaden wurden jedoch vermehrt in verschiedenen Materialien, wie zum Beispiel Cupraten und Eisen-Pnictiden, erhebliche Abweichungen zu obigem Konzept im Skalierungsverhalten thermodynamischer Größen beobachtet. Diese Arbeit behandelt zwei prototypische Systeme, die nicht durch die Fermi-Flüssigkeits-Theorie beschrieben werden können.

Im ersten Teil dieser Arbeit werden zweidimensionale effektive Modelle untersucht, die sich bei halber Füllung in einem Mott-Isolator-Zustand befinden und bei Dotierung mit Löchern eine endliche Leitfähigkeit haben. In einem solchen Mott-Isolator-Zustand sind die Ladungsträger aufgrund von starker Coulomb-Wechselwirkung lokalisiert. Folglich haben auch bei niedriger Lochdotierung starke Korrelationen zwischen den Elektronen einen dominanten Einfluss auf physikalische Grundzustände. In einem ersten Projekt haben wir eine sogenannte Spinon-Dopon-Molekularfeldtheorie verwendet um das zweidimensionale Fermi-Hubbard-Modell bei starker lokaler Wechselwirkung durch effektive Freiheitsgrade darzustellen, die es ermöglichen, die Löcher in eine Quantenspinflüssigkeit einzubetten. Der dazugehörige SU(2)-invariante Grundzustand gehört zur Klasse der fraktionalisierten Fermi-Flüssigkeiten. Das Phasendiagramm der Molekularfeldtheorie enthält zudem auch Zustände mit magnetischer Ordnung. Wir verwenden in unserer Arbeit die Spinon-Dopon-Molekularfeldtheorie, um ein von uns vorgeschlagenes Messverfahren für Experimente in ultrakalten Gasen zu testen, bei dem Zustände mit kurzreichweitiger magnetischer Ordnung über statistische Verteilungen detektiert und von SU(2)-invarianten Zuständen unterschieden werden können. In einem zweiten Projekt untersuchen wir das Quanten-Dimer-Modell, ein effektives Modell basierend auf einem Hilbertraum aufgespannt durch kurzreichweitige Singlets und gebundene fermionische Zuständen aus Löchern und Spins. Der Fokus liegt hierbei auf der Berechnung des Lochanteils der Elektronenspektralfunktion mittels exakter Diagonalisierung und dessen Vergleich mit zwei analytischen Ansätzen, einer diagrammatischen Berechnung der Bethe-Salpeter-Gleichung und einer sogenannten Zwei-Moden-Näherung. Die Elektronenspektralfunktion zeigt einen ähnlichen funktionalen Verlauf im Impulsraum zwischen dem Nodal- und Antinodal-Punkt wie es bei Photoelektronenspektroskopie an Cupraten zu sehen ist. Desweiteren berechnen wir in einer darauffolgenden Arbeit den exakten Grundzustand des Quanten-Dimer-Modells entlang einer bestimmten Parameterlinie. Um das Verhalten der Elektronenspektralfunktion bei Erhöhung der Lochdichte näher zu analysieren, untersuchen wir in einem aktuellen Projekt das zweidimensionale Fermi-Hubbard-Modell mittels dynamischer Molekularfeldtheorie. Wir verwenden hierbei zur Lösung des vierseitigen Störstellenproblems den numerischen Renormierungsgruppenansatz. Numerische Limitierungen zwingen uns jedoch, die Analyse vorerst auf spin-polarisierte Bäder zu beschränken. Anhand der spektralen Daten ist zu erkennen, dass sich das System ähnlich zu dem SU(2)-symmetrischen Fall bei halber Füllung in einem Mott-Isolator-Zustand befindet und bei endlicher Dotierung eine impulsabhängige Energielücke besitzt. Die Topologie der Fermifläche zeigt einen Lifshitz-Übergang beim Erhöhen der

Lochdichte. Hierbei verändert sich die Krümmung der Fermioberfläche von Elektronen- zu Loch-Form. Zum Vergleich wenden wir die dynamische Molekularfeldtheorie auch auf das Quantem-Dimer-Modell an und stellen fest, dass sich dessen Elektronenspektralfunktion bei endlicher Lochdichte qualitativ ähnlich zu dem des zweidimensionalen Fermi-Hubbard-Modells verhält.

Der zweite Teil der Arbeit beschäftigt sich mit der Tomonaga-Luttinger-Flüssigkeitstheorie, die zur Beschreibung der niederenergetischen effektiven Freiheitsgrade von eindimensionale Systemen verwendet wird. Hierbei besprechen wir zunächst eine konzeptionelle Erweiterung der operator-basierten Bosonisierungstheorie für eindimensionalen Systeme. Diese Erweiterung ist insbesondere zur Beschreibung von inhomogenen eindimensionalen Systemen geeignet. Wir betrachten zunächst ein eindimensionales System mit einem lokalen Wechselwirkungspotential und berechnen hierfür eine exakte Lösung des Einteilchenpropagators bei $T = 0$. Der kritische Exponent des Einteilchenpropagators hat eine unkonventionelle funktionelle Form als Funktion der mikroskopischen Tomonaga-Luttinger-Parameter, die nicht unter das ursprünglich von F. Duncan M. Haldane postulierte Luttinger-Paradigma fällt. In einem zweiten Projekt zu eindimensionalen Systemen untersuchen wir den Einfluss von Streuprozessen zwischen niederenergetischen bosonischen Anregungen auf deren Thermalisierungsverhalten. Solche Streuprozesse sind irrelevant auf großen Längenskalen, haben jedoch einen erheblichen Einfluss auf dynamische Eigenschaften. Innerhalb unserer analytischen Arbeit betrachten wir einen experimentellen Aufbau, bei dem instantan ein eindimensionales Bose-Gas in zwei identische, jedoch stark miteinander korrelierte, eindimensionale elektronische Systeme aufgespalten wird. Der resultierende Nichtgleichgewichtszustand durchläuft in der Folge mehrere Regimes in der Zeit, wie zum Beispiel unter anderem einen metastabilen Prethermalisierungsabschnitt. Jedoch oberhalb eines bestimmten Crossovers in der Zeit führen Streuprozesse zu einer effektiven Thermalisierung des Systems. Um dies zu zeigen berechnen wir unter Verwendung des Keldysh-Feldintegralformalismus in einer diagrammatischen Entwicklung die kinetische Gleichung in einer selbstkonsistenten Born-Näherung.

Summary

(Summary in English)

The Fermi liquid theory is a central concept in modern condensed matter physics used to describe conventional metals. A state of this universality class consists of well-defined quasiparticles, which occupy a finite number of states within a Fermi volume defined in momentum space. According to the Luttinger's theorem, such a state encloses a Fermi volume proportional to the electron density modulo the filled bands if no symmetry is broken. In the past decades strong deviations from Fermi liquid theory have been observed in the scaling behavior of thermodynamic observables in different materials, among which are for instance cuprates and iron pnictides. This thesis is about two prototypical systems that can not be described by Fermi liquid theory. The first part of this work investigates two-dimensional effective models, which are in a Mott insulating state at half-filling and have a finite conductivity when doped with holes. In such a Mott insulating state, the charge carriers are strongly localized due to the Coulomb repulsion.

Hence, strong correlations are assumed to have a strong impact on the formation of the ground state, also in the regime of small hole concentration. In a first project we have used a so-called spinon-dopon mean-field theory to represent the two-dimensional Fermi-Hubbard model with strong on-site repulsive interaction in effective degrees of freedom, in which the holes can be embedded into a quantum spin liquid. The corresponding SU(2) invariant ground state belongs to the class of fractionalized Fermi liquids. In a second project we investigate a quantum dimer model, an effective model based on a Hilbert space spanned by short-range singlets and bound states of holes and spins. The focus here is on the calculation of the hole-part of the electron spectral function by using exact diagonalization and its comparison with two analytic methods, a diagrammatic computation based on the Bethe-Salpeter equation and a so-called two-mode approximation. The electron spectral function shows a similar analytic form in momentum space between nodal and antinodal point when compared to results from photoemission spectroscopy experiments on cuprates. Furthermore, in a subsequent work we calculate the exact ground state of the quantum dimer model along a certain parameter line. In order to analyze the behavior of the elctron spectral function when increasing the density of holes, we investigate the Fermi-Hubbard model in a current project using a dynamical mean-field approach. To solve the 4-site cluster impurity problem, we use a numerical renormalization group approach. However, numerical limitations force us to restrict the analysis to spin-polarized baths. According to the spectral data, the system is similar to the SU(2) invariant case at half-filling in a Mott insulating state and posseses a momentum-selective energy gap at finite doping. The topology of the Fermi surface shows a Lifshitz transition when increasing the hole concentration. Here, the curvature of the Fermi surface changes from electron- to hole-like. For comparison we apply the dynamical mean-field theory also to the quantum dimer model and observe that the electron spectral functions at finite doping are qualitatively similar to that of the two-dimensional Fermi-Hubbard model.

The second half of the work is about Tomonaga-Luttinger liquid theory, which is used to describe the low-energy effective degrees of freedom of one-dimensional systems. Here, we first discuss a conceptional extension of the operator-based bosonization theory for one-dimensional systems. This extension is especially suited for inhomogeneous one-dimensional systems. First, we investigate a one-dimensional system with a local interaction potential and compute an exact solution of the single particle propagator at $T = 0$. The critical exponent of the single particle propagator has an unconventional form as a function of the microscopic Tomonaga-Luttinger parameters, which is not covered by the original Luttinger paradigm postulated by F. Duncan M. Haldane. In a second project on one-dimensional systems, we study the impact of scattering processes among bosonic low-energy excitations on the thermalization process. Such scattering processes are irrelevant on large length scales, however strongly affect the dynamics. In our analytic analysis we focus on a experimental setup, where a one-dimensional Bose gas is instantaneously splitted in two identical, however strongly correlated, halves of one-dimensional electronic systems. In the following, the corresponding non-equilibrium state runs through multiple regimes in time, such as a metastable prethermalization regime. However, above a certain threshold in time such scattering processes cause an effective thermalization of the system. In order to demonstrate this, we compute the kinetic equation in the Keldysh field integral formalism from a diagrammatic expansion based on a self-consistent Born approximation.

Publications

This dissertation is based on the following journal articles, listed in chronological order:

P1 *Thermalization dynamics of two correlated bosonic quantum wires after a split*
S. Huber, M. Buchhold, J. Schmiedmayer and S. Diehl
Sec. 5.7.2 / arXiv:1801.05819 Phys. Rev. A 97, 043611 (2018)

P2 *Electron spectral functions in a quantum dimer model for topological metals*
S. Huber, J. Feldmeier and M. Punk
Sec. 3.2.2 / arXiv:1710.00012 Phys. Rev. B 97, 075144 (2018)

P3 *Exact solution of a two-species quantum dimer model for pseudogap metals*
J. Feldmeier, **S. Huber** and M. Punk
Sec. 3.3.2 / arXiv:1712.01854 Phys. Rev. Lett. 120, 187001 (2018)

P4 *Signatures of correlated magnetic phases in the two-spin density matrix*
S. Huber, F. Grusdt and M. Punk
Sec. 2.8.2 / arXiv:1808.03653 Phys. Rev. A 99, 023617 (2019)

P5 *From Luttinger liquids to Luttinger droplets via higher-order bosonization identities*
S. Huber and M. Kollar
Sec. 5.5.2 / arXiv: 1911.03158 submitted to Phys. Rev. Research

P6 *A real-frequency dynamical cluster approximation study of momentum-selective Mott physics*
S. Huber and M. Punk
Sec. 4.4 in preparation

Acknowledgements

I am deeply grateful to my supervisor Matthias Punk for giving me the wonderful opportunity to pursue my Ph.D. in his group, introducing me to the concept of fractionalized Fermi liquids and giving me the academic freedom to work together with external collaborators in the field of one-dimensional systems. His continuous support and guidance helped me to realize various interesting projects and his fresh ideas breathed new life in my work, whenever needed. I am also thankful for his selflessly support in all peripheral aspects of my thesis and in my professional development.

Part of my thesis was developed in collaboration with Michael Buchhold and Sebastian Diehl, who introduced me into the field of non-equilibrium physics. I thank both for many fruitful discussions. I further want to thank Fabian Grusdt-Bohrdt for several interesting discussions on microscopy in ultracold gases. Furthermore, I enjoyed very much sharing my enthusiasm for physics, and especially for on one-dimensional systems, with Marcus Kollar. I am very grateful to his professional and also personal advices. Besides, I very much appreciated the discussions about the dimer-world with Johannes Feldmeier.

I am also thankful to Seung-Sup Lee and Andreas Weichselbaum to allow me to work with QSpace library. In particular, I acknowledge the support of Seung-Sup Lee and Andreas Gleis with whom I had several interesting discussions and who provided me with technical support regarding the QSpace library, whenever needed.

I would like to thank Lode Pollet for coreferring this thesis.

My Ph.D. time was further enriched very much by the people around me. Therefore, I would like to thank all my colleagues, in particular my brother-in-arms Dimitri Pimenov, and my further roommates Johannes Feldmeier, Michael Lichtenegger, Andreas Gleis, Lukas Weidinger, Fabian Kugler, and my fellow Ph.D. students, Elias Walter, Bin-Bin Chen, Johannes Halbinger, Julian Thönniß and Jheng-Wei Li. Special thanks goes to Julian Thönniß, Elias Walter and Andreas Gleis for proofreading this thesis. Furthermore, I want to thank Jan von Delft for providing a good working environment at his chair. I am grateful for the aid and role model function of the previous Ph.D. generation Frauke Schwarz, Benedikt Bruognolo, Katharina Stadler and Dennis Schimmel. I also enjoyed working with and learning from Oleg Yevtushenko. Further, I thank our secretaries Stéphane Schoonover and Kathrin Higgen for kindly taking care of much of the administrative processes.

This work is dedicated to my parents, grandparents, Petra, Peter, Dieter and Anita.

Contents

1 Introduction: Fermi liquid theory

In a seminal work from 1956 Lev D. Landau proposed a concept, the so-called Fermi liquid theory, that describes most metals at low temperatures. He showed that a system of interacting electrons can be described as an almost free gas of fermionic low-energy excitations with an effective mass and finite lifetime generated by interactions. Thus, the overall fermionic system behaves as an almost free Fermi gas of such quasiparticles [AM12, Mah13]. He assumed that switching on the interaction adiabatically, the non-interacting ground state evolves smoothly into its interacting counterpart. Here, no instability in form of a phase transition between both states is implicitely assumed. The quantum numbers, e.g. momentum, charge and spin, are invariants under this adiabatic process. The dynamical properties of the system are modified due to the emergence of an effective mass. An essential second ingredient to the Fermi liquid theory is the Pauli exclusion principle according to which only electrons close to the Fermi surface, which is the highest occupied energy state, interact at low energies. Even though this theoretical concept seems to be very intuitive on the one hand, it is somehow not, since the Fermi energy is just a fraction of the Coloumb energy scale. According to this, Fermi liquid theory holds even though the considered interaction is not a small perturbation on energy scales compared to the free system.

Phenomenological perspective Let us now take a phenomenological perspective on Fermi liquid theory. We consider that the non-interacting fermions have a dispersion ϵ_p^0 and the corresponding states are occupied due to the Fermi-Dirac distribution that reads

$$n_p^0 = \frac{1}{e^{\epsilon_p^0/T} + 1}. \tag{1.1}$$

It converges to a step function in the limit $T \to 0$ (cf. Fig. 1.1). We neglect the electron spin to simplify the explanations. The average occupation n_p^0 at finite temperature is a probability measure. In the presence of interactions the distribution gets washed out at the Fermi momentum p_F with a finite depletion of $\delta n_p = n_p - n_p^0$. The total energy including

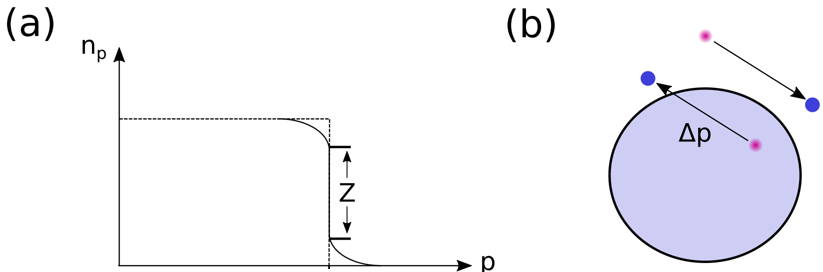

Figure 1.1 (a) The fermionic momentum occupation has according to the Fermi liquid theory a discontinuity proportional to the quasiparticle residuum Z. (b) Quasiparticle excitations have a momentum transfer p. The red (blue) point indicates a hole (occupied state).

the non-interacting ground state energy E_g yields

$$E = E_g + \sum_p \delta n_p \epsilon_p^0 + \frac{1}{2} \sum_{p,p'} f(p,p') \delta n_p \delta n_{p'} + \mathcal{O}(\delta n_p^3), \tag{1.2}$$

where the interaction between the quasiparticles is described by the symmetric Fermi liquid function $f(p,p') = f(p',p)$. A quasiparticle has thus the energy

$$\epsilon_p = \frac{\delta E}{\delta n_p} = \epsilon_p^0 + \sum_{p'} f(p,p') \delta n_{p'} + \mathcal{O}(\delta n_p^2). \tag{1.3}$$

The total momentum of the quasiparticles is

$$\Delta P = \sum_p p \; \delta n_p. \tag{1.4}$$

The quasiparticles are dressed due to the interaction and move with renormalized velocity and mass through the system given by

$$v_F = \partial_p \epsilon_p, \tag{1.5}$$

$$m^* = \frac{p_F}{|v_F|}. \tag{1.6}$$

The density of states at the Fermi surface reads

$$N(\epsilon_F) = \frac{1}{V} \sum_p \delta(\epsilon_p - \mu) = -\frac{1}{V} \sum_p \frac{\partial n_p}{\partial \epsilon_p}, \tag{1.7}$$

where the energy difference of the ground states at consecutive particle numbers is described by the chemcial potential $\mu = E(N+1) - E(N)$. At zero temperature we thus have

$$N(\epsilon_F) = \frac{m^* p_F}{\pi^2 \hbar^3}. \tag{1.8}$$

The probability that an excited electron with momentum p does not scatter is given by the quasiparticle residuum (cf. Fig. 1.1):

$$Z = | \langle \Psi_p | \, c_p^\dagger \, | \Psi_{\mathrm{GS}} \rangle |^2. \tag{1.9}$$

The Fermi liquid approach is very powerful, since it just relies on a few interaction parameters that enter into the Fermi liquid function $f(p,p')$. Of course, a full treatment of all microscopic effects is very challenging and theoretical approaches are usually based on approximating certain microscopic effects.

A system described by a Fermi liquid ground state shows clear experimental signatures in a variety of observables. Accordingly, calculations of the response to an external field for a free Fermi gas of quasiparticles with an effective mass m^* lead to strong predictions for a wide range of ordinary metals, e.g. Cu and Al. We shortly summarize two prominent observables and one physical law that frequently show up in the context of conventional metals:

- *DC electrical conductivity* –

$$\sigma = \frac{ne^2\tau}{m^*}. \tag{1.10}$$

The Drude formula for the DC conductivity is determined by the charge density ne and a factor e/m^* for the acceleration of electrons in an external field. Additionally we need to consider the relaxation time τ, which sets an average time scale within which electrons freely move through the system before they scatter among each other, on impurities or interact with the lattice. Especially the last two contributions dictate the low temperature behaviour of the conductivity and yield $\sigma \propto T^2$.

- *Specific heat* –

$$C_\nu = \frac{\pi^2}{3} N(\epsilon_F) T. \tag{1.11}$$

The specific heat describes the amount of energy needed to increase the temperature of a material. For conventional metals, which belong to the Fermi liquid class, it is determined by the density of states at the Fermi energy and scales linearly with T.

- *Wiedemann-Franz law* –

$$\frac{\kappa}{\sigma} = L\, T, \tag{1.12}$$

where we introduced the Lorentz number L. The electrical σ and thermal conductivity κ are in a fixed relation proportional to the temperature.

These three conclusions in Eq. (1.10)-(1.12) should just give a taste for the strong impact of Fermi liquid theory on the description of ordinary metals. Further details are frequently found in the literature [AM12].

Breakdown of Fermi liquid theory As usual, there are also exceptions to every rule and throughout the last decades systems have been observed where Fermi liquid theory breaks down mostly because of strong correlations. Experimental signatures in thermodynamic quantities or transport measurements have indicated new interesting quantum state of matters that go far beyond our present understanding. New techniques from high-energy physics and string theory, such as gauge theories and holographic gravity duality [FP11], have been adopted to make further progress. Probably the most prominent examples, where Fermi liquid theory fails, are one-dimensional systems. Here, the Luttinger liquid theory including bosonization techniques have been succesfully developed and reveal certain non-Fermi liquid properties [Gia03]. Furthermore, heavy fermion systems and copper-oxide materials have rich phase diagrams including unusual metallic phases not captured by Fermi liquid theory [Sen08].

The following thesis is subdivided into a large Sec. 2-3 devoted to copper-oxide materials and to be more specific the description of the so-called pseudogap phase in terms of a fractionalized Fermi liquid, a rather new and interesting non-Fermi liquid state in copper-oxide phase diagrams. In Sec. 4 we study the two-dimensional Fermi-Hubbard model in a cluster dynamical mean-field approach and compare its electron spectral function to a cluster dimer model with higher order correlated hopping at finite hole doping. In the second part of this manuscript, Sec. 5, we formulate a new constructive bosonization approach to investigate an inhomogeneous one-dimensional system (Sec. 5.1). Last, we study the effect of three-body bosonic interactions on the thermalization dynamics of two coupled one-dimensional systems within the common Luttinger liquid approach (Sec. 5.6).

2 Pseudogap phase and fractionalized Fermi liquid

2.1 Luttinger's theorem

Joaquin M. Luttinger proved in a work from 1960 by a perturbative expansion the Luttinger's theorem: It states that for a Fermi liquid state the enclosed Fermi volume is proportional to the particle number even in the presence of interactions [Lut60]. Masaki Oshikawa picked up the original conclusion of Joaquin M. Luttinger and generalized the proof to Fermi liquid states in arbitrary dimensions without relying on a perturbative approach [Osh00b]. In this section we shortly outline the main aspects of his proof considering a two-dimensional fermionic system of size $L_x \times L_y$ with periodic boundary conditions exposed to an external magnetic flux through one of the holes of the torus. Further, we assume that the total particle number is conserved. The magnetic flux is then adiabatically increased to 2π [Lau81, Osh00a]. In this case, the final and initial Hamiltonians are gauge equivalent.

The following argumentation follows closely Ref. [SC16]. First, in the absence of the magnetic field the ground state is an eigenstate of the translation operator T_x with momentum P_x. After adiabatically switching on an external magnetic field through one of the cycles of the torus, the total momentum of the ground state changes and yields

$$\Delta P_x = N \; \delta p_x \pmod{2\pi}, \tag{2.1}$$

where the momentum is defined modulo 2π. Of course, the total momentum is also conserved in the presence of interaction.

Next, we consider a two-dimensional Fermi liquid of fermionic quasiparticles created by operator $\psi^\dagger(x)$, again with $U(1)$ symmetry in a system of size $L_x \times L_y$ on a torus and insert a 2π flux. The ground state of the Fermi liquid has a Fermi surface of volume V_{FL} with all states are occupied. The number of occupied states yields

$$N_{FL} = V_{FL} \frac{L_x L_y}{4\pi^2}. \tag{2.2}$$

The total additional momentum reads

$$\Delta P_x = N_{FL} \; \delta p_x = V_{FL} \frac{L_x L_y}{4\pi^2} \; \delta p_x \pmod{2\pi}. \tag{2.3}$$

Just the quasiparticles that fill up the entire Fermi sea are shifted due to the external magnetic field. Comparing (2.1) and (2.3) we find

$$\frac{V_{FL}}{4\pi^2} = \frac{N}{L_x L_y} = n = (1 + p), \tag{2.4}$$

where n is the particle density. Following closely the original proof, we consider in the next step also a magnetic flux through the other cycle of the torus and further L_x and L_y to be mutual prime integers [Osh00b]. In this case the Luttinger's theorem follows:

$$\frac{V_{FL}}{4\pi^2} = (1 + p) \pmod{2}, \tag{2.5}$$

where we introduced on the right hand side the hole density p relative to a half-filled band. All fully occupied bands are due to the modulo subtracted.

In conclusion, we have shown the Luttinger's theorem for a Fermi liquid state with a well-defined Fermi surface. Sometimes the Luttinger's theorem also holds if the system is not in a Fermi liquid state. For instance, it is still valid in one-dimensional systems described by a Luttinger liquid [BB97, YOA97], where the Fermi surface just consists of two points and Fermi liquid theory breaks down (s. Sec. 5). However, the violation of the Luttinger's theorem has been reported in many other setups [LSGB95, PLS98, Ros07, DPK13]. In the next section we look at one specific example, namely copper-oxide materials, where the breaking of Luttinger's theorem has been experimentally detected.

2.2 High-temperature superconductivity in copper-oxide materials (cuprates)

2.2.1 History of unconventional superconductivity

Already first indications of unconventional superconductivity were observed at the late 1970s by Frank Steglich in heavy fermion materials, which are intermetallic compounds containing rare earth or actinide elements such as $CeCu_2Si_2$, UPt_3 or $CeRhIn_5$. The valence electrons of heavy fermion materials are located in f-orbitals and have a large effective mass [Col07]. These electrons thus propagate with a low Fermi velocity, which is comparable to the inverse Debye frequency, so that the pairing mechanism can hardly origin from lattice vibrations. Furthermore, the superconducting order parameter has no s-wave form as in conventional superconductors, but shows depending on the considered material different symmetries, e.g. an even parity order parameter in $CeCu_2Si_2$ or $CeRhIn_5$ materials and odd parity in UPt_3. In the first observations the critical temperature T_c was just a few Kelvin. However, these materials already shared some properties with other high-T_c compounds found later. Their phase diagram [SSV05] includes, similar to cuprates, a quantum critical point [Sac10], which seems to play a crucial role among most unconventional superconductors. At such a quantum critical point a second order phase transition at zero temperature driven by a non-thermal control parameter sets in [Sac07]. Moreover, the proximity of magnetic ordering and superconductivity in heavy fermion materials already caused speculations of a new pairing mechanism based solely on the interactions between electrons.

A few years later in 1979, Klaus Bechgaard synthesized the first quasi one-dimensional organic compound $(TMTSF)_2PF_6$, which had, at an external pressure of 11kbar, a comparable a comparable low transition temperature $T_c \approx 0.9K$ [JMRB80]. Today, isotropic three-dimensional carbon configurations, e.g. fulleneres C_{60}, are commonly used as a toy compound to study high-T_c. They usually have a critical temperature around $T_c \approx 30K$ [IYS12]. Interestingly, the phase diagram of such organic materials are similar to that of cuprates and have a strong magnetic insulating phase. Thus, in both materials strong correlations are crucial.

The historical breakthrough was finally achieved by Alex Müller and George Bednorz in 1986 working at IBM on lanthanum and barium copper oxides ($La_{2-x}Ba_xCuO_4$). They have shown a dramatic decrease of the resistivity at a temperature below $T_c \sim 35K$ [BM86]. Shortly after, the Meissner effect was observed in such materials [BTM87] and a critical temperature of $T_c \sim 90K$ has been experimentally verified in a yttrium copper oxide compound ($YBa_2Cu_3O_7$) [WAT+87]. This was expected to be a promising achievement for industrial applications. Whereas in former days liquid helium was needed for cooling down samples to reach a temperature below $30K$, it was now possible to use liquid nitrogen with boiling point $77K$ [HHP53] in order to drive such ceramic compunds into a superconducting state. Furthermore, they had a higher critical magnetic field of approximately 100 Tesla.

Around a decade ago in 2006, iron-based superconductors were discovered by the research group of Hideo Hosono at the Tokyo Institute of Technology [KHH+06, KWHH08], which meanwhile reach critical temperatures of $\sim 50K$ [RCD+08, RYL+08]. The metalic compounds have conducting layers of iron, and pnictogen (like arsenic or phosphorus) or chalcogen (like selenium or tellurium). The materials have a pronounced magnetically ordered phase, which is however not a Mott insulator. The spin-density wave ordered state rather competes with the superconducting phase [JXY15]. Moreover, the crystalline structure of such materials differ strongly from cuprates and the band structure includes even in the low-energy description a larger number of bands. Iron-based superconductors and cuprates have however in common that strong electronic correlations are crucial in order to understand the zoo of exotic quantum matter that appears in both phase diagrams. Furthermore, non-Fermi liquid behaviour was frequently observed for iron-based superconductors [HK09, LI10, ABM+10, HBA+13, FCR+15], for instance in form of the violation of the Mott-Ioffe Regel [HK09, HBA+13]. Such properties are also hallmarks of the cuprate phase diagram (s. Sec. 2.4). We discuss this in the following in more detail.

2.2.2 High-T_c in a ceramic insulator

Historically, high-T_c was first discovered in the seminal work by Alex Müller and George Bednorz in 1986 [BM86]. It was originally observed in $La_{2-x}Ba_xCuO_4$, which is an insulator at half-filling $x = 0$. One year later, both researchers were awarded the Noble Prize in Physics.

At that time conventional superconductivity, which was first observed by Heike Kammerlingh-Onnes in 1911 and facilitated by the liquefaction of helium in 1908 [VDK10], was fully explained within the BCS theory developed and named after John Bardeen, Leon Cooper and John R. Schrieffer [BCS57a]. The central aspect of the theory is the mediation of an attractive force between fermions on opposite sides of the Fermi surface and opposite spins via lattice deformations, namely phonons, at sufficiently low temperature. We use second quantized notation to represent the creation of a fermionic particle by the operator $c^\dagger_{k,\sigma}$. According to this approach, electrons tend to form a singlet, a so-called Cooper pair, described as follows

$$\Delta^\dagger_Q = c^\dagger_{k+Q,\uparrow} c^\dagger_{-k,\downarrow}. \tag{2.6}$$

Such singlets show bosonic statistics and form a Bose condensate below a critical temperature T_c. Within the superconducting phase of conventional metals the macroscopic occupation amplitude $\Delta_0 = \langle \Delta^\dagger_{Q=0} \rangle$ appears in the quasiparticle spectrum of the BCS state in form of a isotropic energy gap $\Delta_0 \sim 2\omega_D \exp\left(-\frac{1}{\nu_0 g}\right)$. Here, g is an interaction parameter, ω_D is the Debye frequency, which equals the binding energy of the Cooper pairs, and ν_0 is the density of states. In the superconducting state, materials repel external magnetic fields, which is called the Meissner effect [BCS57b, AM12, AS10]. Depending on how the superconducting state is destroyed when increasing the magnetic field, superconducting materials are either of type-I with a first order phase transition, or type-II, where a finite crossover region exists, where magnetic vortices are formed [Tin04]. The maximal upper critical temperature T_c for a phonon mediated pairing mechanism is for exisiting materials in the periodic table and alloys expected to be smaller than $\approx 30K$. However, the critical temperature stated in the work by Alex Müller and George Bednorz from 1986 was around $T_c \approx 34K$ [BM86]. Shortly after, further copper-oxide materials with even higher critical temperatures were discovered, which differ among each other by their interlayer substrates. At half-filling all

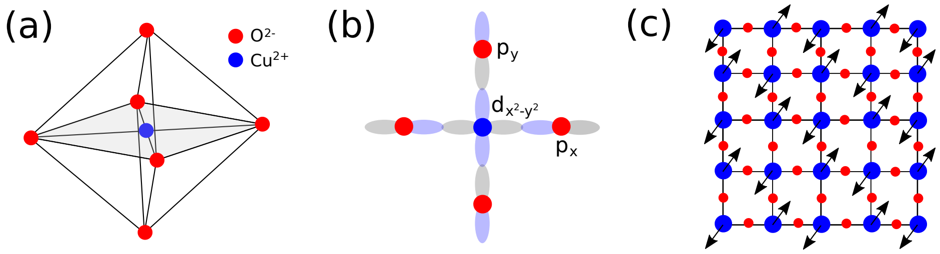

Figure 2.1 (a) Octahedral structure as found in certain cuprate compunds (see main text) with a copper ion in the center and oxygen ions at the corners. (b) The $d_{x^2-y^2}$ has strong covalent bondings with the in-plane oxygen ions. (c) The two-dimensional lattice with copper ions located at the sites and oxygen associated with the bonds. At half-filling cuprates are charge-transfer insulators with antiferromagnetic ordering (indicated by the arrows).

these materials are insulating and thus the pairing mechanism seemed to be rooted in a new mechanism. A unified theoretical approach that explains the essence of high-T_c in such ceramic materials is still missing today. Today, there are roughly five subclasses of hole-doped cuprate materials: $\mathrm{La}_{2-x}\mathrm{M}_x\mathrm{CuO}_4$ (LMCO) type with M to be Ba,Sr or Ca, $\mathrm{YBa}_2\mathrm{Cu}_3\mathrm{O}_{6+x}$ (YBCO) type and Bi-,Tl- and Hg-type compounds. We refer to Ref. [Pla10] for a list of the mentioned representative material classes with explicit compound examples including their maximal transition temperatures T_c^{max} at optimal doping. In the following summary on experimental studies on cuprates, we sometimes refer to a general subclass, such as LMCO or YBCO, or a specific material within a subclass, in this case $\mathrm{La}_{2-x}\mathrm{Sr}_x\mathrm{CuO}_4$ and $\mathrm{YBa}_2\mathrm{Cu}_4\mathrm{O}_8$. Today, the highest transition temperature of $T_c = 164K$ at optimal doping was found in Hg$-$1223 under high external pressure 30GPa. All of the material classes have in common to be composed of copper-oxygen layers with intermediate compounds serving as charge reservoirs.

The anisotropic superconducting order parameter and the high critical temperatures indicate that superconductivity in cuprates might stem from a new mechanism, even though conventional and unconventional superconductivity have also fundamental aspects in common. First of all, they share the formation of Cooper pairs with charge $2e$. This was confirmed for ceramic materials in tunneling experiments by direct measurements of the flux quantum $\phi = hc/2e$ in the presence of an external magnetic field [Pla10]. Further, a decrease of the Knight shift for cuprates in the superconducting state indicates that Cooper pairs are spin singlets [THHF89]. Cuprates belong to type-II superconductors with a rather low critical field H_{c1}, where flux penetration sets in, and a larger critical field H_{c2}, where the material enters a normal state.

On the other hand, the phase diagram of hole-doped cuprates, which is further discussed in Sec. 2.4, shows annomalous properties that are in contradiction to normal metal superconductors.

2.3 Cuprates: From material to a microscopic model

2.3.1 Electronic structure of cuprates

The crystalline structure of cuprates consists of copper-oxide layers separated by intermediate compounds. The copper atoms Cu are ionized in the undoped parent compound and in an electronic configuration d^9, where each copper has nine $3d$-electrons (s. Fig. 2.1 (a)). The degeneracy of the e_g-orbitals, which consist of the $d_{x^2-y^2}$- and d_{z^2}-orbital with lobes centered along the axis, is due to Jahn-Teller distortion lifted, so that the perfect octahedral structure like in $\mathrm{La}_2\mathrm{CuO}_4$ or $\mathrm{YBa}_2\mathrm{Cu}_3\mathrm{O}_{6.5}$ composed of the central copper ion with its six neighboring oxygens is disrupted along the vertical z-axis. The highest partailly occupied d-orbital is located within the x-y-plane with symmetry $d_{x^2-y^2}$ and has a single hole. Without interaction the corresponding lobes hybridize with the neighboring fully occupied p_x- and p_y-orbitals of the surrounding oxygens in a strong covalent bonding predicting a metal with a large overlap element t_{dp} (s. Fig. 2.1 (b)). According to this, a microscopic model consist of the hopping with amplitude t_{dp} between copper $3d$-orbital located at sites i and oxygen $2p$-orbitals with site index l plus an on-site energy potential $\epsilon_{d/p}$ [Vis13]:

$$H_{dp} = \sum_{i,\sigma} \epsilon_d d^\dagger_{i,\sigma} d_{i,\sigma} + \sum_{l,\sigma} \epsilon_p p^\dagger_{l,\sigma} p_{l,\sigma} + \sum_{\langle il \rangle,\sigma} t_{dp}(d^\dagger_{i,\sigma} p_{l,\sigma} + p^\dagger_{l,\sigma} d_{i,\sigma}). \tag{2.7}$$

Here, a hole on the oxygen (copper) site is created by the operaor $p^\dagger_{l,\sigma}$ ($d^\dagger_{i,\sigma}$). In general, also higher order hopping elements between oxygen sites t_{pp} exist, however are comparable small and thus neglected. After hybridization the band structure consists of an antibonding (AB), bonding (B) and non-bonding band (NB), which have the following dispersions:

$$\epsilon_{B/AB} = \frac{\epsilon_p + \epsilon_d}{2} \pm \sqrt{\frac{\epsilon_p - \epsilon_d}{2} + t^2_{dp}(\sin^2{(k_x a/2)} + \sin^2{(k_y a/2)})}, \tag{2.8}$$

$$\epsilon_{NB} = \epsilon_p. \tag{2.9}$$

This is however in strong contrast to the experimental observed charge gap [Pla10]. Indeed, the electrons interact via a large on-site Coulomb repulsion of the form

$$H_U = U \sum_i n_{d,i,\uparrow} n_{d,i,\downarrow}, \tag{2.10}$$

which prohibits that an electron hops onto the partially filled copper orbital $d_{x^2-y^2}$. Thus charge fluctuations are suppressed and the parent material is not a band metal, but instead a Mott insulator, respectively a charge-transfer insulator as proposed by Zaanen-Sawatsky-Allen [ZSA85]. The antibonding band splits into an upper-and lower-Hubbard band (UHB and LHB in Fig. 2.2, s. Ref. [Vis13]). In a microscopic picture the ground state of the charge-transfer insulator consists of a doubly occupied p-orbital associated with the oxygen, which is energetically higher than the d-orbital of the copper. This is in accordance with cluster calculations and x-ray absorption measurements of the copper core level, which have confirmed that the undoped cuprate is a charge-transfer insulator [FTMUO87, BCDS+87, VDMVESH88, ETS90].

In the case of a charge-transfer insulator the lowest possible excitation is given by a hopping of an electron from the oxygen onto the vacancies of the copper ion with an energy difference Δ and amplitude t_{dp}. The charge transfer excitation gap was measured in optical experiments and is approximately $\Delta \sim 2.0eV$ for materials with a octahedral structure (cf. Fig. 2.1) [TKA+90]. If the ratio between the energy difference and hopping is rather large, the hole on the half-filled copper site forms a local moment of spin-1/2. Within this pictures holes hop from the copper onto the oxygen sites within virtual processes, so that the local moments at adjacent copper sites point in opposite directions. Thus, the spins in the insulating phase of copper-oxide materials order antiferromagnetically. Neutron scattering experiments showed a two-dimensional antiferomagnetic correlation length of $\zeta_{AF} > 200$Å [SEB+87, BGK+99]. This is not in contrast to the Mermin-Wagner theorem [Wag66, MW66, Mer68] according to which a two-dimensional system remains magnetically disordered at finite temperature for an isotropic Heisenberg coupling. Here, in realistic three-dimensional materials the coupling parameter is however anistropic. Finally, the according exchange integral is given by $J = t^4_{pd}/\Delta^3$ and quite large on the order of $\sim 0,1eV$ as measured in Raman scattering experiments

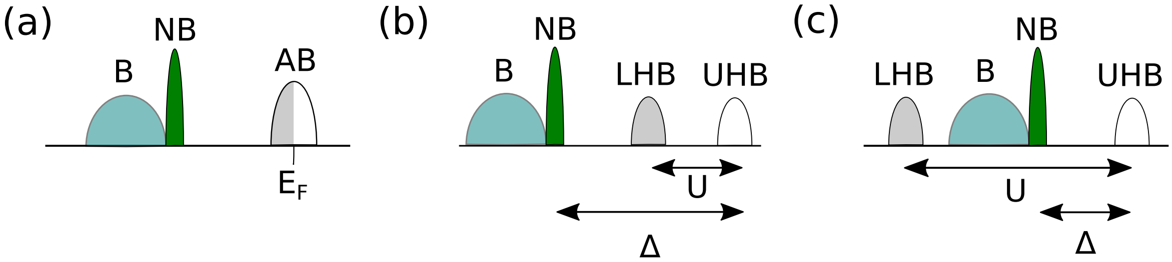

Figure 2.2 (a) As desrcibed within the d-p model, three bands originate from the crystalline structure of copper-oxide materials. In case of a normal metal, the Fermi energy is located within a band. (b) However, for cuprates the antibonding band splits due to a large on-site repulsive interaction into an upper (UHB) and lower (LHB) Hubbard band. In case the system is in a Mott insulating phase, the lowest excitations have an energy $\sim U$. (c) As shown for instance in optical measurements, the cuprates at half-filling are charge-transfer insulators, where the lower Hubbard band is shifted below the non-bonding and bonding bands. Fig. adapted from Ref. [Vis13].

[LFSW88, SSS88, BAK$^+$96, BKK$^+$97] and compared to calculations from spin wave theory [CHA$^+$01]. If the parent compound, for instance $\mathrm{La}_{2-x}\mathrm{Ba}_x\mathrm{CuO}_4$, is substituted with x holes by replacing La_{2+} with Ba_{3+}, additonal vacancies appear on the copper sites. Since this is again energetically unfavorable, the hole fluctuates onto a neighboring oxygen p-orbital. This was also confirmed for instance within angle-resolved photoemission spectroscopy [TMKY$^+$88] and nuclear magnetic resonance studies [THH$^+$89]. Due to translational invariance of the system, the holes are in principle mobile and transport charge. Electron doping on the other hand leads to an additional occupation of the Cu $d_{x^2-y^2}$-orbital [Eme89]. Our focus in the remaining thesis is - except of a short remark in the next section - on the hole-doped part of the cuprate phase diagram.

2.3.2 Effective single-band Hubbard model

Considering the last section, a minimal model for hole doping a cuprate should include 3 bands, one for the copper orbital $d_{x^2-y^2}$ and two bands for the oxygen orbitals $p_{x/y}$, which form the unit cell. This was explicitely formulated in the d-p model [Eme87] on which LDA (local-density approximations) band and cluster calculations were performed in order to determine the microscopic parameters (s. Ref. in Sec. 2.3 of [OF08]). However, as pointed out by Fuchun C. Zhang and Thomas M. Rice, the crucial point is that the doped hole on the copper site resonates with the four surrounding oxygen orbitals and forms a Kondo-like singlet located on the copper site [ZR88]. Such a singlet further hops with an effective amplitude t of the order t_{dp}^2/Δ between adjacent copper sites due to an exchange process between the corresponding hole, which formally represents the Zhang-Rice singlet, and a localized spin. Focusing on the low-energy regime of the singlet with nearest neighbor hopping amplitude t and repulsive interaction given by the energy difference Δ, the d-p band model reduces to a single-band Hubbard model. For large Δ, the low-energy physics boils down to the two-dimensional t-J model (s. Ref. in Sec. 2.4 - 2.6 of [OF08]):

$$H_{\mathrm{tJ}} = \mathcal{P}[-\sum_{\langle ij\rangle,\sigma} t_{ij}\; c_{i,\sigma}^{\dagger} c_{j,\sigma} + J\sum_{\langle ij\rangle}[S_i S_j - \frac{1}{2}n_i n_j]]\mathcal{P}, \tag{2.11}$$

where we introduce the electron creation operator $c_{i,\sigma}^{\dagger}$ acting on site i and spin σ. Doubly occupancies are projected out by the so-called Gutzwiller projector $\mathcal{P} = \prod_i (1 - n_{i,\uparrow} n_{i,\downarrow})$ (for

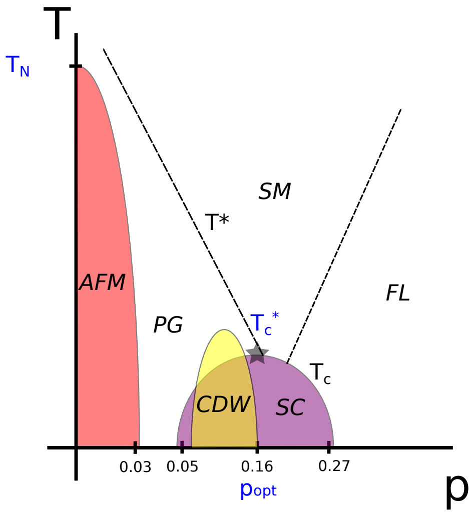

Figure 2.3 The hole-doped phase diagram of cuprates has at low doping an antiferromagnetic ordered insulating phase (AFM), which exists up to a Neel temperature T_N. Attached to it, the pseudogap phase (PG) appears, which is characterized by a finite spin gap and unusual charge carrier properties. It is separated by the boundary T^* to a strange metal state (SM), where the spin gap vanishes. The superconducting dome has its largest critical temperature T_c^* at optimal doping p_{opt}. Additionally, charge order (CDW) was observed at small temperatures in the underdoped regime of the superconducting state (SC) and pseudogap phase (PG). This phase diagram is a schematic scetch of the most important aspects relevant for the remaining thesis.

further discussion s. Sec. 2.6). The local density and spin operators are given by

$$n_i = \sum_{\sigma} c^{\dagger}_{i,\sigma} c_{i,\sigma}, \tag{2.12}$$

$$S_i = \tfrac{1}{2} c^{\dagger}_{i,\alpha} \sigma_{\alpha\beta} c_{i,\beta}. \tag{2.13}$$

For completeness, we mention that the electron-doped cuprates are also described in the low-energy regime by the tJ model [LNW06]. However, the phase diagram shows a strong asymmetry relative to the half-filled system, whereas the tJ model with solely nearest neighbor hopping is electron-hole symmetric. Therefore, it was suggested to consider higher order hopping terms [TM94, GVL94, Toh04]. Other approaches consider an additional $4s$-orbital on the copper site, which might be strongly modulated by the apical oxygens within a octohedral structure for hole-doped cuprates. This can then lead to a change of the ratio t'/t (nearest neighbor $\langle ij \rangle$ hopping amplitude $t_{ij} = t$; next-nearest neighbor $\langle\langle ij \rangle\rangle$ hopping amplitude $t_{ij} = t'$) [ASJL96, PDSD$^+$01]. Since electron-doped cuprates have no such apical oxygens, this might be an explanation for the strong particle-hole asymmetry. In the following we solely focus on the hole-doped phase diagram of cuprates.

2.4 Hole-doped phase diagram

Fig. 2.3 shows the hole-doped phase diagram of cuprates on the plane of temperature T and doping p. It contains the most important features shared among all cuprate subclasses. We cover its most relevant aspects for the remaining thesis. Usually, optimal doping p_{opt} is refered to the point with the highest critical temperature $max_p[T_c(p)]$. This point separates the phase diagram into an underdoped $p < p_{\text{opt}}$ and overdoped region $p > p_{\text{opt}}$.

Antiferromagnetic charge-transfer insulator (AFM CTI)– As discussed earlier the crystalline structure of cuprates favors an antiferromagnetic order at half-filling $p = 0$. The antiferromagnetism ordering vanishes in a phase transition at Neel temperature T_N into a magnetically disordered state (La_2CuO_4: $T_N \approx 300K$ [KBSE98], $YBa_2Cu_3O_6$: $T_N \approx 400K$ [LLM+88]). Above the Neel temperature spins are still localized and materials are still insulating. The superexchange coupling is quite large and as mentioned above of order $0.1eV$ ($0.13 - 0.14eV$ for $La_{2-x}Sr_xCuO_4$ and $0.10 - 0.11eV$ for $YBa_2Cu_3O_{6+\delta}$), known from systematic inelastic neutron [BCIP97] and Raman scattering experiments [LFSW88, SSS88, BAK+96, BKK+97]. Doping strongly reduces the antiferromagnetic ordering, which is for instance in LSCO compounds, such as $La_{2-x}Sr_xCuO_4$, already strongly suppressed above $p \approx 2\%$. However, antiferromagnetic fluctuations are still pronounced within the surrounding phases [NBB+98, KBSE98, TL01, CDMT+16]. Actually the close proximity of the stronlgy correlated antiferromagnetic and superconducting phase provoked theoretical approaches that the pairing mechanism is due to the exchange of spin fluctuations [LNW06, Pla10].

Superconducting state (SC)– The SC state sets in at around 5% doping [Pla10]. Increasing temperature over a threshold T_c destroys the coherence of singlet Cooper pairs. The transition temperatuure T_c^* is largest at the point of optimal doping, i.e. the maximum of the dome-shaped SC region. The order paramater is commonly of d-wave type with pairing symmetry $d_{x^2-y^2}$ [WVHL+93, SDW+93, LNW06]:

$$\Delta_Q = \Delta_0[\cos(Q_x) - \cos(Q_y)]. \tag{2.14}$$

Thus, at the nodal points along the (off-)diagonal of the Brillouine zone, the gap closes and changes sign under a rotation of 90°. Angle-resolved photoemission spectroscopy and tunneling experiments confirmed the anisotropy of the gap. However, also indications of a significant s-wave component in the overdoped region has been pointed out ([LFA+01], s. Ref. in Sec. 5.5 of [Pla10]). In the SC regime 'conventional' Cooper pairs form, i.e. spin singlets with charge $2e$ [THHF89].

Charge and spin density wave order (CDW and SDW) – The CDW order parameter $\Psi_Q = \sum_k \langle c^\dagger_{k+Q,\sigma} c_{k,\sigma}\rangle$ is finite, if the charge carriers order in regular patterns in real space. In case the corresponding real space modulation is a multiple of the lattice constant, the CDW is called commensurate, otherwise incommensurate. Of course, such an instability is also possible in the spin sector, called SDW ordering. From this point of view, antiferromagnetic ordering is a special case of a commensurate SDW with $Q = \pi/a(1, 1)$. Both, CDW and SDW ordering, seem to be crucial for the existence of the SC and PG phase (s. Fig. 2.3), and the concept of competing phases has been proposed to explain the cuprate phase diagram [KLFO02, LNW06]. Charge and spin ordering, unified under the terminology stripe ordering, has been meanwhile verified in many ceramic compounds (s. Ref. in [LNW06, Pla10, PT19]). For instance, inelastic neutron scattering experiments on Sr doped LSCO compounds showed SDW ordering with incommensurate wavevector $Q = \pi/a(1/2 \pm p, 1/2), \pi/a(1/2, 1/2 \pm p)$ for a finite doping regime around $p \approx 0.12$ [TSA+95]. CDW and SDW ordered phases are usually in close proximity to the SC state, which makes them to a key candidate to better understand the formation of singlet Cooper pairs. Just for completeness, we mention that also other types of ordering, such as pair-density wave and nematic ordering, are frequently proposed and have been observed in cuprates [LNW06].

Pseudogap phase (PG) – The pseudogap phase is very often regarded as the precursor phase of the superconducting state. It was first observed in a nuclear magnetic resonance

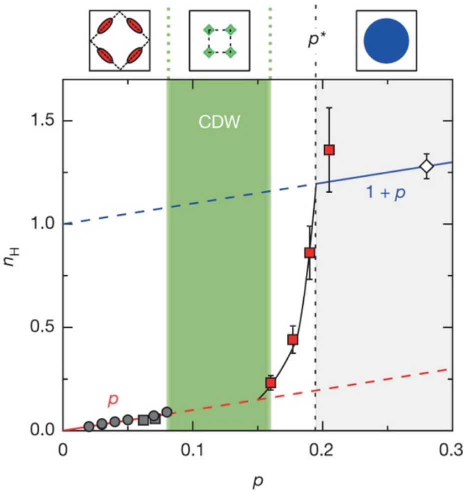

Figure 2.4 The figure shows that the Hall carrier density, which is inversly proportional to the Hall coefficient, at small temperature increases except of a crossover regime $p \approx 0.16 - 0.19$ linearly with doping p (reprinted by permission from Springer Nature Customer Service Centre GmbH: Springer Nature, Nature, Ref. [BTL+16], Copyright (2016)). However, at small doping the carrier density is proportional to doping p, i.e. we literally dope the system relative to the filled bands. At larger doping this changes and the Hall coefficient is given by $n_H \propto 1 + p$. We thus have a large Fermi surface in this regime.

measurement in form of a spin gap [WJWB+89, AOM89, CISD97]. Other experimental techniques, such as tunneling spectroscopy [RRG+98] and angle-resolved photoemission spectroscopy [DHS03], also verified the existence of a crossover temperature T^* [PT19]. In the following the experimental detection of the pseudogap phase is listed and explained in a chronological order.

The original nuclear magnetic resonance measuremnts showed a decrease of the response to an external magnetic field, which is a clear signature for the opening of a spin gap [WJWB+89, AOM89, CISD97]. The external magnetic field normally couples in ordinary metals to the electrons close to the Fermi level, which in turn cause an effective field at the nuclear site. The conclusion from the Knight shift measurements was that the density of states has an anisotropic distribution in momentum space.

A few years later, angle-resolved photoemission spectroscopy measurements, where an electron is ejected from the material due to an external light source, showed that the Fermi surface is reconstructed below a transition temperature T^* in a Fermi-arc structure with a gap opening up at the antinodal points [SDW+93, DNC+96, DHS03, SRL+05, LVT+07, VLH+10, VHH+12, HVH+14a]. Meanwhile angle-resolved photoemission spectroscopy results have confirmed however the coexistence of two gaps. Whereas in the overdoped SC regime the gap has a pure $d_{x^2-y^2}$ symmetry, higher order corrections seem to be present in the underdoped regime of the superconducting state and passed on from the precursory pseudogap phase.

The reduced density of states when entering the pseudogap phase was also detected within measurements of the tunneling density of states [RRG+98], c-axis optical conductivity [HTL+93, Uch97] and specific heat [LMCL93, LLC+01].

Very interestingly the in-plane optical conductivity has a functional form of $\sigma(\omega) \sim (-\mathrm{i}\omega + 1/\tau)^{-1}$ with $1/\tau \sim \omega^2 + T^2$ and magnetoresistance measurements obey Kohler's rule, which both are prominent chracteristicas of normal FL states [CVD+14]. From this point of view a theoretical approach that would also explain the reconstrcution of the Fermi surface could start from considering thermal fluctuations of the order parameter from a proximity phase such as SC, CDW and AFM [LNW06].

However, Drude conductivity and Hall coefficient show a rather peculiar behaviour in strong contrast with normal Fermi liquid theory proportional to doping density p with respect to half-filling [OTM+90, UIT+91, CRK+93, PLD+05, BTL+16]. Sven Badoux et al. studied the response of cuprate material $\mathrm{YBa_2Cu_3Oy}$ exposed to a strong external magnetic field up to 88 Tesla measuring the Hall carrier density n_H summarized in Fig. 2.4 from Ref. [BTL+16]. Here, the Hall carrier density is proportional to the charge carrier density. At small doping the charge carrier density is proportional to doping $n_H \propto p$ with a clear transition at the critical doping value $p^* \approx 0.19$, where due to other measurements also the pseudogap phase vanishes. This implies two crucial points: First, the pseudogap and Mott insulating phase seem to be intrinsically connected, at least the Hall carrier density increases continously and linear with doping entering the PG phase from the Mott insulator. Second, the Fermi surface reconstruction appears at doping $p^{FSR} \approx 0.16$ and comes along with CDW order, indicated in the experiment by the crossover from a positive to negative Hall coefficient below a temperature threshold (s. Fig. 2 in Ref. [BTL+16]). It was shown that CDW ordering and the pseudogap are clearly two distinct phenomena occuring at different doping. This was in contrast to existing data from scanning tunneling microscope on $\mathrm{Bi_2Sr_2CaCuO_{8+\delta}}$ that show a common critical doping below which CDW ordering and the pseudogap phase simultaneously appear (s. discussion and Ref. in [BTL+16]).

In conclusion, the breaking of the Luttinger's theorem, which manifests itself in transport, tunneling and other experiments, has been verified and is obvisiouly intertwined to the pseudogap phase. It is important to recognize that the modification of the charge carrier density could be also rooted in the breaking of translational symmetry as in the CDW phase and thus a reconstruction of the Fermi surface. However, such symmetry breaking was not observed outside the CDW phase in the above experiments, so that in conclusion Luttinger's theorem is here indeed violated outside the CDW phase.

Strange metal (SM) – The strange metal phase is located in the phase diagram above the optimal doping p^* and at intermediate temperatures above T_c, bridging the PG and FL phase. The resistivity grows for small temperature linear $\rho \propto T$ [LNW06, Pla10, PT19], which is in disagreement with normal Fermi liquid theory. In material compounds LSCO a conventional quadratic behaviour was observed at doping $p = 0.33$ that decreases for smaller hole concentration (s. Fig. 2.5 from Ref. [CWV+09]). The scattering rate of the contribution to the resistivity linear in temperature shows in certain compounds a trend to increase linearly with the critical temperature T_c [AJAB+07]. This implies a close relationship between the d-wave superconducting state and unusual behavior in the specific heat. Further, the Mott-Ioffe Regel is, in contrast to a normal metal, broken, which means that the resistivity does not saturate at an upper temperature threshold, where the mean-free path due to interactions is lower than a single interatomic spacing [PT19].

Fermi liquid (FL) – At very high doping cuprates show conventional Fermi liquid behaviour [LNW06, Pla10, PT19]. Therefore, the resistivity for instance goes quadratic in temperature $\rho \propto T^2$ [MKS92, NBM+03] and also the Wiedemann-Franz law $\lambda/\rho \propto T$, with thermal conductivity λ, is again restored [PBH+02]. Closely above the lower threshold p^* the Fermi surface shows cylindric hole-doped shape, first verified in angle-dependent magnetoresistance [HAJC+03] and angle-resolved photoemission spectroscopy measurements [DHS03]. In various materials a Lifshitz-transition at larger doping sets in, where the topology of the Fermi surface changes form hole to electron shape (s. Ref. in [PT19]). Quantum oscillation measurements [BBM+10] and photoemission spectroscopy [DHS03] confirmed the Luttinger's theorem with carrier density proportional to the electron density in the upper partially occupied band, i.e. $n \propto 1 + p$.

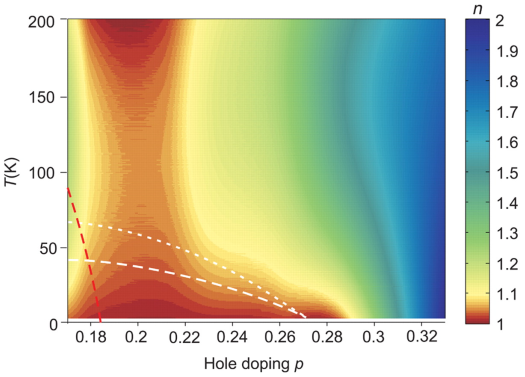

Figure 2.5 Exponent n describing the temperature dependence of the resistivity $\rho \propto T^n$ in the temperature T and doping p plane. (From Ref. [CWV+09]. Reprinted with permission from AAAS.)

Already this short overview covers a variety of interesting and exotic aspects of new quantum matter states in cuprate materials [LNW06, Pla10]. As rundimentary explained in the above summary, different theoretical concepts have been developed out of the above experimental observations.

2.5 Breaking of Luttinger's theorem: Fractionalized Fermi liquid in heavy fermions

The Luttinger's theorem has been investigated for the Kondo-Heisenberg model, which is commonly used to describe heavy fermion systems of localized electrons in d- or f-orbitals and additional conduction electrons in other bands. As mentioned in the former sections, such systems show unconventional superconductivity with a pairing mechanism not based on BCS theory. The Kondo-Heisenberg model consists of a hopping of conduction electrons represented by fermionic creation operators $c_{i,\alpha}^\dagger$ coupled to localized spin-1/2 momenta S_i:

$$H = J_H \sum_{\langle ij \rangle} S_i S_j - \sum_{ij} t_{ij} [c_{i,\alpha}^\dagger c_{j,\alpha} + c_{j,\alpha}^\dagger c_{i,\alpha}] + J_K \sum_j s_j S_j, \tag{2.15}$$

where the spin attributed to the conduction electrons can be expressed as $s_i = c_{i,\alpha}^\dagger \sigma_{\alpha\beta} c_{i,\beta}$ with a three component vector of Pauli matrices $\sigma = (\sigma_x, \sigma_y, \sigma_z)^T$.

Within the work of Todadri Senthil, Subir Sachdev and Matthias Vojta published in 2003 [SSV03], the phase diagram of the Kondo-Heisenberg model has been studied along the parameter line $g = J_K/J_H$ for $J_K > 0$ in form of a mean-field analysis. It includes three regimes close to zero temperature:

$g \gg 1$: The conduction electrons and local moments interact through the Kondo coupling J_K. The local moments are represented by slave-fermions using fermionic operators $f_{i,\alpha}$. The conduction electrons and the local moments form singlets due to the large Kondo coupling. Thus, c and f electrons hybridize and the bosonic operators $B_1 = f_\alpha^\dagger c_\alpha$ and $B_2 = \epsilon_{\alpha\beta} f_\alpha c_\beta$ with the antisymmetric tensor $\epsilon_{\alpha\beta}$ have a finite amplitude. Here, the system is in a Fermi liquid state. The Luttinger's theorem in Eq. (2.5) holds.

$g \sim 1$: In an intermediate parameter regime, where Heisenberg and Kondo coupling are of similar order, the already paired conduction and electrons from the local moments form a condensate that at low temperature has an instability towards a superconducting state.

$g \ll 1$: This regime is of main interest in our study and is most simply understood when considering the limiting case where the Kondo coupling and temperature are zero. Both subsystems - local moments and conduction electrons - are completely decoupled. Two scenarios depending on the specific geometry of the lattice and the details of the interaction on the lattice have to be distinguished:

- *Magnetically ordered metal* – We consider a lattice geometry and interaction, which does not induce frustration. For instance, a square lattice, such that the local moments form a antiferromagnetically ordered ground state. In this case Luttinger's theorem holds, since translational invariance of the system is broken.

- *Spin liquid* – Considering geometric or interaction induced frustration, such as on a Kagome lattice, the formation of a spin liquid is favored. In this case we observe a Fermi surface of sharp electronic quasiparticles in the conduction band, but f-electrons do not contribute to the Fermi surface. Indeed, topological order causes the violation of the Luttinger's theorem and the Fermi surface volume reads

  $$\frac{V_{FL}}{4\pi^2} = p \pmod 2. \tag{2.16}$$

  In the Kondo-Heisenberg model the parameter p describes the density of electrons in the conduction band.

Here, the concept of a fractionalized Fermi liquid has been introduced for the two-band Kondo-Heisenberg model. In the next section we apply the spinon-dopon representation to the single-band Fermi-Hubbard model, which can be used to construct a fractionalized Fermi liquid ground state. Later in this thesis, we explain in more detail that indeed topological excitations of the spin liquid, e.g. visons, are responsible for the violation of Luttinger's theorem (cf. Sec. 3.1).

2.6 Spinon-dopon representation: Fractionalized Fermi liquid ground state

A short recap on Gutzwiller projection and slave-particle formalism Electrons in cuprate materials experience a large on-site Coulomb repulsion such that doubly occupied sites are energetically suppressed: $c^\dagger_{i,\alpha} c_{i,\alpha} \leq 1$. Originally, Martin C. Gutzwiller proposed projectors that reduce the electron Hilbert space to the effective physical subspace with just empty or single occupied sites [Gut63, BR70]

$$c^\dagger_{i,\alpha} \to \mathcal{P} c^\dagger_{i,\alpha} \mathcal{P}, \tag{2.17}$$

where $\mathcal{P} = \prod_i [1 - n_{i,\uparrow} n_{i,\downarrow}]$. Gutzwiller projectors suppress all amplitudes corresponding to states with doubly occupancy. Such a projection is rather difficult to treat exactly [MV87], however has been examined in a variety of approximations.

In an early attempt, the presence of vacancies was considered in a so-called Gutzwiller approximation [ZGRS88, Hsu90], where the coupling and hopping amplitudes in the tJ model are replaced by effective renormalized parameters [Vol84]. The resulting effective tJ model was then solved in a Hartree-Fock-BCS approximation. Furthermore, mean-field approaches were developed in a variety of directions to find a reliable approximation for the non-projected trial wavefunction $|\psi_0\rangle$ [LNW06]. Two prominent examples for such trial wave functions are spin density waves [ALR+04] or s-wave superconducting states [BCS57a]. Frequently in this context, slave-particle representations for fermionic [AA88a, Yos89, CRKL90] and bosonic degrees of freedom [Bar76, Col84, KR86] appear. Both approaches have in common that the local Hilbert space is separated in charge and spin degrees of freedom. If treated exactly, slave-fermion and -boson representations lead to the same results. However, depending on the approximations used within one or the other framework, different types of mean-field ground states can be observed.

Let us focus for a moment on the slave-boson approach. The electron operator is thereby separated into a charge neutral and charge sector relative to the half-filled local occupation:

$$c^\dagger_{i,\alpha} = f^\dagger_{i,\alpha} b_i + \epsilon_{\alpha\beta} f_{i,\beta} d^\dagger_i, \tag{2.18}$$

where the bosonic operators $b^\dagger_i, b_i$ correspond to vacant states, $d^\dagger_i, d_i$ to doubly occupied sites and $f^\dagger_{i,\alpha}, f_{i,\alpha}$ to single occupied sites with spin α [Bar76, Col84]. The correct sign of the fermionic wave functions is taken care of by the antisymmetric tensor $\epsilon_{\uparrow\downarrow} = -\epsilon_{\downarrow\uparrow} = 1$. Projecting out doubly occupied sites reduces the electron operator to a spinon-holon representation of the following form

$$c^\dagger_{i,\alpha} = f^\dagger_{i,\alpha} b_i. \tag{2.19}$$

After rewriting the tJ model in such a slave-particle representation, the Hamiltonian is usually decoupled in particle-hole (hopping) and particle-particle (pairing) channels:

$$\chi_{ij} = \sum_\alpha \langle f^\dagger_{i,\alpha} f_{i,\alpha} \rangle, \tag{2.20}$$

$$\Delta_{ij} = \langle f^\dagger_{i,\uparrow} f^\dagger_{j,\downarrow} - f^\dagger_{i,\downarrow} f^\dagger_{j,\uparrow} \rangle. \tag{2.21}$$

In 1987, Philip W. Anderson proposed as a possible ground state for the tJ model a uniform RVB state with $\chi_{ij} = \chi$ and $\Delta_{ij} = 0$. Other mean-field wave functions followed including d-wave superconducting and staggered flux states [AZHA88, AM88, DFM88]. Later, the approach was extended towards including long-range antiferromagnetic ordering [Hsu90, HMA91]. Away from half-filling, holes represented by bosonic operators like in Eq. 2.19 move through the system, interact and condense below a certain temperature threshold T_{BE} [KL88].

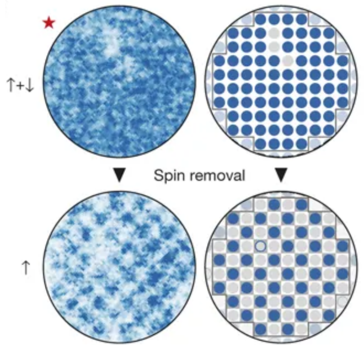

Figure 2.6 The left column contains raw snapshots (red star indicates the parameter values of the experiment; cf. Fig. 2.8) from fluorescence imaging. They have been converted into images showing the according micoscopic spin configurations on a checkerboard background (right column), reprinted by permission from Springer Nature Customer Service Centre GmbH: Springer Nature, Nature, Ref. [MCJ+17], Copyright (2017). One spin species has been removed in the experiment using a laser beam.

On the other hand, within a slave-fermion representation the spin index is attributed to bosons, which are frequently called Schwinger bosons. It was later extended towards a SU(N) description, where the local spin degrees of freedom have N flavors. Such a mean-field approach can be used to describe spin-density and dimerized states [AA88a, RS90, RS91]. In general, the slave-particle formulations bring along gauge redundancies. This was first pointed out by Ganapathy Baskaran and Philip W. Anderson in a work in 1988, in which they explored a U(1) gauge degree of freedom [BA88]. Indeed, fluctuations of the system around the mean-field saddle-point solution can be usually formulated in a gauge theory. We refer to the following literaure for a more detailed discussion on gauge theories in context of the slave-particle mean-field theories [Wen04]. Last, numerical approaches were also frequently used to study the tJ model at finite doping among which are exact diagonalization [GVL94, Toh04], self-consistent Born approximation [SRVR88, NVH+95], variational and Green's function Monte Carlo simulations [DNM95, SMB+02].

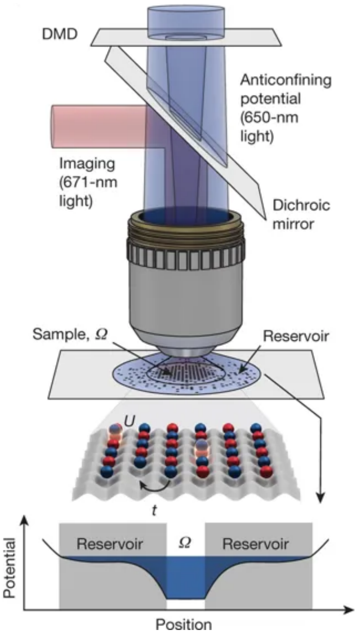

Figure 2.7 The microscopy setup: Trapped ^{6}Li atoms in a two-dimensional optical lattice with an interior region and an exterior entropy reservoir generated by the digital micromirror device (DMD), reprinted by permission from Springer Nature Customer Service Centre GmbH: Springer Nature, Nature, Ref. [MCJ+17], Copyright (2017). We refer for further details on the setup to this article.

Spinon-dopon mean-field description As pointed out in the last section, mean-field approaches have a long tradition in condensed matter physics and are frequently used to construct trial wave functions. Tiago C. Ribeiro an Xiao-Gang Wen proposed in 2006 an extension to slave-particle mean-field theories that is able to describe a variety of different ground state wave fuctions such as Fermi liquid, d-wave superconducting and fractionalized Fermi liquid states [RW06]. In this section we shortly summarize the main idea of this so-called spinon-dopon representation.

Here, the local Hilbert space is first enlarged by an additional local spin-1/2 degree of freedom $|\alpha,\sigma\rangle$ named dopon and represented by the operators $\{d^\dagger_{i,\alpha}, d_{i,\alpha}\}$. The occupation of the first component is measured by the following spin operator: $\tilde{S}^z_i\,|\alpha\sigma\rangle = \alpha\,|\alpha\sigma\rangle$. Tiago C. Ribeiro an Xiao-Gang Wen proposed a mapping between the physical relevant states and the enlarged Hilbert space as follows

$$|\uparrow\rangle_i \leftrightarrow |\uparrow 0\rangle_i\,, \tag{2.22}$$

$$|\downarrow\rangle_i \leftrightarrow |\downarrow 0\rangle_i\,, \tag{2.23}$$

$$|0\rangle_i \leftrightarrow \frac{|\uparrow\downarrow\rangle_i - |\downarrow\uparrow\rangle_i}{\sqrt{2}}, \tag{2.24}$$

According to this, the projected electron operator in the dopon-spinon Hilbert space reads

$$\mathcal{P}c^\dagger_{i,\alpha}\mathcal{P} = s_\sigma \tfrac{1}{\sqrt{2}}\tilde{\mathcal{P}}[(\tfrac{1}{2} + s_\sigma \tilde{S}^z_i) - \tilde{S}^{s_\sigma}_i d_{i,\sigma}]\tilde{\mathcal{P}}, \tag{2.25}$$

What is the benefit from this spinon-dopon representation compared to other particle-slave approaches? Instead of filling up a Fermi sea from the projected fermionic electron operators in Eq. 2.17, Tiago C. Ribeiro and Xiao-Gang Wen took the point of view on the system from the Mott insulating phase. Here, interacting vacancies are included in the background of a magnetic spin state. In contrast to the slave-boson representation, where the holon is assumed to carry solely a charge and no spin, the dopon has charge $+e$ and spin $S = 1/2$. Here, a holon is represented by a local singlet formed between a spinon and dopon (s. Eq. 2.24). In a Mott insulator the creation of a vacancy has a strong impact on the spin background. In the spinon-dopon representation the spin background is literally decoupled by introducing locally a second spin-1/2 degree of freedom. The vacancy can thus be put into any form of magnetic background in accordance with experiments on cuprates that detected short-range antiferromagnetic ordering at small doping (s. Ref. in Sec. 2.4). The tJ Hamiltonian in the spinon-dopon representation takes a form similar to the Kondo-Heisenberg model in Eq. (2.15). Subsequent works have indeed explicitly verified that the single-band tJ model within this framework yields a fractionalized Fermi liquid ground state in certain parameter regimes.

For instance, the Fermi surface volume was calculated in a diagrammatic expansion [PS12]. In the article below, we also calculate a trial wavefunctions from the spinon-dopon mean-field approach with long- and short-range magnetic order.

2.7 Fermionic gas microscope

Ultracold atoms in optical lattice systems provide highly tunable platforms to simulate lattice models [BDZ08, GB17]. Atoms are hereby confined in approximately harmonic optical or magnetic traps. Ultracold gas experiments often use sinusoidal optical lattices created by Gaussian red- or blue-detuned beams to capture atoms in a potential landscape. The eigenstates of electrons are according to band theory given by Bloch functions [AM12], which however decay due to the trap potential over a few lattice spacings. The electrons occupy the Bloch eigenstates from the bottom up according to the dispersion. In the zero temperature limit, the average particle density is inhomogeneous and increases towards the center of the trap [RM04].

In the last few years, the Hubbard model for bosonic particles has been studied extensively in such inhomogeneous optical lattices [GMHB02, GZHC09, SWE$^+$10, BPT$^+$10, FWM$^+$06]. However, for many interesting topics including for instance high-T_c, it is necessary to realize such experiments with fermionic particles. The single-band Fermi-Hubbard model in optical lattices is given by [Ess10]

$$H_{\mathrm{FHM}} = -t \sum_{\langle i,j\rangle,\alpha} [c^\dagger_{i,\alpha} c_{j,\alpha} + \text{h.c.}] + U \sum_i n_{i,\uparrow} n_{i,\downarrow} + \sum_{i,\alpha} \epsilon_i n_{i,\alpha}. \tag{2.26}$$

The first term is associated to tunneling of particles between two nearest neighboring sites in the tight-binding regime [HNUM10]. The hopping amplitude t can be calculated using Wannier states $\phi(r - R_i)$ centered around an ion at position R_i for the lowest band as follows [Geo07]

$$t = -\int d^3r \phi(r - R_i)[-\frac{\hbar^2 \nabla^2}{2m} + V_{\mathrm{latt}}(r)]\phi(r). \tag{2.27}$$

Furthermore, short-range s-wave collisions with scattering length a_s between atoms lead to an effective interaction U. The atoms are neutral and thus do not have mutual Coulomb interaction [BDZ08]. The on-site interaction strength reads

$$U = g \int d^3r |\phi(r)|^4, \tag{2.28}$$

where we consider a pseudopotential of the form $g\delta(r)$ due to pair collisions of atoms in the small temperature regime of mK [BDZ08]. The interaction strength is tunable via the Feshbach resonance.

The last term in Eq. (2.26) is a local energy offset generated by the underlying optical lattice and is not part of the Fermi-Hubbard model itself. Usually, such a scattering potential ϵ_i is treated in a local density approximation in case the variation of the potential is sufficiently smooth [SPOT09].

Meanwhile, quantum gas microscopes are used in ultracold gas experiments and enable site-resolved observation of correlation and fluctuation functions. Such a microscopy technique has been first successfully applied to bosonic systems [BPT$^+$10, SWE$^+$10] to measure spatial and temporal information of observables in context of correlated quantum walks [PMT$^+$15] and dynamical properties of magnetic systems [FSE$^+$13, HFS$^+$14]. Afterwards, technical setups have been developed for fermionic systems [GPM+16, CNL+16, CMD+16] and used in various directions. The experiments usually start with the creation of a two-dimensional gas of ^{6}Li atoms in the two lowest hyperfine ground states. A Feshbach resonance at 832 G is used to tune the interaction independent from the hopping amplitudes t_x/t_y. The latter is fixed by the potential depth. The metal to Mott insulator transition in two-dimensional systems has been observed by varying the s-wave scattering length applying an external magnetic field in the vicinity of the Feshbach resonance [GPM+16]. The gas mixture is then loaded into the optical trap. We refer for more details on evaporation and cooling procedures to the literature [BDZ08]. Finally, optical measurements are performed along two lines: In some experiments a superlattice in combination with an external magnetic field subdivides the overall spin configuration into subsystems with solely spin-up, spin-down, doubly or empty occupied sites [BHS+16]. This procedure enables the independent measurement of charge and spin degrees of freedom and has been successfully applied in one-dimensional systems [BHS+16]. Another method is to first remove all particles of one spin component using for instance an appropriate laser beam and investigate afterwards the charge correlation functions of the remaining particles [PMC+16] (s. Fig. 2.6). Here, the doubly occupied sites are also removed and appear as empty sites. Within both procedures, snapshots of the atom clouds are taken by fluorescence imaging. Fermionic quantum gas microscopy has led to several achievements. For instance, a hidden finite-range antiferromagnetic ordering as a conseuqence of spin-charge separation has been succesfully observed in one-dimensional systems [HSG+17]. The quantum gas microscope has also been applied to two-dimensional systems. Here, transport measurements were performed in the linear response regime and revealed signatures of bad metal behaviour in the conductivity [BMGS+19].

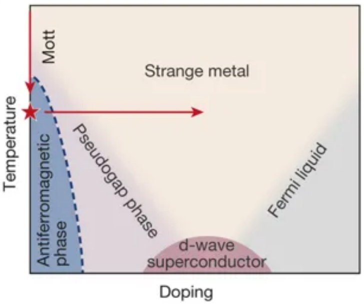

Figure 2.8 Schematic phase diagram of the hole-doped regime of the two-dimensional Fermi-Hubbard model, reprinted by permission from Springer Nature Customer Service Centre GmbH: Springer Nature, Nature, Ref. [MCJ+17], Copyright (2017). The red arrow illustrates the doping and temperature regime currently accessible to quantum Fermi microscopy experiments. The snapshots in Fig. 2.6 are taken at parameter values indicated here by the red star.

Latest studies took machine learning tools to classify snapshots of spin configurations from the doped Hubbard model. The goal was to train a network to assign an appropriate theoretical description to a snapshot [BCJ+19]. Furthermore, the formation of long-range magnetic ordering when doping the two-dimensional Fermi-Hubbard model has recently attracted much attention [PMC+16]. Of course, long-range ordered magnetic states in two-dimensional systems at finite temperature are not possible due to the Mermin-Wagner theorem. Indeed, the correlation length is expected to decrease exponentially with respect to the inverse temperature. In the corresponding experiments the correlation length was approximately eight lattice spacings long, which is relatively large compared to the system size 10 × 10 (s. Fig. 2.7). The overall lattice system itself is actually much larger and consists of an interior region separated from a large entropy reservoir by a lattice potential using a digital micromirror device (DMD) [LKJBH10]. The entropy reservoir is thereby used to reduce the temperature in the interior system [HZ09b]. Temperatures of $T \approx 0.1t$ have been achieved and are in proximity to the onset of the pseudogap phase (s. Fig. 2.8).

The field of microscopy in ultracold gases has developed very fast in the last few years. In case the temperature can be further decreased in such experiments (for literature in this direction s. Ref. [BKG+09, HZ09a]), complex condensed matter concepts, e.g. stripe ordering and frustration, are soon accessible and can be investigated down to single-site resolution.

2.8 Signatures of magnetic ordering

2.8.1 Overview

The phase diagram of the two-dimensional Fermi-Hubbard model potentially contains a variety of exotic phases partially suffused with incommensurate and commensurate spin density wave ordering [LNW06]. According to the last section, quantum gas microscopy experiments start now probing a wide range of the parameter regimes [MCJ+17]. Former measurements have detected magnetic ordering from correlation functions [BDZ08]. Such approaches commonly have the disadvantage to hardly distinguish magnetically ordered from spin liquid states, where in the latter case ordering might be still present on very short distances. Furthermore, such experiments mainly focus on the mean average of observables and thereby neglect the information contained in higher-order correlation functions.

A solution to this discrepancy has been proposed in Ref. [HLS+08] introducing full counting statistics. After splitting a one-dimensional Bose gase trapped on an atom chip [SHA+05, HLF+06, LSH+06, FKS+08], the subsequent time evolution has been studied by performing a sequence of interference experiments. Statistics of thermal and quantum noise have been collected and reveal information on higher-order correlation functions of the one-dimensional system. Such attempts have been also adopted to quantum microscopy experiments for the two-dimensional Fermi-Hubbard model [MCJ+17]. The staggered spin ordering vector $m = (m_x, m_y, m_z)$ was measured for various temperatures at half-filling. In each experimental realization, the spins point into different directions on a sphere due to the SU(2) rotation symmetry of the Hubbard model. The results show that the probability $p(m_z)$ at high temperature is uncorrelated and thus follows a binominal distribution. At lower temperatures the probability distribution gets thermally broadened. Ab intio quantum Monte Carlo simulations of the Heisenberg model have confirmed the experimental measurements.

Our work focuses on the two-spin density matrix ρ^S as the central observable. We project it onto the triplet sector of neareast neighboring spins $\langle t|\,\rho^S\,|t\rangle$ and determine the respective probability distribution (s. Fig. 2.9). In order to eliminate broadening effects due to quantum fluctuations, we perform an averaging process over two-site unit cells within each experimental realization. The statistical distribution of the order parameter is directly reflected in the projected two-spin density matrix. As a consequence, the probability distribution is expected to be solely broadened in case the system is described by a state with long-range magnetic order. We study this using the spinon-dopon representation and perform a mean-field approach for fixed parameter values of hopping amplitudes and interaction. The corresponding phase

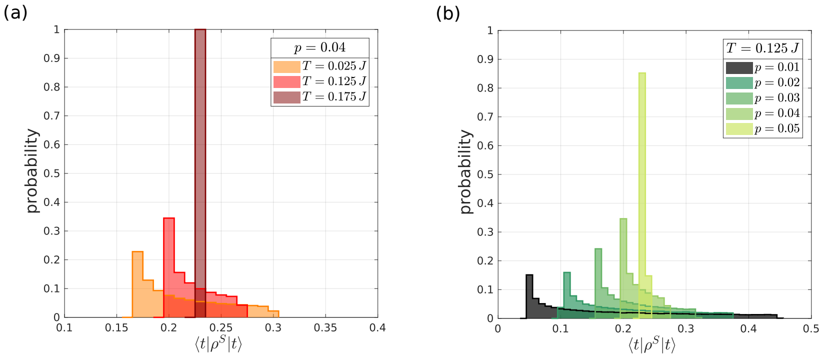

Figure 2.9 (a) The antiferromagnetic state is melted when increasing the temperature until the SU(2) symmetry is completely restored at $T^* = 0.175J$ for fixed doping $p = 0.04$. (b) The probability distribution is sharpened above a critical doping $p^* = 0.05$ at fixed temperature $T = 0.125J$. Fig. is reprinted with permission from Ref. [HGP19]. Copyright (2019) by the American Physical Society.

diagram contains regions with an antiferromagnetically ordered ground state lying next to a SU(2) symmetric fractionalized Fermi liquid ground state. By varying the temperature T and doping p, we can continously tune between the two states. We concluded with the following results:

- The antiferromagnetic ordering was melted when increasing the temperature (s. Fig. 2.9 (a)). In the limit where the ground state is a fractionalized Fermi liquid with restored SU(2) symmetry, the probability distribution is sharp. This measurement protocol is expected to be very sensitive and should be able to distinguish short- and long-range ordered states even if the correlation length is just a few lattice spacings.

- As shown in Fig. 2.9 (b), doping the system induces frustration and has a similar effect as increasing the temperature. The antiferromagnetically ordered background is continuously destroyed due to the presence of holes in the system.

Signatures of correlated magnetic phases in the two-spin density matrix

by

S. Huber, F. Grusdt, and M. Punk

Physics Department, Arnold Sommerfeld Center for Theoretical Physics and Center for NanoScience, Ludwig-Maximilians-Universität München, 80333 München, Germany

reprinted on pages 24–37

with permission from

Phys. Rev. A **99(2), 023617 (2019)**,

DOI: 10.1103/PhysRevA.99.023617.

PHYSICAL REVIEW A **99**, 023617 (2019)

Signatures of correlated magnetic phases in the two-spin density matrix

Sebastian Huber,[1] Fabian Grusdt,[2] and Matthias Punk[1]
[1]*Physics Department, Arnold Sommerfeld Center for Theoretical Physics, and Center for NanoScience, Ludwig-Maximilians University Munich, Munich, Germany*
[2]*Department of Physics, Harvard University, Cambridge, Massachusetts 02138, USA*

(Received 20 August 2018; published 12 February 2019)

Experiments with quantum gas microscopes have started to explore the antiferromagnetic phase of the two-dimensional Fermi-Hubbard model and effects of doping with holes away from half filling. In this work we show how direct measurements of the system averaged two-spin density matrix and its full counting statistics can be used to identify different correlated magnetic phases with or without long-range order. We discuss examples of phases which are potentially realized in the Hubbard model close to half filling, including antiferromagnetically ordered insulators and metals, as well as insulating spin liquids and metals with topological order. For these candidate states we predict the doping- and temperature dependence of local correlators, which can be directly measured in current experiments.

DOI: 10.1103/PhysRevA.99.023617

I. INTRODUCTION

Ultracold atomic gases in optical lattices provide a versatile platform to study strongly correlated phases of matter in a setting with unprecedented control over Hamiltonian parameters [1,2]. Moreover, the development of quantum gas microscopes now allows for the direct measurement of real-space correlation functions with single-site resolution in important model systems like the Fermi-Hubbard model, giving access to viable information that can be used to identify various quantum states of matter. Using state-of-the-art technology the many-body wave function can now be imaged on a single-site and single-fermion level [3–7] and even the simultaneous detection of spin and charge (i.e., particle-number) degrees of freedom has been achieved [6]. In combination with the capability to perform local manipulations, insights can be obtained into the microscopic properties of strongly correlated quantum many-body systems, which are difficult to access in traditional solid-state systems. For example, the hidden string order underlying spin-charge separation in the one-dimensional t-J model has been directly revealed in a quantum gas microscope [8]. Ultracold atom experiments have also revealed charge ordering in the attractive Fermi-Hubbard model at half filling [9] and observed longer-ranged antiferromagnetic (AFM) correlations [10,11]. Furthermore transport properties of the two-dimensional Fermi-Hubbard model were investigated independently for spin and charge degrees of freedom by exposing the system to an external field in the linear-response regime [12,13], where clear signatures of bad metal behavior have been detected in the temperature dependence of the charge conductivity [13]. In all these settings, the ultracold atom toolbox can now be applied to gain insights.

One of the big open problems in the field of strongly correlated electrons is to understand the fate of the AFM Mott insulator in quasi-two-dimensional square lattice systems upon doping it with holes. This problem is particularly relevant in the context of the so-called pseudogap phase in underdoped high-temperature cuprate superconductors [14]. In the last decades many works have shown that the two-dimensional one-band Hubbard model below half filling captures various phenomena which are found in the phase diagram of cuprates, including superconductivity and charge-density-wave ordering, among others [15–17].

Quantum gas microscopy experiments are now starting to probe the interesting temperature and doping regime in the Fermi-Hubbard model where correlation effects in doped Mott insulators become visible across the entire system [11], providing valuable insight into this problem. This immediately raises the question of how the various symmetric or symmetry-broken phases that have been proposed theoretically below half filling can be identified in these experiments. Since accessible temperatures are still rather high, $T \gtrsim 0.5J$ where J is the superexchange energy, the correlation length of symmetry-broken phases is typically on the order of several lattice spacings, making a direct detection of order parameters challenging. Moreover, various symmetric phases which have been proposed as potential ground states away from half filling, such as doped resonating-valence bond (RVB) states [18–20], have very similar short-range spin-spin correlations as magnetically ordered states with a short correlation length. For this reason measurements of spin-spin correlators, which are routinely performed in current quantum gas microscopy experiments, can hardly distinguish these conceptually very different states. In some important cases the symmetric states are characterized by more complicated topological order parameters, which are hard to measure in experiments, however.

In this work we show how measurements of the reduced two-particle density matrix, see Fig. 1, provide a signature of different interesting phases that might be realized in the doped Fermi-Hubbard model at strong coupling. We focus our discussion on phases with strong spin-singlet correlations and show that the presence or absence of SU(2) spin rotation symmetry has a clear signature in the full counting statistics (FCS) of the system-averaged reduced density matrix, allowing

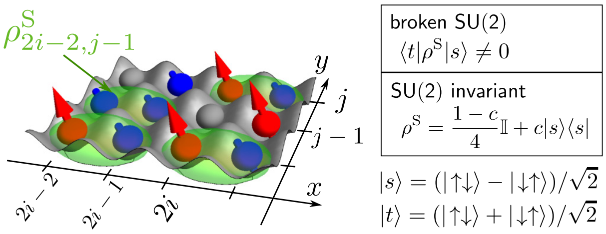

FIG. 1. The two-spin reduced density matrix ρ^{S}, measurable in ultracold atom experiments, and its full counting statistics (FCS) can be used to distinguish between symmetric and symmetry-broken phases in the Fermi-Hubbard model. The ground state on the square lattice at half filling has AFM order, which leads to nonvanishing singlet-triplet matrix elements $\langle t|\rho^{\mathrm{S}}|s\rangle \neq 0$ as well as a broad distribution of the triplet matrix element in the FCS, even if the correlation length is finite. Below half filling the precise nature of the ground state is still under debate, with doped quantum spin liquids as one possible scenario. These give rise to a SU(2) invariant two-spin reduced density matrix with vanishing singlet-triplet matrix elements, as well as a sharp delta-function distribution of the triplet amplitude.

us to distinguish phases with AFM order from symmetric RVB-like phases, even if the correlation length is finite. In addition we provide results for the doping and temperature dependence of nearest-neighbor spin correlators for a metallic antiferromagnet and a doped spin liquid, as a guide for future experiments.

The paper is organized as follows. In Sec. II we introduce the two-spin reduced density matrix and discuss how its elements can be measured in quantum gas microscopy experiments. Furthermore, we show how the FCS of the system-averaged reduced density matrix for two neighboring sites can be utilized to distinguish symmetric from symmetry-broken phases. The following sections provide explicit examples: in Sec. III we discuss the half filled case and present results for Mott insulators with long-range AFM order as well as for insulating quantum spin liquids. Finally, in Sec. IV we calculate the reduced two-spin density matrix and its FCS for two examples below half filling: an AFM metal as well as a metallic state with topological order and no broken symmetries.

II. TWO-SPIN REDUCED DENSITY MATRIX AND FULL COUNTING STATISTICS

In this paper we consider the two-spin reduced density matrix of nearest-neighbor sites, see Fig. 1, which contains information about all local spin-correlation functions. We discuss how its matrix elements can be measured in ultracold atom setups and show how states with broken symmetries and long-range order can be distinguished from symmetric states by considering the FCS of the reduced density matrix from repeated experimental realizations. Our approach thus provides tools to address the long-standing question of how AFM order is destroyed at finite hole doping using ultracold atom experiments at currently accessible temperatures.

A. Two-spin reduced density matrix

The local two-site reduced density matrix $\rho_{i,j}$, corresponding to sites $\boldsymbol{i}$ and $\boldsymbol{j} = \boldsymbol{i} + \boldsymbol{e}_x$ on a square lattice, is defined by tracing out all remaining lattice sites $\boldsymbol{r}$ in the environment, $\rho_{i,j} = \mathrm{tr}_{\boldsymbol{r}\neq i,j}\,\rho$, where ρ is the density matrix of the entire system. In general $\rho = e^{-\beta\mathcal{H}}$ describes a thermal state. We consider states with a definite particle number $[\rho, N] = 0$, where N is the total particle number operator. As a result the two-site density matrix is block diagonal, $\rho_{i,j} = \mathrm{diag}(\rho^{(0)}_{i,j}, \rho^{(1)}_{i,j}, \dots)$ and contains sectors with $n = 0, 1, \dots, 4$ fermions for spin-1/2 systems (see Appendix A for details). In the rest of the paper we will only consider situations where the two sites $\boldsymbol{i}$ and $\boldsymbol{j}$ are occupied by precisely one fermion each, irrespective of the total fermion density, and calculate the two-spin reduced density matrix ρ^{S}. It is obtained from the block with two fermions and proper normalization. Experimentally it can be obtained by postselecting measurement outcomes with two particles on the two sites.

More specifically we will consider spin-1/2 fermions and represent the two-spin reduced density matrix $\rho^{\mathrm{S}}_{i,j}$ in the z basis $\{|\uparrow\uparrow\rangle, |\uparrow\downarrow\rangle, |\downarrow\uparrow\rangle, |\downarrow\downarrow\rangle\}$, where the first spin refers to site $\boldsymbol{i}$ and the second to site $\boldsymbol{j}$. It can be written explicitly in terms of local correlation functions in the z basis,

$$\rho^{S}_{i,j} = \frac{1}{4}\mathbb{1} + \frac{1}{2}\begin{pmatrix} \langle S^z_i\rangle + \langle S^z_j\rangle & \langle S^+_j\rangle & \langle S^+_i\rangle & 0 \\ \langle S^-_j\rangle & \langle S^z_i\rangle - \langle S^z_j\rangle & 0 & \langle S^+_i\rangle \\ \langle S^-_i\rangle & 0 & -\langle S^z_i\rangle + \langle S^z_j\rangle & \langle S^+_j\rangle \\ 0 & \langle S^-_i\rangle & \langle S^-_j\rangle & -\langle S^z_i\rangle - \langle S^z_j\rangle \end{pmatrix} + \begin{pmatrix} \langle S^z_i S^z_j\rangle & \langle S^z_i S^+_j\rangle & \langle S^+_i S^z_j\rangle & \langle S^+_i S^+_j\rangle \\ \langle S^z_i S^-_j\rangle & -\langle S^z_i S^z_j\rangle & \langle S^+_i S^-_j\rangle & -\langle S^+_i S^z_j\rangle \\ \langle S^-_i S^z_j\rangle & \langle S^-_i S^+_j\rangle & -\langle S^z_i S^z_j\rangle & -\langle S^z_i S^+_j\rangle \\ \langle S^-_i S^-_j\rangle & -\langle S^-_i S^z_j\rangle & -\langle S^z_i S^-_j\rangle & \langle S^z_i S^z_j\rangle \end{pmatrix}. \tag{1}$$

Here, $S^\alpha_{\boldsymbol{i}}$ is the spin operator on lattice site $\boldsymbol{i}$ with $\alpha \in \{0, +, -, z\}$ and we define $S^0_{\boldsymbol{i}} = \mathbb{1}_{\boldsymbol{i}}$ as the identity operator. Note that the expectation values $\langle\cdot\rangle$ are defined after postselecting states with precisely one fermion each on sites $\boldsymbol{i}$ and $\boldsymbol{j}$.

For quantum states ρ commuting with S^z, i.e., $[\rho, S^z] = 0$, the two-spin density matrix becomes block diagonal. The first two blocks are one-dimensional and correspond to the ferromagnetic basis states $|\uparrow\uparrow\rangle$ and $|\downarrow\downarrow\rangle$. The third block corresponds to the two-dimensional subspace spanned by the antiferromagnetic states $|\uparrow\downarrow\rangle$ and $|\downarrow\uparrow\rangle$. If the state ρ has an additional $S^z \to -S^z$ symmetry, which follows from a global SU(2) symmetry for example, the reduced density matrix simplifies further because the entire second line of Eq. (1) vanishes identically and we get

$$\rho^{S}_{i,j} = \frac{1}{4}\mathbb{1} + \begin{pmatrix} \langle S^z_i S^z_j\rangle & 0 & 0 & 0 \\ 0 & -\langle S^z_i S^z_j\rangle & \langle S^+_i S^-_j\rangle & 0 \\ 0 & \langle S^-_i S^+_j\rangle & -\langle S^z_i S^z_j\rangle & 0 \\ 0 & 0 & 0 & \langle S^z_i S^z_j\rangle \end{pmatrix}. \tag{2}$$

In this paper we are particularly interested in cases with spontaneously broken or unbroken SU(2) symmetry and how it manifests in the two-spin density matrix. For this purpose it is more convenient to represent the two-dimensional subblock of the reduced density matrix in the singlet-triplet basis defined by

$$|s\rangle = \frac{1}{\sqrt{2}}[|\uparrow\downarrow\rangle - |\downarrow\uparrow\rangle], \tag{3}$$

$$|t\rangle = \frac{1}{\sqrt{2}}[|\uparrow\downarrow\rangle + |\downarrow\uparrow\rangle]. \tag{4}$$

In the rest of this paper we will focus on the following combinations of matrix elements of the two-spin density matrix:

$$p_{\mathrm{f}} = \langle\uparrow\uparrow|\rho^{\mathrm{S}}|\uparrow\uparrow\rangle + \langle\downarrow\downarrow|\rho^{\mathrm{S}}|\downarrow\downarrow\rangle \tag{5}$$

denotes the probability to observe ferromagnetic correlations on the two sites of interest $\boldsymbol{i}$ and $\boldsymbol{j}$. It can be directly measured in the S^z basis. Moreover

$$p_{\mathrm{s}} = \langle s|\rho^{\mathrm{S}}|s\rangle \quad \text{and} \quad p_{\mathrm{t}} = \langle t|\rho^{\mathrm{S}}|t\rangle \tag{6}$$

denote the singlet and triplet probabilities and

$$p_{\mathrm{st}} = \langle s|\rho^{\mathrm{S}}|t\rangle = \tfrac{1}{2}(\langle\uparrow\downarrow|\rho^{\mathrm{S}}|\uparrow\downarrow\rangle - \langle\downarrow\uparrow|\rho^{\mathrm{S}}|\downarrow\uparrow\rangle) + i\mathrm{Im}\langle\uparrow\downarrow|\rho^{\mathrm{S}}|\downarrow\uparrow\rangle \tag{7}$$

is the singlet-triplet matrix element. The real part of p_{st} can be again directly measured in the S^z basis.

The singlet and triplet probabilities $p_{\mathrm{s,t}}$ can be measured in ultracold atom systems by utilizing the single-site control over spin-exchange interactions in optical superlattices pioneered in Ref. [21]. To this end one can first increase the lattice depth, which switches off all superexchange interactions. Next a magnetic-field gradient along the x direction is switched on for a time τ_1 which leads to a Zeeman energy difference Δ of the two states $|\uparrow\downarrow\rangle$ and $|\downarrow\uparrow\rangle$ and drives singlet-triplet oscillations. Choosing $\tau_1 = \pi/(2\delta)$ the singlet-triplet basis $\{|s\rangle, |t\rangle\}$ is mapped to $\{(|\uparrow\downarrow\rangle \pm i|\downarrow\uparrow\rangle)/\sqrt{2}\}$. Subsequently a superlattice can be used to switch on spin-exchange couplings of strength J between sites $(2i, j)$ and $(2i+1, j)$ for a finite time τ_2. By choosing $\tau_2 = \pi/(2J)$ the original singlet-triplet basis $\{|s\rangle, |t\rangle\}$ is now mapped on $\{|\downarrow\uparrow\rangle, |\uparrow\downarrow\rangle\}$. After this mapping a measurement in the z basis directly reveals the singlet and triplet probabilities, $p_{\mathrm{s}} = \langle|\downarrow\uparrow\rangle\langle\downarrow\uparrow|\rangle$ and $p_{\mathrm{t}} = \langle|\uparrow\downarrow\rangle\langle\uparrow\downarrow|\rangle$, where the expectation values $\langle\cdot\rangle$ are taken in the measurement basis.

B. Shot-to-shot full counting statistics

Ultracold atoms not only provide direct access to local correlation functions, but also to the FCSs of physical observables, which contain additional information about the underlying many-body states beyond the expectation values in Eq. (1) [22]. On the one hand the FCSs contain information about quantum fluctuations. On the other hand they can be used to reveal broken symmetries which manifest in long-range order in the system [11].

In this paper we study the local, reduced two-spin density matrix ρ^S and its FCS in an infinite system. Our goal is to distinguish between fully SU(2) symmetric quantum states with short-range correlations, and symmetry-broken states with conventional long-range order, despite the fact that these phases can have very similar properties locally. This can be achieved by considering the FCS of ρ^S as follows: for symmetry broken states the direction of the order parameter varies randomly between experimental shots, giving rise to a specific probability distribution of ρ^S in a given measurement basis. This distribution can be obtained directly from experiments by compiling histograms of a large number of experimental shots. By contrast, this distribution will consist of a single delta-function peak for states with no broken symmetry. It is important to realize, however, that ρ^S also takes different values on different lattice sites within a single experimental shot, which reflects the inherent quantum-mechanical probability distribution of ρ^S. Determining this quantum-mechanical probability distribution is usually referred to as FCS in the condensed-matter literature. In order to single out the effect of order-parameter fluctuations, we first have to average the two-spin density matrix over the entire system in every shot:

$$\rho^{\mathrm{S}} = \frac{2}{L_x L_y} \sum_{\boldsymbol{i}\in\mathrm{UC}} \rho^{\mathrm{S}}_{\boldsymbol{i},\boldsymbol{i}+\boldsymbol{e}_x}, \tag{8}$$

where $L_{x,y} \to \infty$ denotes the linear system size. We divide the lattice into two-site unit cells along x, labeled by one of their site indices $\boldsymbol{i} \in \mathrm{UC}$, in which the reduced two-spin density matrix $\rho^{\mathrm{S}}_{\boldsymbol{i},\boldsymbol{i}+\boldsymbol{e}_x}$ is measured; see Fig. 1. Accordingly, the sum $\sum_{\boldsymbol{i}\in\mathrm{UC}}$ in Eq. (8) is taken over all such unit cells. This corresponds to an average over the quantum-mechanical probability distribution and ensures that the resulting ρ^S is insensitive to quantum fluctuations. Consequently, we can single out effects of the classical probability distribution of ρ^S which arises from different realizations of the order parameter and allows us to distinguish symmetric from symmetry-broken states.

The shot-to-shot FCS of $\rho^{\mathrm{S}}(n)$ is obtained by measuring $\rho^{\mathrm{S}}_{\boldsymbol{i},\boldsymbol{i}+\boldsymbol{e}_x}$ for all unit cells at positions $\boldsymbol{i}$ in a single shot n, which yields a measurement outcome for a specified matrix element of $\rho^{\mathrm{S}}_{\boldsymbol{i},\boldsymbol{i}+\boldsymbol{e}_x}(n)$, and taking the system average in Eq. (8). This procedure is repeated N_{s} times using a fixed measurement basis (e.g., S^z) and histograms of the matrix elements of $\{\rho^{\mathrm{S}}(n)\}_{n=1\ldots N_{\mathrm{s}}}$ yield the desired statistics.

In a translationally invariant system with short-range correlations the state ρ is symmetric and has no long-range order. In this case the shot-to-shot FCS of ρ^{S} becomes a delta function,

$$\mathcal{P}[\rho^{\mathrm{S}}]|_{\mathrm{sym.}} = \delta\big(\rho^{\mathrm{S}} - \rho^{\mathrm{S}}_0\big). \tag{9}$$

Because of the exponentially decaying correlations, taking the average over the infinite system is equivalent to shot-to-shot averaging of a single pair of spins, $\rho^{\mathrm{S}}_0 = \rho^{\mathrm{S}}_{\boldsymbol{i},\boldsymbol{i}+\boldsymbol{e}_x}(n)$. In a finite system, quantum fluctuations give rise to a distribution peaked around ρ^{S}_0 which is expected to have a finite width $w \propto \xi/\sqrt{L_x L_y}$, where $\xi \ll L_{x,y}$ is the finite correlation length.

In a system with a broken symmetry and long-range correlations extending over the entire system, in contrast, spatial and shot-to-shot averaging are not equivalent in general. All measurement outcomes $\rho^{\mathrm{S}}_{\boldsymbol{i},\boldsymbol{i}+\boldsymbol{e}_x}(n) \equiv \rho^{\mathrm{S}}_{\boldsymbol{i},\boldsymbol{i}+\boldsymbol{e}_x}(n, \boldsymbol{\Omega}(n))$ explicitly depend on the order parameter $\Omega(n)$ associated with the long-range correlations in the system for shot n. As a result the system-averaged two-spin density matrix $\rho^{\mathrm{S}}(n) \equiv \rho^{\mathrm{S}}(n, \boldsymbol{\Omega}(n))$ explicitly depends on the order parameter $\boldsymbol{\Omega}(n)$.

In systems with spontaneous symmetry breaking, the order parameter $\mathbf{\Omega}(n)$ fluctuates from shot to shot. Because the averaging over the infinite system in Eq. (8) makes $\rho^{\mathrm{S}}(n)$ insensitive to local quantum fluctuations, it only depends on the order parameter, i.e., $\rho^{\mathrm{S}}(n) \equiv \rho_0^{\mathrm{S}}(\mathbf{\Omega}(n))$. Therefore the shot-to-shot FCS of ρ^{S} reflects the probability distribution $\mathcal{P}[\mathbf{\Omega}]$ of the order parameter $\mathbf{\Omega}(n)$. The probability distribution of the system-averaged reduced density matrix thus takes the form

$$\mathcal{P}[\rho^{\mathrm{S}}]|_{\text{sym.broken}} = \int d\mathbf{\Omega}\,\mathcal{P}[\mathbf{\Omega}]\,\delta\big[\rho^{\mathrm{S}} - \rho_0^{\mathrm{S}}(\mathbf{\Omega})\big]. \tag{10}$$

When the order parameter $\mathbf{\Omega}(n)$ takes a different value in every shot n, the reduced two-spin density matrix is characterized by a broad distribution function in general. Its width w converges to a finite value in the limit of infinite system size.

The reduced density matrix ρ^S defined on neighboring sites $\boldsymbol{i}$ and $\boldsymbol{i}+\boldsymbol{e}_x$, forming two-site unit cells of the square lattice, is sensitive to order parameters indicating spontaneously broken SU(2) symmetries, either ferromagnetic or AFM, and some discrete translational symmetries as expected for valence bond solids (VBSs). We note, however, that ρ^S is insensitive to other order parameters. In such cases the distribution function becomes narrow, as in Eq. (9), and the underlying ordering cannot be detected.

We close this section by a discussion of finite-temperature effects in the two-dimensional Fermi-Hubbard model. Due to the Mermin-Wagner theorem [23], no true long-range order can exist at nonzero temperatures, and the SU(2) symmetry remains unbroken. However, the correlation length increases exponentially with decreasing temperatures [11], until it reaches the finite system size. In this case, the state cannot be distinguished from a symmetry-broken state, and from Eq. (10) we expect broad distribution functions of the entries in the two-spin reduced density matrix. Because of the finite system size, the averaging in Eq. (8) does not eliminate all quantum fluctuations, however, which leads to broadened distribution functions; see Refs. [11,24] for explicit calculations. When the system is too small, a clear distinction between SU(2)-broken and SU(2)-symmetric phases is no longer possible.

III. TWO-SPIN DENSITY MATRIX AND FULL COUNTING STATISTICS AT HALF FILLING

As described above, the shot-to-shot FCS of the reduced two-spin density matrix can be used to distinguish states with broken symmetries from symmetric states. Here we consider two important examples at half filling: an AFM Mott insulator and an insulating spin liquid in the two-dimensional square lattice Fermi-Hubbard model. We emphasize that the ground state is known to be an AFM in this case. The main purpose of the spin-liquid example is to highlight the stark contrast between a magnetically ordered and a symmetric state in the two-particle density matrix in order to set the stage for the discussion of systems below half filling. The FCS of system averaged local observables is a very sensitive probe to distinguish ordered from disordered states, which are particularly hard to discern if the correlation length is short.

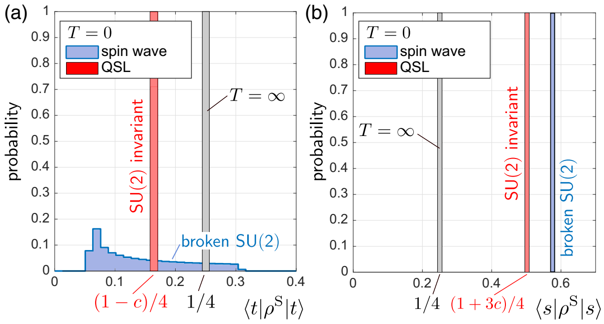

FIG. 2. Fingerprints for the spontaneous breaking of SU(2) invariance in the shot-to-shot FCS of the system-averaged reduced two-spin density matrix ρ^{S}, see Eq. (8). When the SU(2) symmetry is spontaneously broken, the order parameter points in a different direction in every shot. This results in a broad distribution function of some of the matrix elements of ρ^S. (a) We use spin-wave theory to calculate the distribution of the triplet matrix element $\langle t|\rho^{\mathrm{S}}|t\rangle$ in (a) for an infinite Heisenberg AFM at half filling. For a SU(2) invariant quantum spin liquid the distribution function in an infinite system becomes a delta peak. (b) The distribution of the singlet matrix element $\langle s|\rho^{\mathrm{S}}|s\rangle$ is a delta peak in an infinite system even when the SU(2) symmetry is broken, because the singlet state $|s\rangle$ itself is SU(2) invariant.

The ground state of the Fermi-Hubbard model at half filling breaks the SU(2) spin-rotation symmetry, it has long-range AFM order, and it is invariant under translations by integer multiples of $\boldsymbol{e}_x \pm \boldsymbol{e}_y$. The corresponding order parameter is given by the staggered magnetization, $\mathbf{\Omega} = (-1)^{j_x+j_y}\,\langle \boldsymbol{S}_{j_x,j_y}\rangle$. Because $\mathbf{\Omega}$ points in a different direction in every experimental realization and the spins are always measured in the S^z basis, we expect a broad distribution of the reduced two-spin density matrix between different experimental shots.

For example, the real part of the system-averaged singlet-triplet matrix element is given by the staggered magnetization,

$$\begin{aligned}\mathrm{Re}\,p_{\mathrm{s,t}} &= \frac{1}{L_xL_y}\sum_{\boldsymbol{i}\in\mathrm{UC}}\big(\langle\uparrow\downarrow|\rho^{\mathrm{S}}_{\boldsymbol{i},\boldsymbol{i}+\boldsymbol{e}_x}|\uparrow\downarrow\rangle - \langle\downarrow\uparrow|\rho^{\mathrm{S}}_{\boldsymbol{i},\boldsymbol{i}+\boldsymbol{e}_x}|\downarrow\uparrow\rangle\big)\\ &= \frac{1}{L_xL_y}\sum_{\boldsymbol{r}}(-1)^{r_x,r_y}\,\langle S^z_{\boldsymbol{r}}\rangle \equiv M^z_{\mathrm{stag}};\end{aligned} \tag{11}$$

see Eq. (7). Note that the sum $\sum_{\boldsymbol{i}\in\mathrm{UC}}$ in the first line is taken over all two-site unit cells, whereas the sum $\sum_{\boldsymbol{r}}$ in the second line extends over all lattice sites. The distribution function $\mathcal{P}[M^z_{\mathrm{stag}}]$ of the staggered magnetization has been measured in a finite-size system using ultracold fermions [11]. At low temperatures $\mathcal{P}[M^z_{\mathrm{stag}}]$ becomes a broad distribution which approaches a boxlike shape for an infinite system at zero temperature $T = 0$ [24]. In contrast, a narrow distribution would be expected for a SU(2) invariant quantum spin liquid.

In Fig. 2(a) we present the shot-to-shot FCS of the triplet probability p_{t}. For an infinite system at $T = \infty$, i.e., $\rho^{\mathrm{S}} = \mathbb{1}/4$, and $\mathcal{P}[p_{\mathrm{t}}] = \delta(p_{\mathrm{t}} - 1/4)$ becomes a delta function at $p_{\mathrm{t}} = 1/4$. For the quantum Heisenberg AFM at zero temperature, $T = 0$, we predict a broad distribution with $0.05 \leqslant p_{\mathrm{t}} \leqslant 0.3$. Our calculation uses linear spin-wave theory to obtain the two-spin density matrix $\rho^{\mathrm{S}}(\mathbf{\Omega} \propto \boldsymbol{e}_z)$ in a basis where the AFM order $\boldsymbol{\Omega}$ points in the z direction, as discussed in detail in Appendix B. We obtain the shot-to-shot FCS by sampling random directions $\boldsymbol{\Omega}$ and performing basis transformations $U(\boldsymbol{\Omega})$ rotating the AFM order to point along $\boldsymbol{\Omega}$, i.e., $\rho^{S}(\boldsymbol{\Omega}) = U^{\dagger}(\boldsymbol{\Omega})\,\rho^{S}(\boldsymbol{e}_z)\,U(\boldsymbol{\Omega})$.

We extend the spin-wave calculation by an external staggered magnetic field with strength h_z as a control parameter for quantum fluctuations. For a strong magnetic field the ground state is close to a classical Néel configuration and the FCS of the system-average triplet matrix element is boxlike shaped between $0 \leqslant \langle t|\rho^S|t\rangle \leqslant 0.5$ (see Appendix B for details). When we reduce the strength of the external magnetic field h_z we find that the probability distribution $\mathcal{P}[p_t]$ develops an onset at finite $p_t > 0$, as shown for $h_z = 0$ in Fig. 2(a). We conclude that this characteristic onset is due to quantum fluctuations, which are suppressed when h_z is large.

For a SU(2) invariant quantum spin liquid at $T = 0$ the system-averaged triplet probability p_{t} is a delta distribution, i.e., $\mathcal{P}[p_{\mathrm{t}}] = \delta(p_{\mathrm{t}} - p_{\mathrm{t}}^0)$. In contrast to the infinite temperature case, the expectation value p_{t}^0 generically takes values different from $1/4$, however. The SU(2) invariance determines the form of the two-spin density matrix to be [25]

$$\rho^S = \frac{1-c}{4}\mathbb{1} + c|s\rangle\langle s|, \tag{12}$$

up to a nonuniversal number $c \in [0, 1]$, which parametrizes the strength of singlet correlations. The triplet probability is thus given by $p_{\mathrm{t}} = (1 - c)/4$.

In Fig. 2(b) we show the shot-to-shot FCS of the singlet probability p_{s}, averaged over an infinite system. Because the singlet state $|s\rangle$ is invariant under SU(2) transformations, p_{s} is independent of the order parameter $\boldsymbol{\Omega}$ even when the SU(2) symmetry is spontaneously broken. As a result we obtain delta distributions $\mathcal{P}[p_{\mathrm{s}}] = \delta(p_{\mathrm{s}} - p_{\mathrm{s}}^0)$ in all considered scenarios. For a system at infinite temperature $p_{\mathrm{s}}^0 = 1/4$, i.e., $c = 0$ in Eq. (12), for a quantum spin liquid with the two-spin density matrix in Eq. (12) $p_{\mathrm{s}}^0 = (1 + 3c)/4$, and for the quantum Heisenberg AFM with broken SU(2) symmetry we find from a linear spin-wave calculation that $p_{\mathrm{s}}^0|_{\mathrm{AFM}} = 0.57$.

Analyzing the shot-to-shot FCS of the reduced two-spin density matrix represents a powerful method to distinguish states with long-range correlations from symmetric quantum spin liquids. Although we only discussed a spontaneously broken SU(2) symmetry at half filling so far, the approach also allows us to distinguish symmetry-broken states at finite doping from fully symmetric states. Valence-bond solids, which are fully SU(2) invariant but spontaneously break the lattice translation symmetry, can also be identified in this way, which is of particular importance for frustrated quantum magnets as in the J_1-J_2 model [26,27].

IV. TWO-SPIN DENSITY MATRIX AND FULL COUNTING STATISTICS BELOW HALF FILLING

One of the big open questions in studies of the Fermi-Hubbard model is to determine the nature of the ground state for strong interactions slightly below half filling. This is the regime where the infamous metallic pseudogap phase has been observed in cuprate high-temperature superconductors [14], the main properties of which are believed to be captured by the Fermi-Hubbard model [17,28,29], even though controlled, reliable numerical results do not exist. Quantum gas microscopy experiments have started to probe this regime and might provide valuable insight into this problem [11]. While many different scenarios have been proposed theoretically to explain the pseudogap phenomenology in the cuprates, we will focus our discussion of the reduced two-spin density matrix below half filling on two possible phases, in close analogy to the half filled case. The first example is a simple metallic state with long-range AFM order, whereas the second example describes a so-called fractionalized Fermi liquid (FL*), which can be understood as a doped quantum spin liquid with topological order and no broken symmetries [30]. In particular we are going to highlight signatures of these two phases as a function of temperature and as a function of the density of doped holes away from half filling. It is important to emphasize that we always consider the two-spin reduced density matrix for two neighboring, singly occupied sites. Experimentally, this requires a postselection of realizations where each of the two lattice sites in question is occupied by a single atom.

In the following we compute the reduced two-spin density matrix for AFM metals and FL* using a slave-particle approach introduced by Ribeiro and Wen [31]. This approach is quite versatile and allows us to describe a variety of different possible phases in the t-J model, which provides an effective description of the Fermi-Hubbard model in the large-U limit [31–33]. It is important to emphasize, however, that this approach is not quantitatively reliable. Its strength is to provide qualitative predictions for different phases that might be realized in the t-J model. The stability of analogous slave-particle mean-field ground states has been discussed, e.g., in Refs. [34,35]. In the following we briefly summarize the main idea and refer to Appendix C for a detailed discussion.

Our starting point is the t-J Hamiltonian

$$\begin{aligned} H_{tJ} &= J \sum_{\langle ij\rangle \in NN} \left(\mathbf{S}_i \cdot \mathbf{S}_j - \frac{1}{4}\mathcal{P} n_{i,\sigma} n_{j,\sigma}\mathcal{P} \right) \\ &\quad + t \sum_{\langle ij\rangle \in NN} \mathcal{P}(c^{\dagger}_{i,\sigma} c_{j,\sigma} + c^{\dagger}_{j,\sigma} c_{i,\sigma})\mathcal{P}, \end{aligned} \tag{13}$$

where we restrict to nearest-neighbor hopping as in ultracold atom experiments. Here, the spin operator $\mathbf{S}_i$ is given in terms of Gutzwiller projected fermion operators as $\mathbf{S}_i = \frac{1}{2}\mathcal{P} c^{\dagger}_{i,\alpha}\sigma_{\alpha,\beta} c_{i,\beta}\mathcal{P}$, where $\mathcal{P}$ is the Gutzwiller projector which projects out doubly occupied sites.

The main idea of the slave particle description of Ribeiro and Wen is to introduce two degrees of freedom per lattice site: one localized spin-1/2 (represented by the operator $\tilde{\mathbf{S}}_i$), as well as one charged spin-1/2 fermion described by fermionic operators $d^{\dagger}_{i,\sigma}$, $d_{i,\sigma}$, which represents a doped hole (referred to as dopon in the following). The three physical basis states per lattice site of the t-J model are then related to the two slave degrees of freedom per lattice site via the mapping

$$|\uparrow\rangle_i \leftrightarrow |\uparrow 0\rangle_i, \tag{14}$$

$$|\downarrow\rangle_i \leftrightarrow |\downarrow 0\rangle_i, \tag{15}$$

$$|0\rangle_i \leftrightarrow \frac{|\uparrow\downarrow\rangle_i - |\downarrow\uparrow\rangle_i}{\sqrt{2}}, \tag{16}$$

i.e., a physical hole is represented by a spin singlet of a localized spin and a dopon. Other states of the enlarged slave-particle Hilbert space, such as the triplet states $|\uparrow\uparrow\rangle$, $|\downarrow\downarrow\rangle$, $\frac{|\uparrow\downarrow\rangle_i+|\downarrow\uparrow\rangle_i}{\sqrt{2}}$, and doubly occupied dopon states, are unphysical and need to be projected out.

In terms of the slave-particle degrees of freedom, the Gutzwiller projected electron operator of the t-J model takes the form

$$\tilde{c}^{\dagger}_{i,\alpha} = \mathcal{P} c^{\dagger}_{i,\alpha} \mathcal{P} = s_{\sigma} \tfrac{1}{\sqrt{2}} \tilde{\mathcal{P}} \big[\big(\tfrac{1}{2} + s_{\sigma} \tilde{S}^{z}_{i} \big) - \tilde{S}^{s_{\sigma}}_{i} d_{i,\sigma} \big] \tilde{\mathcal{P}}, \tag{17}$$

where $\tilde{\mathcal{P}}$ projects out doubly occupied dopon sites and $s_{\uparrow/\downarrow} = \pm 1$. In this slave-particle representation the t-J Hamiltonian in Eq. (13) takes the form

$$H^{d}_{tJ} = H^{d}_{J} + H^{d}_{t}, \tag{18}$$

where

$$H^{d}_{J} = J \sum_{\langle ij\rangle \in NN} \big(\tilde{\mathbf{S}}_i \tilde{\mathbf{S}}_j - \tfrac{1}{4} \big) \tilde{\mathcal{P}} (1 - d^{\dagger}_{i} d_{i})(1 - d^{\dagger}_{j} d_{j}) \tilde{\mathcal{P}}, \tag{19}$$

$$H^{d}_{t} = \frac{t}{2} \sum_{\langle ij\rangle \in NN} \tilde{\mathcal{P}} \Bigg[(d^{\dagger}_{i} \boldsymbol{\sigma} d_{j}) \cdot \Bigg(i \tilde{\mathbf{S}}_i \times \tilde{\mathbf{S}}_j - \frac{\tilde{\mathbf{S}}_i + \tilde{\mathbf{S}}_j}{2} \Bigg) + \frac{1}{4} d^{\dagger}_{i} d_{j} + d^{\dagger}_{i} d_{j} \tilde{\mathbf{S}}_i \tilde{\mathbf{S}}_j + \text{H.c.} \Bigg] \tilde{\mathcal{P}}. \tag{20}$$

One big advantage of this approach is that the Hamiltonian (18) does not mix the physical states with the unphysical triplet states in the enlarged Hilbert space. A projection to the physical states in the enlarged Hilbert space is thus not necessary. Note that the Hamiltonian (18) resembles a Kondo-Heisenberg model of localized spins $\tilde{\mathbf{S}}_i$ interacting with a band of itinerant spin-1/2 fermions $d^{\dagger}_{i,\sigma}$, $d_{i,\sigma}$, which describe the motion of doped holes. The density p of doped holes away from half filling in the t-J model equals the density of dopons in the slave-particle description, $p = \frac{1}{N} \sum_i \langle d^{\dagger}_{i} d_{i} \rangle$. We conclude that in the low doping regime, where the density of dopons is very small, the Gutzwiller projector $\tilde{\mathcal{P}}$ for the dopons can be neglected. In the same regime the exchange interaction between spins in Eq. (19) is just renormalized by the presence of dopons and can be approximated as $J\tilde{\mathcal{P}}(1 - d^{\dagger}_{i} d_{i})(1 - d^{\dagger}_{j} d_{j})\tilde{\mathcal{P}} \approx J(1-p)^2 \equiv \tilde{J}$. The second part of the Hamiltonian H^{d}_{t} describes the hopping of dopons as well as their interaction with the localized spins.

The two phases of interest in this section can now be understood as follows: in the AFM metal the localized spins $\tilde{\mathbf{S}}_i$ as well as the doped spin order AFM and the dopons form a Fermi liquid on the background of ordered spins. By contrast, the FL* corresponds to a phase where the localized spins are in a spin-liquid state, and the dopons form a Fermi liquid on top [30,32]. The absence of magnetic order requires frustrated spin-spin interactions, which in this case can arise from Ruderman-Kittel-Kasuya-Yosida (RKKY) interactions mediated by the dopons. Note that the FL* state violates the conventional Luttinger theorem [36], which states that the volume enclosed by the Fermi surface in an ordinary metal without broken symmetries is proportional to the total density of electrons (or holes) in the conduction band. Instead, the FL* state has a small Fermi surface with an enclosed volume determined by the density of doped holes away from half filling (p), rather than the full density of holes measured from the filled band $(1 + p)$ [37]. It has been argued that such an FL* state shares many properties with the pseudogap phase in underdoped cuprates [32,33,38–43].

In order to obtain a phenomenological description of the above-mentioned phases we follow Ribeiro and Wen and employ a slave-fermion description of the localized spins,

$$\tilde{\mathbf{S}}_i = f^{\dagger}_{i\alpha} \boldsymbol{\sigma}_{\alpha\beta} f_{i\beta}, \tag{21}$$

where $f_{i\alpha}$ and $f^{\dagger}_{i\alpha}$ are canonical spin-1/2 fermion operators. This description is particularly suited to construct spin-liquid states of the localized spins, where the f fermions describe spinon excitations, as will be discussed later. In the following we introduce the mean fields used to decouple the various interaction terms in the Hamiltonian, and which are the basis of a phenomenological description of the two phases mentioned above.

A. Antiferromagnetic metal

Let us focus on the first part of the Hamiltonian in Eq. (19) describing a renormalized spin-exchange interaction. Here we use a mean-field decoupling which allows for an effective hopping and a pairing amplitude for the spinons:

$$\chi_{ij} = \langle f^{\dagger}_{i,\alpha} f_{j,\beta} \rangle \delta_{\alpha\beta}, \tag{22}$$

$$\Delta_{ij} = \langle f_{i,\alpha} f_{j,\beta} \rangle \epsilon_{\alpha\beta}. \tag{23}$$

Note that the spinon pairing amplitude Δ_{ij} effectively accounts for singlet correlations between the localized spins and we assume that it has a d-wave form, where $\Delta = \pm\langle \Delta_{ij} \rangle$ for $j = i + \hat{e}_{x/y}$.

The second part of the Hamiltonian in Eq. (20) consists of terms describing the hopping of dopons as well as their interaction with localized spins. We now discuss the effect of each of these terms using a mean-field analysis. Since we assume that spins have local AFM correlations, the cross product between spin operators $\langle \tilde{\mathbf{S}}_i \times \tilde{\mathbf{S}}_j \rangle$ vanishes for nearest neighbors. The last term in Eq. (20) can be decoupled either to generate an effective hopping of spinons and/or dopons. In the latter case the dopons are considered to hop in a locally Néel ordered background, i.e., $4\langle \tilde{\mathbf{S}}_i \tilde{\mathbf{S}}_j \rangle \approx (-1)^{i_x - j_x + i_y - j_y}$. This however cancels with the third term in Eq. (20) and thus effectively leads to a vanishing dispersion for the dopons. In contrast numerical and theoretical studies for a single hole described by the t-J model show a dispersion relation with a minimum around $(\pi/2, \pi/2)$ [44–48]. To overcome this discrepancy we allow for further neighbor hopping amplitudes $\{t_1, t_2, t_3\}$, so that dopons can effectively tunnel up to second- and third-nearest-neighbor sites within our mean-field analysis. The nearest-neighbor hopping amplitude is thereby set to $t_1 = t$. As motivated in the work by Ribeiro and Wen, the second- and third-nearest-neighbor hopping amplitudes scale approximately as $t_2 = 2t_3 \approx J$.

Finally the second term of the Hamiltonian in Eq. (20) plays a major role here, since it takes the form of a Kondo coupling between the dopons and the spins. The resonances of the according processes are thus significantly larger in the case of a strongly developed spin ordered background. In order to

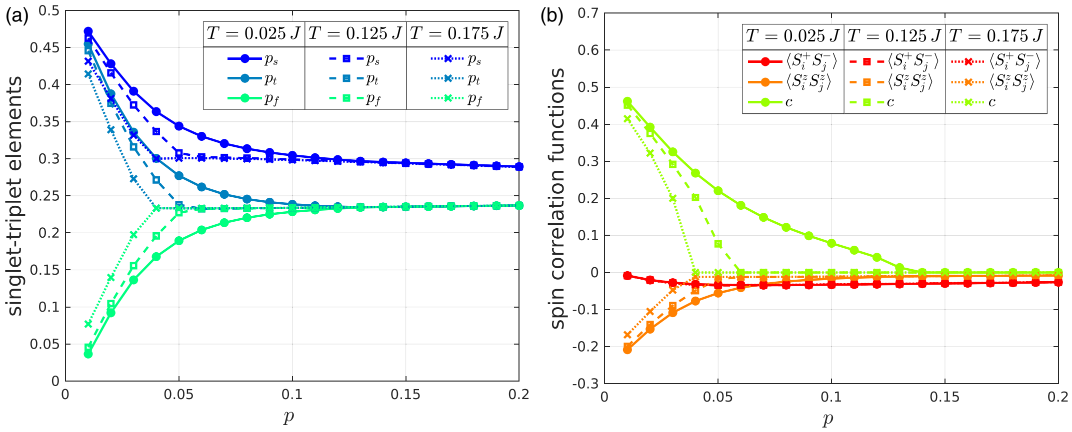

FIG. 3. Doping dependence of local correlations in the AFM metal. Panel (a) of this figure shows the short-range singlet, triplet, and ferromagnetic amplitudes (p_s, p_t, and p_f) as a function of doping p. We show here data for three temperatures, namely $T = 0.025J$ (bold line), $T = 0.125J$ (bold dashed), and $T = 0.175J$ (dotted). The amplitudes decrease with increasing temperature due to larger thermal fluctuations. The triplet and ferromagnetic amplitudes approach each other when doping the system continuously from $p = 0.01$ to $p = 0.2$. The singlet amplitude p_s remains larger than the other two amplitudes at large doping, by an amount determined by $c_{p \gtrsim 0.1} \approx 0.07$ in Eq. (12). The order parameter $\langle S_i^z \rangle$ in panel (b) indicates that the SU(2) symmetry is restored at a critical doping of $p \approx 0.06$ for the temperature $T = 0.125J$.

describe such a macroscopically developed AFM spin background we introduce the following mean-field amplitudes:

$$m^z = (-1)^{i_x+i_y} \frac{1}{2} \langle f^\dagger_{i,\alpha} f_{i,\beta} \rangle \sigma^z_{\alpha\beta}, \tag{24}$$

$$n^z = -(-1)^{i_x+i_y} \sum_{v \in \{2,3\}} \frac{t_v}{8} \sum_{\hat{u}_v} \langle d^\dagger_{i,\alpha} d_{i+\hat{u}_v,\beta} \rangle \sigma^z_{\alpha\beta}. \tag{25}$$

The dopon magnetization n^z measures thereby the net effect of a hole with respect to an AFM ordered background. The first sum runs over further neighbors $v = 2, 3$, whereas the second sum includes the following contributions: $\hat{u}_2 = \pm e_{\hat{x}/\hat{y}} \pm e_{\hat{y}/\hat{x}}$ and $\hat{u}_3 = \pm 2 e_{\hat{x}/\hat{y}}$. The detailed analysis of the mean-field self-consistency equations is part of Appendix C and follows closely Ref. [31]. Note that we do not include a hybridization between spinons and dopons, i.e., mean fields of the form $\langle f_i^\dagger d_i \rangle$. Such terms are only important for a description of the ordinary Fermi liquid at large doping.

In Fig. 3 we show the self-consistent mean-field results for $t = 16J$. Note that we choose such a relatively small value of J because the mean-field computation overestimates the extent of the AFM phase, which is known to vanish at a few percent doping in realistic situations. A small value of J reduces the extent of the AFM phase as a function of doping and thus allows us to compensate for this artifact of mean-field theory. The AFM order parameter as a function of doping for three different temperatures is shown in Fig. 3(b), together with the nearest-neighbor spin correlators. The short-range singlet and triplet probabilities p_s, p_t for pairs of nearest-neighbor sites are shown in Fig. 3(a). Both are close to the value $p_{s/t} \approx 0.5$ at half filling, and decrease with doping. At higher temperatures, thermal fluctuations reduce the absolute values of the amplitudes. Beyond a temperature-dependent threshold between $p \approx 0.05$ and $p \approx 0.1$ the ferromagnetic and triplet amplitude are very close to each other with a value of $p_{t/f} \approx 0.24$, indicating that the SU(2) symmetry is restored. In this regime, the singlet probability p_s deviates from $p_t = p_f$ by an amount which is related to the constant c characterizing the SU(2) invariant two-spin density matrix; see Eq. (12). The comparison in Fig. 4(a) yields an estimate $c_{p \gtrsim 0.1} \approx 0.07$.

In Fig. 3(b) we also show the AFM order parameter $\langle S_z^i \rangle$, which takes nonzero values only if the SU(2) symmetry is spontaneously broken. For all temperatures, we observe a transition from a phase with broken SU(2) symmetry at low doping, to an SU(2)-symmetric phase at higher doping. The transition point shifts to higher doping values when the temperature is decreased. As a result of quantum fluctuations, the noncollinear correlations $\langle S_i^+ S_j^- \rangle$ develop when the doping is increased, and the collinear correlations $\langle S_i^z S_j^z \rangle$ are strongly reduced compared to their value $\langle S_i^z S_j^z \rangle_{p=0,T=0} = -0.25$ in the classical Néel state. The latter is obtained as the mean-field solution at half filling and zero temperature.

Indeed, the SU(2) symmetry-breaking phase transition is clearly visible in the FCS of the system-averaged two-spin density matrix. In Fig. 4(a) we show the FCS of the system-averaged triplet probability, $p_t = \langle t | \rho^S | t \rangle$ at a fixed temperature $T = 0.125J$ and for various doping values, ranging between $p = 0.01$ and $p = 0.05$. We observe how the SU(2) symmetry is gradually restored and the distribution function narrows when the critical doping value, where the transition takes place, is approached. As demonstrated in Fig. 4(b), increasing the temperature at a fixed doping value has a similar effect on the FCS. Beyond the critical doping, respectively temperature, a sharp peak remains and the SU(2) symmetry is fully restored. For a fully mixed state at infinite temperature the triplet probability is $p_t^{T\to\infty} = 0.25$, slightly higher than the value $p_t \approx 0.23$ which we predict in the SU(2) symmetric phase at large doping values.

B. Fractionalized Fermi liquid

As a second example we consider signatures of a FL* phase in the reduced density matrix. This phase is SU(2) symmetric and the mean-field amplitudes n_z and m_z in

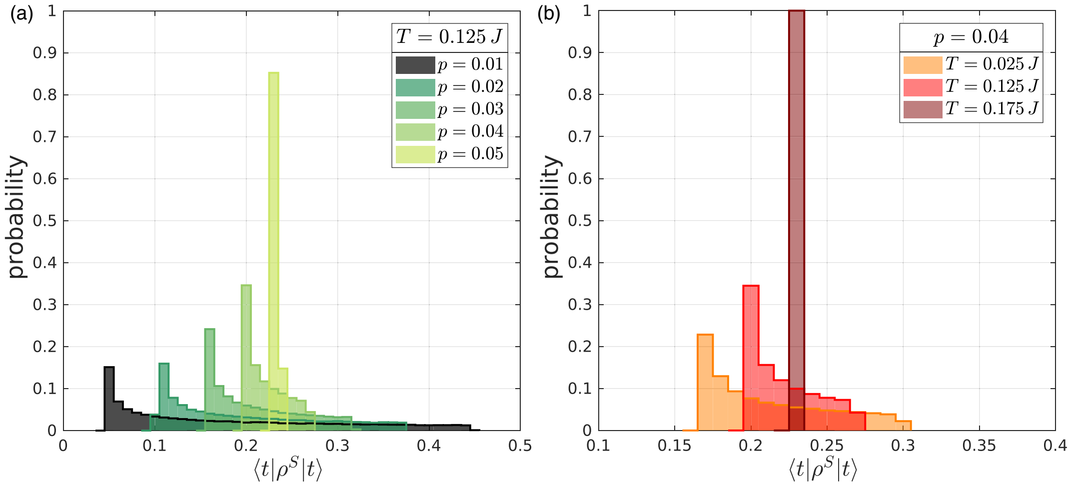

FIG. 4. Full counting statistics of local correlations in the AFM metal. We show the FCS of the system-averaged triplet matrix element $\langle t|\rho^S|t\rangle$ of the two-spin density matrix. The left panel (a) shows the FCS distribution at a fixed temperature $T = 0.125J$ for different doping levels p. It narrows as function of p and turns into a sharp peak at the critical doping $p \approx 0.05$, where the SU(2) symmetry is restored. The sharp peak at a value around 0.23 determines the parameter c in the density matrix in Eq. (12), which takes the value $c_{p\approx 0.05} \approx 0.07$. The right panel (b) shows a similar behavior of the probability distribution as function of temperature at fixed doping, where thermal fluctuations restore the SU(2) symmetry and lead to a narrow peak around a value $\langle t|\rho^S|t\rangle = 0.23$.

Eqs. (24) and (25) vanish identically. Only the mean fields χ_{ij} and Δ_{ij} remain finite. Importantly, there is no hybridization between dopons and spinons, i.e., $\langle f_i^\dagger d_i\rangle = 0$. The localized spins are thus in a spin-liquid state and the dopons form a Fermi liquid with a small Fermi surface ($\sim p$) on the spin-liquid background. Note that a finite hybridization gives rise to a "heavy Fermi liquid" in the Kondo-Heisenberg terminology, which corresponds to an ordinary Fermi-liquid phase in the corresponding t-J model and is expected to appear only at large hole doping levels (see Ref. [31] for a detailed discussion).

After solving the self-consistency equations under the condition $n_z = m_z = 0$ (see Appendix C), we determine the reduced density matrix in the singlet and triplet basis. The results are summarized in Fig. 5. Due to the presence of holes, the singlet amplitude p_s of nearest-neighbor spins, as shown in Fig. 5(a), slowly decreases as function of doping. Thermal fluctuations reduce the singlet amplitude further, but the qualitative doping dependence of the curves remains independent of temperature. Because the state is SU(2) symmetric, the triplet amplitude $p_t = p_f$ is equal to the probability to find ferromagnetically aligned spins. This can be seen by noting that $p_t - p_f = \langle S_i^x S_j^x\rangle + \langle S_i^y S_j^y\rangle - 2\langle S_i^z S_j^z\rangle = 0$. Both $p_t = p_f$ increase when the singlet amplitude p_s decreases. The singlet-triplet matrix element $\langle s|\rho^S|t\rangle = 0$ vanishes because of the SU(2) symmetry, and is not shown in the figure.

In Fig. 5(b) we calculate the doping dependence of spin-spin correlations, for which $\langle S_i^z S_j^z\rangle = \langle S_i^+ S_j^-\rangle/2$ because of the SU(2) symmetry. On nearest neighbors they are very weakly doping dependent and remain negative, corresponding to weak and short-range AFM correlations in the system. The SU(2) invariant two-spin density matrix can be characterized by the parameter c, see Eq. (12), which starts at $c_{p=0.01} \approx 0.08$ for very small doping and continuously decreases to $c_{p=0.1} \approx 0.06$ at higher doping.

C. Numerical results for the *t*-*J* model

Next we perform a numerical study of the two-spin reduced density matrix ρ^S in a periodic 4×4 lattice with one hole; this corresponds to a doping level of $p \approx 6\%$. We perform exact diagonalization (ED) to calculate the zero-temperature ground state, in a sector of the many-body Hilbert space where the single hole carries total momentum $\boldsymbol{k} = (\pi/2, \pi/2)$ and the total spin in the z direction is $S^z = 1/2$. This state describes a magnetic polaron, the quasiparticle formed by a single hole moving in an AFM background [46,49–53]. Even though the considered system size is small, we expected that the local correlations encoded in the two-spin density matrix are close to their values in an infinite system at 6% doping. Because of the limited size of the lattice, we refrain from calculating the FCS of the system-averaged two-spin density matrix.

To study the effect that the mobile hole has on the surrounding spins, we tune the ratio J/t. Although not identical, we expect that the effects of larger tunnelings t/J and higher doping p are comparable in the finite-size system: When $t \gg J$, the hole is moving faster through the antiferromagnet, thus affecting more spins. Indeed, when $J/t \gg 1$ the hole is quasistatic and the surrounding spins have strong AFM correlations; on neighboring sites their strength approaches their thermodynamic values in the two-dimensional Heisenberg model.

In Fig. 6(a) we show how the entries of the nearest-neighbor two-spin density matrix depend on the ratio J/t. When $J/t = 1$ we find that the singlet probability p_s in the doped system is still close to the value 0.57 expected from linear spin-wave theory in an undoped system. For smaller values of J/t the hole has a more pronounced effect on the spin environment, which leads to a decrease of the singlet probability p_s. In addition, the probability p_f to find ferromagnetic correlations increases to values larger than 0.29 expected at zero doping from linear spin-wave theory. For

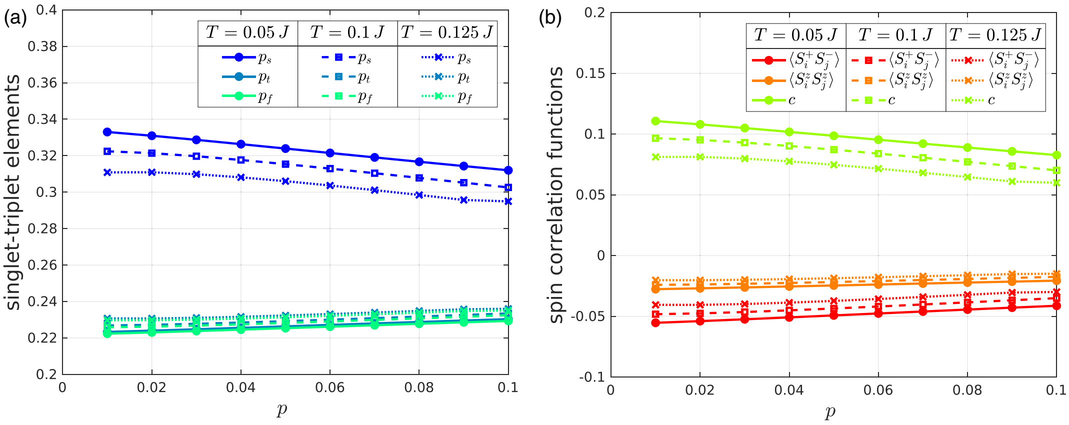

FIG. 5. Doping dependence of local correlations in the FL* phase. We show the doping dependence of the short-range singlet, triplet, and ferromagnetic amplitudes (p_s, p_t, and p_f) in (a), for various temperatures [$T = 0.05J$ (bold line), $T = 0.1J$ (bold dashed), and $T = 0.125J$ (dotted)] at $t = 4J$. In (b) the doping dependence of spin-correlation functions and the parameter c, as defined in Eq. (12), is shown for the same parameters. The singlet amplitude in (a) decreases for larger doping and temperature due to the presence of holes, respectively thermal fluctuations. Since the state is SU(2) symmetric, triplet and ferromagnetic amplitude are identical. The magnitude of short-range spin correlations decreases by the presence of holes that destroy the AFM background ordering.

very small values of $J/t < 0.1$, we observe a phase transition in the finite-size system, which is expected to be related to the formation of a Nagaoka polaron [53,55].

Qualitatively similar behavior is expected in an undoped system when frustrating next-nearest-neighbor couplings J_2 are switched on, in addition to the nearest-neighbor interactions $J_1 = J$. To demonstrate this, we use ED to calculate the reduced two-spin density matrix in a J_1-J_2 model on the same 4×4 lattice. As shown in Fig. 6, increasing J_2 from zero to $J_2 = 0.5J_1$ has a similar effect as decreasing J/t from a value of 1 to 0.1. I.e., locally the doped t-J model cannot be distinguished from a frustrated quantum magnet described by the J_1-J_2 Hamiltonian.

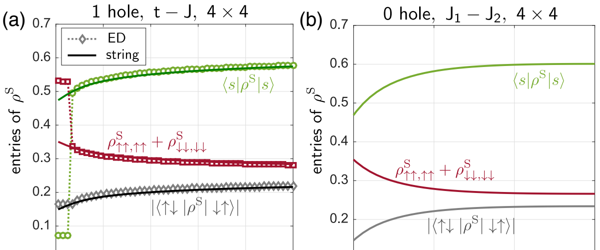

FIG. 6. (a) Entries of the reduced two-spin density matrix in a 4×4 system doped with a single hole, as a function of J/t. We used ED simulations for the ground state with total momentum $\boldsymbol{k} = (\pi/2, \pi/2)$ and with total spin $S^z = 1/2$. We compare our numerically exact results (symbols) to predictions by the geometric string theory (solid lines); for details see Ref. [54], where the ratio J/t tunes the length of the string of displaced spins. The reduced two-spin density matrix of the doped system closely resembles the two-spin density matrix in an undoped but frustrated quantum magnet: In (b) we calculate ρ^S for a frustrated J_1-J_2 model on a periodic 4×4 lattice with $S^z = 0$, with diagonal next-nearest-neighbor couplings J_2. Locally the two systems become indistinguishable, and we find that larger values of t/J correspond to larger values of J_2/J_1.

Our exact numerical results in the 4×4 system are consistent with the physical picture derived previously from the doped carrier formalism. Smaller values of t/J, expected to reflect high doping values, lead to a decrease of the singlet amplitude, which is directly related to the $\langle \boldsymbol{S}_i \cdot \boldsymbol{S}_j \rangle$ correlations, on nearest-neighbor sites.

Additional quantitative understanding of the J/t dependence in the single-hole problem can be obtained by the geometric string approach introduced in Refs. [54,56]. There, one describes the motion of the hole along a fluctuating string of displaced spins and applies the frozen-spin approximation [56]: It is assumed that the quantum state of the surrounding spins is determined by a parent state $|\tilde{\Psi}\rangle$ in the undoped system, and the hole motion only modifies the positions of the parent spins in the two-dimensional lattice, otherwise keeping their quantum states unmodified. To calculate the two-spin density matrix ρ^S_{NN} on a given nearest-neighbor bond, we trace over all possible string configurations. Because the strings modify the positions of the parent spins, ρ^S_{NN} describes a statistical mixture of nearest-neighbor ($\tilde{\rho}^S_{\mathrm{NN}}$), next-nearest-neighbor ($\tilde{\rho}^S_{\mathrm{NNN}}$),... two-spin density matrices, with coefficients p_{NN}, p_{NNN},.... The results in Fig. 6(a) (solid lines) are obtained by using the exact ground state of the undoped Heisenberg model in the 4×4 lattice as the parent state. The weights p_{NN}, p_{NNN},... are determined by averaging over string states with a string length distribution calculated as described in Ref. [54].

V. CONCLUSION AND OUTLOOK

Our work demonstrates that a magnetically ordered state can be identified by measuring the statistical distribution of the nearest-neighbor triplet amplitude of the system-averaged two-spin density matrix, which arises due to random orientations of the order parameter between different experimental shots. In fact, it is sufficient to measure the FCS of a generic local operator which does not transform like an SU(2) singlet in order to identify the AFM phase from local measurements. Moreover, we have calculated the nearest-neighbor singlet and triplet amplitudes as a function of the hole concentration away from half filling within the doped carrier formalism and demonstrated that the triplet probability distribution has a finite width in the magnetically ordered phase, which decreases continuously with doping and temperature. At the phase transition from the magnetically ordered to a paramagnetic state, such as the FL*, the distribution turns into a sharp peak.

The fact that the information about symmetry broken states is contained in the FCS of the system-averaged two-spin density matrix shows that the FCS distribution can be measured experimentally without the use of a quantum gas microscope. Experiments with superlattice potentials where the average over all double wells is taken automatically during the readout after each shot work equally well. This might even be an advantage due to the larger system sizes that can be reached compared to setups with a quantum gas microscope.

Even though our work focused on AFM ordered states, we emphasize that measuring the FCS with respect to different order-parameter realizations can also be used to detect other types of broken symmetries, such as states that break lattice symmetries like charge-density waves or valence bond solids. We also note that our analysis can be straightforwardly extended to study correlations beyond nearest neighbors.

The tools introduced in this work potentially allow quantum gas microscopy experiments at currently accessible temperatures to shed light on the long-standing puzzle about the nature of the pseudogap state in underdoped cuprate superconductors. Another interesting route to study effects of doping a Mott insulator is to measure the single-particle spectral function in analogy to ARPES experiments in the solid-state context [57]. In combination with the tools discussed in this work, quantum gas microscopy should be able to characterize the properties of doped Mott insulators to a high degree, providing a valuable benchmark for theoretical proposals.

ACKNOWLEDGMENTS

We thank E. Demler, M. Kanasz-Nagy, R. Schmidt, D. Pimenov, A. Bohrdt, and D. Greif for valuable discussions. S.H. and M.P. were supported by the German Excellence Initiative via the Nanosystems Initiative Munich (NIM). F.G. acknowledges financial support by the Gordon and Betty Moore Foundation under the EPiQS program.

APPENDIX A: SYMMETRY OF THE REDUCED DENSITY MATRIX

The block-diagonal form of the reduced density matrix in Sec. II is a direct consequence of the global particle conservation. This is actually shown for a pure state in Ref. [58] using a singular value decomposition. In the following we verify that this also holds for any thermalized system with a global conserved quantity under certain, rather weak, limitations.

We thus start with a Hamiltonian with a conserved quantity O, i.e., $[H, O] = 0$, and an associated system that is described by the density matrix $\rho = e^{-\beta H}$. Quite generally, the operator O can be decomposed as $O = \sum_j O_j$, where j labels, e.g., different lattice sites. In the absence of spontaneous symmetry breaking the operator O also commutes with the density matrix $[\rho, O] = 0$, i.e., the state ρ has the same symmetry as the Hamiltonian. In such a case we can show that the reduced density matrix $\rho_A = \mathrm{tr}_{\bar{A}}(\rho)$ of a subsystem A commutes with the operator $O_A = \sum_{j\in A} O_j$ (here $\bar{A}$ is the complement of A):

$$[\rho_A, O_A] = \mathrm{tr}_{\bar{A}}(\rho)O_A - O_A\mathrm{tr}_{\bar{A}}(\rho) = \mathrm{tr}_{\bar{A}}(\rho O_A - O_A\rho), \tag{A1}$$

$$0 = \mathrm{tr}_{\bar{A}}([\rho, O]) = \mathrm{tr}_{\bar{A}}(\rho O_A - O_A\rho) + \mathrm{tr}_{\bar{A}}(\rho O_{\bar{A}} - O_{\bar{A}}\rho). \tag{A2}$$

If we now use that the trace is cyclic, i.e., $\mathrm{tr}_{\bar{A}}(\rho O_{\bar{A}}) = \mathrm{tr}_{\bar{A}}(O_{\bar{A}}\rho)$, and combine this with Eqs. (1) and (2) from above, we see immediately that $[\rho_A, O_A] = 0$. So we can conclude that the two-site density matrix can always be written in a block-diagonal form, if the above requirements are satisfied. In Sec. II A of the main text we use this result to show that the global U(1) symmetry (i.e., particle number conservation) of the Fermi-Hubbard model together with the fact that we only consider states with a definite particle number implies that the reduced density matrix can be written in a block-diagonal form, where each block can be labeled by the number of electrons in the subsystem. This is independent of the presence or absence of long-range magnetic order, which only has consequences for the block-diagonal form of the reduced density matrix in different spin sectors, but does not affect the block-diagonal form in the different particle number sectors.

APPENDIX B: SPIN-WAVE THEORY AT HALF FILLING

In this first part of the Appendix we want to summarize a Holstein-Primakoff analysis (HP) of the antiferromagnetic Heisenberg model on a bipartite lattice at half filling [59]. We thus aim to study the spin system deep in an AFM phase, where neighboring spins tend to point in opposite directions. In order to tune the strength of quantum fluctuations, we allow for an additional external staggered magnetic field h_z along the z direction, which explicitly breaks the SU(2) invariance of the system and fixes the magnetization direction. We associate all spins pointing upwards (downwards) with sublattice A (B). Quantum fluctuations around the classical Néel state are represented by bosonic excitations in the HP analysis.

1. Method

This quite standard approach is based on a canonical mapping between spin and bosonic operators given by

$$S^z_i = (S - b^\dagger_i b_i), \quad S^z_j = (-S + b^\dagger_j b_j), \tag{B1}$$

$$S^-_i \simeq \sqrt{2S}b^\dagger_i, \quad S^+_j \simeq \sqrt{2S}b^\dagger_j, \tag{B2}$$

$$S^+_i \simeq \sqrt{2S}b_i, \quad S^-_j \simeq \sqrt{2S}b_i, \tag{B3}$$

where $i \in A$ and $j \in B$ and we have taken the semiclassical large S limit. Furthermore, we have to constrict the local Hilbert space by $2n_{b,i} \leqslant S$, where $n_{b,i}$ is the boson occupation on site i. We now perform a rotation around the x axis on sublattice B and expand the Heisenberg model in $1/S$. For a small number of excitations, i.e., $|S_i^z| \approx S$, we can neglect terms of order $O(1/S)$ and the spin-wave Hamiltonian takes the form

$$H^{SW} = -S^2 JN\frac{z}{2} - SJN\frac{z}{2} + \sum_{\mathbf{k}} \omega_{\mathbf{k}} \left(a_{\mathbf{k}}^{\dagger} a_{\mathbf{k}} + \frac{1}{2} \right), \tag{B4}$$

where z is the coordination number and

$$\gamma_{\mathbf{k}} = \frac{1}{2}[\cos k_x + \cos k_y], \tag{B5}$$

$$a_{\mathbf{k}} = \cosh\theta_{\mathbf{k}} b_{\mathbf{k}} - \sinh\theta_{\mathbf{k}} b_{-\mathbf{k}}^{\dagger}, \tag{B6}$$

$$\tanh(2\theta_{\mathbf{k}}) = -\Delta\gamma_{\mathbf{k}} \text{ with } \Delta = \frac{JSz}{JSz - h_z}, \tag{B7}$$

$$\omega_{\mathbf{k}} = |J|Sz\sqrt{1 - \gamma_{\mathbf{k}}^2}. \tag{B8}$$

The ground state has no magnon excitation, i.e., $a_{\mathbf{k}}|\mathrm{GS}\rangle = 0$ and the ground-state energy is then $E_0 = -JN\frac{z}{2}S(S+1) + \frac{1}{2}\sum_{\mathbf{k}} \omega_{\mathbf{k}}$. The ground-state wave function itself has the form

$$|\mathrm{GS}\rangle = \mathcal{N} \exp\left[\frac{1}{2} \sum_{\mathbf{k}} \tanh\theta_{\mathbf{k}} b_{\mathbf{k}}^{\dagger} b_{-\mathbf{k}}^{\dagger} \right] |0\rangle, \tag{B9}$$

where $\mathcal{N}$ is a normalization constant.

2. Results

We now determine the two-particle reduced density matrix at zero temperature by computing the expectation values $\langle S_i^{\alpha} S_j^{\beta} \rangle$ [see Eq. (1)] for the AFM ground-state wave function at zero temperature. The entries of the reduced density matrix show that the system is close to a Néel state, so that the matrix element in Eq. (7) is given by

$$p_{\mathrm{st}} = M_z, \tag{B10}$$

with the local staggered magnetization

$$M_z = |\langle S_i^z \rangle| = S - \frac{1}{4\pi^2} \int_{\text{1st BZ}} d^2k \sinh^2(\theta_{\mathbf{k}}). \tag{B11}$$

When the external staggered field is absent, i.e., $h_z = 0$, the local staggered magnetization is smaller than the total spin S due to quantum fluctuations. Increasing the external staggered field, the excitation of bosonic quasiparticles gets more unfavorable, so that the local magnetization converges against the total spin $M_z \to S$. This is also shown Fig. 7(a), which shows the convergence of p_{st} against the total spin S with increasing h_z. The difference of singlet and triplet elements is given by

$$\begin{aligned} p_{\mathrm{s}} - p_{\mathrm{t}} = 2g_z &= -[\langle S_i^- S_j^+ \rangle + \langle S_i^+ S_j^- \rangle] \\ &= -\frac{1}{4\pi^2} \int_{\text{1st BZ}} d^2k \cos(\mathbf{kd}) \sinh(2\theta_{\mathbf{k}}), \end{aligned} \tag{B12}$$

with $\mathbf{d} = \mathbf{R}_i - \mathbf{R}_j$. It decreases from approximately $g_z(h_z = 0) \approx 0.13$ to $g_z(h_z = 10) \approx 0.01$ [see Fig. 7(a)] and thus shows that the state associated with the reduced density matrix approaches an equal superposition of triplet and singlet component when increasing the external staggered magnetic field h_z. This is in agreement with the former result that the three elements p_{st}, p_{t}, and p_{s} converge to the total spin S with growing h_z. Finally the ferromagnetic element decreases with increasing h_z and is given by [see Eq. (5)]

$$p_{\mathrm{f}} = \tfrac{1}{4} - M_z^2 - g_z^2 - f_z^2, \tag{B13}$$

where

$$f_z = \frac{1}{4\pi^2} \int_{\text{1st BZ}} d^2k \cos(\mathbf{kd}) \sinh^2(\theta_{\mathbf{k}}). \tag{B14}$$

By explicitly breaking the SU(2) invariance due to the external staggered magnetic field any ferromagnetic alignment of neighboring spins is unfavorable. We observe this effect also in the FCS shown in Fig. 7(b). For further discussion see also Sec. III of the main text.

APPENDIX C: DOPED CARRIER ANALYSIS OF THE *t*-*J* HAMILTONIAN

Here we complete the doped carrier mean-field calculation introduced in the main text in Sec. IV based on Ref. [31]. Ribeiro and Wen showed that the phase diagram generally includes a pseudogap regime, where the mean-field amplitudes are in agreement with a fully SU(2) symmetric ground state for a small parameter regime of doping $0 \lesssim p \lesssim 0.1$ and temperature $0.1J \lesssim T \lesssim 0.2J$ consistent with a pseudogap metal, where spinon and dopon do not hybridize and no ordering develops in the system (see the phase diagram in Ref. [31]). In this phase fermionic spinons form d-wave Cooper pairs and a gap opens in the electronic spectral function, as expected from angle-resolved photoemission spectroscopy measurements in the pseudogap regime of underdoped cuprates. Moreover, the phase diagram has a very dominant antiferromagnetic phase centered around half filling, which gets more pronounced when the ratio t/J is lowered. Other phases such as a d-wave superconductor and an ordinary metal are also present in the phase diagram. These phases are characterized by a finite hybridization matrix element between spinons and dopons.

In the following we show the mean-field Hamiltonian in momentum space and determine the self-consistency equations. We restrict our analysis on special regimes of the mean-field phase diagram. As discussed in more detail in Sec. IV of the main text we are interested in the antiferromagnetic phase at low doping, as well as in the pseudogap regime, which is modelled as a fractionalized Fermi liquid in this approach.

1. Overview on mean-field amplitudes

Let us first assume that the system exhibits a finite magnetization $\langle \mathbf{S}_i \rangle \neq 0$. We fix the magnetization direction to be along the z axis and define the following operators:

$$m_i^z \sigma_{\alpha\beta}^z = f_{i,\alpha}^{\dagger} f_{i,\beta}, \tag{C1}$$

$$n_i^z \sigma_{\alpha\beta}^z = -\frac{1}{4} \sum_{v \in \{2,3\}} \frac{t_v}{8} \sum_{\hat{u}_v} d_{i,\alpha}^{\dagger} d_{i+\hat{u}_v,\beta}, \tag{C2}$$

where the latter includes further neighbor hopping amplitudes t_v with $v \in \{2, 3\}$ and the second sum runs over the

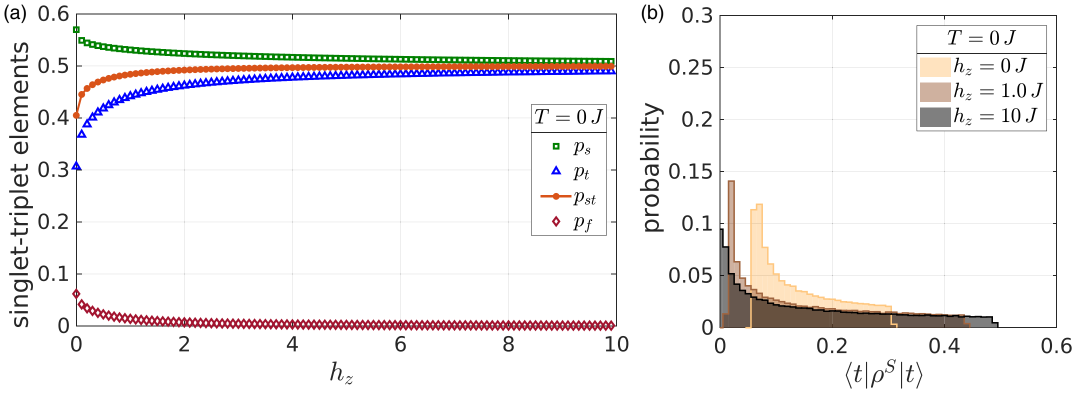

FIG. 7. Panel (a) shows the singlet p_s, triplet p_t, and ferromagnetic p_f matrix elements as a function of the external staggered field h_z. Increasing the staggered field drives the state closer to a classical Néel configuration. Panel (b) shows the full counting statistics of the triplet amplitude for different values of h_z. A strong external staggered magnetic field suppresses quantum fluctuations and we observe a continuous distribution of the triplet amplitude in the range $0 \leqslant \langle t|\rho^S|t\rangle \leqslant 0.5$. Since quantum fluctuation locally disturbs the antiparallel alignment, the distribution has an onset at a finite value for a small external staggered field.

respective unit vectors $\hat{u}_2 = \pm e_{\hat{x}/\hat{y}} \pm e_{\hat{y}/\hat{x}}$ and $\hat{u}_3 = \pm 2e_{\hat{x}/\hat{y}}$. We consider then the following mean-field amplitudes $m^z = (-1)^{i_x+i_y}\langle m_i^z\rangle$ and $n^z = (-1)^{i_x+i_y}\langle n_i^z\rangle$. The amplitude n^z measures thereby the hopping of dopons and describes a net magnetization of holes with respect to an AFM ordered spin background.

In principle it is also possible that spinons and dopons hybridize, although in regimes of our interest this is not the case, we consider them here for completeness. If the ground state is for instance a normal Fermi liquid, we expect this amplitude to be finite. The hybridization between spinons and dopons is described by the operator $\kappa_{ij}\delta_{\alpha\beta} = 2d_{i,\alpha}^\dagger f_{j,\beta}$ and its expectation values

$$b_0 = \langle\kappa_{ii}\rangle, \tag{C3}$$

$$b_1 = \frac{3}{16}\sum_{\nu\in\{2,3\}}\frac{t_\nu}{8}\sum_{j=i+\hat{u}_\nu}\langle\kappa\rangle_{ij}. \tag{C4}$$

Finally we also recap that the spinons are assumed to form Cooper pairs in the d-wave channel Δ and we also allow for a finite spinon hopping amplitude χ as described in Sec. IV.

2. Mean-field Hamiltonian

After decoupling the Hamiltonian in these channels and using the compact Nambu notation $\psi_k^\dagger = [f_{k,\uparrow}^\dagger, f_{-k,\downarrow}]$ and $\eta_k^\dagger = [d_{k,\uparrow}^\dagger, d_{-k,\downarrow}]$, the mean-field Hamiltonian in momentum space takes the form

$$\begin{aligned} H_{tJ}^{\mathrm{MF}} = {} & \frac{3}{4}\tilde{J}N(\Delta^2+\chi^2) - N\mu_d + 2\tilde{J}N|m^z|^2 - 4Nn^z m^z - 4Nb_0b_1 - N\mu_d + \sum_{\mathbf{k}}[\psi_k^\dagger\ \eta_k^\dagger]\begin{bmatrix}\alpha_k^x\sigma_x+\alpha_k^z\sigma_z & \beta_k\sigma_z\\ \beta_k\sigma_z & \gamma_k\sigma_z\end{bmatrix}\begin{bmatrix}\psi_k\\ \eta_k\end{bmatrix} \\ & + \sum_{\mathbf{k}}[\psi_{k+Q}^\dagger\ \eta_{k+Q}^\dagger]\begin{bmatrix}[4n^z-4\tilde{J}m^z]\sigma_0 & 0\\ 0 & -4m^z[\gamma_k+\mu_d]\sigma_0\end{bmatrix}\begin{bmatrix}\psi_k\\ \eta_k\end{bmatrix}, \end{aligned} \tag{C5}$$

where

$$\alpha_k^x = -\tfrac{3}{4}\tilde{J}\Delta[\cos(k_x) - \cos(k_y)], \tag{C6}$$

$$\alpha_k^z = \lambda + pt_1[\cos(k_x)+\cos(k_y)] - \tfrac{3}{4}\tilde{J}\chi[\cos(k_x)+\cos(k_y)], \tag{C7}$$

$$\beta_k = b_1 + \tfrac{3}{8}b_0\{t_1[\cos(k_x)+\cos(k_y)] + 2t_2[\cos(k_x)\cos(k_y)] + t_3[\cos(2k_x)+\cos(2k_y)]\}, \tag{C8}$$

$$\gamma_k = \tfrac{1}{2}t_2\cos(2k_x)\cos(2k_y) + \tfrac{1}{4}t_3[\cos(2k_x)+\cos(2k_y)] - \mu_d. \tag{C9}$$

The chemical potential μ_d is used to adjust the dopon density in the system. We further use $\sigma_0 = \mathbb{1}_{2\times2}$ and $Q = (\pi/a, \pi/a)$.

3. Antiferromagnetic metal: $b_0 = b_1 = 0; n^z \neq 0, m^z \neq 0$

The hybridization between spinons and dopons of the form $\langle f_i^\dagger d_i\rangle$ is now neglected, i.e., $b_0 = b_1 \approx 0$, since magnetic ordering and superconductivity are not assumed to be present at the same time. In this case the spinon-density Lagrange parameter $\lambda = 0$. The eigenenergies of the above mean-field

Hamiltonian H^{MF}_{tJ} for the spinon and dopon sector then read

$$\epsilon^{\pm}_{s,\mathbf{k}} = \pm\sqrt{\left(\alpha^x_k\right)^2 + \left(\alpha^z_k\right)^2 + (\nu_k)^2}, \tag{C10}$$

$$\epsilon^{\pm}_{d,\mathbf{k}} = (1 \mp 4|m^z|) - \mu_d, \tag{C11}$$

where $\nu_k = -4(\tilde{J}m^z - n^z)$. The set of self-consistency equations are determined from minimizing the free-energy density $f = F/N$ for a fixed density of dopons p and read

$$\begin{aligned}
m^z - \frac{1}{N}\sum_k \frac{\tilde{J}m^z_s - n^z}{\epsilon^+_{s,k}} \frac{\sinh\left(\beta\epsilon^+_{s,k}\right)}{1+\cosh\left(\beta\epsilon^+_{s,k}\right)} &= 0,\\
n^z + \frac{1}{2N}\sum_k \gamma_k \frac{\sinh\left[\beta(\gamma_k - \mu_d)\right]}{1+\cosh\left[\beta(\gamma_k - \mu_d)\right]} &= 0,\\
\chi + \frac{1}{2N}\sum_k \frac{\alpha^z_k[\cos(kx) + \cos(ky)]}{\epsilon^+_{s,k}} \frac{\sinh\left(\beta\epsilon^+_{s,k}\right)}{1+\cosh\left(\beta\epsilon^+_{s,k}\right)} &= 0,\\
\Delta + \frac{1}{2N}\sum_k \frac{\alpha^x_k[\cos(kx) - \cos(ky)]}{\epsilon^+_{s,k}} \frac{\sinh\left(\beta\epsilon^+_{s,k}\right)}{1+\cosh\left(\beta\epsilon^+_{s,k}\right)} &= 0,\\
x - 1 + \frac{1}{N}\sum_k \frac{\sinh\left[\beta(\gamma_k - \mu_d)\right]}{1+\cosh\left[\beta(\gamma_k - \mu_d)\right]} &= 0.
\end{aligned} \tag{C12}$$

Note that we use a rescaled exchange coupling of $\tilde{J} \rightarrow 0.6\tilde{J}$ here, as proposed by Ribeiro and Wen to counteract the overemphasized AFM ordering tendency in such a mean-field analysis. The rescaling factor is motivated by experimental results on AFM ordering in cuprates.

4. Fractionalized Fermi liquid: $b_0 = b_1 = n^z = m^z = 0$

Since we focus on a SU(2) symmetric ground state as proposed for the pseudogap regime, ordering is absent and again $b_0 = b_1 = 0$. We can thereby most simply adapt the above self-consistency equations (C12) and enforce the constraint $n^z = m^z = 0$.

---

[1] I. Bloch, J. Dalibard, and S. Nascimbene, Nat. Phys. **8**, 267 (2012).
[2] C. Gross and I. Bloch, Science **357**, 995 (2017).
[3] G. J. A. Edge, R. Anderson, D. Jervis, D. C. McKay, R. Day, S. Trotzky, and J. H. Thywissen, Phys. Rev. A **92**, 063406 (2015).
[4] E. Haller, J. Hudson, A. Kelly, D. A. Cotta, B. Peaudecerf, G. D. Bruce, and S. Kuhr, Nat. Phys. **11**, 738 (2015).
[5] M. F. Parsons, A. Mazurenko, C. S. Chiu, G. Ji, D. Greif, and M. Greiner, Science **353**, 1253 (2016).
[6] M. Boll, T. A. Hilker, G. Salomon, A. Omran, J. Nespolo, L. Pollet, I. Bloch, and C. Gross, Science **353**, 1257 (2016).
[7] L. W. Cheuk, M. A. Nichols, K. R. Lawrence, M. Okan, H. Zhang, E. Khatami, N. Trivedi, T. Paiva, M. Rigol, and M. W. Zwierlein, Science **353**, 1260 (2016).
[8] T. A. Hilker, G. Salomon, F. Grusdt, A. Omran, M. Boll, E. Demler, I. Bloch, and C. Gross, Science **357**, 484 (2017).
[9] D. Mitra, P. T. Brown, E. Guardado-Sanchez, S. S. Kondov, T. Devakul, D. A. Huse, P. Schauss, and W. S. Bakr, Nat. Phys. **14**, 173 (2018).
[10] P. T. Brown, D. Mitra, E. Guardado-Sanchez, P. Schauß, S. S. Kondov, E. Khatami, T. Paiva, N. Trivedi, D. A. Huse, and W. S. Bakr, Science **357**, 1385 (2017).
[11] A. Mazurenko, C. S. Chiu, G. Ji, M. F. Parsons, M. Kanász-Nagy, R. Schmidt, F. Grusdt, E. Demler, D. Greif, and M. Greiner, Nature (London) **545**, 462 (2017).
[12] M. A. Nichols, L. W. Cheuk, M. Okan, T. R. Hartke, E. Mendez, T. Senthil, E. Khatami, H. Zhang, and M. W. Zwierlein, Science **363**, 383 (2019).
[13] P. T. Brown, D. Mitra, E. Guardado-Sanchez, R. Nourafkan, A. Reymbaut, C.-D. Hébert, S. Bergeron, A.-M. S. Tremblay, J. Kokalj, D. A. Huse, P. Schauss, and W. S. Bakr, Science **363**, 379 (2019).
[14] P. A. Lee, N. Nagaosa, and X.-G. Wen, Rev. Mod. Phys. **78**, 17 (2006).
[15] P. A. Lee and N. Nagaosa, Phys. Rev. B **46**, 5621 (1992).
[16] M. Jarrell, T. Maier, M. Hettler, and A. Tahvildarzadeh, Europhys. Lett. **56**, 563 (2001).
[17] E. Gull, O. Parcollet, and A. J. Millis, Phys. Rev. Lett. **110**, 216405 (2013).
[18] P. W. Anderson, Mater. Res. Bull. **8**, 153 (1973).
[19] P. W. Anderson, Science **235**, 1196 (1987).
[20] P. W. Anderson, G. Baskaran, Z. Zou, and T. Hsu, Phys. Rev. Lett. **58**, 2790 (1987).
[21] S. Trotzky, P. Cheinet, S. Fölling, M. Feld, U. Schnorrberger, A. M. Rey, A. Polkovnikov, E. Demler, M. Lukin, and I. Bloch, Science **319**, 295 (2008).
[22] S. Hofferberth, I. Lesanovsky, T. Schumm, A. Imambekov, V. Gritsev, E. Demler, and J. Schmiedmayer, Nat. Phys. **4**, 489 (2008).
[23] N. D. Mermin and H. Wagner, Phys. Rev. Lett. **17**, 1133 (1966).
[24] S. Humeniuk and H. P. Büchler, Phys. Rev. Lett. **119**, 236401 (2017).
[25] S. S. Roy, H. S. Dhar, D. Rakshit, A. Sen(De), and U. Sen, Phys. Rev. A **97**, 052325 (2018).
[26] L. Wang, Z.-C. Gu, F. Verstraete, and X.-G. Wen, Phys. Rev. B **94**, 075143 (2016).
[27] H.-C. Jiang, H. Yao, and L. Balents, Phys. Rev. B **86**, 024424 (2012).
[28] M. Ferrero, P. S. Cornaglia, L. De Leo, O. Parcollet, G. Kotliar, and A. Georges, Phys. Rev. B **80**, 064501 (2009).
[29] E. Gull, M. Ferrero, O. Parcollet, A. Georges, and A. J. Millis, Phys. Rev. B **82**, 155101 (2010).
[30] T. Senthil, S. Sachdev, and M. Vojta, Phys. Rev. Lett. **90**, 216403 (2003).
[31] T. C. Ribeiro and X.-G. Wen, Phys. Rev. B **74**, 155113 (2006).
[32] M. Punk and S. Sachdev, Phys. Rev. B **85**, 195123 (2012).
[33] J.-W. Mei, S. Kawasaki, G.-Q. Zheng, Z.-Y. Weng, and X.-G. Wen, Phys. Rev. B **85**, 134519 (2012).
[34] M. Hermele, T. Senthil, M. P. A. Fisher, P. A. Lee, N. Nagaosa, and X.-G. Wen, Phys. Rev. B **70**, 214437 (2004).
[35] X.-G. Wen, Phys. Rev. B **44**, 2664 (1991).
[36] M. Oshikawa, Phys. Rev. Lett. **84**, 3370 (2000).
[37] T. Senthil, M. Vojta, and S. Sachdev, Phys. Rev. B **69**, 035111 (2004).

[38] R. K. Kaul, Y. B. Kim, S. Sachdev, and T. Senthil, Nat. Phys. **4**, 28 (2008).

[39] Y. Qi and S. Sachdev, Phys. Rev. B **81**, 115129 (2010).

[40] S. Sachdev and D. Chowdhury, Prog. Theor. Exp. Phys. **2016**, 12C102 (2016).

[41] M. Punk, A. Allais, and S. Sachdev, Proc. Natl. Acad. Sci. USA **112**, 9552 (2015).

[42] S. Huber, J. Feldmeier, and M. Punk, Phys. Rev. B **97**, 075144 (2018).

[43] J. Feldmeier, S. Huber, and M. Punk, Phys. Rev. Lett. **120**, 187001 (2018).

[44] C. Kim, P. J. White, Z.-X. Shen, T. Tohyama, Y. Shibata, S. Maekawa, B. O. Wells, Y. J. Kim, R. J. Birgeneau, and M. A. Kastner, Phys. Rev. Lett. **80**, 4245 (1998).

[45] G. Martinez and P. Horsch, Phys. Rev. B **44**, 317 (1991).

[46] Z. Liu and E. Manousakis, Phys. Rev. B **45**, 2425 (1992).

[47] E. Dagotto, A. Nazarenko, and M. Boninsegni, Phys. Rev. Lett. **73**, 728 (1994).

[48] T. Tohyama and S. Maekawa, Supercond. Sci. Technol. **13**, R17 (2000).

[49] S. Schmitt-Rink, C. M. Varma, and A. E. Ruckenstein, Phys. Rev. Lett. **60**, 2793 (1988).

[50] C. L. Kane, P. A. Lee, and N. Read, Phys. Rev. B **39**, 6880 (1989).

[51] S. Sachdev, Phys. Rev. B **39**, 12232 (1989).

[52] M. Brunner, F. F. Assaad, and A. Muramatsu, Phys. Rev. B **62**, 15480 (2000).

[53] S. R. White and I. Affleck, Phys. Rev. B **64**, 024411 (2001).

[54] F. Grusdt, M. Kanasz-Nagy, A. Bohrdt, C. S. Chiu, G. Ji, M. Greiner, D. Greif, and E. Demler, Phys. Rev. X **8**, 011046 (2018).

[55] Y. Nagaoka, Phys. Rev. **147**, 392 (1966).

[56] F. Grusdt, Z. Zhu, T. Shi, and E. Demler, SciPost Phys. **5**, 057 (2018).

[57] A. Bohrdt, D. Greif, E. Demler, M. Knap, and F. Grusdt, Phys. Rev. B **97**, 125117 (2018).

[58] H. Li and F. D. M. Haldane, Phys. Rev. Lett. **101**, 010504 (2008).

[59] A. Auerbach, *Interacting Electrons and Quantum Magnetism* (Springer Science & Business Media, New York, 2012).

3 Spectral function of a quantum dimer model for topological metals

3.1 Fractionalized Fermi liquid lattice realization: Quantum dimer model

Many essential aspects of the underdoped regime of cuprates are rooted in the motion of holes in an antiferromagnetic background. The holes tend to delocalize in order to minimze their energy and thereby destroy the perfect Néel ordered background. The competition between kinetic and potential energy induces frustration. The correlation length is already drastically reduced at small doping. In the early days of high-T_c, Philip W. Anderson proposed a theoretical concept, the so-called resonating valence bond theory, that seemed to explain many of these features. The central idea is that pairs of spins form singlets [And73]:

$$|(ij)\rangle = \frac{1}{\sqrt{2}}[|\uparrow_i\downarrow_j\rangle - |\downarrow_i\uparrow_j\rangle]. \tag{3.1}$$

Next, we consider all partitions P of spin pairs on a lattice. One such partition, where the lattice is completely covered by a unique configuration of singlets, is commonly called a valence bond state $|\mathrm{VB}\rangle = \prod_{\mathrm{pairs}} |(ij)\rangle$. A state deep in a singlet-dominated phase is then described by a superposition of such valence bond states:

$$|\Psi\rangle = \sum_P A(P)\, |\mathrm{VB}(P)\rangle \, . \tag{3.2}$$

Such a ground state has total spin zero. In the early days, Philip W. Anderson proposed that the coefficients $A(P)$ in Eq. (3.2) factorize into a product over functions that depend on the distance between the spin pairs of the considered valence bond state $A(P) = \prod_{\mathrm{pairs}} a(|i-j|)$ [BZA87]. The idea of a resonating valence bond state was born, which is SU(2) symmetric and invariant under all point-group transformations of the lattice. The magnetic order of the corresponding wave function depends crucially on the analytical properties of the function $a(|i-j|)$. In certain cases, it can be even Néel ordered with a finite correlation length [LDA88]. This concept became very famous in the context of high-T_c, since a ground state of real space singlets could in principle explain the short-range antiferromegnetic ordering at finite doping on the one hand, and the formation of Cooper pairs on the other hand [LNW06]. At finite doping charge transport could set in due to the holes in the system that move in a background of singlets. Later, we focus on a short-range resonating valence bond state constructed from nearest neighbor singlets, respectively dimers [KRS87, RK88]. Such a dimer is created by the following operator [PAS15]:

$$D^\dagger_{i,\eta} = \frac{1}{\sqrt{2}}[c^\dagger_{i,\uparrow}c^\dagger_{i+\eta,\downarrow} - c^\dagger_{i,\downarrow}c^\dagger_{i+\eta,\uparrow}], \tag{3.3}$$

which describes the creation of a singlet connecting sites i and $i+\eta$ on a square lattice with $\eta \in \{x, y\}$. Such a dimer has no charge and spin relative to a half-filled background.

It satisfies in a Hilbert space solely spanned by dimer configurations bosonic commutation relations. Later in this thesis, we discuss such a dimer space in more detail.

Philip W. Anderson originally proposed the resonating valence bond wave function could be the ground state of the Heisenberg model (i.e. at half-filling) even in the limit of zero temperature. So, he assumed that the system remains in a spin disordered state and no spontaneous symmetry breaking sets in at $T = 0$ due to frustration or other reasons. Today, we know that the ground state of the Heisenberg model on the square lattise has Néel order. The resonating valence bond wave function is a protoypical spin liquid state inheriting topological order.

Meanwhile, also other systems have been investigated in order to observe signatures of spin liquid characteristics. Numerical works using exact diagonalization for an unfrustrated model have shown that a long-range resonating valence bond state is a good description of the ground state, even though signatures of ordering are present [LDA88]. Furthermore, numerical results on frustrated systems point in a rather different direction: Spins on a triangular lattice favor a non-collinear magnetically ordered state, where the spins within a triangle are rotated by an angle of 120° relative to each other [SH92, ESY93]. The ground state on a kagome lattice has the tendency towards a spin disordered wave function with a spin gap as described by a spin liquid or valence bond crystal state [LE93]. Density matrix renormalization group [JYB12] and tensor-product simulations [WGVW16] have shown that the frustrated $J_1 - J_2$ spin-1/2 quantum antiferromagnet on the square lattice has a pronounced phase region with a $\mathbb{Z}_2$ spin liquid ground state. This was earlier proposed within a mean-field study by Christopher Mudry and Eduardo Fradkin [MF94].

In the following we use a dimer model first proposed by Daniel S. Rokhsar and Steve Kivelson based on hard-core short-range dimer coverings in order to dive deeper into the details of resonating valence bond theory [KRS87, RK88]. Spin correlation functions of such a sort-range dimer wave functions describe ground states of Hamiltonian with a finite spin gap.

Projection of a spin Hamiltonian onto the dimer Hilbert space Daniel S. Rokhsar and Steve Kivelson adopted the concept of a valence bond state and started to consider a drastically simplified Hilbert space purely spanned by hard-core short-range singlet coverings $\mathcal{C}$ (cf. Fig. 3.1). The hard-core constraint thereby forbids the overlap of two dimers on a single site. It leads to a drastic reduction of the full Hilbert space towards a physically relevant subspace. Such a local constraint is always an indication for the existence of a gauge theory [Kog79].

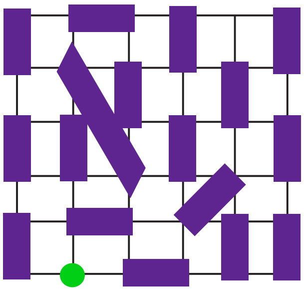

Figure 3.1 Lattice mostly occupied by short-range dimers connecting nearest neighboring sites. The configuration has also vacancies and monomers (empty site and green circle) as well as long-range valence bonds.

They frequently appear also in a variety of other systems, e.g. in form of the Bernal-Fowler ice rules to describe the arrangement of H_2O molecules in ice [BF33] or when projecting out doubly occupied sites because of large on-site Coulomb repulsion in the Fermi-Hubbard model [Spa07].

An exact treatment of such a local constraint is often difficult. It is thus frequently softened in a mean-field approximation. However, the size of the Hilbert space is smaller compared to that of fermions, due to the local constraint. In case of a square lattice with N sites, the local Hilbert space grows just as $(1.3385...)^N$ [Kas61, Fis61]. We now focus on the technical aspects regarding the dimer Hilbert space.

Following closely the original work of Daniel S. Rokhsar and S. Kivelson [RK88], we present here a constructive approach to formulate a low-energy dimer Hamiltonian from a SU(2) invariant spin model. From time to time, we make short references on interesting directions within the field of dimer models. We first consider the complete Fock space constructed from a local fermionic Hilbert space of spin-1/2 particles. Next, we select all hard-core singlet configurations $|\psi_{\mathcal{C}}\rangle$. On common lattice geometries, such as square, triangular, kagome etc., the set of all such nearest neighbor dimer coverings are due to current understanding linearly independent (s. discussion in [LMM11]). An orthonormal basis set of dimer configurations $|\mathcal{C}\rangle$ is then constructed from this subset in a Gram-Schmidt process:

$$|\mathcal{C}\rangle = \sum_{\mathcal{C},\mathcal{C}'} (S_{\mathcal{C}\mathcal{C}'})^{-1/2} |\psi_{\mathcal{C}}\rangle \, . \tag{3.4}$$

The overlap element $S_{\mathcal{C}\mathcal{C}'} = \langle\psi_{\mathcal{C}}| |\psi_{\mathcal{C}'}\rangle$ can be calculated exactly on the square lattice using a transition graph [Sut88], where both configurations are matched in one and the same lattice (cf. Fig. 3.2). So far, we have avoided to fix a sign convention for the valence bonds, however the overlap element crucially depends on it. Let us focus on the square lattice for now. We choose the sign of a singlet such that the overlap between two dimer configurations on a single plaquette, one with horizontal and the other with vertical dimers, yields $-2x^4$. According to this, a transition graph, which consists of $n(C, C')$ closed loops with a total length $L(C, C')$, has the following overlap element:

$$S_{\mathcal{C}\mathcal{C}'} = 2^{n(\mathcal{C}\mathcal{C}')} x^{-L(\mathcal{C}\mathcal{C}')}, \tag{3.5}$$

where $x = 1/\sqrt{2}$. It can be further expanded on the square lattice in loop orders

$$S_{\mathcal{C}\mathcal{C}'} = \delta_{\mathcal{C}\mathcal{C}'} - 2 \, \Box_{\mathcal{C}\mathcal{C}'} \, x^4 + \mathcal{O}(x^6). \tag{3.6}$$

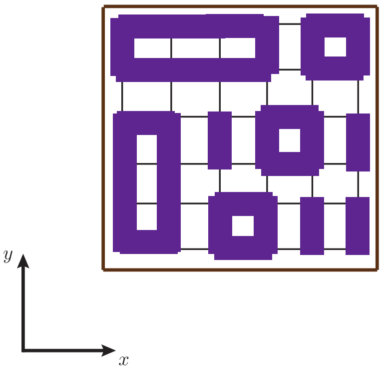

Figure 3.2 Transition graph where two singlet configurations (purple rectangle) are matched on a square lattice. We assume periodic boundary conditions (indicated by brown lines).

Here, $\Box_{\mathcal{C}\mathcal{C}'}$ equals one if both electron configurations differ by a single plaquette flip and is otherwise zero. For larger systems it is expected that the probability for an overlap element (3.5) to be rather small is higher since the existence of a larger loop within the transition graph is more probable.

Next, we use Eq. (3.6) to project a general spin Hamiltonian onto the dimer Hilbert subspace spanned by the states in Eq. (3.4):

$$\mathcal{H}_{\mathcal{C}\mathcal{C}'} = \sum_{D,D'} \left(S^{-1/2}\right)_{\mathcal{C}D} H_{DD'} \left(S^{-1/2}\right)_{D'\mathcal{C}'} . \tag{3.7}$$

A concrete example for such a spin Hamiltonian $H_{DD'}$ could include nearest neighbor exchange coupling J_{ex} and a plaquette spin interaction ν for instance [RMS05]. After performing an expansion in the coefficient x, the leading order terms are equivalent to the Rokhsar-Kivelson Hamiltonian [RK88]:

$$\begin{aligned} H_{RK} = & - J \sum_i D^\dagger_{i,x} D^\dagger_{i+\hat{y},x} D_{i,y} D_{i+\hat{x},y} + \text{x} \leftrightarrow \text{y} \\ & + V \sum_i D^\dagger_{i,x} D^\dagger_{i+\hat{y},x} D_{i,x} D_{i+\hat{y},x} + \text{x} \leftrightarrow \text{y}. \end{aligned} \tag{3.8}$$

The effective parameters of the Rokhsar-Kivelson Hamiltonian depend on the couplings of the plaquette spin model as follows $J = J_{\text{ex}} \, x^4$ and $V = \nu$. The Hamiltonian (3.8)

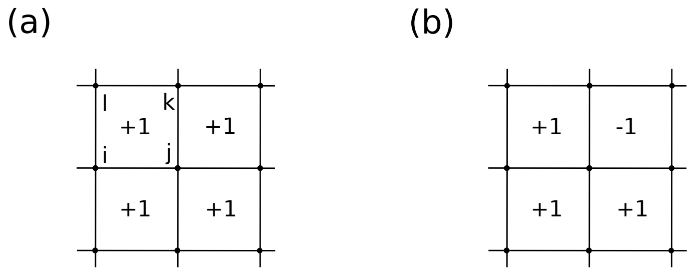

Figure 3.3 (a) The ground state of the $\mathbb{Z}_2$ lattice gauge Hamiltonian (3.9) in the parameter regime $t \gg h$ has $\prod_{\text{plaq.}} \sigma^x_{ij}\sigma^x_{jk}\sigma^x_{kl}\sigma^x_{li} = 1$ on each plaquette. There is one type of excitations: (b) When a confuguration has at one of its plaquettes an odd number of singlets, we call this topological excitation a vison.

describes resonances on a plaquette. The first term with parameter J is a kinetic energy, where two parallel dimers are flipped on a plaquette. The second term adds a potential energy proportional to the flippable plaquettes. Equivalent dimer Hamiltonians have been investigated on triangular and honeycomb lattices with the according smallest possible plaquettes [MS01a, MS01b]. Such approaches have been further developed in different directions. For instance, it was shown that multiple sites on the links stabilize the expansion in the coefficient x [RMS05]. Commonly, mean-field approaches are used to describe dimer states [LNW06]; e.g. dimerized states are obtained from a SU(N) system with spin flavors $\alpha = 1, ..., N$ by performing a large 1/N expansion [AA88b, RS89]. For further details we refer to the literature [LMM11]. Dimer models occur also in ceratin limits of frustrated Ising models [MS01a].

Rokhsar-Kivelson model as a $\mathbb{Z}_2$ lattice gauge theory The Rokhsar-Kivelson model on the square lattice can be mapped onto a $\mathbb{Z}_2$ lattice gauge theory. The corresponding Ising variables σ^z_{ij} are located on bonds between neighboring sites i and j. They can take two values $\{1, -1\}$, where the latter indicates that the bond is occupied by a singlet. We can partially incorporate the hard-core dimer constraint by enforcing $\prod_{+} \sigma^z_{ij} = -1$ for each lattice site i, where $+$ indicates the bonds emanating from this site. Thus, each lattice site is occupied by either one or three singlets. The corresponding $\mathbb{Z}_2$ lattice gauge theory associated with the Rokhsar-Kivelson Hamiltonian at $V = 0$ (cf. Eq. (3.8)) reads then

$$H = -t \sum_{\text{plaq.}} \sigma^x_{ij}\sigma^x_{jk}\sigma^x_{kl}\sigma^x_{li} + h \sum_{\text{bonds}} \sigma^z_{ij}. \tag{3.9}$$

The first sum runs over all plaquettes, where each consists of sites $\{i, j, k, l\}$, and describes plaquette flips (cf. Fig. 3.3). Further, we energetically penalize the occupation of three singlets on a single site by including the second term. Different Ising configurations $\{\sigma_{ij}\}$ and $\{\tilde{\sigma}_{ij}\}$ are related by a gauge transformation $\tilde{\sigma}_{ij} = s_i\ \sigma_{ij}\ s_j$ with $s_i \in \{1, -1\}$.

In the regime $t \gg h$ the ground state of the lattice gauge Hamiltonian yields a state with $\prod_{\text{plaq.}} \sigma^x_{ij}\sigma^x_{jk}\sigma^x_{kl}\sigma^x_{li} = 1$ on each plaquette (cf. Fig. 3.3). The excitation spectrum of the above lattice gauge Hamiltonian has one type of quasiparticles:

- *Visons* – A vison excitation lives on the dual lattice (cf. Fig. 3.3 (b)). It can be viewed as a vortex excitation of the $\mathbb{Z}_2$ gauge field and is given by a plaquette with $\sigma^x_{ij}\sigma^x_{jk}\sigma^x_{kl}\sigma^x_{li} = -1$ (cf. Fig. 3.3 (b)). The parameter h induces hopping of vortices, since

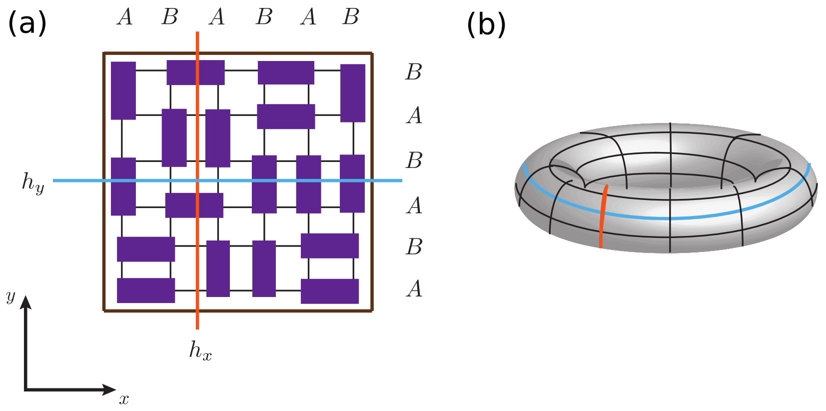

Figure 3.4 (a) Purple rectangles indicate bosonic dimers. Configuration with reference lines and alternated labeling of rows and columns. (b) System on a torus with orange and blue reference lines. Fig. is adapted from our publication Ref. [HFP18]. (Reprinted with permission from Ref. [HFP18]. Copyright (2018) by the American Physical Society.)

acting with Ising variable σ^z_{ij} on bond (i,j) leads to a sign flip of adjacent plaquettes $\prod_{\text{plaq.}} \sigma^x_{ij}\sigma^x_{jk}\sigma^x_{kl}\sigma^x_{li}$.

Vortex excitations carry neither spin nor charge, but in case a spinon excitation encircles such a vortex an additional Aharonov-Bohm phase of π is picked up. These are the topological excitations that cause the violation of the Luttinger's theorem (2.16) within the concept of a fractionalized Fermi liquid (cf. Sec. 2.5 and Sec. 2.6). In order to demonstrate this more explicitly, a topological quantum field theory can be constructed that contains the essential features of a $\mathbb{Z}_2$ spin liquid [SC16]. Assuming the system to be on a torus, equivalent as in Sec. 2.1, and inserting a flux through one of its holes, we indeed observe an additional contribution of the states enclosed by the Fermi surface since the visons couple to the magnetic field. This in addition to the elementary fermionic quasiparticles of Fermi liquid theory cause the formation of a small Fermi surface with volume proportional to doping. A large number of literature exists that contains this and further interesting aspects of topological field theory [Wen04, Fra13].

Separating the dimer Hilbert space into topological sectors In principle we can start from the above $\mathbb{Z}_2$ lattice gauge Hamiltonian and define so-called Wilson-loop operators that wind around the polo- and toroidal direction when putting the two-dimensional systems with periodic boundary conditions on a torus. The Wilson-loop operators can be then used to define topological sectors [Wen04, Fra13]. In the following we provide a different perspective on the same concept.

Let us start from considerng the dimer hard-core constraint, which strongly affects the dynamics within the Hilbert space. A single dimer can never move from one to another link, respectively a dimer process always involes the motion of a sequence of dimers arranged in loops. Let us consider two reference lines as shown in Fig. 3.4, a horizontal h_x and a vertical h_y, both intersecting several dimers. Such a loop crosses the reference lines an even number of times. Resonance processes of dimers along such a closed loop can not change the parity of how often the reference lines intersect dimers. However, if we assume the system to have periodic boundary conditions, a resonance loop can also wind around the polo- or toroidal direction of the corresponding torus and thereby intersect the reference lines an odd number of times.

The corresponding resonance process could then in principle change this invariant, which is then called a nonlocal process. The Rokhsar-Kivelson model is from this point of view

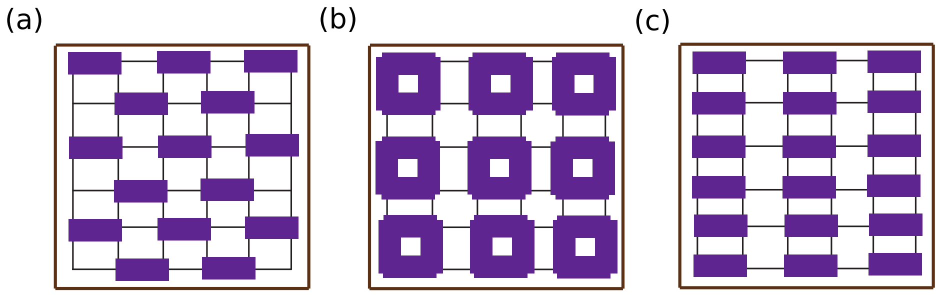

Figure 3.5 Valence bond crystals: (a) Staggered state, (b) plaquette state and (c) columnar state.

highly local, since it just includes processes on small loops around an elementary plaquette. As a consequence the Hamiltonian subdivides the dimer Hilbert space in so-called topological sectors. Each sector is labeled by the mentioned invariants, which are usually called winding numbers. Of course, the position of the reference lines determines the exact numbers of the invariants, however what is important that they are protected under the dynamics of the Hamiltonian. Different sectors are just connected by nonlocal processes. A general dimer system has $2g$ topological sectors, where g labels the genus of the topology on which the system is embedded (e.g. sphere $g = 0$; torus $g = 1$). We consider a system on a torus in the following.

The winding numbers are given by loop operators defined as

$$\mathcal{W}_x = \sum_{i_x} (-1)^{i_x} D^\dagger_{i,y} D_{i,y}, \tag{3.10}$$

$$\mathcal{W}_y = \sum_{i_y} (-1)^{i_y} D^\dagger_{i,x} D_{i,x}. \tag{3.11}$$

The topological sectors are labeled by their integer winding numbers $\mathcal{W} = (\mathcal{W}_x, \mathcal{W}_y)$. It can be shown that both operators, (3.10) and (3.11), commute with the Rokhsar-Kivelson Hamiltonian. The kinetic energy term on the square lattice is ergodic and the topological sectors can not be further subdivided [RK88]. The ground state is thus degenerate with quantum numbers according to the topological sectors. However, for other lattice geometry, such as the triangular lattice, this is not always the case [MS01b].

Phase diagram of the Rokhsar-Kivelson model The dimer model in Eq. (3.8) depends on two parameters. By tuning their ratio J/V, the ground state of the system changes between a variety of crystalline phases. The structure of the phase diagram depends crucially on dimensionality and coordinate number of the lattice. If not otherwise stated, we refer to results for the two-dimensional square lattice in the following. For $J < V$, the ground state at $T = 0$ has a staggered order with a vanishing number of flippable plaquettes (s. Fig. 3.5). The translaional symmetry is broken, respectively just holds, when shifting the dimer configuration an even number of lattice constants. Increasing the kinetic energy parameter such that $J > V$, makes the system favor flip dynamics. One distinguishes two regions separated by a critical V_c: In case $V_c < V < J$, the ground state of the system is described by a plaquette configuration with increased number of flippable plaquettes. However, the dimer orientations on different plaquettes can have different directions. Such a plaquette state is shown in Fig. 3.5 [JS91]. Here, the thick lines indicate larger probabilities for the presence of a dimer. When further decreasing the potential parameter below the critical value $V < V_c < J$, the ground state has columnar order (cf. Fig. 3.5). The columnar and the staggered phase break the point-group symmetry of the lattice, however the plaquette phase is rotational and translational invariant. Other exotic states have been observed in numerical works on the square and honeycomb lattice [LMM11] including also types of 'mixed' phases [LMM11]. Such crystalline orders have been verified using exact diagonalization [LCR96] and quantum Monte Carlo simulations [JS91]. All these crystalline phases, including plaquette, columnar and staggered order, have in common that monomers are confined. It is energetically unfavorable for them to move around due to the ordered singlet background. However, the system for the two-dimensional square lattice at the so-called RK-point $J = V$ is described by a liquid state, where dimer correlation functions decay exponentially. Here, the Hamiltonian can be represented as a sum of projectors:

$$H_{\mathrm{RK}} = \sum_{\text{plaquettes}} J[D^{\dagger}_{i,y}D^{\dagger}_{i+\hat{x},y} - D^{\dagger}_{i,x}D^{\dagger}_{i+\hat{y},x}][D_{i,y}D_{i+\hat{x},y} - D_{i,x}D_{i+\hat{y},x}]. \tag{3.12}$$

The ground state is then the equal superposition of all dimer configurations within a topological sector

$$|\mathrm{RVB}\rangle = \frac{1}{\sqrt{\mathcal{N}}}\sum_{\mathcal{C}}|\mathcal{C}\rangle\,, \tag{3.13}$$

where the normalization constant $\mathcal{N}$ is given by the number of configurations. The ground state is topological degenerate and has fractional excitations. Consider breaking a single dimer within a configuration by flipping one of both spins, the Rokhsar-Kivelson Hamiltonian acts as commonly on this state except on the two sites having the two monomers. Such spinon excitations change the total spin of the original configuration by an integer $S_z = \pm 1$. Furthermore, both monomers are deconfined since the according energy of the state is independent of the position of both monomers. In conclusion, the Rokhsar-Kivelson Hamiltonian on the two-dimensional square lattice has at $J = V$ a deconfined critical point with a resonating valence bond ground state, a prototype for a $U(1)$ spin liquid. Such a critical point also exists for two-dimensional non-bipartite lattices, however is then commonly part or at the boundary of a broader liquid phase. A prominent example is the triangular lattice, where the dimer model has a finite phase region with $\mathbb{Z}_2$ topological order and deconfined fractional excitations [MS01b, RFB$^+$05]. Bipartite lattices in higher dimensions also bear extended liquid phases [HKMS03, MS03, HFB04]; e.g. the phase diagram of the cubic lattice contains a $U(1)$ RVB liquid phase.

Analytical and numerical approaches for dimer models The ground state wave function at the RK-point is an equal superposition of all hard-core dimer configurations (3.13). The expectation value of an observable diagonal in the dimer basis is thus an equal sampling over all dimer configurations. This corresponds to a classical dimer problem at infinite temperature and is frequently used to calculate both, spatial [PAS15, Kas61, Fis61] and temporal [Hen97] correlation functions. For instance, the probability to observe two dimers at distance x and equal orientation on a bipartite lattice has been determined using Pfaffian methods and decays similar to $\propto 1/x^2$ [FS63]. Thus, the ground state has no long-range dimer order at the RK-point. It is also not a liquid, since the dimer correlation function does not decay exponentially. Such calculations have been also performed on the triangular lattice using numerical and field integral methods. Again, the dimer correlation functions do not exhibit long-range order, but decay already over one lattice spacing. Here, the short-range resonating valence bond state describes a liquid phase [MS01b, FMS02]. Also methods that focus on analytical predictions on the excitation spectrum exist. Daniel S. Rokhsar and Steven A. Kivelson used in their original work a single-mode approximation to investigate excitations with a fixed momentum p relative to the ground state [RK88]. The energy of such a trial wave function in principle provides an upper threshold on the excitation spectrum at that momentum and verifies if the spectrum has no gap. Without going here into the details of the method, they revealed the existence of soft excitations, so-called resonons, at the RK-point and momentum $q = (\pi, \pi)$ with excitation energy $\omega_p \propto p^2$. Similar results also exist in higher dimensions, where the structure of the problem is similar to Maxwell's theory and the excitations are usually called photons [MS03, HFB04, Wen04]. The single-mode approximation verifies also that for non-bipartite lattices no gapless excitations do exist in accordance with the $\mathbb{Z}_2$ topological order of the spin liquid ground state (e.g. triangular lattice cf. Ref. [MS03]). For completeness, we mention that also other analytical approaches exist to formulate dimer models in a continuum field theory such as the height representation. It has been applied to dimer models on two-dimensional bipartite lattices at the RK-point [Hen97]. On the numerical side, the classical problem is commonly solved using standard Monte Carlo simulations [HKMS03, MS03]. However, the general quantum dimer problem is not always solveable by quantum Monte Carlo methods due to the constrainted Hilbert space, even though no sign problem occurs. Further information to references on this topic are available in the literature [RFB$^+$05]. Very often, exact diagonalization is used to study dimer models on a finite lattice (e.g. Ref. [MTS04, SMP04, PAS15]), where the constraint leads to a rather large reduction of the Hilbert space compared to usual fermionic models.

Doping the dimer model Doping holes into the dimerized system leads to a breaking of singlets. What remains are fractions of two particles, one with charge $+e$, a so-called holon, and the other with spin $S = 1/2$, a spinon. In the early days of dimer models, works appeared where hole monomers were considered in a singlet background. It was thereby shown that the violation of the Luttinger's theorem and the formation of the Fermi-arc stucture is not explained within this picture [PAS15].

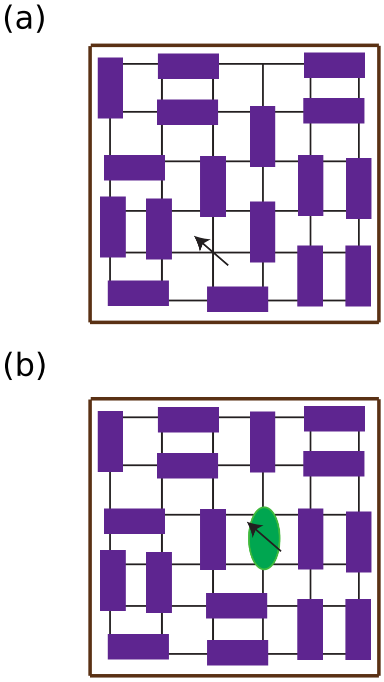

Figure 3.6 (a) A singlet bond is broken and two monomers, spinon and holon, exist in the system. (b) Recombination of spinon and holon to a spinful fermionic dimer (green ellipse; spin $S = +1/2$).

A few years ago Matthias Punk, Andrea Allias and Subir Sachdev followed another route and considered that the free holons recombine with spinons to form a so-called short-range fermionic dimer with charge $+e$ and spin $S = \pm 1/2$ (cf. Fig. 3.6). The according fermionic dimer operator is defined as

$$F^{\dagger}_{i,\eta,\alpha} = \frac{1}{\sqrt{2}} [c^{\dagger}_{i,\alpha} + c^{\dagger}_{i+\eta,\alpha}]. \tag{3.14}$$

The formation of such fermionic bound states are solely due to energitic favourability. Here, $\alpha \in \{\uparrow, \downarrow\}$ denotes the spin of the fermionic dimer. The Hilbert space is then spanned by hard-core dimer configurations of two dimer species. The number of fermionic dimers N_F determines the doping $p = N_F/N$. The formation of such fermionic bound states has been confirmed in a 2-site cluster DMFT analysis of the two-dimensional Fermi-Hubbard model [FCDL$^+$09].

Both states, bosonic (3.3) and fermionic dimers (3.14), had in this study the largest statistical weights at intermediate doping. According to this, a local quantum dimer Hamiltonian was proposed that consists of the following short-range plaquette resonances between fermionic and bosonic dimers [PAS15]

$$H = H_{RK} + H_1, \tag{3.15}$$

where

$$\begin{aligned} H_1 = &- t_1 \sum_i D^\dagger_{i,x} F^\dagger_{i+\hat{y},x,\alpha} F_{i,x,\alpha} D_{i+\hat{y},x} + 3 \text{ terms} \\ &- t_2 \sum_i D^\dagger_{i+\hat{x},y} F^\dagger_{i,y,\alpha} F_{i,x,\alpha} D_{i+\hat{y},x} + 7 \text{ terms} \\ &- t_3 \sum_i D^\dagger_{i+\hat{x}+\hat{y},x} F^\dagger_{i,y,\alpha} F_{i+\hat{x}+\hat{y},x,\alpha} D_{i,y} + 7 \text{ terms} \\ &- t_3 \sum_i D^\dagger_{i+2\hat{y},x} F^\dagger_{i,y,\alpha} F_{i+2\hat{y},x,\alpha} D_{i,y} + 7 \text{ terms.} \end{aligned} \tag{3.16}$$

Additional terms are related to the ones shown here by lattice symmetries. We note that further terms describing resonances between two fermionic dimers can be included as well, but are not expected to play an important role at low doping, where the density of fermionic dimers is small.

Since the quantum dimer Hamiltonian acts locally, the Hilbert space is again subdivided into toplogial sectors. The Hamiltonian just connects dimer configurations with the same winding numbers, which can be again determined by reference lines as shown in Fig. 3.4. The corresponding nonlocal operators to measure the winding numbers read

$$\mathcal{W}_x = \sum_{i_x} (-1)^{i_x} [\sum_\alpha F^\dagger_{i,y,\alpha} F_{i,y,\alpha} + D^\dagger_{i,y} D_{i,y}], \tag{3.17}$$

$$\mathcal{W}_y = \sum_{i_y} (-1)^{i_y} [\sum_\alpha F^\dagger_{i,y,\alpha} F_{i,y,\alpha} + D^\dagger_{i,x} D_{i,x}]. \tag{3.18}$$

The authors further showed that the original physical electrons can be represented in the dimer Hilbert space as

$$c_{i,\alpha} = \frac{\epsilon_{\alpha\beta}}{2} \sum_\eta \left(F^\dagger_{i-\hat{\eta},\eta,\beta} D_{i-\hat{\eta},\eta} + F^\dagger_{i,\eta,\beta} D_{i,\eta} \right), \tag{3.19}$$

where $\epsilon_{\alpha\beta}$ is the unit antisymmetric tensor and a sum over repeated spin indices β is implicitly assumed. It satisfies the fermionic anticommutation relations within the dimer Hilbert subspace.

At the RK-point (J=V) the fermionic dimers are embedded in a spin liquid background formed by bosonic dimers. Exactly at this critical point, the quantum dimer model is a one-band lattice realization of a fractionalized Fermi liquid with topological order and charge carrier density proportional to p (s. Sec. 2.5). The original work [PAS15] mainly investigated the following two aspects:

- The dispersion of the fermionic dimers was determined in a mean-field calculation.
- The quasiparticle weight $\mathcal{Z}_K = |\langle k | c_{\mathbf{k},\alpha} | 0 \rangle|^2$ (excited state with momentum k: $|k\rangle$; ground state: $|0\rangle$) was computed by exact diagonalization of an 8×8 system at zero temperature. It is anisotropic with a sharp crossover at $p \approx (\pi/2, \pi/2)$.

3.2 Study of the electron spectral functions in a quantum dimer model

3.2.1 Overview

The previously explained quantum dimer model is a lattice realization of a fractionalized Fermi liquid. Earlier works have confirmed that the electron dispersion at zero temperature yields a Fermi pocket in accordance with the violation of the Luttinger's theorem [PS12, PAS15]. The precise development of the momentum dependent gap for the quantum dimer model in Eq. (3.15) remains an open question. Especially, angle-resolved photoemission spectroscopy measurements revealed with high resolution that the gap in the underdoped regime changes its analytical form in the proximity of the pseudogap and superconducting phase [SDW+93, DNC+96, DHS03, SRL+05, LVT+07, VLH+10, VHH+12, HVH+14a]. Whereas at very low temperature it shows a pure d-wave symmetric structure, it accumulates higher order corrections at intermediate temperatures in the pseudogap regime, exactly where the quantum dimer model is expected to capture the essential physics. The functional form of the gap could further shed light onto the relation between pseudogap and superconducting phase: As shown in pathbreaking works, an antiferromagentic interaction could in principle explain the formation of a gap with d-wave symmetry [Sca95] and be the driving mechanism of Cooper pair formation. In this context the pseudogap phase is frequently expected to be a precursor phase of the superconducting state. However, the angle-resolved photoemission spectroscopy measurements show additional to the pure d-wave symmetry gap additional effects and fingerprints in the gap function rooted solely in the pseudogap state. Even though such higher order corrections have been mostly detected in angle-resolved photoemission spectroscopy measurements, also other experimental setups show clear signatures in this direction (cf. Ref. in [HVH+14b]. In our work, we have in the first step perfomed an exact diagonalization study on the quantum dimer model, where the full spectrum has been calculated and the corresponding gap function has been investigated.

The full exact diagonalization algorithm is implemented according to the following steps: The Hilbert space of dimer configurations is constructed by specifying the dimer orientation and flavor on every second lattice site. Within our scheme we fix the doping to the case of one fermionic dimer on a $N \times N$ lattice, where $N \in \{4, 6\}$. So, we consider just states with zero or one fermionic dimer. Next, we separate the Hilbert space into topological sectors and focus on states with a certain winding number sector (in our implementation $(\mathcal{W}_x, \mathcal{W}_y) = (0, 0)$). Since twisted boundary conditions are assumed and the system can be wrapped around a torus, we Fourier transform the dimer configurations by using translation operators $T_{x/y}$. Next, we construct a block for each subset of configurations labeled by a fixed total particle number and momentum. Each block is straightforward constructed by projecting a certain state according to the quantum dimer Hamiltonian onto its final state. The diagonalization of all blocks is performed in parallel. The overall calculation was done multiple times assuming different flux through the torus, so that the momentum grid is shifted. Finally, the hole-part of the spectral function is computed in Lehmann representation for various temperatures. The largest block size for a 6×6 lattice is roughly 32000×32000.

We also used a Lanczos algorithm to efficiently compute the many-body ground state of the quantum dimer Hamiltonian on a 8×8 lattice. The Lanczos algorithm is an iterative diagonalization scheme that is still used today as a standard technique in numerical applications to find the extremal eigenvalue of a Hermitian $N \times N$ matrix H [Lan50, Koc11]. The main idea is to start from any initial state $|v_0\rangle$ within the considered Hilbert space, in our case the dimer Hilbert space, and to construct stepwise by a deepest-decent minimization procedure the approximate ground state. The algorithm was implemented as follows:

1. First, we set up the $L+1$ dimensional Krylov space of the Hamiltonian H over a normalized state $|v_0\rangle$ according to:

$$\mathcal{K}_L(|v_0\rangle) = \{|v_0\rangle, H|v_0\rangle, ..., H^L|v_0\rangle\}. \tag{3.20}$$

2. From this we construct a Krylov basis $\{|v_0\rangle, |v_1\rangle, ..., |v_L\rangle\}$ within a Gram-Schmidt procedure:

$$b_{n+1}|v_{n+1}\rangle = |\tilde{v}_{n+1}\rangle = H|v_n\rangle - \sum_{i=0}^{n} |v_i\rangle \langle v_i| H |v_n\rangle, \tag{3.21}$$

   where $b_{n+1} = \langle \tilde{v}_{n+1}| |\tilde{v}_{n+1}\rangle$. Actually, this shows that each new basis vector is just a linear combination of three other vectors given by

$$H|v_n\rangle = b_n|v_{n-1}\rangle + a_n|v_n\rangle + b_{n+1}|v_{n+1}\rangle, \tag{3.22}$$

   where $a_n = \langle v_n| H |v_n\rangle$.

3. According to the last step, the Hamiltonian is tridiagonal in the Krylov basis. Diagonalizing this matrix yields an approximate ground state within the Krylov subspace (3.20).

In our implementation we constructed the Hamiltonian 'on the fly'. This means that we just saved within each construction step of the Hamiltonian the minimal necessary number of vectors in the Krylov basis, namely three (cf. Eq. (3.22)).

In summary, we found in agreement with experiments the following results illustrated in Fig. 3.7:

- The antinodal region at momentum $p = (\pi, 0)$ shows a finite gap. The incoherent peak gets broadened at finite temperature. Obvisiouly excited states of the Rokshar-Kivelson Hamiltonian contribute to the spectrum and lead to a shift of the spectral weight with increasing temperature.

- We extract the gap function defined as the onset of the spectral function at low energies. It describes a lower bound for the pseudogap extracted to the spectral function. The gap function Δ_k shows clear deviation from a pure d-wave form factor in accordance with angle-resolved photoemission spectroscopy measurements [LVT$^+$07, VLH$^+$10].

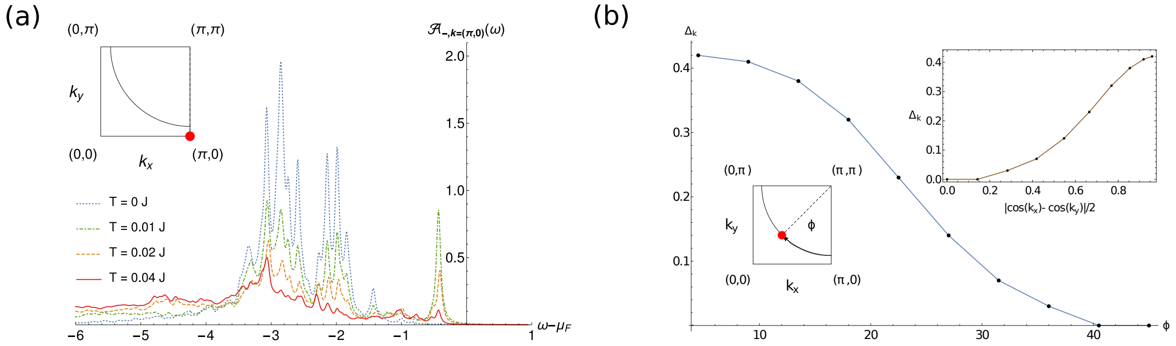

Figure 3.7 (a) The temperature dependence of the spectrum at the antinodal point $p = (\pi, 0)$. Additional spectral weight appears in the gap from higher excitations of the Rokhsar-Kivelson model. (b) The corresponding gap function (for the definition of Δ_k see article below) is not pure d-wave symmetric. Fig. is adapted from our publication Ref. [HFP18]. (Reprinted with permission from Ref. [HFP18]. Copyright (2018) by the American Physical Society.)

As explained above, Daniel S. Rokhsar and Steven A. Kivelson considered a trial wave function of the excitation spectrum with momentum p above the ground state. It was found that such an apporach in combination with variational methods reveals information if the excitation spectrum is gapless [RK88, Aue12]. We made this approach suitable to the dimer Hilbert space in form of a two-mode approximation. The trial wave function was hereby explicitely represented using dimer operators. The spectrum of such excitations were further determined in a semianalytical computation using a mean-field approach similar to [GCC17]. When comparing the outcome of this semianalytic approach with exact diagonalization, we came to the following conclusions:

- The onset of the gap function from our semianalytic calculations is in principle in agreement with the numerical results. Both incoherent spectra have similar broad features.
- The coherent peak at the nodal point is not captured in the two-mode approximation.

Last, we adopted a diagrammatic expansion to calculate the electron spectral function. The locality and hard-core constraint of the quantum dimer Hamiltonian forbids the generation of a dispersion for the fermionic dimers. Thus, our approach can not explain the formation of a broad spectral feature, but just captures the coherent excitation spectrum. We formulated a Bethe-Salpeter equation based on the m-rung particle-hole ladder diagrams [AS10, Mah13] to compute self-consistently the vertex corrections of the quantum dimer model. Thereby, we stayed in the vicinity of the RK-point, where the fermionic dimers are embedded within a mean-field picture into a translational invariant singlet background. The hard-core dimer constraint was included to leading order from the dimer correlation functions of the classical problem [FS63, Sam80]. The main findings of this analysis are as follow:

- The coherent part of the spectrum is in good agreement with numerical results.
- The dispersion is equivalent to that from a perturbative approach in the original work. On top, we calculated the quasiparticle residuum within the above explained approximations.

Electron spectral functions in a quantum dimer model for topological metals

by

S. Huber, J. Feldmeier, and M. Punk

Physics Department, Arnold Sommerfeld Center for Theoretical Physics and Center for NanoScience, Ludwig-Maximilians-Universität München, 80333 München, Germany

reprinted on pages 52–63

with permission from

***Phys. Rev. B* 97(7), 075144 (2018)**,

DOI: 10.1103/PhysRevB.97.075144.

PHYSICAL REVIEW B **97**, 075144 (2018)

Editors' Suggestion

Electron spectral functions in a quantum dimer model for topological metals

Sebastian Huber, Johannes Feldmeier, and Matthias Punk

Physics Department, Arnold Sommerfeld Center for Theoretical Physics and Center for NanoScience, Ludwig-Maximilians-University Munich, 80333 Munich, Germany

(Received 11 October 2017; published 23 February 2018)

We study single-electron spectral functions in a quantum dimer model introduced by Punk, Allais, and Sachdev in Ref. [M. Punk, A. Allais, and S. Sachdev, Proc. Natl. Acad. Sci. U.S.A. **112**, 9552 (2015)]. The Hilbert space of this model is spanned by hard-core coverings of the square lattice with two types of dimers: ordinary bosonic spin singlets, as well as fermionic dimers carrying charge $+e$ and spin $1/2$, which can be viewed as bound states of spinons and holons in a doped resonating valence bond (RVB) liquid. This model realizes a metallic phase with topological order and captures several properties of the pseudogap phase in hole-doped cuprates, such as a reconstructed Fermi surface with small hole pockets and a highly anisotropic quasiparticle residue in the absence of any broken symmetries. Using a combination of exact diagonalization and analytical methods, we compute electron spectral functions and show that this model indeed exhibits a sizable antinodal pseudogap, with a momentum dependence deviating from a simple d-wave form, in accordance with experiments on underdoped cuprates.

DOI: 10.1103/PhysRevB.97.075144

I. INTRODUCTION

Since the discovery of high-temperature superconductivity in cuprates [1], many efforts have been made to understand the underlying pairing mechanism. A potential solution to this problem might come from a better understanding of the so-called pseudogap state at low doping, out of which the superconducting phase develops upon further doping. By now, we know from a wide range of experiments that the pseudogap state is largely dominated by antiferromagnetic fluctuations [2–5] and has a tendency to charge density-wave ordering (CDW) [6–10].

During the last decades, experiments have explored the complex physics of the pseudogap phase in much detail. Early studies of the Knight shift in NMR measurements have shown that the magnetic susceptibility decreases below a characteristic temperature scale, indicative of a spin gap [11,12]. Soon, measurements of the tunneling density of states [13], c-axis optical conductivity [14,15], and specific heat [16,17] revealed that the opening of the pseudogap appears in both, charge and spin degrees of freedom.

Interestingly, some transport experiments show rather ordinary metallic properties in the pseudogap phase. For example, in-plane optical conductivity and magnetoresistance measurements show Fermi liquidlike behavior [18,19]. However, Hall coefficient as well as the Drude weight indicate that the charge carrier density is small and proportional to the density p of doped holes away from half-filling [20–24], rather than $1+p$ as expected from Luttinger's theorem and observed in the Fermi liquid regime at large doping. On the other hand, angle-resolved photoemission (ARPES) experiments show a distinct Fermi-arc spectrum and a gap opening in the vicinity of the antinodes in momentum space [25–32]. Taken together, these observations are hard to reconcile with a Fermi liquid picture, where the Fermi surface is reconstructed by some thermally fluctuating order parameter. In this case, one would expect some signatures of the order parameter correlation length to be observable, e.g., in transport measurements.

A different set of theoretical ideas, based on Anderson's resonating valence bond (RVB) picture [33–35], tries to approach the pseudogap from the Mott insulating state at low doping [36]. Upon doping the RVB state with holes, electrons fractionalize into neutral spin-$1/2$ spinon excitations, as well as spinless holons, carrying charge $+e$. While electron fractionalization in quasi-two-dimensional systems has been a topic of considerable interest on its own, it became clear early that simple incarnations of the RVB state do not capture the sharp Fermi-arc features observed in photoemission experiments, which requires that a certain part of the low-energy spectrum behaves like electron or holelike quasiparticles which carry both spin and charge.

One possible solution to this puzzle might be provided by the idea of fractionalized Fermi liquids (FL*), introduced originally in the context of heavy fermion systems [37]. In the context of cuprates, a fractionalized Fermi liquid can be viewed as a doped RVB liquid where spinons and holons form bound states. These holelike bound states then form a Fermi liquid, with the size of the Fermi surface proportional to the density p of doped holes. Note that the FL* inherits topological order from the RVB background, which accounts for the violation of Luttinger's theorem [38–43]. The quantum dimer model introduced in Ref. [44] provides an explicit and intuitive lattice realization of a fractionalized Fermi liquid and allows to directly compute electronic properties. Subsequent numerical work indeed showed clear signatures of a small Fermi surface, indicative of a FL* ground state [45]. In this model, bound states between spinons and holons are represented by fermionic dimers on nearest-neighbor sites, which resonate with the background of bosonic spin-singlet dimers. At vanishing doping, the model reduces to the well-known Rokhsar-Kivelson model [46]. An exact solution has been

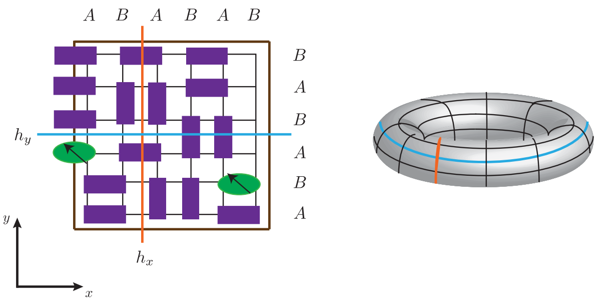

FIG. 1. (Left) One specific dimer configuration with two fermionic spin $S = 1/2$ and charge $+e$ dimers (green ellipses) in a background of bosonic spin singlets (purple rectangles). The blue and orange lines are reference lines to determine the winding numbers of the configuration. (Right) Using periodic boundary conditions, the reference lines map onto noncontractible loops on the torus.

found along a special line in parameter space for an arbitrary density of fermionic dimers and the ground state can be shown to be an FL* in the vicinity of this line [47]. We note that doped quantum dimer models have been studied previously, with doped holes as monomers occupying a single lattice site, carrying no spin [46,48,49].

In this work, our aim is to compute electronic spectral functions for the dimer model introduced in Ref. [44]. Using a combination of exact diagonalization and analytical approaches, we show that this model exhibits a sizable pseudogap in the antinodal region of the Brillouin zone close to momentum $\mathbf{k} = (0,\pi)$ and symmetry related momenta, in accordance with experimental observations in the pseudogap regime of underdoped cuprates.

This paper is organized as follows. In Sec. II, we give a short overview of the quantum dimer model introduced in Ref. [44], define the single hole spectral function and show how it is related to dimer correlation functions. In Sec. III, we discuss our numerical results for ground-state properties as well as the spectral functions at zero and at finite temperature. Section IV contains an analysis of the spectral functions in terms of a two-mode approximation for the low-energy spectrum of the dimer model. Finally, in Sec. V, we present a diagrammatic approach to compute the electron dispersion as well as the coherent quasiparticle residuum. We conclude with a discussion in Sec. VI.

II. DIMER MODEL

The Hamiltonian of the quantum dimer model introduced in Ref. [44] acts on a Hilbert space $\mathcal{H}_\mathcal{D} = \{|\mathcal{C}\rangle\}$ spanned by close-packed hard-core configurations $|\mathcal{C}\rangle$ of two types of dimers living on the links of a two-dimensional square lattice (see Fig. 1): the usual bosonic spin-singlet dimers, represented by bosonic operators $D_{i,\eta}$, as well as fermionic spin-1/2 dimers carrying charge +e, represented by fermionic operators $F_{i,\eta,\alpha}$. Here, i denotes the lattice site, $\alpha \in \{\uparrow, \downarrow\}$ is a spin $S = 1/2$ index, and $\eta \in \{x,y\}$ distinguishes x and y links on the square lattice. A fermionic dimer represents a single electron, delocalized in the bonding orbital between two neighboring lattice sites. Alternatively, one can view it as a bound state of a spinon and a holon in a doped RVB liquid.

Within the restricted Hilbert space of the dimer model, the annihilation operator of an electron with spin α on lattice site i can be uniquely expressed in terms of the bosonic and fermionic dimer annihilation and creation operators as [44]

$$c_{i,\alpha} = \frac{\epsilon_{\alpha\beta}}{2} \sum_{\eta} (F^\dagger_{i-\hat{\eta},\eta,\beta} D_{i-\hat{\eta},\eta} + F^\dagger_{i,\eta,\beta} D_{i,\eta}), \tag{1}$$

where $\epsilon_{\alpha\beta}$ is the unit antisymmetric tensor and a sum over repeated spin indices β is implied.

We follow Ref. [44] and consider a Hamiltonian, which acts on the states $|\mathcal{C}\rangle$ by resonating dimers of both types along short, flippable loops. The corresponding quantum dimer Hamiltonian reads

$$H = H_{RK} + H_1, \tag{2}$$

where

$$\begin{aligned} H_{RK} = &- J \sum_i D^\dagger_{i,x} D^\dagger_{i+\hat{y},x} D_{i,y} D_{i+\hat{x},y} + 1 \text{ term} \\ &+ V \sum_i D^\dagger_{i,x} D^\dagger_{i+\hat{y},x} D_{i,x} D_{i+\hat{y},x} + 1 \text{ term}, \end{aligned} \tag{3}$$

is the standard Rokhsar-Kivelson Hamiltonian [46] and

$$\begin{aligned} H_1 = &- t_1 \sum_i D^\dagger_{i,x} F^\dagger_{i+\hat{y},x,\alpha} F_{i,x,\alpha} D_{i+\hat{y},x} + 3 \text{ terms} \\ &- t_2 \sum_i D^\dagger_{i+\hat{x},y} F^\dagger_{i,y,\alpha} F_{i,x,\alpha} D_{i+\hat{y},x} + 7 \text{ terms} \\ &- t_3 \sum_i D^\dagger_{i+\hat{x}+\hat{y},x} F^\dagger_{i,y,\alpha} F_{i+\hat{x}+\hat{y},x,\alpha} D_{i,y} + 7 \text{ terms} \\ &- t_3 \sum_i D^\dagger_{i+2\hat{y},x} F^\dagger_{i,y,\alpha} F_{i+2\hat{y},x,\alpha} D_{i,y} + 7 \text{ terms} \end{aligned} \tag{4}$$

describes dimer resonances between a bosonic and a fermionic dimer. Additional terms are related to the ones shown explicitly by lattice symmetries. We note that further terms describing resonances between two fermionic dimers can be included as well, but are not expected to play an important role at low doping, where the density of fermionic dimers is small.

The overlap between two possible dimer configurations can be caluclated using transition graphs and decreases strongly with system size [46,50]. We therefore demand that two different dimer configurations $|\mathcal{C}\rangle \in \mathcal{H}_\mathcal{D}$ are orthogonal by construction $\langle\mathcal{C}|\mathcal{C}'\rangle = \delta_{\mathcal{C},\mathcal{C}'}$.

In the following, we use periodic boundary conditions (see Fig. 1). The Hilbert space $\mathcal{H}_\mathcal{D}$ then splits into different topological sectors labeled by a set of two integer winding numbers $\mathcal{W} = \{\mathcal{W}_x, \mathcal{W}_y\}$ defined by

$$\mathcal{W}_x = \sum_{i_x} (-1)^{i_x} \left(\sum_\alpha F^\dagger_{i,y,\alpha} F_{i,y,\alpha} + D^\dagger_{i,y} D_{i,y} \right), \tag{5}$$

$$\mathcal{W}_y = \sum_{i_y} (-1)^{i_y} \left(\sum_\alpha F^\dagger_{i,x,\alpha} F_{i,x,\alpha} + D^\dagger_{i,x} D_{i,x} \right), \tag{6}$$

where the sums run over a line of lattice sites in one direction, counting the staggered number of dimers that cross the reference lines in Fig. 1. Note that any local Hamiltonian like (2) has nonzero matrix elements only between states in the same

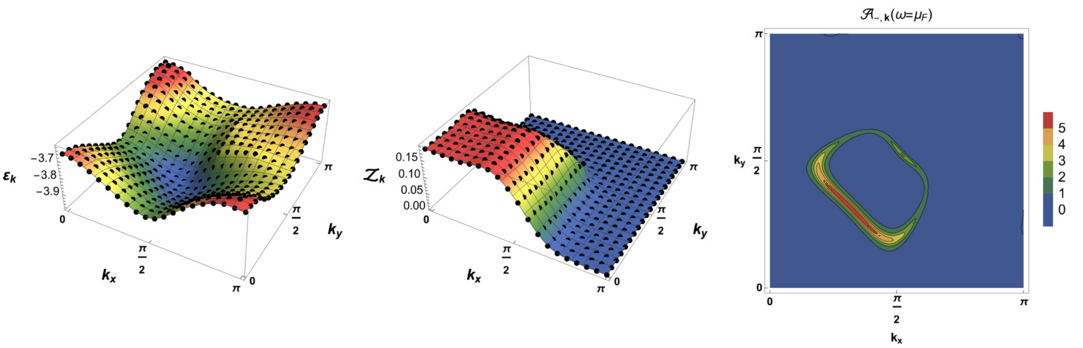

FIG. 2. (Left) Energy dispersion $\varepsilon_{\mathbf{k}}$ of a single fermionic dimer in a background of bosonic dimers, plotted in one quadrant of the Brillouin zone, computed using Lanczos on a 8×8 lattice with twisted boundary conditions. Hamiltonian parameters: $J=V=1$, $t_1=-1.05$, $t_2=1.95$, and $t_3=-0.6$. (Middle) Corresponding quasiparticle residue $\mathcal{Z}_{\mathbf{k}}=|\langle\mathbf{k}|c_{\mathbf{k},\alpha}|0\rangle|^2$. Note the pronounced dispersion minimum in the vicinity of $\mathbf{k}=\frac{1}{2}(\pi,\pi)$, giving rise to pocket Fermi surfaces at a finite density of fermionic dimers, as well as the sharp drop of the quasiparticle residue for momenta larger than $\pi/2$. (Right) Schematic plot of the coherent part of the spectral function $\mathcal{A}_{\mathbf{k}}(\omega)\simeq\mathcal{Z}_{\mathbf{k}}\delta(\omega-\varepsilon_{\mathbf{k}}+\mu)$ as function of momentum with Lorentzian broadening. Here the chemical potential μ has been adjusted such that the hole density equals $p\simeq 1/8$.

topological sector. Matrix elements between states in different topological sectors vanish.

We further make use of symmetries of the quantum dimer Hamiltonian that allow to reduce the computational cost for exact diagonalization. Particle number conservation as well as SU(2) spin-rotation symmetry is implicit in the dimer representation. Finally, the Hamiltonian (2) is invariant under translations as well as square lattice point group symmetries. We make use of these symmetries in our numerical implementation to reach a maximum system size of $N=6\times 6$ lattice sites for which we calculate the full spectrum for one fermionic dimer embedded in a background of bosonic dimers using exact diagonalization, and a maximum size of $N=8\times 8$ sites for the computation of ground-state wave functions using a Lanczos algorithm.

In this work our main quantity of interest is the single-electron spectral function, which is directly measurable in ARPES experiments [25–32]. The mapping in Eq. (1) allows us to directly compute the hole-part of the electron spectral function

$$\mathcal{A}_{-,\mathbf{k}}(\omega)=\frac{2\pi}{Z}\sum_{m,n}e^{-\beta E_m}\,|\langle n|c_{\mathbf{k},\alpha}|m\rangle|^2\delta(\omega-E_m+E_n+\mu),\tag{7}$$

where $\{|n\rangle\}$ denotes a complete set of eigenstates of the dimer model with energy E_n and

$$c_{\mathbf{k},\alpha}=\frac{\epsilon_{\alpha\beta}}{2}\sum_{\mathbf{q},\eta}(1+e^{ik_\eta})F^\dagger_{\mathbf{k}+\mathbf{q},\eta,\beta}D_{\mathbf{q},\eta}\tag{8}$$

is the electron annihilation operator in the dimer representation. For our numerical computation we fix the particle number and take $|m\rangle$ to be eigenstates of the undoped Rokhsar-Kivelson model, whereas $|n\rangle$ are eigenstates of the dimer model with one fermionic dimer. The full single-electron spectral function $\mathcal{A}_{\mathbf{k}}(\omega)=(1+e^{-\beta\omega})\mathcal{A}_{-,\mathbf{k}}(\omega)$ follows from the hole-part via detailed balance and is usually normalized as $\int_\omega\frac{d\omega}{2\pi}\mathcal{A}_{\mathbf{k}}(\omega)=1$. It is important to note here that the electron annihilation operator defined in Eq. (8) does not obey canonical anticommutation relations, because it is a composite operator. For this reason, the positive definite electron spectral function computed here does not satisfy the above normalization condition. The reason for this is that the electron annihilation operator has a nonlocal representation in the dimer Hilbert space and is dressed by the form factor $f_\eta(\mathbf{k})=1+e^{ik_\eta}$. The normalization of the spectral function at zero temperature indeed depends explicitly on momentum $\mathbf{k}$ and is given by $\frac{1}{4}(\cos^2 k_x+\cos^2 k_y)$, which is thus an upper bound to the quasiparticle residuum shown in Fig. 2. The spectrum of the dimer model in our finite size numerics is discrete and the spectral functions are thus composed of a series of delta function peaks with different weight. For better visibility, we broaden the delta functions in our figures using a Lorentzian with a width $\delta=0.04J$. In order to extract quantitative results for the pseudogap from our numerical spectral function data, we define the gap function $\Delta_{\mathbf{k}}$ as the distance between lowest energy state at fixed momentum $\mathbf{k}$ and the Fermi energy. It is important to realize that this is a lower bound for the energy gap in the spectral function, because our numerical data show that the lowest energy states in the spectrum carry a vanishingly small weight in the zero temperature spectral function as one approaches the antinode (see also Fig. 2 middle), shifting the apparent gap to larger energies. This is no longer true at finite temperatures, however.

III. NUMERICAL RESULTS

A. Fermi pockets and quasiparticle residue

The ground-state energy $\varepsilon_{\mathbf{k}}$ of a single fermionic dimer at fixed total momentum $\mathbf{k}$ in a background of bosonic dimers has already been computed in Ref. [44], together with the corresponding quasiparticle residue $\mathcal{Z}_{\mathbf{k}}=|\langle\mathbf{k}|c_{\mathbf{k},\alpha}|0\rangle|^2$. Here, $|\mathbf{k}\rangle$ denotes the ground state of (2) with one fermionic dimer at fixed total momentum $\mathbf{k}$, and $|0\rangle$ is the ground state of the undoped RK-model. In Fig. 2, we show similar data, but with strongly increased momentum resolution, obtained using a Lanczos algorithm for a 8×8 lattice with twisted, rather than periodic boundary conditions, which allows us to compute $\varepsilon_{\mathbf{k}}$ and $\mathcal{Z}_{\mathbf{k}}$ for any momentum in the Brillouin zone.

Our results for parameters $J=V=1$, $t_1=-1.05$, $t_2=1.95$, and $t_3=-0.6$, which follow from electron hopping parameters in an effective t-J model appropriate for cuprates (see Ref. [44] for details), show a pronounced dispersion minimum in the vicinity, but not directly at momentum $\mathbf{k} = (\pi/2,\pi/2)$. We note that the position of the dispersion minimum depends on microscopic details and the precise value of the t_i amplitudes. At a finite density of fermionic dimers, this would give rise to a Fermi surface comprised of small hole pockets with an area proportional to the density of fermionic dimers, which equals the density p of doped holes away from half filling, realizing a fractionalized Fermi liquid. The corresponding quasiparticle residue $\mathcal{Z}_\mathbf{k}$ drops sharply for momenta larger than $\pi/2$ and the associated photoemission response, which is proportional to the hole-part of the electron spectral function, indeed shows Fermi-arc like features due to the highly anisotropic quasiparticle residue. Note that the ground state at a finite density of fermonic dimers potentially breaks symmetries in certain parameter regimes and is not necessarily a fractionalized Fermi liquid with a Fermi surface encompassing an area proportional to the density of fermionic dimers. While the precise nature of the ground state is not yet known in the full parameter space, numerical studies showed the presence of Friedel oscillations associated with a small Fermi surface in accordance with an FL* ground state [45]. Moreover, a recent exact solution of the dimer model also shows that the ground state is an FL* in an interesting parameter regime [47].

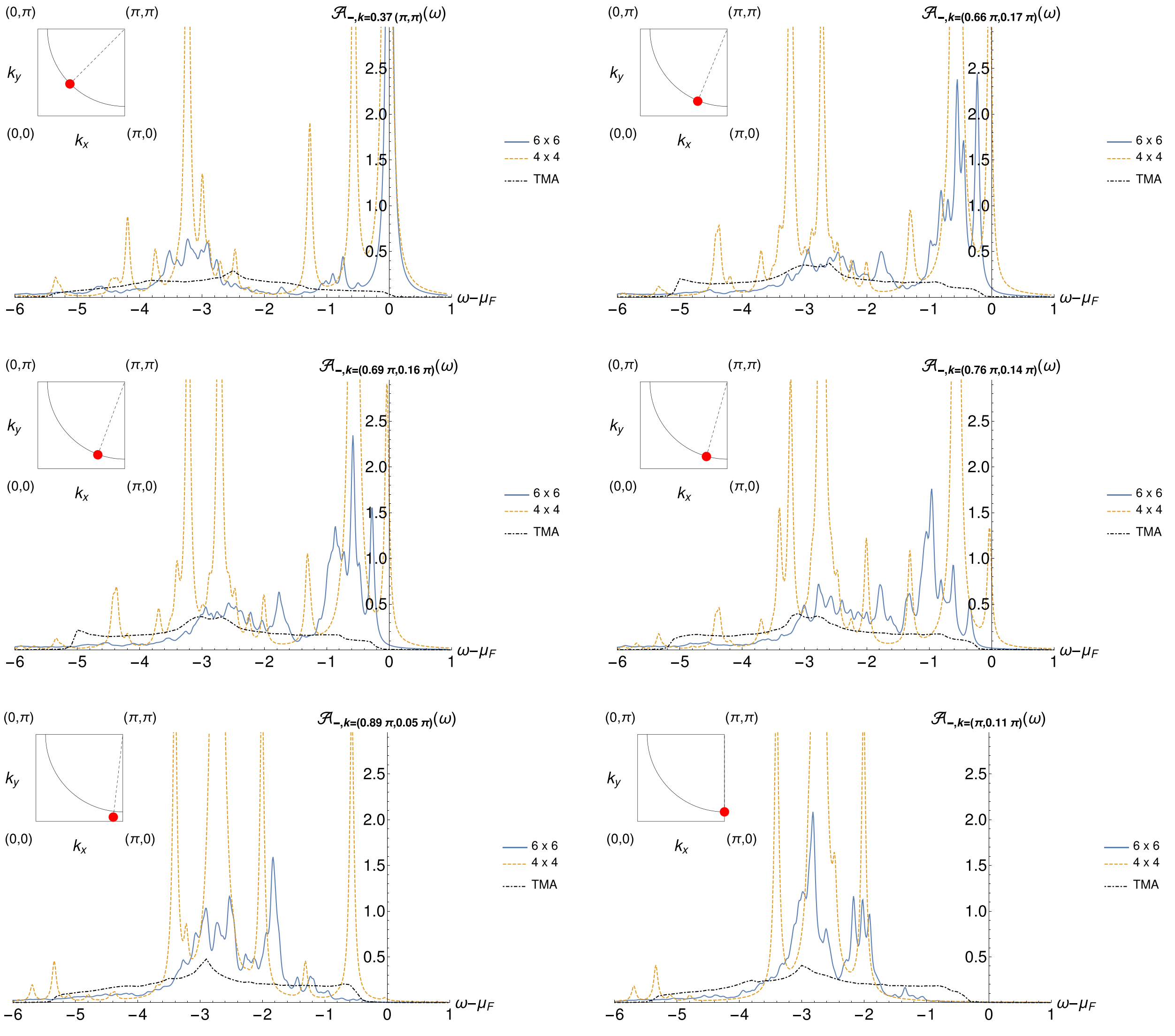

FIG. 3. Top left to bottom right: hole spectral function $\mathcal{A}_{-,\mathbf{k}}(\omega)$ at zero temperature for different momenta $\mathbf{k}$ between the nodal and antinodal region, computed using exact diagonalization for two different system sizes, 4×4 (dashed orange line) and 6×6 (blue solid line). Parameters: $J = V = 1$, $t_1 = -1.05$, $t_2 = 1.95$, and $t_3 = -0.6$. Insets show the respective momentum in the Brillouin zone. The black dash-dotted line corresponds to a two-mode approximation (TMA). The spectral function shows a clear signature of the opening of a pseudogap upon approaching the antinode, independent of system size. At the node (top left), the spectrum exhibits a coherent peak at the Fermi energy, the weight of which is redistributed to the incoherent part of the spectrum at negative frequencies as we move closer to the antinode (bottom right). Note that the TMA is not able to reproduce the coherent peak.

B. Spectral functions and pseudogap

In Fig. 3, we display results for the hole spectral function Eq. (7) at zero temperature along a series of momenta between the nodal point on the Fermi pocket and the antinode at $\mathbf{k} = (\pi,0)$ for two different system sizes, 4×4 and 6×6 lattice sites, where we use the same parameters in the Hamiltonian as in the previous section ($J = V = 1$, $t_1 = -1.05$, $t_2 = 1.95$, and $t_3 = -0.6$). At zero temperature, we only have to consider matrix elements between the RVB ground state of the Rokhsar-Kivelson model and eigenstates of (2) with one fermionic dimer that belong to the zero winding number sector $(\mathcal{W}_x,\mathcal{W}_y) = (0,0)$. At $J = V = 1$ the RVB ground state $|\Psi\rangle_{\mathrm{RVB}} = \sum_{\mathcal{C}} |\mathcal{C}\rangle$ is an equal amplitude superposition of all dimer configurations and has vanishing energy. Again, we used twisted boundary conditions to access arbitrary momenta within the first Brillouin zone.

The top left panel shows $\mathcal{A}_{-,\mathbf{k}}(\omega)$ at the nodal point, which has a sharp peak at the Fermi surface ($\omega = \mu_F$) independent of system size, as expected from our ground-state computations. The incoherent part of the spectrum, containing ∼40% of the hole spectral weight, is broadly distributed with a maximum located around $\omega - \mu_F \approx -3.1J$. The 6×6 data clearly show that the spectral weight of the central peak vanishes and a gap opens as we go away from the nodal point towards the antinode, where the spectral weight is redistributed to lower frequencies. In the antinodal region around $\mathbf{k} = (\pi,0)$, the spectral function exhibits a sizable pseudogap on the order of J, independent of system size (see Fig. 3 bottom right). The complete spectral weight is now distributed over a broad peak of width $\sim 3J$ centered around $\omega - \mu_F \approx -2.8J$.

In Fig. 4, we plot the pseudogap $\Delta_{\mathbf{k}}$ as function of the angle ϕ between the antinode ($\phi = 0$) and the node ($\phi = 45^\circ$) for a fixed distance from $\mathbf{k} = (\pi,\pi)$, extracted from our numerical data for a lattice size of 6×6 sites. We emphasize again that $\Delta_{\mathbf{k}}$ corresponds to the onset of the spectral function at low energies and represents a lower bound for the pseudogap extracted from the spectral function, because the low-energy states in the spectrum turn out to have a vanishingly small weight in the antinodal region, which leads to an apparently larger gap in the spectral function. This effect is only seen at zero temperature, however. Nonetheless, the dimer model features a sizable pseudogap on the order of $\Delta_{\mathbf{k}} \sim 0.4$ at the antinode. It is also important to note that the pseudogap shows a clear deviation from a simple d-wave form $\Delta_{\mathbf{k}} \sim \cos k_x - \cos k_y$ (see inset in Fig. 4) and is thus clearly distinguishable from the superconducting gap. This is in agreement with a wide range of experiments that found evidence for corrections to the d-wave symmetry for the pseudogap in the underdoped regime, in stark contrast to the superconducting gap [30,32,51].

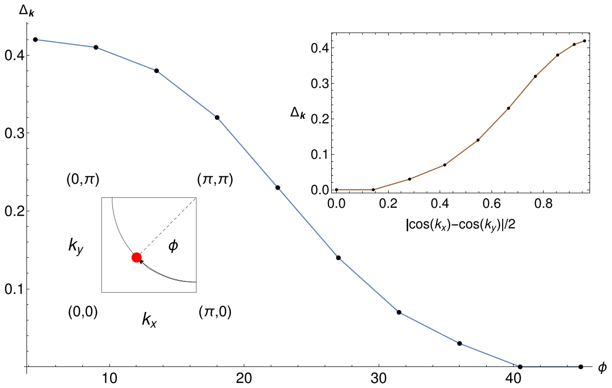

FIG. 4. Pseudogap $\Delta_{\mathbf{k}}$, defined as the energy difference between the onset of the spectrum at fixed total momentum $\mathbf{k}$ and the chemical potential, plotted as a function of the angle between the antinode and the node (see bottom left inset for a definition of the angle) for a 6×6 lattice. Hamiltonian parameters are identical to Fig. 3. The top right inset shows the clear deviation of $\Delta_{\mathbf{k}}$ from a pure d-wave form factor $\sim \cos k_x - \cos k_y$.

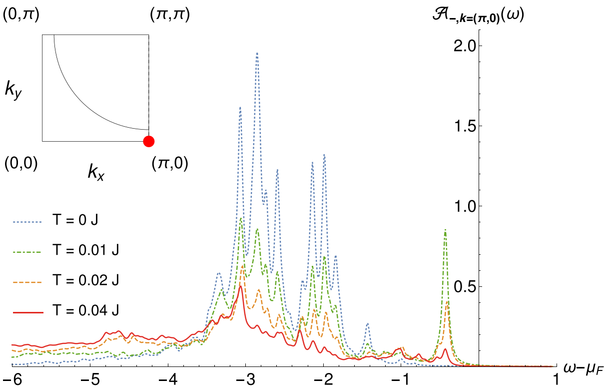

FIG. 5. Hole spectral function $\mathcal{A}_{-,\mathbf{k}}(\omega)$ at the antinode $\mathbf{k} = (0,\pi)$ for four different temperatures $T = 0$, $0.01J$, $0.02J$, and $0.04J$. The Hamiltonian parameters are the same as in Fig. 3 and only numerical data for 6×6 lattices are shown. At finite temperature, the gap corresponds to $\Delta_{\mathbf{k}}$ plotted in Fig. 4, whereas at zero temperature the gap is apparently larger because the low-energy states have a vanishingly small weight.

Finally, in Fig. 5, we show finite temperature results for the hole spectral function in the antinodal region. At finite temperature, matrix elements involving excited states of the Rokshar-Kivelson model contribute to the spectrum as well, which leads to a thermal broadening of the incoherent peak and a shift of spectral weight to lower energies. More interestingly, the finite temperature results show that the low-energy states do contribute finite weight to the spectral function at the antinode, and the pseudogap is indeed given by $\Delta_{\mathbf{k}}$ shown in Fig. 4. This is in contrast to the zero temperature case, where low-energy states have a vanishingly small weight and the pseudogap appears to be larger in the spectral function.

IV. TWO-MODE APPROXIMATION

In this section, we present a semianalytic description of the hole spectral function in terms of a two-mode approximation, where we assume that the low-energy part of the spectrum of excited states can be captured by states of the form

$$|p\rangle_k = \tilde{F}^{\dagger}_{k+p,1}\tilde{D}_{p,1}|\mathrm{GS}\rangle, \tag{9}$$

where the fermionic (bosonic) operator $\tilde{F}_{k,1}$ ($\tilde{D}_{k,1}$) is a linear combination of $F_{k,x}$ ($D_{k,x}$) and $F_{k,y}$ ($D_{k,y}$) and describes the lower of the two fermionic (bosonic) bands. $|\mathrm{GS}\rangle$ denotes the ground state of (2) at a given doping. In order to determine the matrix elements relating $\tilde{F}_{k,1}$ and $F_{k,\eta}$, we use a mean-field approximation to diagonalize the Hamiltonian (2), as outlined below. A similar mean-field approach has been used previously in Ref. [52].

It is important to note here that the two-mode approximation captures the incoherent part of the hole spectral function, but is not able to reproduce the coherent peak, as we explain in detail below. Moreover, the mean-field approach violates the hard-core constraint for the dimers, which is a very crude approximation. Nevertheless, the main features of the pseudogap are correctly reproduced when approaching the antinodal region in momentum space.

We start by outlining the mean-field approximation for the description of a small, but finite density of fermionic dimers interacting with a background of bosonic dimers forming an RVB spin liquid. In total, we need five real, homogeneous and isotropic fields to decouple the dimer Hamiltonian in all possible bosonic channels,

$$\chi_z^s = \langle D_{i,\eta}^\dagger D_{j,\eta'} \rangle, \tag{10}$$

where $s = 0$ denotes on-site terms ($i = j$), whereas $s = 1$ are nearest-neighbor terms ($j = i \pm \hat{x}, \hat{y}$). The index $z = ||, \perp$ denotes parallel ($\hat{\eta} \,||\, \hat{\eta}'$) or perpendicular ($\hat{\eta} \perp \hat{\eta}'$) dimer configurations.

We demand that the mean-field solutions represent a state with no broken symmetries, thus χ_z^s must be invariant under the symmetry group of the square lattice. From this follows that the mean fields $\chi_\perp^1$ and $\chi_\perp^0$ have to be equal. The RK mean-field Hamiltonian thus takes the form

$$H_{\rm RK}^{\rm MF} = \sum_q (D_{q,x}^\dagger, D_{q,y}^\dagger) \begin{pmatrix} V\chi_{||}^0 + V\chi_{||}^1 \cos(q_y) & -\frac{J}{2}\chi_\perp^0(1 + e^{i(q_x - q_y)}) - \frac{J}{2}\chi_\perp^1(e^{-iq_y} + e^{iq_x}) \\ -\frac{J}{2}\chi_\perp^0(1 + e^{-i(q_x - q_y)}) - \frac{J}{2}\chi_\perp^1(e^{iq_y} + e^{-iq_x}) & V\chi_{||}^0 + V\chi_{||}^1 \cos(q_x) \end{pmatrix} \begin{pmatrix} D_{q,x} \\ D_{q,y} \end{pmatrix}. \tag{11}$$

Similarly, the interaction term H_1 between fermionic and bosonic dimers can be decoupled using the mean fields (10) and reads

$$H_1^{\rm MF} = \sum_q (F_{q,x}^\dagger, F_{q,y}^\dagger) \begin{pmatrix} -2t_1\chi_{||}^1 \cos(q_y) & -t_2\chi_\perp^1 h_{2,q} - t_3\chi_\perp^2 h_{3,q} \\ -t_2\chi_\perp^1 \bar{h}_{2,q} - t_3\chi_\perp^2 \bar{h}_{3,q} & -2t_1\chi_{||}^1 \cos(q_x) \end{pmatrix} \begin{pmatrix} F_{q,x} \\ F_{q,y} \end{pmatrix}, \tag{12}$$

with

$$h_{2,q} = (1 + e^{iq_x} + e^{-iq_y} + e^{i(q_x - q_y)}), \tag{13}$$

$$h_{3,q} = (e^{i(q_y - 2q_x)} + e^{iq_x} + e^{-i2q_x} + e^{i(q_x + q_y)} + e^{i2q_y} + e^{i(2q_y - q_x)} + e^{-iq_y} + e^{-i(q_x + q_y)}). \tag{14}$$

We diagonalize the mean-field Hamiltonian using a Bogoliubov transformation $(D_{q,x}, D_{q,y})^T = M_q\ (\tilde{D}_{q,1}, \tilde{D}_{q,2})^T$ and $(F_{q,x}, F_{q,y})^T = N_q\ (\tilde{F}_{q,1}, \tilde{F}_{q,2})^T$, which provides the matrix elements relating $\tilde{F}$ and F, as mentioned above. The single-particle operators $\tilde{F}_{q,\alpha}$ and $\tilde{D}_{q,\alpha}$ describe excitations with dispersion relations $\xi_{q,\alpha}^{\tilde{F}}$ and $\xi_{q,\alpha}^{\tilde{D}}$, respectively, with band index $\alpha \in \{1,2\}$.

Assuming that the electronic spectrum is well approximated by excitations of the form (9), the corresponding eigenenergies of the excitations are then given by

$$H^{\rm MF}|p\rangle_k = \big[\xi_{k+p,1}^{\tilde{F}} - \xi_{p,1}^{\tilde{D}} + \xi_{\rm GS}\big]|p\rangle_k,$$

where $H^{\rm MF} = H_{\rm RK}^{\rm MF} + H_1^{\rm MF}$ and $H^{\rm MF}|{\rm GS}\rangle = \xi_{\rm GS}|{\rm GS}\rangle$.

The hole part of the spectral function at zero temperature in this mean-field approximation reads

$$\mathcal{A}_{-,\mathbf{k}}(\omega) = \sum_p Q_{\mathbf{k}}(\mathbf{p})\, \delta\big(\omega + \xi_{k+p,1}^{\tilde{F}} - \xi_{p,1}^{\tilde{D}} + \xi_{\rm GS}\big), \tag{15}$$

where

$$Q_{\mathbf{k}}(\mathbf{p}) = \big[f_k(p)\big(1 - n_F\big(\xi_{k+p,1}^{\tilde{F}}\big)\big)n_B\big(\xi_{p,1}^{\tilde{D}}\big)\big]^2,$$

$$f_k(\mathbf{p}) = \frac{1}{\sqrt{2N_xN_y}}\big[\bar{N}_{p+k}^{11} M_p^{11} f_{\hat{x}}(k) + \bar{N}_{p+k}^{21} M_p^{21} f_{\hat{y}}(k)\big].$$

Note that the spectral function in the two-mode approximation cannot have a sharp, coherent delta-function peak, because Eq. (15) always involves an integral over momenta. We use the numerical data of the dispersion ε_k in Fig. 2 to constrain the fitting of the mean-field dispersions $\xi_{k,1}^{\tilde{F}}$ and $\xi_{k,1}^{\tilde{D}}$ by using the relation $\varepsilon_k = \min_p[\xi_{k+p,1}^{\tilde{F}} - \xi_{p,1}^{\tilde{D}}]$, which determines the onset of the spectrum. Furthermore, we approximate the momentum distribution of fermionic dimers $n_F(\xi_{k+p,1}^{\tilde{F}})$ by a simple Fermi-Dirac distribution, which is appropriate within the mean-field description. For the bosonic dimers, a Bose-Einstein distribution would not be appropriate, however, because it does not capture the important hard-core constraint of bosonic dimers. For this reason, we take the bosonic dimer distribution to be a constant, as expected for hard core bosons in a semiclasscial limit [53].

In Fig. 3, we plot the spectral functions together with the two-mode approximation for different momenta. Even though this approach is not capable to reproduce the coherent peak of the spectral function, we find a finite weight at the chemical potential. Upon approaching the antinodal region, the pseudogap slowly opens as function of momentum and has a similar size as in the ED results (see Fig. 3 bottom left). The semianalytic mean-field approach describes the spectral function at the antinode reasonably well, where it shows a clear signature of the pseudogap with a dominant incoherent peak at $\omega - \mu_F \approx -3J$ (see Fig. 3 bottom right).

In conclusion, the two-mode approximation is able to reproduce some common features of the spectral function. Its drawback is that it does not capture the coherent quasiparticle peak, however. Such a coherent peak would appear in the two-mode approximation only if we allow for a boson condensate. Since there is no physical basis for the appearance of a condensate in a hard-core boson system at integer filling, we refrained from such a modification. Another modification would be the inclusion of corrections to the boson distribution n_B beyond the semiclassical limit, as discussed in Ref. [53]. These corrections give rise to a term $\sim 1/p$ in the momentum distribution of the bosonic dimers, which leads to the appearance of an additional peak in the spectral function at high energies around $\omega - \mu_F \approx -6J$, but do not change the qualitative behavior at lower energies, in particular the onset of the pseudogap.

V. DIAGRAMMATIC RESULTS

In this section, we present a systematic diagrammatic approach to compute the electron spectral function and the coherent quasiparticle residuum in particular. Since the Hamiltonian of the dimer model does not feature a quadratic part, there formally does not exist a small parameter in the system that would rigorously justify the use of such perturbative means. We pursue this approach nonetheless and for $|t_i| \ll J = 1$ find good agreement with numerical results. The essential ingredient is the expansion around the exactly solvable $t_i = 0$ RK point [46], where dimer-dimer correlations take a classical form, see, e.g., Ref. [54].

Within the domain $|t_i| \ll J$, fermionic dimers are inserted into an RK-like bosonic background, which most importantly allows to consider the ground state to be translationally invariant. We expect the coherent part of the spectral function to be induced by the part H_1 of the dimer Hamiltonian (2) in which we will conduct a perturbative expansion starting from the action S of the model in momentum space:

$$
\begin{aligned}
S = & \sum_{q_1,q_2,q_3,q_4} \{H[\bar{F}(q_1),F(q_4),\bar{D}(q_2),D(q_3)]\} \\
& + \sum_{q,\eta,\alpha} \bar{F}_{\boldsymbol{q},\eta,\alpha}(i\omega)(-i\omega - \mu_f)F_{\boldsymbol{q},\eta,\alpha}(i\omega) \\
& + \sum_{q,\eta} \bar{D}_{\boldsymbol{q},\eta}(i\omega)(-i\omega - \mu_b)D_{\boldsymbol{q},\eta}(i\omega), \qquad (16)
\end{aligned}
$$

where in the notation $q \equiv (i\omega_q, \boldsymbol{q})$, momentum and energy conservation $q_1 + q_2 = q_3 + q_4$ is understood. The fields $\bar{F}$ and F correspond to anticommuting Grassmann variables, while $\bar{D}$ and D are complex fields. Since SU(2) symmetry is manifest, we drop the spin index for the fermionic fields in the following. As a further approximation, we do not enforce the hard-core dimer constraint exactly for the moment, but introduce chemical potentials μ_f and μ_b to fix the fermionic and bosonic dimer densities on average [we comment on how to enforce the hard-core constraint below Eq. (24)]. Since the individual terms in the Hamiltonian obey the hard-core constraint locally, this turns out to be a good approximation. The bare dimer propagators thus are

$$
G^0_{f/b}(i\omega) = \frac{1}{i\omega + \mu_{f/b}}, \qquad (17)
$$

with doping dependent chemical potentials fixing the average dimer densities on a given link of the lattice to $n_F(-\mu_f) = \frac{p}{4}$ and $n_B(-\mu_b) = \frac{1-p}{4}$. Within the Matsubara formalism, we can compute the electronic spectral function $\mathcal{A}_{\boldsymbol{p}}(\omega_p) = -2\Im[G^R_{\boldsymbol{p}}(\omega_p)]$ from the electronic imaginary time ordered Green's function via analytic continuation $G^R_{\boldsymbol{p}}(\omega_p) = \mathcal{G}_{\boldsymbol{p}}(i\omega_p \to \omega_p + i0^+)$. In the dimer Hilbert space [see Eq. (1)], $\mathcal{G}$ can be obtained from the relation

$$
\begin{aligned}
\mathcal{G}_{\boldsymbol{p}}(i\omega_p) = & \frac{1}{4\beta N} \sum_{\eta_1,\eta_2 \epsilon \{x,y\}} (1 + e^{-ip_{\eta_1}})(1 + e^{ip_{\eta_2}}) \\
& \times \sum_{q_1,q_2} \langle F_{q_2,\eta_2} D_{q_1+p,\eta_1} \bar{D}_{q_2+p,\eta_2} \bar{F}_{q_1,\eta_1} \rangle, \qquad (18)
\end{aligned}
$$

where the average $\langle F_{q_2,\eta_2} D_{q_1+p,\eta_1} \bar{D}_{q_2+p,\eta_2} \bar{F}_{q_1,\eta_1} \rangle$ is to be evaluated in the framework of the action S from Eq. (16) (N is the number of sites). The corresponding spectral function for holes is then given by $\mathcal{A}_{-\boldsymbol{p}}(-\omega)$.

We can write the four point dimer correlator in full generality as

$$
\begin{aligned}
& \langle F_{q_2,\eta_2} D_{q_1+p,\eta_1} \bar{D}_{q_2+p,\eta_2} \bar{F}_{q_1,\eta_1} \rangle \\
& \quad = \delta_{q_1,q_2} \delta_{\eta_1,\eta_2} G_f(q_1) G_b(q_1 + p) \\
& \qquad + G_f(q_2) G_b(q_1 + p)\, \tilde{\Gamma}^{\eta_1,\eta_2,\eta_1,\eta_2} \\
& \qquad \times (q_1,q_2 + p,q_1 + p,q_2)\, G_b(q_2 + p) G_f(q_1), \qquad (19)
\end{aligned}
$$

where we have introduced the full interaction vertex $\tilde{\Gamma}^{\eta_1,\eta_2,\eta_1,\eta_2}(q_1,q_2 + p,q_1 + p,q_2)$ and the full (dressed) propagators G_f and G_b. It is important to realize that the full propagators can not develop a dispersion at any order in perturbation theory, as the interaction terms in the Hamiltonian locally respect the hard-core constraint. Any diagram with only two external lines thus necessarily has propagators on the same lattice site for the incoming and outgoing lines. Typically, we expect the full propagators to contain finite lifetimes for the two dimer species which merely lead to a Lorentzian broadening of delta-type peaks in the spectral function. We thus approximate $G_{f/b} \to G^0_{f/b}$ in Eq. (19). The first term in Eq. (19) corresponds to the zeroth-order contribution and upon insertion into Eq. (18) results in the electronic spectral function

$$
\mathcal{A}^0_{\boldsymbol{p}}(\omega_p) = \frac{1}{4}\left(\cos^2\left(\frac{p_x}{2}\right) + \cos^2\left(\frac{p_y}{2}\right)\right) 2\pi\delta(\omega_p) \qquad (20)
$$

for the noninteraction limit $t_i = 0$. Here, $\mu_{f/b} \xrightarrow{T\to 0} 0$, which leads to the peak position at $\omega_p = 0$, was used. It can be verified that this expression indeed reproduces the exact quasiparticle residuum at this specific point in parameter space. We have thus shown that our expansion around an RK-like background at $t_i = 0$ reproduces the correct result right at the expansion point as required for a meaningful ansatz.

We now seek to find a good approximation to the full vertex by considering particle-hole-like ladder diagrams. These turn out to correspond to repeated exchange hoppings of a fermionic dimer in the bosonic background and are thus expected to yield good estimates for considering exchange terms only. The effective vertex is then determined by solving a Bethe-Salpeter equation, which is displayed diagrammatically in Fig. 6. For

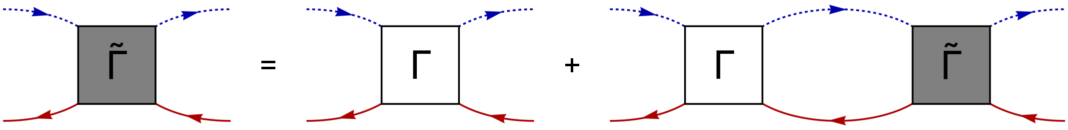

FIG. 6. Bethe-Salpeter equation for the effective two-particle vertex $\tilde{\Gamma}$. Dashed blue lines correspond to bare bosonic, solid red lines to bare fermionic propagators. The approach effectively sums up all particle-hole like ladder diagrams.

the vertex from Eq. (19), this equation reads

$$\begin{aligned}
&\tilde{\Gamma}^{\eta_1\eta_2\eta_1\eta_2}(q_1,q_2+p,q_1+p,q_2)\\
&\quad=\Gamma^{\eta_1\eta_2\eta_1\eta_2}(q_1,q_2+p,q_1+p,q_2)\\
&\quad\quad+\sum_{\tilde{\eta}_f,\tilde{\eta}_b}\beta\psi(i\omega_p)\Bigg\{\sum_{\tilde{q}}\Gamma^{\eta_1\tilde{\eta}_b\eta_1\tilde{\eta}_f}(q_1,\tilde{q}+p,q_1+p,\tilde{q})\\
&\quad\quad\times\,\tilde{\Gamma}^{\tilde{\eta}_f\eta_2\tilde{\eta}_b\eta_2}(\tilde{q},q_2+p,\tilde{q}+p,q_2)\Bigg\}, \qquad (21)
\end{aligned}$$

where Γ corresponds to the bare vertex (see Appendix), which is derived from the Hamiltonian, while the particle-hole bubble $\psi(i\omega_p)=\frac{1}{4}\frac{1}{i\omega_p+\mu_b-\mu_f}$ corresponds to the Matsubara sum of an antiparallel pair of bare fermionic and bosonic propagators.

To solve this integral equation for $\tilde{\Gamma}$, we note that in principle only the exchange interactions t_1 and t_3 contribute to the ladder diagrams of Eq. (21). This is due to the external dimer orientations in Eq. (21) being fixed such that the orientation of the ingoing (outgoing) fermionic (bosonic) dimer η_2 (η_1) matches the orientation of the outgoing (ingoing) bosonic (fermionic) dimer. A t_2 flip term would induce a different relative orientation between ingoing and outgoing dimers and thus cannot contribute to the particle-hole ladder. However, we can include the t_2 terms in an effective manner by substituting them with the following exchange terms:

$$H_{t_2}\to\tilde{H}_{t_2}=-t_2\sum_i D^{\dagger}_{i,y}F^{\dagger}_{i+\hat{y},x,\alpha}F_{i,y,\alpha}D_{i+\hat{y},x}+7\text{ terms.} \qquad (22)$$

Even though this term explicitly violates the hard-core constraint, the physical reasoning for this replacement is the following: we expect the major contributions by t_2 processes to come via induced exchange interactions, i.e., a t_2 flip combines with a t_1 or t_3 exchange and a subsequent bosonic J-plaquette flip, which restores the starting configuration of the bosonic background. Such a sequence effectively acts as an exchange. Since our ladder approach does not include the purely bosonic background interactions, we account for these by assigning to t_2 an effective first-order exchange interaction that induces the correct exchange interactions at higher order. Note that although the terms in Eq. (22) project on nonconstraint configurations, we still expect this substitution to be valid as we consider a translational invariant dimer density in our approach. Comparing our diagrammatic results to numerical data shows that this approximation indeed works very well.

For exchange terms only, the Bethe-Salpeter equation can be solved exactly as the bare vertex $\Gamma^{\eta_1\eta_2\eta_1\eta_2}(q_1,q_2+p,q_1+p,q_2)=\Gamma^{\eta_1\eta_2\eta_1\eta_2}(\boldsymbol{p})$ only depends on the electronic momentum $\boldsymbol{p}$. We can hence assume $\tilde{\Gamma}=\tilde{\Gamma}(p)$ and the sum over $\tilde{\boldsymbol{q}}$ in Eq. (21) can be evaluated trivially.

Equation (21) can then be brought into a simple matrix form by defining the vector

$$\vec{\Gamma}(\boldsymbol{p})\equiv(\Gamma^{xxxx}(\boldsymbol{p}),\quad\Gamma^{xyxy}(\boldsymbol{p}),\quad\Gamma^{yxyx}(\boldsymbol{p}),\quad\Gamma^{yyyy}(\boldsymbol{p})) \qquad (23)$$

(and likewise for $\vec{\tilde{\Gamma}}$) and writing $\vec{\Gamma}(\boldsymbol{p})=\mathcal{M}(p)\cdot\vec{\tilde{\Gamma}}(p)$ with

$$\mathcal{M}(p)=\begin{pmatrix}1-\beta N\psi\,\Gamma^{xxxx} & 0 & -\beta N\psi\,\Gamma^{xyxy} & 0\\ 0 & 1-\beta N\psi\,\Gamma^{xxxx} & 0 & -\beta N\psi\,\Gamma^{xyxy}\\ -\beta N\psi\,\Gamma^{yxyx} & 0 & 1-\beta N\psi\,\Gamma^{yyyy} & 0\\ 0 & -\beta N\psi\,\Gamma^{yxyx} & 0 & 1-\beta N\psi\,\Gamma^{yyyy}\end{pmatrix}. \qquad (24)$$

Straightforward matrix inversion then yields the effective vertex.

We first shortly discuss how to implement the hard-core constraint beyond the mean-field level of chemical potentials. To this end, we note that for every m-rung real space particle-hole ladder diagram, antiparallel bosonic and fermionic propagator lines correspond to the same link on the lattice. This is due to ingoing bosonic links matching outgoing fermionic ones and vice versa on every interaction line in exchange processes. As the particle-hole bubble is proportional to the total average dimer density on the corresponding link, the contribution of an m-rung process is proportional to the product $\prod_{s=0}^{m}n_D(j_s,n_s)$ over the total dimer densities $n_D=1/4$ of all links (j_s,n_s) occuring in the process. Because we expand around the $t_i=0$ RK point, we may substitute this product with the classical probability of having all the links occuring in the process occupied, denoted by $Q_c[(j_0,n_0),\dots,(j_m,n_m)]$. These correlations can be computed from a Grassmann field theory for the classical dimer problem [55]. Attention has to be paid only for interaction lines corresponding to $\tilde{H}_{t_2}$, where the classical probability of having both occurring links occupied would vanish. Instead, we consider the probability

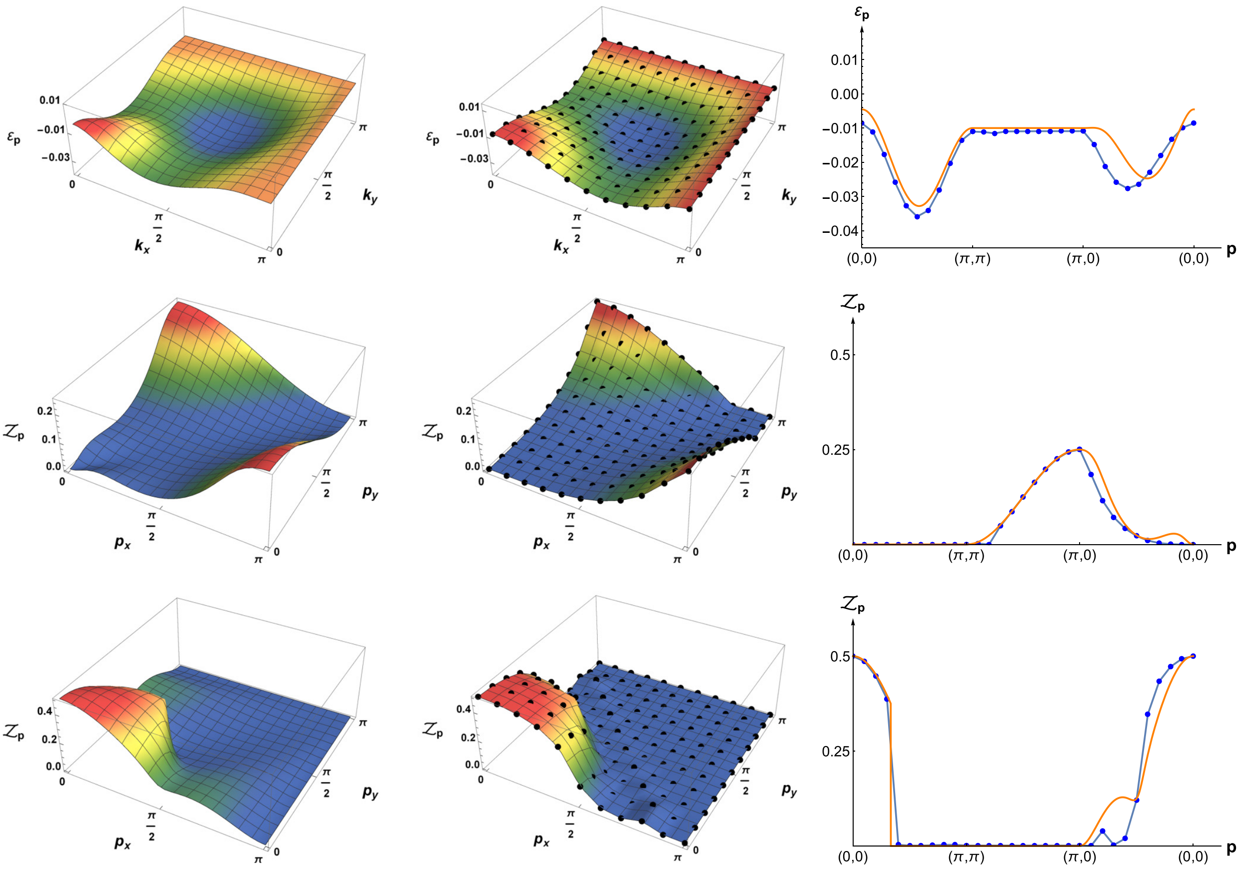

FIG. 7. Comparison of the dimer dispersion and quasiparticle residuum, computed using the ladder ansatz and exact diagonalization (ED) for a lattice with 6 × 6 sites. Left column: results from ladder approach. Middle column: results from ED. Right column: line cuts of $\varepsilon_{\boldsymbol{p}}$ or $\mathcal{Z}_p$ (orange: ladder approach; blue: ED). Top row: dispersion for $t_1 = -0.01,\ t_2 = -0.02,\ t_3 = 0.01$. Middle row: residuum for $t_1 = -0.01,\ t_2 = -0.02,\ t_3 = 0.01$. Bottom row: residuum for $t_1 = t_3 = 0.01,\ t_2 = 0$.

of having the two dimers in a relative position which corresponds to the original t_2 flip. By this reasoning, the classical dimer correlations can in principle be implemented exactly into our approach. We can achieve a first-order approximation by the simple replacement $t_i \to t_i\, 16\, Q_c[(j_s,n_s),(j_s + r_{t_i},n_s + \Delta n_{t_i})]$, where $(r_{t_i},\Delta n_{t_i})$ correspond to the displacement vector and relative orientation change in a single t_i process. In analogy to Ref. [44], this leads to the simple replacements $t_1 \to 4/2\, t_1$, $t_2 \to 4/2\, t_2$, and $t_3 \to 4/\pi\ t_3$ that have to be made in all our diagrammatic results presented below.

Using the effective vertex from above and introducing a finite peak width γ via $i\omega_p \to \omega_p + i\gamma$ yields the electronic spectral function

$$\mathcal{A}_{\boldsymbol{p}}(\omega_p) = 4\gamma\, \frac{8\mathcal{Z}^0_{\boldsymbol{p}}\big(16(\gamma^2+\omega_p^2)+K_1(\boldsymbol{p})\big)+2K_2(\boldsymbol{p})(4\omega_p - t_1\cos(p_x) - t_1\cos(p_y))}{\big[16(\gamma^2-\omega_p^2)+8\omega_p t_1(\cos(p_x)+\cos(p_y))+K_1(\boldsymbol{p})\big]^2+[8\gamma(4\omega_p - t_1\cos(p_x) - t_1\cos(p_y))]^2}, \tag{25}$$

which assumes the form of a sum of two Lorentzians $\mathcal{A} = \mathcal{Z}_{1,\boldsymbol{p}} \cdot \frac{2\gamma}{(\omega_p-\omega_1)^2+\gamma^2} + \mathcal{Z}_{2,\boldsymbol{p}} \cdot \frac{2\gamma}{(\omega_p-\omega_2)^2+\gamma^2}$. The functions $K_1(\boldsymbol{p})$ and $K_2(\boldsymbol{p})$ are given in Appendix, while $\mathcal{Z}^0$ is the residuum at $t_i = 0$. The peak positions of Eq. (25) are given by the singularities in the limit $\gamma \to 0$ and turn out to be

$$\omega_{1,2} = \tfrac{1}{4}t_1\big(\cos(p_x)+\cos(p_y)\big) \pm \tfrac{1}{4}\sqrt{t_1^2(\cos(p_x)+\cos(p_y))^2 + K_1(\boldsymbol{p})}. \tag{26}$$

Note that the spectral function (25) only has two sharp peaks and no incoherent background due to the fact that the dimer propagators cannot obtain a dispersion at any order in perturbation theory. Consequently, the particle-hole bubble of a bosonic and a fermionic dimer has a simple pole on the real frequency axis, which gives rise to the simple two-peak structure in the spectral function.

As the insertion of holes corresponds to the removal of the highest band electrons, we can relate the dispersion and residuum for the holes with the rightmost peak of Eq. (25)

to obtain

$$\varepsilon_{\boldsymbol{p}} = -\,\omega_1(\boldsymbol{p}), \tag{27}$$

$$\mathcal{Z}_{\boldsymbol{p}} = \mathcal{Z}_{1,\boldsymbol{p}} = \lim_{\gamma\to 0} \tfrac{1}{2}\gamma \mathcal{A}_{\boldsymbol{p}}(\omega_1(\boldsymbol{p})) \tag{28}$$

for hole dispersion and hole residuum. Examples for different values of t_i are compared to ED results in Fig. 7. For the chosen parameter regime $t_i \ll J$, the assumption of an RK background is valid and yields good agreement with ED results. This includes parameter sets with nonvanishing t_2 interactions, which were treated via the effective exchange interaction of Eq. (22). We note that the hole dispersion of Eq. (27) reproduces exactly the dispersion obtained in Ref. [44] by a perturbative ansatz. Our approach can hence be viewed as an extension of this ansatz, which additionally yields the quasiparticle residuum.

VI. DISCUSSION AND CONCLUSIONS

Our numerical results show that the dimer model introduced in Ref. [44] has a sizable pseudogap in the antinodal region of the Brillouin zone close to $\mathbf{k} = (0,\pi)$ and symmetry related momenta. Moreover, its momentum dependence clearly deviates from a simple d-wave form, in accordance with observations in the pseudogap regime of underdoped cuprates.

It is important to emphasize here that we always fine tune our model to the RK point at $J = V$, where the ground state of the undoped model is a U(1) spin liquid. Away from this point, the U(1) spin liquid is confining and unstable towards sym-metry broken valence bond solid states. Upon doping away from the RK-point, the dimer model (2) thus realizes a U(1)-FL*, which again is expected to be confining at long length scales. This problem can be circumvented by allowing for diagonal dimers between next-nearest-neighbor sites as well. In this case, the undoped RK model has a stable Z_2 spin liquid ground state in an extended parameter regime [56]. Accordingly, upon doping, the ground state of the appropriately modified model in Eq. (2) is expected to be a Z_2-FL*, which is a stable phase of matter [57]. Nevertheless, we do not expect a qualitatively different behavior of the single-electron spectral function when including diagonal dimers. In particular, the pseudogap in the antinodal region is expected to be a robust property of the dimer model. We leave a detailed analysis of this problem open for further study.

It is also worthwhile to contrast our results with numerical dynamical cluster approximation (DCA) studies of the Hubbard model on the square lattice, where a sizable pseudogap in the spectral function at the antinode was found as well [58,59]. We point out here that two-site cluster dynamical mean field theory (DMFT) studies of the Hubbard model indeed showed that the electron configuration on the two-site cluster at low dopings is dominated by the same two states that are used here to span the Hilbert space of the dimer model on the full lattice, i.e., the bosonic and the fermionic dimer [60]. This suggests that the dimer model introduced in Ref. [44] provides an effective low-energy description of the square lattice Hubbard model at large U and low doping.

ACKNOWLEDGMENTS

We thank D. Pimenov and F. Dorfner for valuable discussions and S. Sachdev for comments on the manuscript. This research was supported by the German Excellence Initiative via the Nanosystems Initiative Munich (NIM).

APPENDIX: DIAGRAMMATIC APPROACH

We provide some additional information on the ladder approach of Sec. V. The bare vertex $\Gamma(\boldsymbol{p})$ from the Bethe-Salpeter equation (21) is determined from the momentum space form of the dimer Hamiltonian H_1, including $\tilde{H}_{t_2}$. The relevant bare vertices in Eqs. (23) and (24) are

$$\Gamma^{xxxx}(p) = \frac{2t_1}{\beta N}\cos(p_y), \tag{A1}$$

$$\Gamma^{yyyy}(p) = \frac{2t_1}{\beta N}\cos(p_x), \tag{A2}$$

$$\begin{aligned}\Gamma^{xyxy}(p) &\equiv C(\boldsymbol{p}) \qquad\qquad (A3)\\ &= \frac{t_3}{\beta N}\big(e^{i(p_x+p_y)} + e^{ip_x} + e^{i(p_y-2p_x)} + e^{-2ip_x} + e^{2ip_y} + e^{i(2p_y-p_x)} + e^{-ip_y} + e^{-i(p_x+p_y)}\big) + \frac{t_2}{\beta N}(1+e^{ip_x})(1+e^{-ip_y}),\end{aligned}$$

$$\Gamma^{yxyx}(p) = C^*(\boldsymbol{p}) = C(-\boldsymbol{p}). \tag{A4}$$

The functions $K_1(\boldsymbol{p})$ and $K_2(\boldsymbol{p})$, which contribute to the spectral function from Eq. (25), are given by

$$\begin{aligned}K_1(\boldsymbol{p}) = t_3^2[&8 + 4\cos(p_x) + 4\cos(3p_x) + 2\cos(p_x - 3p_y) + 4\cos(p_x - 2p_y) + 4\cos(2p_x - 2p_y) + 4\cos(p_x - p_y)\\ &+ 4\cos(2p_x - p_y) + 2\cos(3p_x - p_y) + 4\cos(p_y) + 4\cos(3p_y) + 4\cos(p_x + p_y) + 4\cos(2p_x + 2p_y)\\ &+ 4\cos(2p_x + p_y) + 2\cos(3p_x + p_y) + 4\cos(p_x + 2p_y) + 2\cos(p_x + 3p_y)]\\ &- t_1^2[2\cos(p_x - p_y) + 2\cos(p_x + p_y)]\\ &+ t_2^2[4 + 4\cos(p_x) + 4\cos(p_y) + 2\cos(p_x - p_y) + 2\cos(p_x + p_y)]\\ &+ t_2t_3[4 + 6\cos(p_x) + 6\cos(p_y) + 4\cos(2p_x) + 4\cos(2p_y) + 2\cos(3p_x) + 2\cos(3p_y) + 4\cos(p_x - 3p_y)\end{aligned}$$

$$\begin{aligned}
&+4\cos(3p_x-p_y)+2\cos(2p_x-3p_y)+2\cos(3p_x-2p_y)4\cos(p_x-2p_y)+4\cos(2p_x-p_y)+4\cos(2p_x-2p_y)\\
&+8\cos(p_x+p_y)+2\cos(2p_x+p_y)+2\cos(p_x+2p_y)],\\
K_2(\boldsymbol{p}) = {}& t_3[2+3\cos(p_x)+2\cos(2p_x)+\cos(3p_x)+2\cos(3p_x-p_y)+\cos(2p_x-3p_y)+2\cos(p_x-2p_y)\\
&+2\cos(2p_x-2p_y)+\cos(3p_x-2p_y)+2\cos(2p_x-p_y)+2\cos(3p_x-p_y)+3\cos(p_y)+2\cos(2p_y)+\cos(3p_y)\\
&+4\cos(p_x+p_y)+\cos(2p_x+p_y)+\cos(p_x+2p_y)]-t_1[2\cos(p_x)+\cos(2p_x)+2\cos(p_y)+\cos(2p_y)]\\
&+t_2[4+4\cos(p_x)+4\cos(p_y)+2\cos(p_x-p_y)+2\cos(p_x+p_y)]. \qquad \text{(A5)}
\end{aligned}$$

Note that these functions satisfy $K_{1/2}(-\boldsymbol{p}) = K_{1/2}(\boldsymbol{p})$ and K_1 is even in the parameters t_i while K_2 is odd. We use the notation $K_{1,\{-t_i\}} = K_{1,\{t_i\}}$, $K_{2,\{-t_i\}} = -K_{2,\{t_i\}}$. From these properties and the expression (25) for the spectral function, we can easily deduce

$$\begin{aligned}
\mathcal{A}_{-\boldsymbol{p}}(\omega_p) &= \mathcal{A}_{\boldsymbol{p}}(\omega_p),\\
\mathcal{A}_{\{-t_i\},\boldsymbol{p}}(\omega_p) &= \mathcal{A}_{\{t_i\},\boldsymbol{p}}(-\omega_p),\\
\varepsilon_{\{a\cdot t_i\},\boldsymbol{p}} &= a\cdot\varepsilon_{\{t_i\},\boldsymbol{p}},\\
\mathcal{Z}_{\{a\cdot t_i\},\boldsymbol{p}} &= \mathcal{Z}_{\{t_i\},\boldsymbol{p}} \qquad \text{(A6)}
\end{aligned}$$

for any positive a. Using the second of these equations, one can prove by a straightforward calculation the interesting relation

$$\mathcal{Z}_{\{-t_i\},\boldsymbol{p}} + \mathcal{Z}_{\{t_i\},\boldsymbol{p}} = \lim_{\gamma\to 0}\tfrac{1}{2}\gamma[\mathcal{A}_{\{t_i\},\boldsymbol{p}}(\omega_1(\boldsymbol{p})) + \mathcal{A}_{\{t_i\},\boldsymbol{p}}(\omega_2(\boldsymbol{p}))] = \mathcal{Z}^0_{\boldsymbol{p}} = \tfrac{1}{4}[\cos^2(p_x/2)+\cos^2(p_y/2)]. \qquad \text{(A7)}$$

---

[1] J. G. Bednorz and K. A. Müller, Z. Phys. B **64**, 189 (1986).

[2] Ch. Niedermayer, C. Bernhard, T. Blasius, A. Golnik, A. Moodenbaugh, and J. I. Budnick, Phys. Rev. Lett. **80**, 3843 (1998).

[3] M. A. Kastner, R. J. Birgeneau, G. Shirane, and Y. Endoh, Rev. Mod. Phys. **70**, 897 (1998).

[4] J. L. Tallon and J. W. Loram, Physica C (Amsterdam) **349**, 53 (2001).

[5] M. K. Chan, C. J. Dorow, L. Mangin-Thro, Y. Tang, Y. Ge, M. J. Veit, G. Yu, X. Zhao, A. D. Christianson, J. T. Park, Y. Sidis, P. Steffens, D. L. Abernathy, P. Bourges, and M. Greven, Nat. Commun. **7**, 10819 (2016).

[6] T. Wu, H. Mayaffre, S. Krämer, M. Horvatić, C. Berthier, W. N. Hardy, R. Liang, D. A. Bonn, and M.-H. Julien, Nature **477**, 191 (2011).

[7] G. Ghiringhelli, M. L. Tacon, M. Minola, S. Blanco-Canosa, C. Mazzoli, N. B. Brookes, G. M. De Luca, A. Frano, D. G. Hawthorn, F. He, T. Loew, M. M. Sala, D. C. Peets, M. Salluzzo, E. Schierle, R. Sutarto, G. A. Sawatzky, E. Weschke, B. Keimer, and L. Braicovich, Science **337**, 821 (2012).

[8] J. Chang, E. Blackburn, A. T. Holmes, N. B. Christensen, J. Larsen, J. Mesot, R. Liang, D. A. Bonn, W. N. Hardy, A. Watenphul, M. v. Zimmermann, E. M. Forgan, and S. M. Hayden, Nat. Phys. **8**, 871 (2012).

[9] S. Blanco-Canosa, A. Frano, T. Loew, Y. Lu, J. Porras, G. Ghiringhelli, M. Minola, C. Mazzoli, L. Braicovich, E. Schierle, E. Weschke, M. Le Tacon, and B. Keimer, Phys. Rev. Lett. **110**, 187001 (2013).

[10] R. Comin, R. Sutarto, F. He, E. H. da Silva Neto, L. Chauviere, A. Fraño, R. Liang, W. N. Hardy, D. A. Bonn, Y. Yoshida, H. Eisaki, A. J. Achkar, D. G. Hawthorn, B. Keimer, G. A. Sawatzky, and A. Damascelli, Nat. Mater. **14**, 796 (2015).

[11] H. Alloul, T. Ohno, and P. Mendels, Phys. Rev. Lett. **63**, 1700 (1989).

[12] N. J. Curro, T. Imai, C. P. Slichter, and B. Dabrowski, Phys. Rev. B **56**, 877 (1997).

[13] C. Renner, B. Revaz, J.-Y. Genoud, K. Kadowaki, and Ø. Fischer, Phys. Rev. Lett. **80**, 149 (1998).

[14] C. C. Homes, T. Timusk, R. Liang, D. A. Bonn, and W. N. Hardy, Phys. Rev. Lett. **71**, 1645 (1993).

[15] S. Uchida, Physica C (Amsterdam) **282-287**, 12 (1997).

[16] J. W. Loram, K. A. Mirza, J. R. Cooper, and W. Y. Liang, Phys. Rev. Lett. **71**, 1740 (1993).

[17] J. W. Loram, J. Luo, J. R. Cooper, W. Y. Liang, and J. L. Tallon, J. Phys. Chem. Solids **62**, 59 (2001).

[18] S. I. Mirzaei, D. Stricker, J. N. Hancock, C. Berthod, A. Georges, E. van Heumen, M. K. Chan, X. Zhao, Y. Li, M. Greven, N. Barišić, and D. van der Marel, Proc. Natl. Acad. Sci. U.S.A. **110**, 5774 (2013).

[19] M. K. Chan, M. J. Veit, C. J. Dorow, Y. Ge, Y. Li, W. Tabis, Y. Tang, X. Zhao, N. Barišić, and M. Greven, Phys. Rev. Lett. **113**, 177005 (2014).

[20] J. Orenstein, G. A. Thomas, A. J. Millis, S. L. Cooper, D. H. Rapkine, T. Timusk, L. F. Schneemeyer, and J. V. Waszczak, Phys. Rev. B **42**, 6342 (1990).

[21] S. Uchida, T. Ido, H. Takagi, T. Arima, Y. Tokura, and S. Tajima, Phys. Rev. B **43**, 7942 (1991).

[22] S. L. Cooper, D. Reznik, A. Kotz, M. A. Karlow, R. Liu, M. V. Klein, W. C. Lee, J. Giapintzakis, D. M. Ginsberg, B. W. Veal, and A. P. Paulikas, Phys. Rev. B **47**, 8233 (1993).

[23] W. J. Padilla, Y. S. Lee, M. Dumm, G. Blumberg, S. Ono, K. Segawa, S. Komiya, Y. Ando, and D. N. Basov, Phys. Rev. B **72**, 060511 (2005).

[24] S. Badoux, W. Tabis, F. Laliberté, G. Grissonnanche, B. Vignolle, D. Vignolles, J. Béard, D. A. Bonn, W. N. Hardy, R. Liang, N. Doiron-Leyraud, L. Taillefer, and C. Proust, Nature **531**, 210 (2016).

[25] A. Damascelli, Z. Hussain, and Z.-X. Shen, Rev. Mod. Phys. **75**, 473 (2003).

[26] K. M. Shen, F. Ronning, D. H. Lu, F. Baumberger, N. J. C. Ingle, W. S. Lee, W. Meevasana, Y. Kohsaka, M. Azuma, M. Takano, H. Takagi, and Z.-X. Shen, Science **307**, 901 (2005).

[27] M. Hashimoto, I. M. Vishik, R.-H. He, T. P. Devereaux, and Z.-X. Shen, Nat. Phys. **10**, 483 (2014).

[28] Z.-X. Shen, D. S. Dessau, B. O. Wells, D. M. King, W. E. Spicer, A. J. Arko, D. Marshall, L. W. Lombardo, A. Kapitulnik, P. Dickinson, S. Doniach, J. DiCarlo, T. Loeser, and C. H. Park, Phys. Rev. Lett. **70**, 1553 (1993).

[29] H. Ding, M. R. Norman, J. C. Campuzano, M. Randeria, A. F. Bellman, T. Yokoya, T. Takahashi, T. Mochiku, and K. Kadowaki, Phys. Rev. B **54**, R9678(R) (1996).

[30] W. S. Lee, I. M. Vishik, K. Tanaka, D. H. Lu, T. Sasagawa, N. Nagaosa, T. P. Devereaux, Z. Hussain, and Z.-X. Shen, Nature **450**, 81 (2007).

[31] I. M. Vishik, M. Hashimoto, R.-H. He, W.-S. Lee, F. Schmitt, D. Lu, R. G. Moore, C. Zhang, W. Meevasana, T. Sasagawa, S. Uchida, K. Fujita, S. Ishida, M. Ishikado, Y. Yoshida, H. Eisaki, Z. Hussain, T. P. Devereaux, and Z.-X. Shen, Proc. Natl. Acad. Sci. U.S.A. **109**, 18332 (2012).

[32] I. M. Vishik, W. S. Lee, R.-H. He, M. Hashimoto, Z. Hussain, T. P. Devereaux, and Z.-X. Shen, New J. Phys. **12**, 105008 (2010).

[33] P. W. Anderson, Mater. Res. Bull. **8**, 153 (1973).

[34] P. Fazekas and P. W. Anderson, Philos. Mag. **30**, 423 (1974).

[35] P. W. Anderson, G. Baskaran, Z. Zou, and T. Hsu, Phys. Rev. Lett. **58**, 2790 (1987).

[36] P. A. Lee, N. Nagaosa, and X.-G. Wen, Rev. Mod. Phys. **78**, 17 (2006).

[37] T. Senthil, S. Sachdev, and M. Vojta, Phys. Rev. Lett. **90**, 216403 (2003).

[38] T. Senthil, M. Vojta, and S. Sachdev, Phys. Rev. B **69**, 035111 (2004).

[39] R. K. Kaul, Y. B. Kim, S. Sachdev, and T. Senthil, Nat. Phys. **4**, 28 (2008).

[40] Y. Qi and S. Sachdev, Phys. Rev. B **81**, 115129 (2010).

[41] J.-W. Mei, S. Kawasaki, G.-Q. Zheng, Z.-Y. Weng, and X.-G. Wen, Phys. Rev. B **85**, 134519 (2012).

[42] M. Punk and S. Sachdev, Phys. Rev. B **85**, 195123 (2012).

[43] S. Sachdev and D. Chowdhury, Prog. Theor. Exp. Phys. **2016**, 12C102 (2016).

[44] M. Punk, A. Allais, and S. Sachdev, Proc. Natl. Acad. Sci. U.S.A. **112**, 9552 (2015).

[45] J. Lee, S. Sachdev, and S. R. White, Phys. Rev. B **94**, 115112 (2016).

[46] D. S. Rokhsar and S. A. Kivelson, Phys. Rev. Lett. **61**, 2376 (1988).

[47] J. Feldmeier, S. Huber, and M. Punk, arXiv:1712.01854 (2017).

[48] D. Poilblanc, Phys. Rev. Lett. **100**, 157206 (2008).

[49] C. A. Lamas, A. Ralko, D. C. Cabra, D. Poilblanc, and P. Pujol, Phys. Rev. Lett. **109**, 016403 (2012).

[50] B. Sutherland, Phys. Rev. B **37**, 3786 (1988).

[51] B. Loret, S. Sakai, S. Benhabib, Y. Gallais, M. Cazayous, M. A. Measson, R. D. Zhong, J. Schneeloch, G. D. Gu, A. Forget, D. Colson, I. Paul, M. Civelli, and A. Sacuto, Phys. Rev. B **96**, 094525 (2017).

[52] G. Goldstein, C. Chamon, and C. Castelnovo, Phys. Rev. B **95**, 174511 (2017).

[53] T. Coletta, N. Laflorencie, and F. Mila, Phys. Rev. B **85**, 104421 (2012).

[54] M. E. Fisher and J. Stephenson, Phys. Rev. **132**, 1411 (1963).

[55] S. Samuel, J. Math. Phys. **21**, 2806 (1980).

[56] R. Moessner and S. L. Sondhi, Phys. Rev. Lett. **86**, 1881 (2001).

[57] A. A. Patel, D. Chowdhury, A. Allais, and S. Sachdev, Phys. Rev. B **93**, 165139 (2016).

[58] E. Gull, M. Ferrero, O. Parcollet, A. Georges, and A. J. Millis, Phys. Rev. B **82**, 155101 (2010).

[59] E. Gull, O. Parcollet, and A. J. Millis, Phys. Rev. Lett. **110**, 216405 (2013).

[60] M. Ferrero, P. S. Cornaglia, L. De Leo, O. Parcollet, G. Kotliar, and A. Georges, Phys. Rev. B **80**, 064501 (2009).

3.3 Exact solution of a quantum dimer model

3.3.1 Overview

The Rokhsar-Kivelson Hamiltonian on the two-dimensional square lattice has an isolated critical point, the RK-point for $J = V$, at which an exact solution exists. The corresponding solution yields a resonance valence bond state, which is fully symmetric under lattice and spin transformations [RK88]. Its direct correspondence to a classical problem at infinite temperature makes a wide range of approaches applicable [Kas61, Fis61, Hen97]. The Rokhsar-Kivelson model has to be called with other famous models, such as the Kitaev [Kit06] or the Tomonaga-Luttinger model [Tom50, Lut63, ML65], where exact solutions exist. All of them are toy models to investigate modern theoretical concepts, e.g. gauge theories and topological order, and are guidelines for experimental measurements.

On the technical side, the Rokhsar-Kivelson model at the RK-point can be represented as a sum of projectors. It is thus positive semidefinite and therefore exactly solvable within the dimer Hilbert space. We adopted this idea and added terms to the original quantum dimer Hamiltonian as proposed in Eq. (3.15) such that it was separable into projectors along a certain parameter line. Using a product ansatz for the ground state, we determined an exact solution of the quantum dimer model for two fermionic dimers. An extension to a larger density of fermionic dimers is straightforward. The main outcomes of this work are summarized in the following:

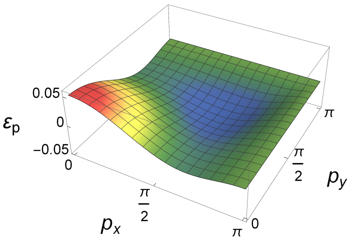

Figure 3.8 The dispersion from exact diagonalization and our analytical approach are in good agreement. The dispersion shows for small δt_3 in proximity to the RK line the formation of a Fermi pocket. Fig. is adapted from our publication Ref. [FHP18]. (Reprinted with permission from Ref. [FHP18]. Copyright (2018) by the American Physical Society.)

- The formation of Fermi pockets in the vicinity close to $p = (\pi/2, \pi/2)$ occured in a first order perturbative calculation around the exactly solveable parameter line.

- The dimer model can be mapped onto a system of free fermions

  $$H = \sum_p \varepsilon_p f_p^\dagger f_p. \tag{3.23}$$

  The corresponding free fermions are in a direct relation to the physical electrons, respectively represent a dressed version of them, with respect to the half-filled resonating valence bond ground state:

  $$f_p = \frac{4}{\sqrt{|1 + e^{ip_x}|^2 + |1 + e^{ip_y}|^2}} c_{-p}. \tag{3.24}$$

  This verfies that the ground state of the quantum dimer model at small doping is indeed a fractionalized Fermi liquid.

Exact Solution of a Two-Species Quantum Dimer Model for Pseudogap Metals

by

J. Feldmeier, S. Huber, and M. Punk

Physics Department, Arnold Sommerfeld Center for Theoretical Physics and Center for

NanoScience, Ludwig-Maximilians-Universität München, 80333 München, Germany

reprinted on pages 66–71

with permission from

Phys. Rev. Lett. **120(18), 187001 (2018)**,

DOI: 10.1103/PhysRevLett.120.187001.

PHYSICAL REVIEW LETTERS **120,** 187001 (2018)

Exact Solution of a Two-Species Quantum Dimer Model for Pseudogap Metals

Johannes Feldmeier, Sebastian Huber, and Matthias Punk
Physics Department, Arnold Sommerfeld Center for Theoretical Physics and Center for NanoScience,
Ludwig-Maximilians-University Munich, 80333 Munich, Germany

(Received 12 December 2017; published 3 May 2018)

We present an exact ground state solution of a quantum dimer model introduced by Punk, Allais, and Sachdev [Quantum dimer model for the pseudogap metal, Proc. Natl. Acad. Sci. U.S.A. **112**, 9552 (2015).], which features ordinary bosonic spin-singlet dimers as well as fermionic dimers that can be viewed as bound states of spinons and holons in a hole-doped resonating valence bond liquid. Interestingly, this model captures several essential properties of the metallic pseudogap phase in high-T_c cuprate superconductors. We identify a line in parameter space where the exact ground state wave functions can be constructed at an arbitrary density of fermionic dimers. At this exactly solvable line the ground state has a huge degeneracy, which can be interpreted as a flat band of fermionic excitations. Perturbing around the exactly solvable line, this degeneracy is lifted and the ground state is a fractionalized Fermi liquid with a small pocket Fermi surface in the low doping limit.

DOI: 10.1103/PhysRevLett.120.187001

Quantum dimer models have been a very useful tool to study paramagnetic ground states of quantum antiferromagnets. Originally introduced by Rokhsar and Kivelson to elucidate the physics of Anderson's resonating valence bond (RVB) state in the context of high-temperature superconductors [1–4], these models provide an effective description of low energy singlet excitations in antiferromagnets and feature rich phase diagrams, including a variety of different valence bond solids with broken lattice symmetries, as well as symmetric spin-liquid phases [5–9]. Subsequently, interesting connections to lattice gauge theories and loop gas models have been found, raising interest in quantum dimer models from various perspectives [10–14].

In this work we consider an extension of the Rokhsar-Kivelson (RK) model on the square lattice introduced by Punk, Allais and Sachdev [1], which provides an effective low-energy description of hole-doped antiferromagnets in two dimensions. The Hilbert space is constructed by hard-core coverings of the square lattice with two flavors of dimers: the standard nearest-neighbor bosonic spin-singlets of the RK model, as well as fermonic dimers carrying charge $+e$ and spin $1/2$. These fermionic dimers can be viewed as bound states of a spinon and a holon in hole-doped RVB states [15–21]. It has been argued in Refs. [1,22] that this model features a so-called fractionalized Fermi liquid ground state [23], with a small Fermi surface enclosing an area proportional to the density of doped holes away from half filling. This apparent violation of Luttinger's theorem, which states that the Fermi surface should enclose an area proportional to the total number of holes with respect to the completely filled band in metallic phases without broken symmetries [24], is possible due to the presence of topological order [25,26].

One of the most interesting aspects of this model is the fact that it captures various properties of the metallic pseudogap phase in underdoped high-T_c cuprate superconductors, such as the presence of a small hole-pocket Fermi surface with a highly anisotropic, electronic quasiparticle residue, providing a potential explanation for the observation of Fermi arcs in photoemission experiments. Moreover, this model exhibits a large pseudogap in the antinodal region of the Brillouin zone around momenta $\boldsymbol{k} \sim (0, \pi)$ and symmetry related points [27].

While previous studies of this quantum dimer model were mostly based on numerical approaches, we present an exact analytical solution for the ground state at an arbitrary density of fermionic dimers in this work. This solution is based on a generalization of the original idea by Rokhsar and Kivelson that the Hamiltonian can be written as a sum of projectors in certain parameter regimes. While it is easy to see that the corresponding ground state is a simple equal weight superposition of all possible dimer coverings in the RK case, this is no longer true in the presence of fermionic dimers, because the equal weight superposition is not antisymmetric under the exchange of two fermions. Nevertheless, it is still possible to construct the exact ground state wave function, as we show in detail below. Interestingly, we find that fermionic excitations are dispersionless and form a flat band at this generalized RK line in parameter space. Perturbing away from the exactly solvable line we can show that the ground state of this model is indeed a fractionalized Fermi liquid at low densities of fermionic dimers.

We start from the dimer model introduced in Ref. [1] and add an additional potential energy term for configurations with pairs of parallel fermionic and bosonic dimers within a flippable plaquette configuration. The Hamiltonian $H = H_{\rm RK} + H_1$ consists of two parts: the standard Rokhsar-Kivelson Hamiltonian for bosonic dimers,

$$H_{\rm RK} = \sum_{i,\eta} [-J D^\dagger_{i,\eta} D^\dagger_{i+\hat{\bar{\eta}},\eta} D_{i,\bar{\eta}} D_{i+\hat{\eta},\bar{\eta}} \\ + V D^\dagger_{i,\eta} D^\dagger_{i+\hat{\bar{\eta}},\eta} D_{i,\eta} D_{i+\hat{\bar{\eta}},\eta}], \qquad (1)$$

as well as similar terms with plaquette resonances and potential energy terms between a bosonic and a fermionic dimer

$$\begin{aligned} H_1 = &-t_1 \sum_i [D^\dagger_{i,x} F^\dagger_{i+\hat{y},x} F_{i,x} D_{i+\hat{y},x} + 3\text{terms}] \\ &+ v_1 \sum_i [D^\dagger_{i,x} F^\dagger_{i+\hat{y},x} F_{i+\hat{y},x} D_{i,x} + 3\text{terms}] \\ &- t_2 \sum_i [D^\dagger_{i,x} F^\dagger_{i+\hat{y},x} F_{i,y} D_{i+\hat{x},y} + 7\text{terms}] \\ &- t_3 \sum_i [D^\dagger_{i,x} F^\dagger_{i+2\hat{x},y} F_{i,x} D_{i+2\hat{x},y} + 15\text{terms}]. \qquad (2) \end{aligned}$$

Here, $D_{i,\eta}$ ($F_{i,\eta}$) is an annihilation operator for a bosonic (fermionic) dimer on the bond emanating from lattice site i in direction $\eta \in \{x, y\}$, while $\hat{\eta} \in \{\hat{x}, \hat{y}\}$ denotes basis vectors in x and y directions (the lattice constant has been set to unity throughout this Letter). Finally, $\bar{\eta}$ denotes the complement of η, i.e., $\bar{\eta} = x$ if $\eta = y$ and vice versa. The terms which are not explicitly displayed are related by lattice symmetry operations and Hermitian conjugation. Note that in contrast to Ref. [1] we omit a possible spin index for the fermionic dimers. Nevertheless, all our results can be generalized to spinful fermions easily. Further terms involving resonances of two or more fermionic dimers are possible as well, but are not expected to be important in the interesting regime of low doping, where the density of fermionic dimers is small. Moreover, we will focus exclusively on the topological sector of the Hilbert space of hard-core coverings with zero winding number throughout this work [27].

In the next step we identify a line in parameter space which allows us to rewrite the Hamiltonian H as a sum of projectors. As the model then takes a form similar to the original RK Hamiltonian at $J = V$ [4], we shall speak of an RK line in the following. Setting the parameters to $J = V$, $t_3 = 0$ and $v_1 = t_2 = -t_1$, the full Hamiltonian can be expressed graphically as a sum of projectors

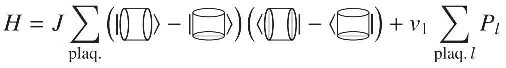

(3)

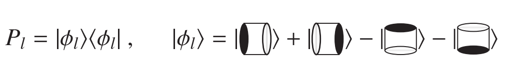

(4)

where empty (full) ellipses represent bosonic (fermionic) dimers.

As a consequence of the special form of Eq. (3), the Hamiltonian is positive definite, i.e., $\langle\psi|H|\psi\rangle \geq 0$ for all wave functions ψ. The ground state can hence be determined by the condition $H|\psi_0\rangle = E_0|\psi_0\rangle = 0$. We now construct ground state wave functions $|\psi_0\rangle$ in an arbitrary sector of the (conserved) number of fermionic dimers N_f. In the following calculation we restrict to the case $N_f = 2$, the generalization to arbitrary fermion numbers is straightforward. We assume the ground state to be a common eigenstate of $H_{\rm RK}$ and H_1. As we already know that the bosonic part $H_{\rm RK}$ is minimized by an equal weight superposition of all hard-core coverings with bosonic dimers, we define the basis states

$$|(i_1,\eta_1),(i_2,\eta_2)\rangle \\ = \frac{1}{\sqrt{N_t}} F^\dagger_{i_1,\eta_1} F^\dagger_{i_2,\eta_2} |0\rangle_{(i_1,\eta_1),(i_2,\eta_2)} \otimes \Bigg(\sum_{c\epsilon\mathcal{C}_{(i_1,\eta_1),(i_2,\eta_2)}} |c\rangle \Bigg), \qquad (5)$$

where the sum runs over all possible bosonic configurations $|c\rangle$ covering the entire lattice with the exception of the bonds (i_1, η_1) and (i_2, η_2) which are already occupied by fermionic dimers. Note that $H_{\rm RK}|(i_1,\eta_1),(i_2,\eta_2)\rangle = 0$ is a zero energy eigenstate of $H_{\rm RK}$ by construction. We choose to normalize $|(i_1,\eta_1),(i_2,\eta_2)\rangle$ with respect to the number N_t of all possible classical dimer configurations on the entire lattice. The norm of such a basis state is hence given by

$$\||(i_1,\eta_1),(i_2,\eta_2)\rangle\|^2 = \frac{N_{(i_1,\eta_1),(i_2,\eta_2)}}{N_t} = Q_c[(i_1,\eta_1),(i_2,\eta_2)], \qquad (6)$$

where $Q_c[(i_1,\eta_1),(i_2,\eta_2)]$ is the classical dimer correlation function. $N_{(i_1,\eta_1),(i_2,\eta_2)}$ denotes the number of all classical configurations with two dimers fixed at (i_1,η_1) and (i_2,η_2). With these correlations we implicitly enforce the hard-core constraint, as any constraint-violating configuration C yields a vanishing norm $Q_c[C] = 0$.

In order to construct a ground state $|\psi_0\rangle$ of the full Hamiltonian $H = H_{\rm RK} + H_1$ we start with a general expansion

$$|\psi_0\rangle = \sum_{i_1,\eta_1,i_2,\eta_2} A_{(i_1,\eta_1),(i_2,\eta_2)} |(i_1,\eta_1),(i_2,\eta_2)\rangle. \qquad (7)$$

Applying the Hamiltonian we obtain

$$H|\psi_0\rangle = v_1 \sum_l \sum_{i_1\eta_1,i_2,\eta_2} A_{(i_1,\eta_1),(i_2,\eta_2)} P_l |(i_1,\eta_1),(i_2,\eta_2)\rangle. \qquad (8)$$

Note that P_l acts nontrivially only on plaquettes containing a single fermionic dimer and thus

$$\begin{aligned} &P_l|(i_1,\eta_1),(i_2,\eta_2)\rangle \\ &\quad = (\delta_{l,i_1} + \delta_{l+\hat{\hat{\eta}}_1,i_1} + \delta_{l,i_2} + \delta_{l+\hat{\hat{\eta}}_2,i_2})P_l|(i_1,\eta_1),(i_2,\eta_2)\rangle. \end{aligned} \tag{9}$$

Furthermore, we find

$$\delta_{l,i_1}P_l|(i_1,\eta_1),(i_2,\eta_2)\rangle = \delta_{l,i_1}(-1)^{s_{\eta_1}}|\phi_l,(i_2,\eta_2)\rangle \tag{10}$$

and similar relations for the remaining three terms of Eq. (9), where we defined the states

$$|\phi_l,(i,\eta)\rangle = \frac{1}{\sqrt{N_t}}F^\dagger_{i,\eta}|0\rangle_{(i,\eta)} \otimes |\phi_l\rangle \otimes \left\{\sum_{c\epsilon\mathcal{C}_{(l,x),(l+\hat{y},x),(i,\eta)}} |c\rangle\right\}, \tag{11}$$

and further $s_{\eta=x} = 1$, $s_{\eta=y} = 0$. Again, normalization of these states resorts to classical correlations and effectively projects onto the physical space of hard-core configurations.

Inserting Eq. (10) into Eqs. (9) and (8), and demanding that all coefficients for the states $|\phi_l,(i_2,\eta_2)\rangle$ vanish results in the two conditions

$$\begin{aligned} &A_{(l,x),(i_2,\eta_2)} - A_{(l,y),(i_2,\eta_2)} + A_{(l+\hat{y},x),(i_2,\eta_2)} - A_{(l+\hat{x},y),(i_2,\eta_2)} = 0, \\ &A_{(i_1,\eta_1),(l,x)} - A_{(i_1,\eta_1),(l,y)} + A_{(i_1,\eta_1),(l+\hat{y},x)} - A_{(i_1,\eta_1),(l+\hat{x},y)} = 0, \end{aligned} \tag{12}$$

which can be solved by a simple product ansatz $A_{(i_1,\eta_1),(i_2,\eta_2)} = a_{i_1,\eta_1}a_{i_2,\eta_2}$, leading to

$$a_{i_m,x} - a_{i_m,y} + a_{i_m+\hat{y},x} - a_{i_m+\hat{x},y} = 0 \tag{13}$$

for $m = 1, 2$. At this point, the generalization to an arbitrary number of fermionic dimers in the system is straightforward and can be done by extending Eq. (13) to $m = 1, \ldots, N_f$. We introduce the lattice momenta $\boldsymbol{p}_m$ and make the ansatz

$$a_{i_m,\eta_m} = a_{i_m,\eta_m}(\boldsymbol{p}_m) = C_{\eta_m}(\boldsymbol{p}_m)e^{i\boldsymbol{p}_m\cdot\boldsymbol{i}_m}, \tag{14}$$

where the factors $C_\eta(\boldsymbol{p})$ can be interpreted as weight factors for the two possible dimer orientations and $\boldsymbol{i}_m$ denotes the lattice position of site i_m. Using this ansatz in Eq. (13) and choosing the normalization $|C_x(\boldsymbol{p})|^2 + |C_y(\boldsymbol{p})|^2 = 4/N$ for later convenience, we obtain

$$C_\eta(\boldsymbol{p}) = \frac{2}{\sqrt{N}}\frac{1+e^{ip_\eta}}{\sqrt{|1+e^{ip_y}|^2 + |1+e^{ip_x}|^2}}, \tag{15}$$

where N is the number of lattice sites. One can thus write exact ground states of H on the RK line with two fermionic dimers as

$$|\psi_0\rangle = |\boldsymbol{p}_1,\boldsymbol{p}_2\rangle = \sum_{i_1,\eta_1,i_2,\eta_2} a_{i_1,\eta_1}(\boldsymbol{p}_1)a_{i_2,\eta_2}(\boldsymbol{p}_2)|(i_1,\eta_1),(i_2,\eta_2)\rangle. \tag{16}$$

Note that $\boldsymbol{p}_1$ and $\boldsymbol{p}_2$ take arbitrary values in the first Brillouin zone and $|\boldsymbol{p}_1,\boldsymbol{p}_2\rangle = -|\boldsymbol{p}_2,\boldsymbol{p}_1\rangle$ is antisymmetric under the exchange of $\boldsymbol{p}_1$ and $\boldsymbol{p}_2$. The ground state degeneracy corresponds to the $N(N-1)/2$ possibilities to choose $\boldsymbol{p}_1$, $\boldsymbol{p}_2$. Interestingly, this result implies that fermionic dimers have a flat dispersion at the RK line, which we confirmed independently by an exact diagonalization of the Hamiltonian on the RK line for a finite system. We also note that the state in Eq. (16) is properly normalized in the limit $N \to \infty$ [28].

For an arbitrary number N_f of fermionic dimers the ground states take the form $|\psi_0\rangle = |\boldsymbol{p}_1, \ldots, \boldsymbol{p}_{N_f}\rangle$ and there are $N!/((N-N_f)!N_f!)$ possibilities to choose the N_f momenta $(\boldsymbol{p}_1, \ldots, \boldsymbol{p}_{N_f})$. It is important to emphasize that the states $|\boldsymbol{p}_1, \ldots, \boldsymbol{p}_{N_f}\rangle$ are in general *not* linearly independent, and the number of possible momenta $(\boldsymbol{p}_1, \ldots, \boldsymbol{p}_{N_f})$ does not correspond to the ground state degeneracy in sectors with a large density of fermionic dimers. In fact, it is easy to see that the number of possible choices for the N_f momenta exceeds the number of basis states at large N_f. However, in the low doping limit

$$N_f = \text{const}, \qquad N \to \infty, \tag{17}$$

the $|\boldsymbol{p}_1, \ldots, \boldsymbol{p}_{N_f}\rangle$ become orthonormal and we indeed obtain the ground state degeneracy via the above relation.

It is instructive to note how the states $|\boldsymbol{p}\rangle$ for $N_f = 1$ are related to the usual bosonic RK ground state, if the fermionic dimer is replaced with a bosonic one. As shown in the Supplemental Material [28], the purely bosonic states $|\boldsymbol{p}\rangle$ vanish identically for $\boldsymbol{p} \neq 0$, which only leaves the ordinary RK state with $\boldsymbol{p} = 0$, i.e., the equal superposition of all bosonic dimer coverings, as the unique ground state.

In the following we want to study how perturbations ΔH of the Hamiltonian away from the RK line change the ground state structure. We consider perturbations of the form $H + \Delta H = H(t_i \to t_i + \delta t_i)$. As expected, the huge ground-state degeneracy will be lifted and the fermions will acquire a dispersion. The perturbative ground state in the vicinity of the RK line is then unique and similar to a Fermi gas, where the lowest energy momentum states $\boldsymbol{p}_m$ will be filled with N_f fermions. We restrict our discussion to the limit of Eq. (17), where the degenerate ground states $|\boldsymbol{p}_1, \ldots \boldsymbol{p}_{N_f}\rangle$ are properly normalized. Moreover, we only consider terms in ΔH which exchange two dimers, i.e., δt_1 and δt_3 terms. Flip interactions like t_2 will be neglected for simplicity, but can be included as well.

Within first order perturbation theory the eigenstates remain unchanged, but their energy is given by $\Delta E = \langle \boldsymbol{p}_1, \ldots \boldsymbol{p}_{N_f} | \Delta H | \boldsymbol{p}_1, \ldots \boldsymbol{p}_{N_f} \rangle$. Evaluating the matrix elements for the case $N_f = 2$ we get $\Delta E = \varepsilon(\boldsymbol{p}_1) + \varepsilon(\boldsymbol{p}_2)$ with

$$\varepsilon(\boldsymbol{p}) = -4 \sum_{i=1,3} \delta t_i Q_c[(0,x),(r_{t_i}^{1,x}, x+\eta_{t_i})] \times \sum_{\eta} \frac{(1+e^{ip_\eta})(1+e^{-ip_{\eta+\eta_{t_i}}})}{|1+e^{ip_y}|^2 + |1+e^{ip_x}|^2} \sum_{s=1}^{S_{t_i}} [e^{-ir_{t_i}^{s,\eta} \cdot \boldsymbol{p}}], \qquad (18)$$

where $r_{t_i}^{s,\eta}$ and η_{t_i} correspond to displacement vector and relative change in orientation for a given t_i process which annihilates a fermionic dimer with initial orientation η. The sum over the possible $r_{t_i}^{s,\eta}$ corresponding to a given t_i depends on the orientation index η and runs from $s = 1$ to $S_{t_1} = 2$, $S_{t_3} = 8$. The classical probabilities $Q_c[(0,x),(r_{t_i}^{1,x}, x+\eta_{t_i})]$ are $1/8$ and $1/(4\pi)$ for t_1 and t_3, respectively, and can be obtained from the exact solution of the classical dimer problem [29,30]. Details of the computation can be found in the Supplemental Material [28]. We show an example for $\varepsilon(\boldsymbol{p})$ together with exact diagonalization results on a 6×6 lattice with one fermionic dimer and twisted boundary conditions in Fig. 1. For $|\delta t_i| \ll |v_1|$, J we find excellent agreement. Note the formation of hole pockets around $(\pi/2, \pi/2)$ at a finite density of fermionic dimers for perturbations in δt_3.

The preceeding results demonstrate that the energy of a state $|\boldsymbol{p}_1, \ldots, \boldsymbol{p}_{N_f}\rangle$ is additive in the single particle energies in the low doping limit, indicating a system with Fermi-liquid like behavior. Now we show that in the same limit the ground states $|\boldsymbol{p}_1, \ldots, \boldsymbol{p}_{N_f}\rangle$ can be constructed using creation and annihilation operators that fulfill canonical fermionic anticommutation relations.

We start by defining the vaccum state of the theory to be the usual RK ground state, i.e., $|0^*\rangle = |\mathrm{RK}\rangle$, which corresponds to the equal weight superposition of all possible hard-core coverings of the lattice with bosonic dimers. We add the star in this notation to emphasize the difference to the vacuum state $|0\rangle$ used previously. By defining the operator

$$f_{\boldsymbol{p}}^\dagger = \sum_{i,\eta} a_{i,\eta}(\boldsymbol{p}) F_{i,\eta}^\dagger D_{i,\eta}, \qquad (19)$$

we can express the possible ground states along the RK line as

$$|\boldsymbol{p}_1, \ldots, \boldsymbol{p}_{N_f}\rangle = \prod_{i=1}^{N_f} f_{\boldsymbol{p}_i}^\dagger |0^*\rangle. \qquad (20)$$

We aim to show that the corresponding Hamiltonian $H = \sum_{\boldsymbol{p}} \varepsilon(\boldsymbol{p}) f_{\boldsymbol{p}}^\dagger f_{\boldsymbol{p}}$ describes the model in the vicinity of the RK line as a system of noninteracting fermionic excitations. We hence need to show that the canonical anticommutation relations

$$\{f_{\boldsymbol{p}_1}^\dagger, f_{\boldsymbol{p}_2}\} = \delta_{\boldsymbol{p}_1 \boldsymbol{p}_2} \qquad (21)$$

are satisfied in the limit of Eq. (17). Note that we require specification of the Hilbert space on which Eq. (21) is supposed to hold. In usual fermionic theories the anticommutation relations must hold on the Fock space spanned by the set of states $\{\prod_{i=1}^{N_f} c_{\boldsymbol{k}_i}^\dagger |0\rangle\}$. In direct analogy we demand that in our model Eq. (21) should hold on the Hilbert space spanned by the states $\{\prod_{i=1}^{N_f} f_{\boldsymbol{k}_i}^\dagger |0^*\rangle\}$. Thus, even though the operators of Eq. (19) do not constitute fermionic operators on a Hilbert space built upon the actual vacuum state $|0\rangle$, we still can prove them to be fermionic within our relevant Hilbert space. The quantity we aim to compute is now $\{f_{\boldsymbol{p}_1}^\dagger, f_{\boldsymbol{p}_2}\}|0^*\rangle$ and we want to show that this expression yields $\delta_{\boldsymbol{p}_1, \boldsymbol{p}_2}|0^*\rangle$. From the relation $\{f_{\boldsymbol{p}_1}^\dagger, f_{\boldsymbol{p}_2}\} = \sum_{i,\eta} a_{i,\eta}(\boldsymbol{p}_1) a_{i,\eta}^*(\boldsymbol{p}_2) \hat{N}_{i,\eta}$, where $\hat{N}_{i,\eta}$ corresponds to the total dimer number operator on the link (i, η), we deduce

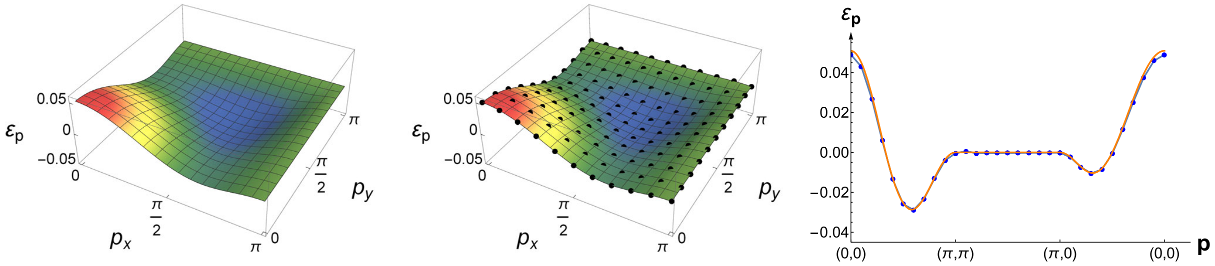

FIG. 1. Comparison between $\varepsilon(\boldsymbol{p})$ from Eq. (18) (left) and the dispersion obtained from exact diagonalization (ED) for 6×6 lattice sites with one fermionic dimer and twisted boundary conditions (middle) for $J = V = 1$, $v_1 = t_2 = -t_1 = 1$ and $\delta t_3 = -0.02$. Right: corresponding line cut through the Brillouin zone [blue line with dots: ED, orange line: Eq. (18)].

that $\|\{f^\dagger_{\boldsymbol{p}_1}, f_{\boldsymbol{p}_2}\}|0^*\rangle\|^2$ is given by the Fourier transformed classical dimer correlation function (see the Supplemental Material for details [28]), which reduces to $\delta_{\boldsymbol{p}_1,\boldsymbol{p}_2}$ for $N \to \infty$ as claimed, with corrections of order $\mathcal{O}[\log(N)/N]$. The appearance of the total dimer number operator $\hat{N}_{i,\eta}$ then ensures that this result remains valid for all states in our Hilbert space provided that Eq. (17) be fulfilled. Beyond this limit, where the Fourier transform of the classical dimer correlation function reduces to a delta function, we show in the Supplemental Material that Eq. (21) is exact for arbitrary system sizes if the momenta $\boldsymbol{p}_1$ and $\boldsymbol{p}_2$ lie on the Brillouin zone diagonal.

Finally, we can also relate the operator $f_{\boldsymbol{p}}$ to the actual electron annihilation operator $c_{\boldsymbol{p}}$. In Ref. [1] it was shown that the electron annihilation operator in the dimer Hilbert space takes the form

$$c_{\boldsymbol{p},\alpha} = \frac{\varepsilon_{\alpha\beta}}{2\sqrt{N}} \sum_{j,\eta} (1 + e^{-ip_\eta}) F^\dagger_{i,\eta,\beta} D_{i,\eta} e^{-i\boldsymbol{p}\cdot\boldsymbol{i}_j}; \qquad (22)$$

i.e., removing an electron on lattice site i corresponds to replacing a bosonic with a fermionic dimer on all adjacent bonds. Here we included a spin index α and $\varepsilon_{\alpha\beta}$ is the unit antisymmetric tensor. Surpressing the electronic spin index and comparing this expression with the definition of the $f_{\boldsymbol{p}}$ operator in Eq. (19) it immediately follows that

$$f^\dagger_{\boldsymbol{p}} = \frac{4}{\sqrt{|1 + e^{ip_x}|^2 + |1 + e^{ip_y}|^2}} c_{-\boldsymbol{p}}. \qquad (23)$$

This relation is particularly useful, because it shows that the Fermi surface of fermionic dimers directly translates to the electronic Fermi surface. Moreover, from the fact that the $f_{\boldsymbol{p}}$ fermions form a free Fermi gas, we can infer that the electron spectral function in the vicinity of the RK line takes the form $A_e(\boldsymbol{p}, \omega) = \mathcal{Z}_{\boldsymbol{p}} \delta[\omega - \varepsilon(\boldsymbol{p})]$ with a quasiparticle weight $\mathcal{Z}_{\boldsymbol{p}} = [\cos^2(p_x/2) + \cos^2(p_y/2)]/4$, which is distributed anisotropically around the Fermi surface (see also Refs. [1,27] for a discussion. Similar results have been obtained in a SU(2) slave-particle approach [32] as well as in projected wave function studies [33]). Note that the electron spectral function at the RK line only features a coherent peak, but no incoherent background. Perturbing away from the RK line incoherent weight appears, but not within first order perturbation theory. Numerical results obtained by ED confirm this result.

In summary, we provided an exact ground-state solution for the dimer model introduced in Ref. [1] on a particular line in parameter space, for arbitrary densities of fermionic dimers. At this line the ground state is massively degenerate and can be interpreted as a fermionic flat band. Perturbing away from the exactly solvable line lifts this degeneracy and we were able to show that the ground state is a fractionalized Fermi liquid, at least in the limit of small fermionic dimer densities. In this limit the ground state can be constructed by applying canonical fermion creation operators to a suitably chosen vacuum state and the energy of these fermions is additive. Moreover, these fermionic operators are directly related to electron creation operators in the restricted Hilbert space of our model. Even though we limited the discussion to spinless fermionic dimers, our construction can be easily generalized to spin-$1/2$ fermionic dimers. We also note that the very same construction works for other lattice geometries as well, such as a triangular lattice, where we expect that the fractionalized Fermi liquid ground state is stable over a wider parameter regime. Indeed, the $U(1)$ spin liquid in the square lattice RK model at half filling is unstable towards confining, symmetry broken states away from the special RK point $J = V$. On nonbipartite lattices an extended Z_2 spin liquid phase exists, however [7]. Analogous considerations hold for hole doped RK models [34,35] as well as the fractionalized Fermi liquid phase discussed here [26,36]. Including diagonal, next-nearest neighbor dimers in our model is thus an interesting point for future study. In conclusion, our results provide a rare example of a strongly correlated, fermionic lattice model in two dimensions, which is exactly solvable and potentially relevant for the description of the metallic pseudogap phase in underdoped cuprates.

This research was supported by the German Excellence Initiative via the Nanosystems Initiative Munich (NIM).

[1] M. Punk, A. Allais, and S. Sachdev, Quantum dimer model for the pseudogap metal, Proc. Natl. Acad. Sci. U.S.A. **112**, 9552 (2015).

[2] P. W. Anderson, The resonating valence bond state in La_2CuO_4 and superconductivity, Science **235**, 1196 (1987).

[3] S. A. Kivelson, D. S. Rokhsar, and J. P. Sethna, Topology of the resonating valence-bond state: Solitons and high-T_c superconductivity, Phys. Rev. B **35**, 8865 (1987).

[4] D. S. Rokhsar and S. A. Kivelson, Superconductivity and the Quantum Hard-Core Dimer Gas, Phys. Rev. Lett. **61**, 2376 (1988).

[5] S. Sachdev, Spin-Peierls ground states of the quantum dimer model: A finite-size study, Phys. Rev. B **40**, 5204 (1989).

[6] P. W. Leung, K. C. Chiu, and K. J. Runge, Columnar dimer and plaquette resonating-valence-bond orders in the quantum dimer model, Phys. Rev. B **54**, 12938 (1996).

[7] R. Moessner and S. L. Sondhi, Resonating Valence Bond Phase in the Triangular Lattice Quantum Dimer Model, Phys. Rev. Lett. **86**, 1881 (2001).

[8] P. Fendley, R. Moessner, and S. L. Sondhi, Classical dimers on the triangular lattice, Phys. Rev. B **66**, 214513 (2002).

[9] O. F. Syljuåsen, Plaquette phase of the square-lattice quantum dimer model: Quantum Monte Carlo calculations, Phys. Rev. B **73**, 245105 (2006).

[10] E. Fradkin and S. Kivelson, Short range resonating valence bond theories and superconductivity, Mod. Phys. Lett. B **04**, 225 (1990).

[11] R. Moessner, S. L. Sondhi, and E. Fradkin, Short-ranged resonating valence bond physics, quantum dimer models, and Ising gauge theories, Phys. Rev. B **65**, 024504 (2001).

[12] A. Kitaev, Fault-tolerant quantum computation by anyons, Ann. Phys. (Amsterdam) **303**, 2 (2003).

[13] N. Shannon, G. Misguich, and K. Penc, Cyclic exchange, isolated states, and spinon deconfinement in an XXZ Heisenberg model on the checkerboard lattice, Phys. Rev. B **69**, 220403 (2004).

[14] F. Pollmann, J. J. Betouras, K. Shtengel, and P. Fulde, Fermionic quantum dimer and fully packed loop models on the square lattice, Phys. Rev. B **83**, 155117 (2011).

[15] S. Kivelson, Statistics of holons in the quantum hard-core dimer gas, Phys. Rev. B **39**, 259 (1989).

[16] N. Read and B. Chakraborty, Statistics of the excitations of the resonating-valence-bond state, Phys. Rev. B **40**, 7133 (1989).

[17] L. Balents, L. Bartosch, A. Burkov, S. Sachdev, and K. Sengupta, Putting competing orders in their place near the Mott transition. II. The doped quantum dimer model, Phys. Rev. B **71**, 144509 (2005).

[18] D. Poilblanc, F. Alet, F. Becca, A. Ralko, F. Trousselet, and F. Mila, Doping quantum dimer models on the square lattice, Phys. Rev. B **74**, 014437 (2006).

[19] P. A. Lee, N. Nagaosa, and X.-G. Wen, Doping a Mott insulator: Physics of high-temperature superconductivity, Rev. Mod. Phys. **78**, 17 (2006).

[20] D. Poilblanc, Properties of Holons in the Quantum Dimer Model, Phys. Rev. Lett. **100**, 157206 (2008).

[21] M. Punk and S. Sachdev, Fermi surface reconstruction in hole-doped $t-J$ models without long-range antiferromagnetic order, Phys. Rev. B **85**, 195123 (2012).

[22] J. Lee, S. Sachdev, and S. R. White, Electronic quasiparticles in the quantum dimer model: Density matrix renormalization group results, Phys. Rev. B **94**, 115112 (2016).

[23] T. Senthil, S. Sachdev, and M. Vojta, Fractionalized Fermi Liquids, Phys. Rev. Lett. **90**, 216403 (2003).

[24] M. Oshikawa, Topological Approach to Luttinger's Theorem and the Fermi Surface of a Kondo Lattice, Phys. Rev. Lett. **84**, 3370 (2000).

[25] T. Senthil, M. Vojta, and S. Sachdev, Weak magnetism and non-Fermi liquids near heavy-fermion critical points, Phys. Rev. B **69**, 035111 (2004).

[26] S. Sachdev and D. Chowdhury, The novel metallic states of the cuprates: Topological Fermi liquids and strange metals, Prog. Theor. Exp. Phys. **2016**, 12C102 (2016).

[27] S. Huber, J. Feldmeier, and M. Punk, Electron spectral functions in a quantum dimer model for topological metals, Phys. Rev. B **97**, 075144 (2018).

[28] See Supplemental Material at http://link.aps.org/supplemental/10.1103/PhysRevLett.120.187001 for a detailed computation, which includes Refs. [29–31].

[29] M. E. Fisher and J. Stephenson, Statistical mechanics of dimers on a plane lattice. II. Dimer correlations and monomers, Phys. Rev. **132**, 1411 (1963).

[30] S. Samuel, The use of anticommuting variable integrals in statistical mechanics. I. The computation of partition functions, J. Math. Phys. (N.Y.) **21**, 2806 (1980).

[31] R. Youngblood, J. D. Axe, and B. M. McCoy, Correlations in ice-rule ferroelectrics, Phys. Rev. B **21**, 5212 (1980).

[32] S. Bieri and D. A. Ivanov, SU(2) approach to the pseudogap phase of high-temperature superconductors: Electronic spectral functions, Phys. Rev. B **79**, 174518 (2009).

[33] S. Bieri and D. Ivanov, Quasiparticle spectral weights of gutzwiller-projected high-T_c superconductors, Phys. Rev. B **75**, 035104 (2007).

[34] H. Ribeiro, S. Bieri, and D. Ivanov, Single hole and vortex excitations in the doped Rokhsar-Kivelson quantum dimer model on the triangular lattice, Phys. Rev. B **76**, 172301 (2007).

[35] C. A. Lamas, A. Ralko, D. C. Cabra, D. Poilblanc, and P. Pujol, Statistical Transmutation in Doped Quantum Dimer Models, Phys. Rev. Lett. **109**, 016403 (2012).

[36] A. A. Patel, D. Chowdhury, A. Allais, and S. Sachdev, Confinement transition to density wave order in metallic doped spin liquids, Phys. Rev. B **93**, 165139 (2016).

4 Momentum-selective Mott physics in the Fermi-Hubbard model

4.1 Cluster study of effective cuprate models

The two-dimensional Fermi-Hubbard model is widely believed to capture the in-plane physics of cuprate materials in a wide range of doping and temperature [MPJ02, FCDL+09, GPM13, GFP+10, WSC+18, SCW+18]. We aim within this work to study its electron spectral function by a cluster dynamical mean-field approach with a numerical renormalization group impurity solver. The two-dimensional Fermi-Hubbard model is defined as follows [Hub63]

$$H_{\mathrm{FHM}} = -\sum_{\langle\langle i,j\rangle\rangle} t_{ij}\ [c^\dagger_{i,\alpha} c_{j,\alpha} + h.c] + U\sum_i n_{i,\uparrow} n_{i,\downarrow}, \tag{4.1}$$

where we consider up to second nearest neighbor hopping indicated by $\langle\langle\cdot,\cdot\rangle\rangle$. In the following we first explain general technical details of cluster approaches 4.2. We then outline the numerical renormalization group method as a real-frequency cluster impurity solver 4.3. After that, we discuss shortly former works within the field of cluster analysis of the two-dimensional Fermi-Hubbard model that go in similar directions as our work and outline our goals (s. Sec. 4.4). Finally, we summarize our main results for spin-polarized baths coupled to a 4-site cluster (s. Sec. 4.5). The results are compared to a similar cluster calculation of the quantum dimer model in the full electron Hilbert space (s. Sec. 4.5).

4.2 Cluster approaches

In this section we give a short overview on the main ideas behind cluster dynamical mean-field theory (DMFT) calculations [MJP05, GKKR96], where we first begin in real space cluster coordinates (cDMFT) [LK00, KSPB01, BK01] and then continue with the dynamical cluster approximation (DCA) for periodic intracluster cell boundary conditions [HTZJ+98, HMJK00, JMHM01].

Cavity mode approximation Let us consider electrons on a lattice, which are annihilated by the following operators $f_{R_i,\alpha}$. Here, R_i indicates a lattice site and $\alpha \in \{\uparrow,\downarrow\}$ is the spin flavor. A cluster approximation consist of two steps. First, a mapping of the lattice problem onto an effective cluster problem has to be defined. Thus, let us consider to subdivide the original d dimensional lattice into cluster cells of size $N_c = L^d$; in our application later, we consider the case $L = 2$ and $d = 2$ (cf. Fig. 4.1). Similar to Ref. [KSPB01, BK01], each original coordinate on the lattice $|R_i\rangle$ is replaced by a tuple $|i, I\rangle$ with cell coordinate i and interior cluster position I.

The electron operator in cluster coordinates reads $c_{i,I,\alpha} = \sum_{R_i} T_{i,I,R_i} f_{R_i,\alpha}$. Old and new variables are connected via a transformation matrix T_{i,I,R_i}. Since the lattice has periodic boundaries the transformation matrix simplifies to $T_I(i - R_i)$. We use later the following notation for the associated momentum $i \leftrightarrow \tilde{k}$. The 'local' cluster operator is further given by $c_{I,\alpha} = c_{0,I,\alpha}$.

After we transform the Hamiltonian into the new cluster coordinates, the according action in terms of Grassmann variables reads

$$Z = \int \prod D\bar{c}_{i,I,\alpha} D c_{i,I,\alpha} e^{-S}, \tag{4.2}$$

where $S = S_c + S_{ce} + S_e$. The first and last component of the action consists just of local cluster, respectively bath, degrees of freedom. Whereas the boundary term S_{ce} connects environment and cluster. We aim to integrate out the environment, which would lead to an effective action

$$\frac{1}{Z_0} e^{-S_0} = \frac{1}{Z} \int \prod D\bar{c}_{i\neq 0,I,\alpha} D c_{i\neq 0,I,\alpha} e^{-S}. \tag{4.3}$$

However, this is very often not doable and would in principle generate terms of arbitrary higher order. Within the cluster DMFT approximation we neglect quartic and higher order terms. A detailed description of this so-called cavity construction is part of Ref. [GKKR96]. The analysis shows that for larger cluster sizes the boundary terms become indeed negligible.

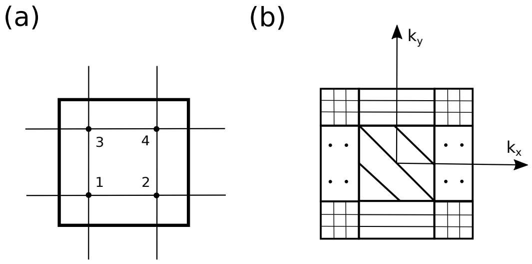

Figure 4.1 Cluster separation of the lattice: (a) The original lattice is separated into cluster cells of size $N_c = L^d = 4$. (b) The corresponding DCA resolves the momentum dependence of the self-energy according to four patches centered around the momenta $(K_x, K_y) = (n_x, n_y)\frac{2\pi}{L}$, where $n_x, n_y \in \{0, 1\}$.

Instead, we assume a parametrized action in terms of a Weiss field G_0:

$$S' = S_0[\bar{c}_{I,\alpha}, c_{I,\alpha}, G_0] + S_{\text{int}}[\bar{c}_{I,\alpha}, c_{I,\alpha}]. \tag{4.4}$$

The interaction is thereby restricted to the local cluster cell. Thus, we resolve non-local correlations up to a distance $L/2$.

Impurity Hamiltonian Commonly, instead of a parametrized action (4.4), a cluster impurity Hamiltonian is used for specific model applications [MJP05, GKKR96, KSPB01]:

$$H = H_{\text{c}} + H_{\text{B}} + H_{\text{c-B}}, \tag{4.5}$$

where

$$H_{\text{c}} = H_0 + H_{\text{int}} = \sum_{I,J} t_{IJ}\, c^{\dagger}_{I,\alpha} c_{J,\alpha} + H_{\text{int}}, \tag{4.6}$$

$$H_{\text{B}} = \sum_{I,J} \sum_{\tilde{k}} \lambda(\tilde{k})|_{I,J}\, a^{\dagger}_{I,\tilde{k},\alpha} a_{J,\tilde{k},\alpha}, \tag{4.7}$$

$$H_{\text{c-B}} = \sum_{I,J} \sum_{\tilde{k}} [\mathbf{V}(\tilde{k})|_{IJ}\, a^{\dagger}_{I,\tilde{k},\alpha}\, c_{J,\alpha} + \text{h.c.}]. \tag{4.8}$$

Summation over the spin index is implicitly assumed. $\mathbf{t}$ is the hopping amplitude on the cluster and $\lambda(\tilde{k})$ is the dispersion of the bath. The cluster is coupled to the bath via the coupling $\mathbf{V}(\tilde{k})$. Bold coupling parameters and dispersion relations are matrices in the real cluster space. After integrating out the bath, we determine the hybridization function

$$\mathbf{\Delta}(\omega) = \sum_{\tilde{k}} \mathbf{V}^{\dagger}(\tilde{k})[\omega - \lambda(\tilde{k})]^{-1} \mathbf{V}(\tilde{k}). \tag{4.9}$$

It accumulates the information of dynamical processes between cluster and bath. The cluster Green's function is then

$$\mathbf{G}^c(\omega) = -\mathcal{FT}\left[\langle \mathcal{T}_t c^\dagger c\ \rangle\right] = \left[\omega - \mathbf{t} - \mathbf{\Delta}(\omega) - \mathbf{\Sigma}^c(w)\right]^{-1}. \tag{4.10}$$

$\mathcal{FT}$ refers to the Fourier transformation from time to frequency space and $\mathcal{T}_t$ is the time-ordering operator. In the above equation and in the following we frequently use a compact notation for the cluster and bath operators

$$c\ = (c_{1,\uparrow}, c_{2,\uparrow}, c_{3,\uparrow}, c_{4,\uparrow}, c_{1,\downarrow}, c_{2,\downarrow}, c_{3,\downarrow}, c_{4,\downarrow}). \tag{4.11}$$

According to this, the cluster Green's function is a matrix of size $2N_c \times 2N_c$. On the other hand, the lattice Green's function reads

$$G(k,\omega) = -\mathcal{FT}[\langle \mathcal{T}_t c_k^\dagger c_k\rangle] = [\omega - \lambda_k - \Sigma(k,w)]^{-1} \tag{4.12}$$

with the continuous momentum k. Within the cluster DMFT approach, we iteratively update the hybridization function until the following self-consistency equation is satisfied

$$\mathbf{G}^c(\omega) = \frac{N_c}{N}\sum_{\tilde{k}} G(\tilde{k},\omega)|_{\mathbf{\Sigma}(\tilde{k},w)\to\mathbf{\Sigma}^c(w)} \equiv \bar{\mathbf{G}}(\omega). \tag{4.13}$$

In seminal works it was shown that the solution of the above self-consistency equation also minimizes the grand potential under the constraint of a local self-energy [MJP05, Pot04]. The grand potential is the generating functional of thermodynamic static quantities. As a remark on the edge, the grand potential Ω is closely related to the Luttinger-Ward functional Φ evaludated at the exact Green's function

$$\Phi[G] = T\Omega[G] + \mathrm{Tr}\ln G - \mathrm{Tr}\ \Sigma G. \tag{4.14}$$

The Luttinger Ward functional is the summation of all vacuum to vacuum skeleton diagrams.

Usually, the coarse-grained Green's function in Eq. (4.13) is represented using the density of states $\rho_0(\epsilon)$:

$$\begin{aligned}\bar{\mathbf{G}}(\omega) &= \frac{N_c}{N}\sum_{\tilde{k}} G(\tilde{k},\omega)|_{\mathbf{\Sigma}(\tilde{k},w)\to\mathbf{\Sigma}^c(w)} = \frac{N_c}{N}\sum_{\tilde{k}}\left[\omega - \lambda(\tilde{k}) - \mathbf{\Sigma}^c(\omega)\right]^{-1} \\ &= \int_\epsilon \frac{\rho_0(\epsilon)}{\omega - \epsilon - \mathbf{\Sigma}^c(\omega)}.\end{aligned} \tag{4.15}$$

Former works have shown that the above cluster scheme is causal [HMJK00, KSPB01]. This is a very substantial aspect, since it means that the analytic structure of the resulting self-energy is physical meaningful, i.e. the imaginary part of the self energy is negative $\mathrm{Im}[\Sigma(\omega] < 0$.

Historically, first attempts to extend the dynamical mean-field calculations with $N_c = 1$, which is exact at infinite dimension d [MV89, GK92], to a cluster scheme indeed broke causality while they expanded in a $1/d$ series [VD94, SI95]. The above cluster DMFT has been proven to be causal and corresponds to an expansion in cluster size $1/N_c$ [HMJK00, JMHM01].

Symmetries and DCA According to the lattice symmetries, the system is invariant under translation $T_{x/y}$ and for our specific models, the Fermi-Hubbard model and the correlated dimer hopping model, also reflection $M_{14/23}$ (cf. Fig. 4.1). The latter refers to the reflection of the system along the diagonal (M_{14}), respectively off-diagonal axis (M_{23}), within the 4-site cluster plaquette. The simultaneous eigenvectors of the translation operators is of course identical to a Fourier transformation with respect to the cluster cell $I \leftrightarrow K$. In this case we come to the DCA ansatz, which is further discussed at the end of this subsection [HTZJ$^+$98, HMJK00, JMHM01].

In the presence of the mirror symmetry, we have on top a two-fold degeneracy. We summarize the simultaneous eigenstates of translation and mirror operators in a transformation matrix T. Self-energy, bath dispersion $\lambda_{\tilde{k}}$, hopping amplitude $\mathbf{t}$ and coupling $\mathbf{V}_{\tilde{k},\alpha}$ are diagonal in this basis. It is then straightforward to show that this property carries over to the lattice Green's function (4.12):

$$G(k,\omega) = T^{-1} G(k,\omega) T. \tag{4.16}$$

Considering Eq. (4.10) and the self-consistency equation (4.13), we can conclude that also the hybridization function defined as

$$\Delta_K(\omega) = \omega - \epsilon_K - \Sigma^c_K(\omega) - \left[\bar{G}_K(\omega)\right]^{-1} \tag{4.17}$$

is diagonal within this basis.

For completeness we mention that the cluster methods can be also interpreted from diagrammatic point of view when considering the momentum conservation at each internal vertex described by the Laue function [MJP05, HMJK00, JMHM01]

$$\Delta_{\text{Laue}} = N \delta_{k_1+k_2+\ldots,k'_1+k'_2}. \tag{4.18}$$

Here, we introduce incoming $\{k_i\}$ and outgoing momenta $\{k'_i\}$. The DMFT with $N_c = 1$ is derived in case of neglecting any momentum transfer by setting $\Delta_{\text{Laue}} = 1$ [GKKR96].

As we have discussed and explicitely shown above, for a translation invariant cluster the self-consistency equation drastically simplifies and gets diagonal in the corresponding Fourier coordinate K. Again, looking at the Laue function, this is identical to the following approximation

$$\Delta_{\text{DCA}} = N_c \delta_{M(k_1)+M(k_2)+\ldots,M(k'_1)+M(k'_2)}. \tag{4.19}$$

where the function $M(\cdot)$ maps a momentum k_i onto the corresponding momentum K of its patch P_K (cf. Fig. 4.1) to which it belongs. It is identical to approximate the self-energy as follows

$$\Sigma_K(\omega) = \frac{N_c}{N} \sum_{\tilde{k}} \Sigma(K+\tilde{k},\omega), \tag{4.20}$$

where we have on the left-hand side the cluster Fourier transform of the matrix $\mathbf{\Sigma}(\omega)$ and on the right-hand side the full lattice self-energy. Diagrammatically, all objects, like vertices, Green's functions etc., are replaced within the DCA approach by their coarse-grained counterparts and the momentum conservation at each vertex is approximated according to Δ_{DCA}. This and further interesting aspects of cluster theories are explained in more detail for instance in Ref. [MJP05].

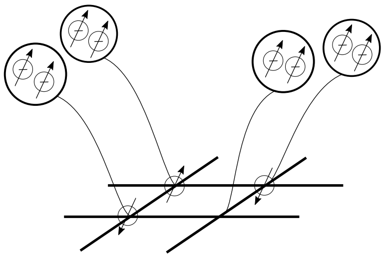

Figure 4.2 Each site of the cluster is coupled to a bath. There is no interbath-coupling in the DCA approach. We assume four identical spin polarized baths. The dynamics on the cluster in our analysis are based on the two-dimensional Fermi-Hubbard model and the dimer correlated hopping model.

DCA loop and the self-consistency equation Thus, the DCA approach consists of several steps. Here, we summarize them in an overview:

1. We fix by an initial appropriate guess, e.g. from a perturbative approach, the cluster self-energy $\Sigma_K(\omega)$.
2. Then, the coarse-grained lattice Green's function is calculated:
$$\bar{G}_K(\omega) = \int_\epsilon \frac{\rho_{K,0}(\epsilon)}{\omega - \epsilon - \Sigma^c_K(\omega)}, \tag{4.21}$$
where $\rho_{K,0}(\epsilon)$ is the non-interacting density of states.
3. The bare cluster Green's function yields:
$$\left[G^{c,0}_K(\omega)\right]^{-1} = \left[\bar{G}_K(\omega)\right]^{-1} + \Sigma^c_K(\omega). \tag{4.22}$$
4. We determine now the parameters in the effective cluster problem. This includes the calculation of the hybridization function $\Delta_K(\omega)$ and a subsequent fitting process to determine $V_K(\tilde{k})$ and $\lambda_K(\tilde{k})$.
5. The cluster self-energy $\Sigma^c_K(\omega)$, respectively $G^c_K(\omega)$, is calculated by a quantum cluster solver. In the next section we introduce the numerical renormalization group technique, which is a real-frequency impurity solver for the low-energy spectrum (s. Sec. 4.3).
6. The loop closes by re-calculating the coarse-grained Green's function as in step 3 with the new cluster self-energy. The convergence of the self-consistency is reached if
$$\bar{G}_K(\omega) = G^c_K(\omega). \tag{4.23}$$

DCA with spin-polarized baths As we explain in the next section, the numerical renormalization group method is an iterative diagonalization procedure, where we couple in each step an additional supercell of 4 bath sites to the existing system. According to this, the Hilbert space increases exponentially. State-of-the-art numerical renormalization group impurity solvers can treat a maximum of three SU(2)-baths. Since our 4-site cluster requires 4 baths, we make a crude approximation and restrict our analysis to spin-polarized baths (cf. Fig. 4.2). The SU(2) symmetry is then broken and just the total magnetization of the system is conserved. As explained in the former paragraph, translational symmetry and periodic boundary conditions on the cluster simplifies the cluster DMFT ansatz and lead to momentum conservation withn the cluster patches. The corresponding basis is simply the Fourier transform of the real space operators $c_{K,\alpha} = \frac{1}{\sqrt{N_c}} \sum_I e^{iKI} c_{I,\alpha}$ (for definition of K s. Fig. 4.1). Due to the mirror symmetry of the lattice, we have a degeneracy within the subspace $K_2 = (0, \pi)$ and $K_3 = (\pi, 0)$.

Since the impurity model couples to spin-polarized baths, we just assume to have a finite hybridization function for the corresponding spin sector. According to this and the fact that the total magnetic is conserved, the self-energy is diagonal in the spin index and the self-consistency relation (4.13) decouples into two equations, one for each spin sector. So, we just update within the DMFT runs the hybridization in one spin sector, e.g. $\alpha =\uparrow$ in case of Fig. 4.2.

Determination of the continuous lattice self-energy A specific cluster approach also includes an interpolation or reperiodization scheme to yield the continuous lattice self-energy from their cluster counterparts. Such procedures have to preserve lattice symmetries and the lattice self-energy needs to be causal $\mathrm{Im}[\Sigma(k, \omega)] < 0$. Here, the momentum k is a continuous variable. The DCA approach leads to self-energies, which are constant within each patch and thus have to be interpolated, while the cDMFT calculation demands a reperiodization of the real cluster self-energy. Different schemes have been developed [MPJ02, BK02]. Apart from the self-energy and the cluster Green's function [KKS+06], lately the continuation of the cumulant has been shown to work best, especially in systems of strong correlations [SCHK06, SK06, FCDL+09]. The reason is that strong correlations manifest in the self-energy with large off-diagonal entities in real space cluster coordinates, i.e. the self-energy is thereby highly non-local. In contrast, the cumulant, which is the propagator in the atomic limit and defined on the cluster as follows

$$M_K(\omega) = \left[\omega + \mu - \Sigma^{c}_{K}(\omega)\right]^{-1}, \tag{4.24}$$

remains however also in the presence of strong correlations, e.g. in the Mott phase, local. According to this, the cumulant is the natural object within a cluster scheme for interpolation/reperiodization, since it is expected to be a rather smooth quantity in momentum space. The cluster formalism has thus been also developed by expanding the Luttinger-Ward functional around the atomic limit [Shv03, SK04]. In our DCA approach below, we interpolate the cumulant following Ref. [SCHK06] as follows

$$M(k,\omega) = M_{11}(\omega) + \alpha(k)M_{12}(\omega) + \beta(k)M_{14}(\omega), \tag{4.25}$$

where $\alpha(k) = \cos(k_x) + \cos(k_y)$ and $\beta(k) = \cos(k_x)\cos(k_y)$. Here, M_{IJ} with $I, J \in \{1,2,3,4\}$ are the cumulants in real space cluster coordinates (cf. Fig. 4.1). After the interpolation, the lattice self-energy is given by

$$M(k,\omega) = \left[\omega + \mu - \Sigma(k,\omega)^{-1}\right]. \tag{4.26}$$

Using such a interpolation/reperiodization scheme already at the stage of the self-conistency equation, may however affect the causality of the self-energy. For a discussion on reperiodization in case of the cDMFT scheme, we refer to the literature [SCHK06].

4.3 Numerical renormalization group as a cluster solver

The numerical renormalization group method was first proposed by Kenneth Wilson in 1975 [Wil75] and is applicable to impurity systems with small degrees of freedom that are coupled to a bath of non-interacting fermionic or bosonic particles [BCP08]. Here, we explain the application of the numerical renormalization group as a quantum cluster solver for the effective cluster description [MJP05].

Logarithmic discretization The bath of the effective cluster model couples to the cluster impurity as follows:

$$\begin{aligned} H_{\text{B+c}} &= H_{\text{B}} + H_{\text{c-B}} \\ &= \sum_{K,\tilde{k},\alpha} \lambda(K+\tilde{k}) a^{\dagger}_{K+\tilde{k},\alpha} a_{K+\tilde{k},\alpha} + \sum_{K,\tilde{k},\alpha} [V(K+\tilde{k}) a^{\dagger}_{K+\tilde{k},\alpha} c_{K,\alpha} + \text{h.c.}]. \end{aligned} \tag{4.27}$$

We assume that $\lambda(K+\tilde{k}) \in [-D_K, D_K]$ for $\forall\ \tilde{k}$ following Ref. [BCP08]. For convinience we set $D_K = 1$. The state directly coupled to the impurity cluster is represented by the operator

$$f_{0,K,\alpha} = \sum_{\tilde{k}} \frac{V(K+\tilde{k})}{V_K} a_{K+\tilde{k},\alpha}, \tag{4.28}$$

where $V_K^2 = \sum_{\tilde{k}} |V(K+\tilde{k})|^2$. The corresponding bath density of states reads:

$$\rho_K(\omega) = \sum_{\tilde{k}} \frac{|V(K+\tilde{k})|^2}{V_K^2} \delta(\omega - \lambda(K+\tilde{k})). \tag{4.29}$$

It is proportional to the imaginary part of the hybridization function $\Gamma_K(\omega^+)$, where $\omega^+ = \omega + i\eta$ with $\eta > 0$:

$$\Gamma_K(\omega) = -i\ \mathrm{Im}[\Delta_K(\omega^+)] = V_K^2 \pi \rho_K(\omega). \tag{4.30}$$

The hybridization function is due to Kramers-Kronig relations uniquely defined by the hybridization strength $\Gamma_K(\omega)$. Very often the DCA, and also cDMFT, loop is initialized considering a specific initial density of states, e.g. that of a Bethe lattice. Actually, it was shown that for lattice systems with an infinite coordinate number, such as the Bethe lattice, the DMFT approximation of a local self-energy becomes exact [MV89, MH89]. In this limiting case the self-consistency equations can be even solved exactly [GKKR96].

We discretize the density of states at bath site K with the goal to reproduce the exact density of states $\rho_K(\omega)$ as good as possible. The discretization-mesh points $\epsilon_n^{\pm,K}$, where $n \in \mathbb{N}_0$ and ± stands for the positive, respectively negative, energy axis, are defined considering the following constraints:

$$\epsilon_{n=0}^{K,\pm} = \pm 1, \tag{4.31}$$

$$\epsilon_{n+1}^{K,+} < \epsilon_n^{K,+} \text{ and } \epsilon_{n+1}^{K,-} > \epsilon_n^{K,-}, \tag{4.32}$$

$$\lim_{n\to\infty} \epsilon_n^{K,\pm} = 0. \tag{4.33}$$

In order to verify high resolution for small frequencies, we consider a logarithmic discretization with the following mesh points:

$$\epsilon_n^{K,\pm} = \pm \Lambda_K^{-n}, \tag{4.34}$$

where $\Lambda_K > 1$. So we have splitted the energy axis in intervals:

$$I_{K,n} = \underbrace{[\epsilon_n^{K,-}, \epsilon_{n+1}^{K,-}[}_{I_{K,-,n}} \cup \underbrace{[\epsilon_{n+1}^{K,+}, \epsilon_n^{K,+}[}_{I_{K,+,n}}. \tag{4.35}$$

An estimate for the energy resolution is obtained by comparing the width of an energy interval $I_{K,n}$ to the total energy as follows:

$$\frac{\Delta\epsilon_n^{K,+}}{\epsilon_n^{K,+}} = \frac{d_{K,+,n}}{\epsilon_{n+1}^{K,+} + \epsilon_n^{K,+}} = \frac{1 - \Lambda_K^{-1}}{1 + \Lambda_K^{-1}}, \tag{4.36}$$

where $d_{K,n} = \Lambda_K^{-n}(1 - \Lambda_K^{-1})$ is the width of an interval on the positive frequency axis. Of course, the same estimation is true for negative frequencies. The accuracy of the resolution grows in the limit $\Lambda_K \to 1$.

We consider now a Hilbert space spanned by operators $\{a_{K,(r,n),\alpha}^\dagger, a_{K,(r,n),\alpha}\}$ with quantum numbers $\{K, r, n, \alpha\}$, where $r = \pm$. A discretized form of the density of states is then given by:

$$\tilde{\rho}_K(\omega) = \sum_n \sum_{r=+,-} w_n^{K,r} \delta(\omega - E_n^{K,r}). \tag{4.37}$$

Here, we introduced the representative energies $E_n^{K,\pm}$ and weights $w_n^{K,\pm}$ for each subset $I_{K,\pm,n}$.
In order to ensure that the spectral function corresponding to the operator $f_{0,K,\alpha}$ is normalized, the weights have to fullfill:

$$w_n^{K,\pm} = \int_{I_{K,\pm,n}} \rho_K(\omega)\ d\omega. \tag{4.38}$$

One commonly uses different approaches for the calculation of the representative energies motivated by mathematical or phycial arguments. This is for example discussed in the literature, s. Ref. [BCP08]. We assume the following definition:

$$E_n^{K,\pm} = \frac{\int_{I_{K,\pm,n}} \omega\ \rho_K(\omega)\ d\omega}{\int_{I_{K,\pm,n}}\ \rho_K(\omega)\ d\omega}. \tag{4.39}$$

In conclusion, an effective cluster Hamiltonian operating on the Hilbert space spanned by operators living on the discretized frequency axis reads:

$$\begin{aligned} H_{\text{B+c}} &= H_{\text{B}} + H_{\text{c-B}} \\ &= \sum_{K,(n,r),\alpha} E_n^{K,r} a^\dagger_{K,(r,n),\alpha} a_{K,(r,n),\alpha} + \sum_{K,(r,n),\alpha} [\sqrt{w_n^{K,r}} a^\dagger_{K,(r,n),\alpha} c_{K,\alpha} + \text{h.c.}]. \end{aligned} \tag{4.40}$$

From this Hamiltonian one can straightforward verify that the discretized density of states is given by Eq. (4.37). We use this discretization scheme during the numerical renormalization group mapping. Of course, each bath can be discretized individually, which leads in the long run to different coupling amplitudes associated with each bath. This is the corner stone of the so-called iNRG method (cf. discussion below).

Semi-infinite Wilson chain The discretized Hamiltonian can be mapped on a semi-infinite tight-binding chain by tridiagonalization. The corresponding seed state is given by

$$f^\dagger_{K,0,\alpha} = \sum_{(r,n)} \frac{\sqrt{w_n^{K,r}}}{t_{K,0}} a^\dagger_{K,(r,n),\alpha}, \tag{4.41}$$

where $t_{K,0} = \sqrt{\sum_{(r,n)} w_n^{K,r}}$.
The Wilson chain Hamiltonian reads then as follows

$$H = H_{\text{c}} + H_{\text{chain}}, \tag{4.42}$$

where

$$H_{\text{chain}} = \sum_{K,\alpha} [g_{K,0} f^\dagger_{K,0,\alpha} f_{K,0,\alpha} + (t_{K,0} c^\dagger_{K,\alpha} f_{K,0,\alpha} + \text{h.c.})] + \sum_{m>0} H_m, \tag{4.43}$$

$$H_m = \sum_{K,\alpha} [g_{K,m} f^\dagger_{K,m,\alpha} f_{K,m,\alpha} + (t_{K,m} f^\dagger_{K,m,\alpha} f_{K,m-1,\alpha} + \text{h.c.})]. \tag{4.44}$$

Important is that the hopping between neighboring chain sites $t_{K,m}$ and chain parameter values $g_{K,m}$ decreases exponentially with large m:

$$t_{K,m} \propto \Lambda^{-\frac{m}{2}}, \tag{4.45}$$

$$g_{K,m} \propto \Lambda^{-\frac{m}{2}}, \tag{4.46}$$

where $\Lambda > 1$. This is a direct consequence of the logarithmic discretization. According to this, we can resolve the low-energy physics correct even when we interrupt the renormalization group flow after a finite number of steps. Higher order terms are negligible, which becomes clear if we consider a perturbative expansion in Λ and consider the scaling behavior of $t_{K,m}$.

Iterative diagonalization The Wilson chain allows to introduce a renormalization group scheme. The chain is straightforward written in form of a series:

$$H = \lim_{N\to\infty} \Lambda^{-\frac{N}{2}} H_N, \tag{4.47}$$

where

$$H_N = \Lambda^{\frac{N}{2}}[H_c + \sum_{K,\alpha}[g_{K,0} f^{\dagger}_{K,0,\alpha} f_{K,0,\alpha} + (t_{K,0} c^{\dagger}_{K,\alpha} f_{K,0,\alpha} + \text{h.c.})] + \sum_{m=1}^{N} H_m].$$

The scaling of H_N is fixed such that the prefactor cancels the largest hopping amplitude $t_{K,N}$, which is commonly a reasonable choice for a fixed point analysis in the renormalization group flow. We define further the following iteration equation:

$$H_{N+1} = \sqrt{\Lambda} H_N + \Lambda^{\frac{N}{2}}[\underbrace{g_{K,N+1} f^{\dagger}_{K,N+1,\alpha} f_{K,N+1,\alpha}}_{Y_{N+1,N+1}} + \underbrace{t_{K,N+1}\ (f^{\dagger}_{K,N+1,\alpha} f_{K,N,\alpha} + \text{h.c.})}_{X_{N,N+1}}]. \tag{4.48}$$

Here, summation over spin α is implicitely assumed. The Hamiltonian separates in each iteration step in three blocks $\{H_N, Y_{N+1,N+1}, X_{N,N+1}\}$. The operators $Y_{N+1,N+1}$ is a compact notation for the on-site interaction on the new chain site in the iteration step $N \to N+1$. The last block, $X_{N,N+1}$, connects the former last chain site with the new site via the hopping amplitudes $t_{K,N+1}$.

The Hilbert space $\mathcal{H}_{m+1}$ at iteration step $m+1$ is thus separable:

$$\mathcal{H}_{m+1} = \mathcal{H}_m \otimes \mathcal{H}, \tag{4.49}$$

where $m \in \mathrm{N}_0$ and $\mathcal{H}_0 = \mathcal{H}_\mathrm{c} \otimes \mathcal{H}$.

Let us further assume to have the eigenspectrum of H_N given by $|e_N\rangle$ and a local basis of the subsequent chain site $|s_{N+1}\rangle$. A basis set of the enlarged Hilbert space with $N+1$ chain sites is then straightforward written in form of product states:

$$|(e,s)_{N+1}\rangle = |e_N\rangle \otimes |s_{N+1}\rangle\,. \tag{4.50}$$

The cluster Hamiltonian is represented in this basis as follows:

$$\begin{aligned}\langle (e,s)_{N+1}|\, H_{N+1}\, |(e,s)_{N+1}\rangle = &\sqrt{\Lambda}\, \langle e_N|\, H_N\, |e_N\rangle + \Lambda^{\frac{N}{2}}\, \langle s_{N+1}|\, Y_{N+1,N+1}\, |s_{N+1}\rangle \\ &+ \Lambda^{\frac{N}{2}}\, \langle s_{N+1}|\, X_{N,N+1}\, |e_N\rangle + \Lambda^{\frac{N}{2}}\, \langle e_N|\, X_{N,N+1}\, |s_{N+1}\rangle\,.\end{aligned} \tag{4.51}$$

In conclusion, the Hilbert space grows in each iteration step by a factor of states in the subspace $\mathcal{H}$:

$$\mathcal{H}_N = \mathcal{H}_0 \otimes \underbrace{\mathcal{H} \otimes \ldots \otimes \mathcal{H}}_{N-1 \text{ chain sites}} . \tag{4.52}$$

In order to suppress the increase of the Hilbert space, we implement a truncation scheme after a certain iteration step N_S. This is a reasonable approximation due to the decrease of the hopping amplitudes when increasing the chain size. For further discussions of common truncation schemes and the renormalization group flow we refer to Ref. [BCP08, Wei12b].

Thus, the numerical renormalization group scheme is a iterative diagonalization procedure along the following steps:

1. Truncate the Hilbert space to the lowest N_{keep} eigenstates $\{|e_N\rangle\}$ in the energy spectrum $E_N(e)$ with respect to the ground state. The eigenenergy of the ground state is set to zero.

2. Construct a set of the enlarged Hilbert space by one chain site according to Eq. (4.50) and represent the Hamiltonian H_{N+1} in Eq. (4.48) in the subspace spanned by this basis.

3. Diagonalize the Hamiltonian H_{N+1} and get the enlarged energy eigenspectrum with states $|e_N\rangle$ and eigenvalues $E_{N+1}(e)$.

We emphasize that the eigenspectrum has to be rescaled after each iteration step by Λ^{N+1}. Finally, the low-energy spectrum follows a renormalization group flow and converges in proximity to corresponding fixed pointes [KMWW80]. Specific examples of energy flow diagrams and related discussions are part of Sec. 4.5. In all our calculations we use a discretization parameter $\Lambda = 6$.

Technical details In our calculation below we use the QSpace library implemented by Seung-Sup Lee and Andreas Weichselbaum, which includes a numerical renormalization group package based on tensor network states that make use of non-abelian symmetries (cf. Ref. [Wei12b, Wei12a]). It has been applied in a variey of different contexts, such as for the three-band Hund metals [SYvD$^+$15] and the SU(N) Hubbard model [LVDW18]. The library has been continuously improved during the last decade and includes the following technical subtleties:

- *Full density matrix numerical renormalization group (fdmNRG)*
  After each iteration step the truncated states are used to construct a full density matrix [WvD07] from approximated eigenstates of the Wilson chain [AS05]. Thereby, previous problems such as double counting of states are solved and higher resolution of dynamical response functions on the real-frequency axis are achievable.

- *Z-averaging*
  Each numerical renomalization group flow is constructed from multiple parallel sub-computations with shifted grids, so called z-shifts [OLFY91, OO94]. Thus, observables in real-frequency space can be calculated from this 'pool' of data with higher resolution. This also leads to an improved determination of Wilson chain parameters [ŽP09, Žit09b]. In our calculations below we use two z-shifts.

- *Adaptive broadening*
  Originally, Gaussian schemes were used to broaden spectral functions [BCP08]. The

numerical renomalization group implementation of the QSpace library uses further the information from different z-shift calculations to distinguish numerical artefacts from physical meaningful characteristics of observables in frequency space [LW16].

- *Interleaved numerical renormalization group (iNRG)*
  The cluster momentum sites are grouped in subsets and an energy scale separation among them is generated by implementation [MGWF+14, SMvDW16]. Thus, cluster and bath sites that belong to different cluster momenta are treated differently. Accordingly, symmetries between them are broken. As mentioned, our caluclations below use the dynamical cluster approximation and are performed in cluster momentum space. The two models have a mirror symmetry that lead to a degeneracy of momenta $(\pi, 0)$ and $(0, \pi)$. Thus, we separate cluster and bath sites in three subgroups corresponding to momenta $\{(0,0), (\pi,\pi), (\pi,0)/(0,\pi)\}$.

4.4 Earlier cluster studies of the Fermi-Hubbard model

Within the past years the two-dimensional Fermi-Hubbard model has been frequently studied using cluster approaches [MPJ02, MJP05, FCDL+09, GFP+10, GPM13, WSC+18, SCW+18, WSFG19]. The method was conceptional continuously improved. This process was also fueled by the more detailed insights into strongly correlated materials from the experimental side. In this section we take a closer glance at some of the currently discussed topics within this subfield.

In accordance with experiments a change of the topology of the Fermi surface and the violation of Luttinger's theorem have been verified in cDMFT and DCA computations [MJP05]. For instance, a DCA approach based on a quantum Monte Carlo solver using a maximum method verified the change of the Fermi surface from hole- to electron-like form by doping the system within a relevent parameter regime for cuprates [MPJ02]. Whereas at low-doping the Fermi surface turns out to be hole-like, i.e. centered around momentum $M = (\pi, \pi)$, it changes at larger doping into an electron Fermi surface located around $\Gamma = (0, 0)$. The shape of the Fermi surfaces clearly indicates the violation of Luttinger's theorem in certain parameter regimes close to half-filling ($p \approx 0.05$). Further, non-Fermi liquid and particle-hole asymmetry was observed in such systems by looking at the imaginary part of the self-energy. All these calculations were done at rather large temperatures of $T = 1/30\ eV$. Besides, the interplay of superconductivity and the pseudogap in the Fermi-Hubbard was debated including their possible close relation to a Mott insulating state [GPM13]. Numerical caluclations based on a DCA approach scanned the ground state characteristics of the two-dimensional Fermi-Hubbard model. They observed that superconductivity quite frequently appears in close proximity to normal and non-Fermi liquid pseudogap states. It was shown that the ground state properties were similar between an 8-site and 16-site cluster calculation. The analysis also confirmed that over a wide parameter regime superconducting and pseudogap state compete. Close to the Mott insulating state first a normal pseudogap state appears, which then passes over into a state with superconducting and pseudogap characteristics. Here, the gap in the spectral function at the antinodal point $k = (\pi, 0)$ was deformed while decreasing the temperature and indeed a supercondcting gap appeared below a certain temperature threshold. In another work, it was shown that the connection between the topological transition of the Fermi surface and the formation of a pseudogap goes back to a asymmetry pole-like feature in the antinodal self-energy [WSC+18]. Thereby, the results were in good agreement with an analytic approach based on a SU(2) lattice gauge model with topological order [SCW+18]. In 2009 Michel Ferrero et al. continued to investigate the opening of the pseudogap and the formation of Fermi arcs [FCDL+09], which are according to their analysis

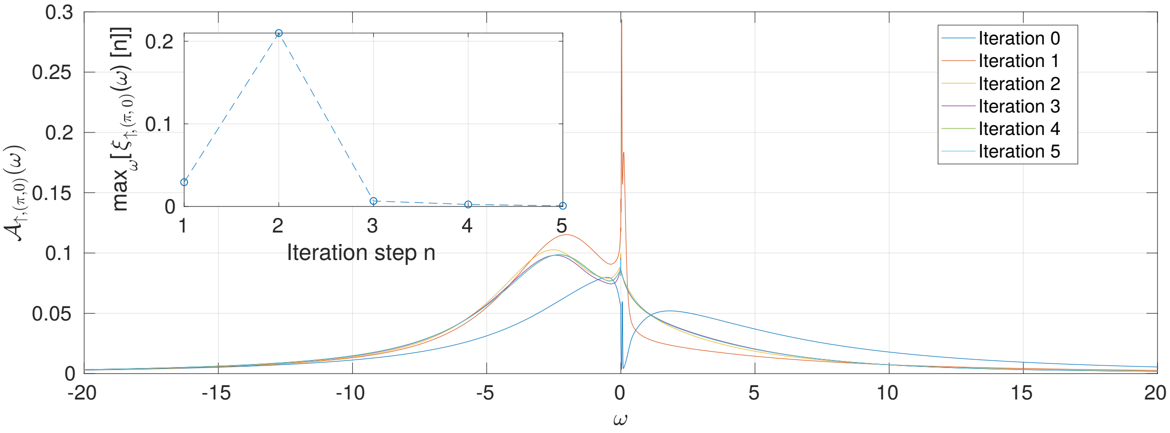

Figure 4.3 The figure shows one component of the spectral function $\mathcal{A}_{\uparrow,(\pi,0)}(\omega)$ of the two-dimensional Fermi-Hubbard model with parameters $U = 3t$, $t' = -3t/10$, $T = t/300$ and $\mu = 2t/3$ for six successive DCA iteration steps labled by $n = 0, ..., 5$. The initial spectral function has a dip close to zero frequency and is strongly modified within the first few iteration steps. Inset: As a convergence criterion we calculate $\max_\omega[\xi_{\uparrow,(\pi,0)}(\omega)[n]]$ (cf. main text for definition) that increases in the first step before it converges.

closely related to a momentum dependent Mott transition. Again, they used a quanum Monte Carlo solver and calculated the spectral functions for a minimal cluster of two momentum points. The calculations showed that the statistical weights of states on the cluster have a strong tendency to be constructed from fermionic and bosonic dimers in an intermediate hole doping regime. In another work, the impact of different DCA patchings on the momentum dependence of the self-energy and the formation of a gap in the spectral function at the antinodal point was resolved for various regimes of electron and hole doping [GFP+10]. It was shown that the hole-doped part of the numerical phase diagram when compared to the electron side consists of an additional section, which was called sector-selective regime. Here, the system shows non-Fermi liquid charactersitics and has an interaction-induced gap at the antinodal points. For completeness, we mention that recently it was emphasized that Van Hove singularities might play a major role in the formation of the pseudogap [WSFG19].

In our caluclation below, we show that even for spin-polarized baths, momentum-selective Mott physics for small doping is observed. We then increase doping and discover also the topological transition of the Fermi surface. In contrast to former approaches, we use a real-frequency numerical renormalization group solver and our calculations are performed at lower temperatures.

4.5 Results: Spectrum of the two-dimensional Fermi-Hubbard model

4.5.1 Definition of electron spectral function

In the following we frequently show figures of the electron spectral function, which is defined as follows

$$\mathcal{A}_\alpha(k,\omega) = -\frac{1}{\pi}\mathrm{Im}[\mathcal{FT}[G^R_\alpha(k,t)]], \qquad (4.53)$$

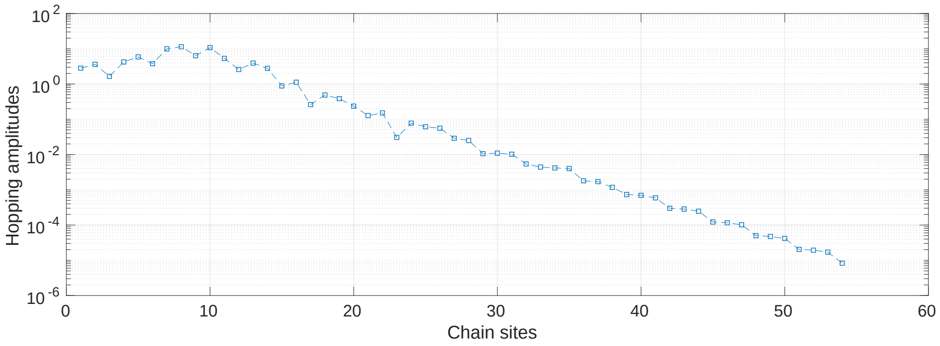

Figure 4.4 Hopping amplitudes along the chain sites in a semi-log plot. The data are from our calculation of the two-dimensional Fermi-Hubbard model at $U = 3t$, $t' = -3t/10$, $T = t/300$ and $\mu = 2t/3$. In total there are 54 chain sites, which originate from the three iNRG subchannels (cf. Sec. 4.3) each with 18 sites.

where the retarded Green's function is given by

$$G^R_\alpha(k,t) = -i\ \theta(t)\langle[c^\dagger_{k,\alpha}(t), c_{k,\alpha}(0)]_+\rangle. \tag{4.54}$$

Here, $\mathcal{FT}$ refers to the Fourier transformation from time to frequency space and $[\cdot,\cdot]_+$ is the anticommutator. Within the DCA approach we assume the system to be translational invariant, so that methodically we do not consider magnetically ordered states on the cluster. As a consequence the spectral function is diagonal in the spin subspace and thus we label the according components either with a single spin-up ($\alpha =\uparrow$) or spin-down index ($\alpha =\downarrow$).

4.5.2 Discussion: Convergence criterion, truncation and energy flow diagram

As we have already discussed, our impurity cluster is coupled to four chains and there is no interchain coupling in the DCA formalism. In a standard numerical renormalizaton group approach at each iteration step a complete supercell consisting of four cluster chain sites, which can be associated with the momenta $\{(0,0),(\pi,0),(0,\pi),(\pi,\pi)\}$, are added at once to the already existing system. The total number of what we simply call chain sites is then the product of supercells times the cluster sites within each supercell. In the following we stick to this terminology, however additionally use the iNRG scheme, so that the above momenta are separated into three channels (cf. paragraph 'Technical details' in Sec. 4.3).

Convergence criterion Each DCA iteration step includes the calculation of the impurity model parameters from the hybridization function and solving the resulting cluster impurity model by using the numerical renormalization group method. Then, we compute the impurity spectral function and self-energy from the corresponding low-energy spectrum. Finally, we also determine the coarse-grained lattice Green's function, where we substitute the self-energy by its cluster counterpart. In our implementation we define the DCA approach to be converged when all momentum and spin components differ in frequency space between two subsequent impurity Green's functions at most by a certain threshold m (in our implementation we set $m = 10^{-2}$):

$$\max_\omega[\xi_{\alpha,K}(\omega)[n]] < m, \tag{4.55}$$

where $\xi_{\alpha,K}(\omega)[n] = \mathcal{A}_{\alpha,K}[n+1] - \mathcal{A}_{\alpha,K}[n]$ with $n \in \mathbb{N}_0$ and spin $\alpha \in \{\uparrow,\downarrow\}$.

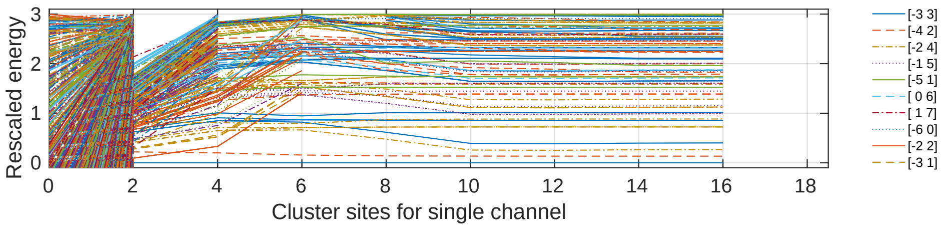

Figure 4.5 Energy flow diagram along cluster sites associated with a specific iNRG channel. The data are from the calculation of the two-dimensional Fermi-Hubbard model at $U = 3t$, $t' = -3t/10$, $T = t/300$ and $\mu = 2t/3$. We conclude that after 30 chain sites the low-energy spectrum converges against a stable fixed point that can be associated with a Fermi liquid state.

Fig. 4.3 shows the development of the impurity spectral function for the two-dimensional Fermi-Hubbard model with parameters $U = 3t$, $t' = -3t/10$ and $\mu = 2t/3$ at momentum $K = (\pi, 0)$ and for spin component $\alpha = \uparrow$ at six consecutive iteration steps. Initially, the spectral function has a strong dip close to zero frequency, which however vanishes and developes to a peak structure. The inset shows that the spectral function initially developes into a new structure, so that $\xi_{\alpha,K}(\omega)[n]$ strongly increases from step $n = 1$ to $n = 2$, however then converges against a value of roughly $\max_\omega[\xi_{\uparrow,(\pi,0)}(\omega)[5]] \approx 10^{-4}$. According to this, the updated and former component of the spectral function do not significantly differ within two subsequent iteration steps. In case the system is close to a phase transition, the spectral function sometimes also jumps between two solutions. This causes difficulties to get a reliable converged result. Here, it sometimes helps to average over a finite number of past hybridization functions before starting a new iteration step in order to enable the system to find its inherent solution more smoothly and faster [Zit09a]. This might prevent the iteration process to get stuck in an unstable fixed point. The above convergence criterion was used for all of the following calculations. Of course, we always double check the convergence of the spectral functions by plotting the impurity Green's functions and monitoring their development.

Truncation When iteratively diagonalizing the semi-infinite Wilson chain, the Hilbert space increases exponentially by adding at each iteration step an additional chain site. Our implementation uses the iNRG technique that introduces an additional energy separation within the cluster sites of a single supercell. The total number of chain sites N_{chain} is approximately given by $T \approx \Lambda^{-N_{\text{chain}}}$. In principle it is reasonable to start the truncation of the Hilbert space in the numerical renormalization group flow when the hopping amplitudes start to continuously decrease. For our specific implementation of the two-dimensional Fermi-Hubbard and quantum dimer model the hopping amplitudes develop usually as shown in Fig. 4.4. Here, we plot the hopping amplitudes in ascendent order according to the three iNRG channels each with 18 sites. According to this, the total chain consists of 72 sites. From this analysis we conclude that the Hilbert space should not be truncated before at least 7 or 8 chain sites are coupled to the system, and even above that we do not have a continuous decrease of the hopping amplitudes. So in practice we need to be very careful here and thus usually when performing our calculation we increase stepwise our truncation threshold until the spectral functions converge. In our implementation we see that usually two or three supercells each with 4 cluster sites, i.e. in total 8-12 chain sites, are enough to get reasonably good results for the spectral functions.

Energy flow diagram As already mentioned earlier, a tool to monitor the development of the numerical renormalization group is given by the energy flow diagram. Fig. 4.5 shows the energy flow diagram corresponding to the calculation in Fig. 4.3 and Fig. 4.4. Here, the number of kept multiplets, which is a group of states with equal symmetry labels, was initially set to 30000. We recognize in Fig. 4.5 that frequently in the first few iteration steps energy states are excluded, respectively run out during the energy flow. There are three reasons for this: First, we continuously adopt the number of kept multiplets and decrease them down to 16000 after a few iteration steps. Second, some energy states evolve towards very large energy regimes such that they can be simply excluded from further calculations of the low-energy spectrum. Last, at a later stage in the iterative diagonalization process we start to truncate the Hilbert space in energy space by setting $E_{\text{trunc}} = 9$.

Each line in the energy flow diagram represents an energy state with a certain symmetry label. In our case, the model has total spin and charge conservation (s. legend in Fig. 4.5). During the iterative diagonalization procedure, we resolve continuously the energy eigenspectrum more accurately and zoom in the low-energy spectrum. Here, after 40 chain sites, respectively 12 cluster chain sites for a single channel, the energy flow diagram converges. The corresponding energy spectrum has a structure that can be associated with that of a Fermi liquid state. If not mentioned otherwise, the following calculations come with an energy flow diagram that has a similar form, respectively structure, as the one shown here. For further information on the renormalization group technique we refer to the common literature [BCP08, Wei12a].

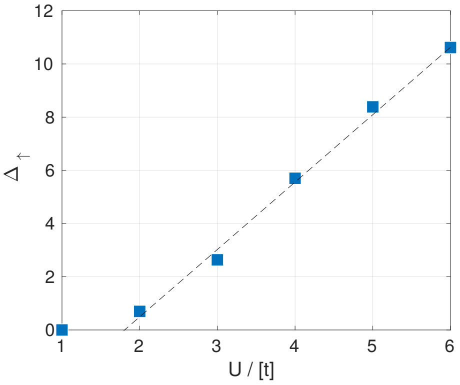

Figure 4.6 The two-dimensional Fermi-Hubbard model ($t' = 0t$, $T = t/300$) coupled to spin-polarized baths develops a Mott gap. We show here the gap $\Delta_\uparrow$ in the spin-up cluster spectral function at momentum $(\pi, 0)$. The linear dashed fit indicates that the critical on-site interaction above which a gap appears is approximately $U_{\text{crit}} \approx 1.85t$. Similar behavior is also observed in the spectral function of the other spin-component, even though it is not coupled to a bath.

4.5.3 Mott insulating gap at half-filling

In this section we study the formation of the Mott insulating gap in the two-dimensional Fermi-Hubbard model with solely nearest neighbor hopping on the square lattice at half-filling. The Fermi-Hubbard model with solely nearest neighbor hopping is invariant under the following particle-hole transformation that exchanges the role of creation and annihilation operators:

$$d^\dagger_{i,\alpha} = (-1)^{i_x+i_y} c_{i,\alpha}, \tag{4.56}$$

where $c_{i,\alpha}$ is the original fermionic creation operator with spin α and site i. Such a transformation interchanges the occupations $n_i = 0, 1$. The Hubbard interaction accumulates a shift in the chemical potential under the transformation (4.56) and gets an additional constant energy term. In case the particle-hole symmetry holds, the system is exactly half-filled for $\mu = U/2$. As shown in Fig. 4.7, for large U the spectral function has indeed no spectral weight at the Fermi energy $\omega = 0$ at all cluster momenta. Even though the cluster is just coupled to spin-up baths, this holds for both spin components of the spectral functions. The spectral function at cluster momentum $(\pi, 0)$ has a Mott gap. The corresponding width is usually defined as the distance from the left to the right side-band, which are usually called the upper and lower Hubbard-bands. The width $\Delta_\uparrow$ extracted from the spin-up spectral function is shown in Fig. 4.6. When decreasing the on-site interaction below $U < 2t$, the gap closes, i.e. a finite spectral weight appears at the Fermi energy. The critical value at which the Mott gap closes can be seen from the dashed interpolation line in Fig. 4.6 and is approximately $U_{\text{crit}} \approx 1.85t$.

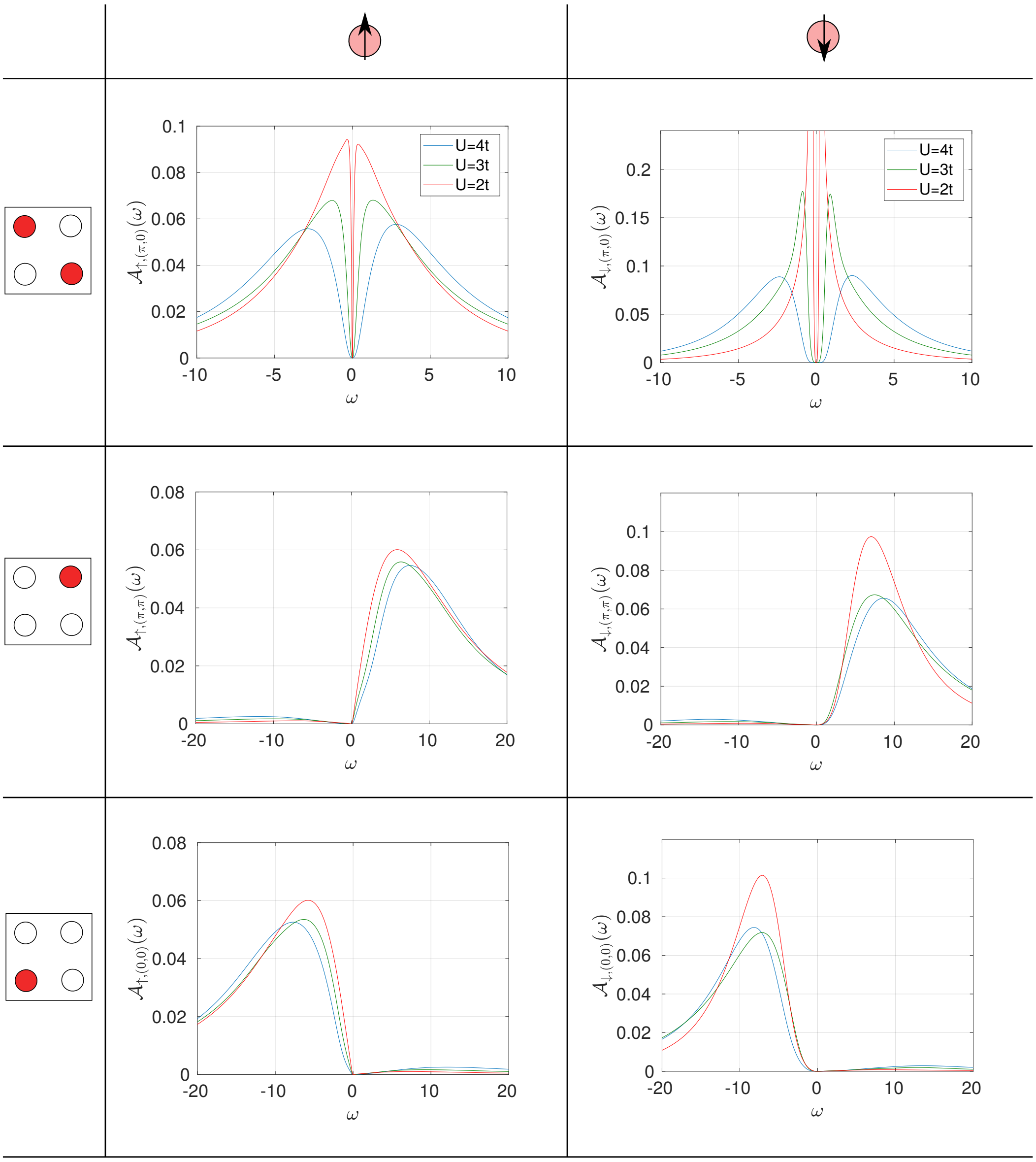

Figure 4.7 Electron spectral functions of the two-dimensional Fermi-Hubbard model on the square lattice at half-filling with solely nearest neighbor hopping at parameters $t' = 0t$ and $T = t/300$ calculated using a DCA approach with spin-up polarized baths. The columns show the spin-up and spin-down components of the spectral functions, whereas rows are associated with the cluster momenta. We see that both spin components behave in general qualitatively similar. The first row shows the formation of a Mott gap that increases with the on-site interaction U. Below the critical on-site interaction U_{crit}, the Mott gap closes.

In comparison, 4-site cluster calculations of the two-dimensional Fermi-Hubbard model using a quantum Monte Carlo solver have determined a critical repulsive interaction that is more than twice as large, namely $U_{\mathrm{crit}} \approx 4.5t$ [GPM13]. We assume that the discrepancy is again a consequence of the spin-polarized baths, since electrons with a spin component that is not coupled to the bath basically block the positions on the cluster if the on-site interaction is already comparably small. The gap in the spin-down spectral function vanishes approximately at the same critical value. In conclusion, we clearly see that even though the system is just coupled to one spin species, both spectral functions form a Mott gap above a certain critical threshold U_{crit} that vanishes when decreasing the repulsive on-site interaction. Furthermore, the spectral functions for both spin species are in most regimes qualitatively similar. So the Fermi-Hubbard model is expected to behave similar to what we know from the SU(2) invariant case and thus further investigation including next-nearest neighbor hopping and finite doping seems to be worthwile.

Momentum-selective Mott gap at finite hole doping Next, we consider the Fermi-Hubbard model on the square lattice with next-nearest neighbor hopping $t' = -3t/10$, $U = 3t$ at a temperature $T = t/300$. Such parameter values are in accordance with cuprate materials, respectively the pseudogap phase in such materials.

At small doping the gap in the spin-up component of the spectral function (cf. Fig. 4.9 bold lines) is still present in both components. However, at momentum (0,0) the spin-up spectral function has a finite weight at the Fermi energy $\omega = 0$. Such a momentum-selective formation of a gap has been also proposed in other works [FCDL$^+$09, GFP$^+$10]. However, in our case the Mott gap is just present in one spin component. The formation of such a momentum-selective gap thus depends on the fact that this spin component is coupled to a bath and the corresponding spin density is able to fluctuate. Otherwise, there are again some similarities regarding the distribution of the spectral weight in the spin-up and spin-down components of the spectral functions such as for instance the functional form at momentum (π, π). An additional discrepancy is given by the strong peak at frequency $\omega \approx -0.3$ in the patch $(\pi, 0)$. Again, this could be an artefact from the localization of this spin-component within the 4-site impurity cluster.

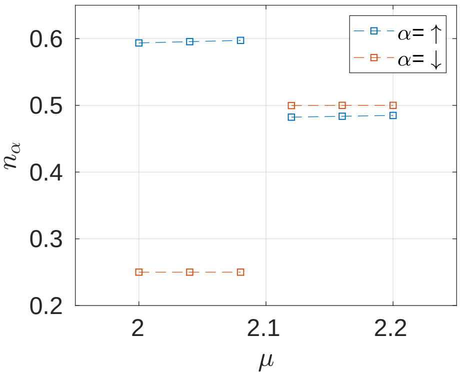

Figure 4.8 The particle density on the cluster shows a sudden jump when decreasing the chemical potential. The density of the spin-down particles, which can not lower their energy via hopping into the bath, suddenly decreases.

Now, we decrease the chemical potential and thus the particle density. Here, we discover an artefact rooted in the spin-polarization of the baths. In general, particles tend to lower their energy via hopping through the system, respectively into the bath. Since in our implementation this is just possible for the spin-up component, we observe a strong jump in the particle densities (cf. Fig. 4.8). According to this, the density of spin-down particles is stronlgy lowered at a certain chemical potential, whereas the spin-up component is slightly increased. As a consequence, we just get stable results of the spectral function at a doping value of approximately $p \approx 15\%$, respectively higher hole densities (cf. Fig. 4.10). Here, the spin-up spectral function has a large weight at the Fermi energy. The spectral weight of the other component is still close to zero at the Fermi energy for all momenta. We clearly see that the spectral function of spin-down at momentum $(\pi, 0)$ is in contrast to Fig. 4.9 just finite on the positive frequency axis, i.e. the spin-down particle density at this momentum is drastically reduced. This is of course in agreement with our former observation (cf. Fig. 4.8).

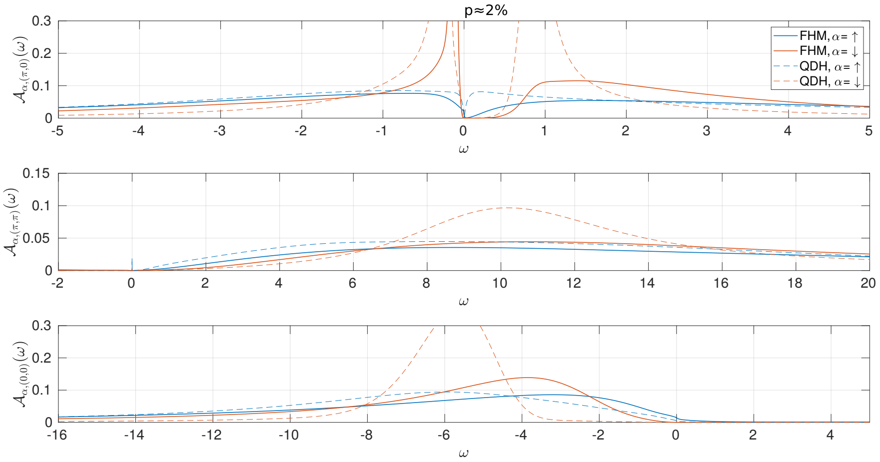

Figure 4.9 The electron spectral functions for spin-up (blue) and spin-down components (red) according to the Fermi-Hubbard (FHM) ($t' = -3t/10,\ U = 3t,\ T = t/300$) and quantum dimer model (QDH) ($t' = -3t/10,\ J = V = t/3,\ t_1 = -0.35t,\ t_2 = 0.65t,\ T = t/300$) at low doping $p \approx 2\%$. The top figure shows that both systems have a gap at momentum $(\pi, 0)$, i.e. no spectral weight at the Fermi energy. In contrast, the spectral function at momentum $(0, 0)$ has a finite weight for the spin-up component, which interacts with the bath. We thus observe a momentum-selective Mott gap. The spectral functions for both models and spin components show in most regimes qualitative similar behaviors.

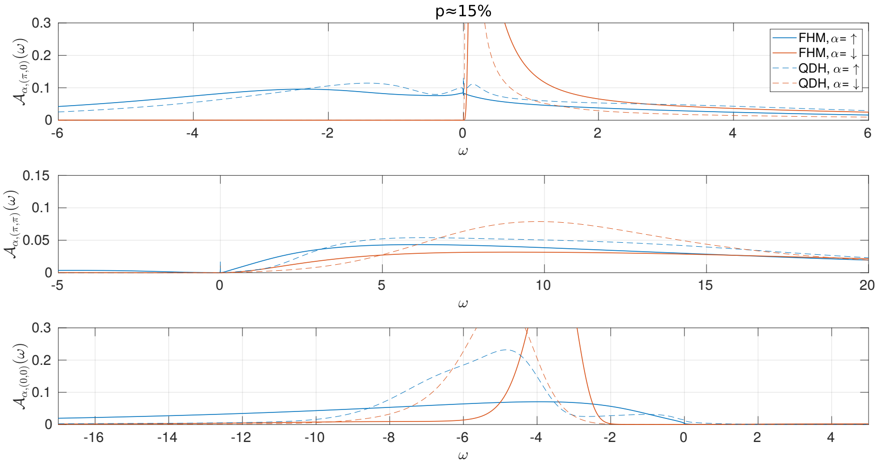

Figure 4.10 The figures show the electron spectral functions at parameters equal to that in Fig. 4.9, however at larger doping $p \approx 15\%$. The spin-up component of the spectral function at momentum $(\pi, 0)$ has a finite spectral weight at the Fermi energy. Here, the occupation of spin-down particles strongly decreases and thus the spectral weight is all located on the positive semi-axis. The other two spectral functions at momenta $(0, 0)$ and (π, π) are again qualitatively similar.

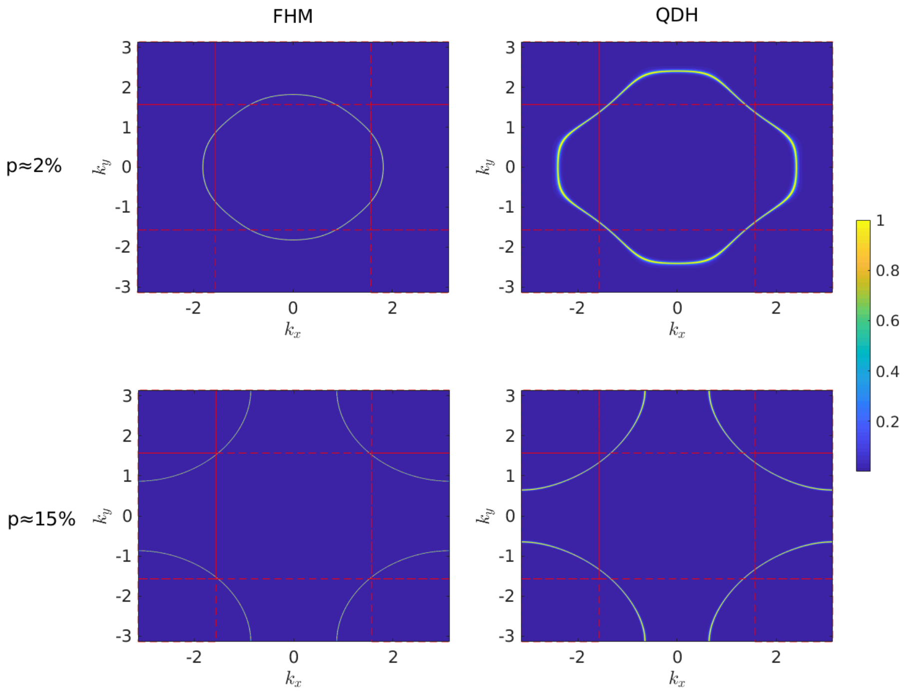

Figure 4.11 Here, we show the lattice spin-up spectral function for both models (for parameters cf. Fig. 4.9 and 4.10) at the Fermi energy in momentum space. It was calculated using an interpolation scheme based on the cumulant (cf. Sec. 4.2). We clearly see that the topology of the Fermi surface of the Fermi-Hubbard model changes with doping. Due to our spin-polarized baths, the exact doping position of the corresponding Lifshitz transition can not be determined within our scheme. The same is true for the quantum dimer model, however here the Fermi surface at small doping has different curvatures close to nodal and antinodal points.

Short comparison to the quantum dimer model– We compare the former results to a DCA analysis of the quantum dimer model embedded in the full electron Hilbert space, i.e. we assume that the electrons on the cluster interact in a form given by quantum dimer correlated hopping (QDH) as desrcibed by the quantum dimer model (3.15). We set the parameters to $J = V = t/3$, $t_1 = -0.35t$ and $t_2 = 0.65t$. The corresponding results are shown in Fig. 4.9 and 4.10 with dashed lines. First, we see that the spin-up spectral functions show a momentum-selective Mott gap similar to the Fermi-Hubbard model, which however vanishes when increasing doping from $p \approx 2\%$ to $p \approx 15\%$. Of course, the artificial strong jump in the density appears also in the quantum dimer model. Furthermore, the spectral functions for both, small and large doping, of the quantum dimer model are in general similar to that of the Fermi-Hubbard model. Just at doping $p \approx 2\%$, the quantum dimer model at momentum $(\pi, 0)$ and for the spin-down component has a strong peak on the positive axis in contrast to a plateau that we find in the results of the Fermi-Hubbard model.

Interpolated electron spectral functions– According to Sec. 4.3, we use the cumulant to interpolate the cluster Green's function in order to yield its lattice counterpart. Although this interpolation scheme has been proven in various works and seems to be a good candidate for systems in proximity to a Mott insulator, we emphasize that it has to be taken with a grain of salt, since there is no rigorous analytic argument why it should provide reliable results.

In Fig. 4.11 the Fermi surfaces in momentum space for the two dopings, $p \approx 2\%$ and $p \approx 15\%$, are shown at the Fermi energy $\omega = 0$. The Fermi surface of the Fermi-Hubbard model calculated from the spin-up retarded Green's function is electron-like at low doping and appears to be hole-like at larger hole concentration. As explained in Sec. 4.4, the corresponding Lifshitz transition has been frequently reported in the literature. Similar, the Fermi surface of the spin-up spectral function of the quantum dimer model undergoes such a transition. However here, the curvature of the Fermi surface at low doping is different at the nodal and antinodal point in contrast to the Fermi-Hubbard model.

4.6 Summary

Our implementation scheme of the two-dimensional Fermi-Hubbard and quantum dimer correlated hopping model uses a numerical renormalization group approach to solve the corresponding cluster impurity problem. In this case our computations are perfomed directly on the real-frequency axis. However, to overcome numerical limitations, we restrict our analysis to spin-polarized baths. We observe in the results of the electron spectral functions that even though SU(2) symmetry is broken, at least the qualitative behavior is present. This is for instance confirmed by the very important fact that we observe a Mott insulating gap in the spectral function. Increasing the hole concentration, spectral weight appears at the Fermi level of certain momenta. In conclusion, we observe a momentum-selective Mott gap in agreement with former results. This holds for both cluster impurity models. Unfortunately, the spin-polarized baths lead to a sudden jump in the cluster density. We are thus just able to resolve spectral functions at very small ($p \approx 2\%$) and large ($p \approx 15\%$) doping. Here, we see by interpolating the cumulant that the topology of the Fermi surface changes from electron- to hole-like when increasing doping.

According to the fact that their is no occupation at the Fermi level in the patch (π, π) (cf. Fig. 4.11), we propose for further analysis to just couple three SU(2) spin baths at the remaining cluster sites. This analysis should in principle capture the main processes close to the Fermi surface.

5 Interacting one-dimensional systems

5.1 Speciality of one-dimensional systems

5.1.1 Spectrum of one-dimensional systems

One-dimensional systems are peculiar due to their geometrical constraint. The movement of a single particle automatically effects its neighbors and leads to a collective excitation. Furthermore, the Fermi surface consists just of two points separated by $Q = 2k_F$ (cf. Fig. 5.1). The according Peierls instability in one-dimensional lattice systems is responsible for charge-density wave order [AM12, AS10]. In higher dimensions such instabilities normally just occur in certain limits of interaction and filling. For instance, the formation of Cooper pairs is based on the BCS superconducting instability due to which electrons on opposite sites of the Fermi surface pair up [BCS57a, BCS57b]. Besides, spins align antiferromagnetically in the two-dimensional Fermi-Hubbard model for large repulsive on-site interaction at half-filling [AS10]. However, the instability in one-dimensional systems according to the nesting vector $Q = 2k_F$ is independent of the strength of the interaction and always present. As a consequence the Lindhard response function at zero temperature has usually a strong singularity at $Q = 2k_F$. The excitation spectrum of one-dimensional systems are dominated by so-called particle-hole excitations, where an electron takes a momentum p from a state at momentum k below the Fermi surface and is thereby excited above the Fermi level. Excitations with momentum transfer p in higher dimensions can take arbitrarily low energy, since the phase space is not restricted. The according spectrum has then a continuum of excitations down to zero energy for all momenta below Q (cf. Fig. 5.1 (a)). This is in strong contrast to one-dimensional systems, where low-energy excitations are just possible for momentum transfer close to $p = 0$ and $p = 2k_F$ (cf. Fig. 5.1 (b)). Furthermore, the dispersion in the low-energy regime is usually expanded around the Fermi points

$$\epsilon_k = v_F(k - k_F) + \frac{1}{2m}(k - k_F)^2 \tag{5.1}$$

according to which the dispersion relation of the particle-hole excitations is given by

$$E_p + \delta E_p = v_F p + \frac{1}{2m}p^2. \tag{5.2}$$

Thus, particle-hole excitations are described by an energy E_p directly proportional to their momenta p. The next higher order term δE_p vanishes for $p \to 0$ much faster than the dispersion. According to this, particle-hole excitations have a finite lifetime and are therefore well-defined quaiparticles.

5.1.2 One-dimensional spin models

A strong impact on the methodical development of physics in one-dimensions goes back to research on spin models such as the spin-1/2 Heisenberg chain. The latter has been studied by a variety of different methods among which are Bethe ansatz calculations, mapping to the sine-Gordon and sigma model, and using non-abelian bosonization techniques (cf. Ref. in [Gia03, GNT04, EFG$^+$05, Fra13]).

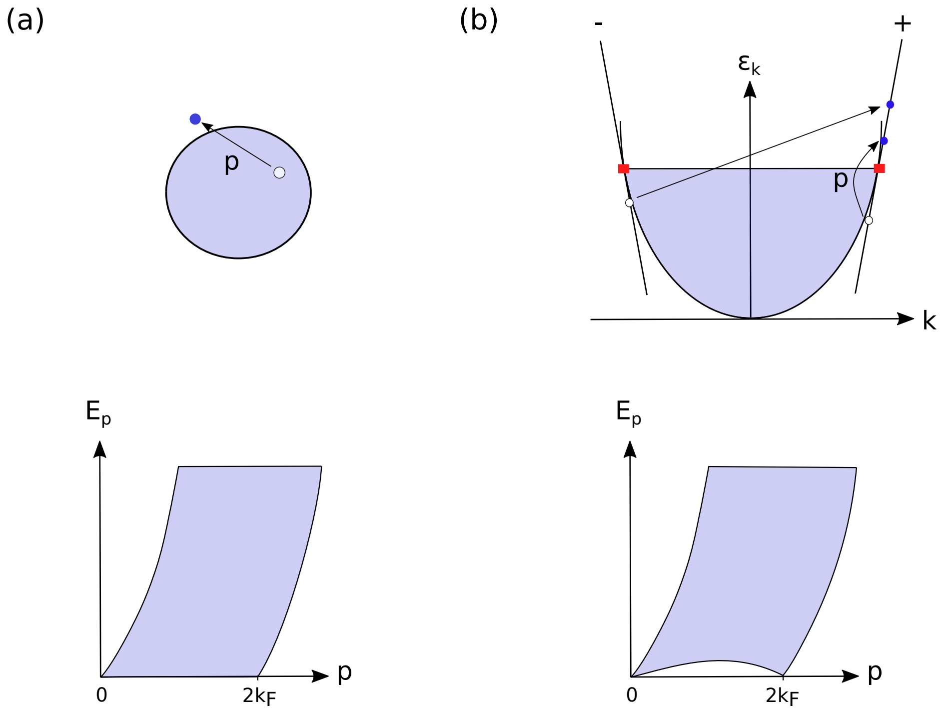

Figure 5.1 (a) Particle excitations with momentum p in higher dimensions create a continuum of spectral weight for all momenta between zero and $2k_F$. (b) Particle-hole excitations with momentum transfer p are the dominant processes that determine the low-energy behaviour of one-dimensional systems. The spectrum in the low-energy regime has a finite gap that just vanishes for momenta $p = 0$ and $p = 2k_F$.

In the past, the Bethe ansatz [Bet31] was used to analyze a variety of one-dimensional models including the Kondo and Anderson model [Gau83, Gia03, EFG$^+$05]. It solves the Schroedinger equation for a specific parametric representation of the eigenstates. Today, we know that such an approach is especially suited for integrable models with an infinite number of conservation laws.

Another approach to solve the Heisenberg model considers the mapping of spin operators onto spinless fermions, which is called Jordan-Wigner transformation [JW28]. The corresponding fermions are not equivalent to the physical electrons in the original Fermi-Hubbard model. The original spin-1/2 Hilbert space $\{|\uparrow\rangle, |\downarrow\rangle\}$ is constructed from a vacuum state that corresponds to the unoccupied site $f \ \ |0\rangle = f \ \ |\downarrow\rangle = 0$. According to this, the spin-up state is given by $|\uparrow\rangle = f^\dagger |0\rangle$. Of course, in case we have a chain with multiple sites the correct overall sign of the fermionic wave function has to be considered such that the anticommutation relations hold. The spin operators need to have Jordan-Wigner strings 'attached' that measure the occupation of spin-up states until the site of interest is reached [JW28, LSM61]:

$$S_l^+ = f_l^\dagger e^{i\pi \sum_{j<l} n_j}, \tag{5.3}$$

$$S_l^- = e^{-i\pi \sum_{j<l} n_j} f_l \,, \tag{5.4}$$

$$S_l^z = f_l^\dagger f_l - \frac{1}{2}. \tag{5.5}$$

The Jordan-Wigner representation maps the spin-1/2 anisotropic Heisenberg model, which reads as follows

$$H = \sum_i \frac{J_\perp}{2}[S^+_{i+1}S^+_i + S^+_i S^-_{i+1}] + J_z S^z_i S^z_{i+1}, \tag{5.6}$$

onto the following fermionic representation including hopping and nearest-neighbor Coulomb interaction

$$H = \sum_i \frac{J_\perp}{2}[f^\dagger_i f_{i+1} + \text{h.c.}] + J_z[\frac{1}{4} - f^\dagger_i f_i \; + f^\dagger_i f_i \, f^\dagger_{i+1} f_{i+1}]. \tag{5.7}$$

This Hamiltonian reduces to the XY-model for $J_z = 0$. Here, the fermions do not interact and the dispersion yields $\epsilon_p = J_\perp \cos p$. For completeness, we emphasize that the anisotropic Heisenberg model with couplings (J_x, J_y, J_z) exposed to an external magnetic field h along the z-direction was originally solved in different limiting cases. In the classical limit with $J_x = J_y = 0$, Ising originally determined that no magnetic ordering sets in when varying the temperature for a vanishing external field [Ons44]. The transverse field Ising model with $J_y = J_z = 0$ and $h \neq 0$ [Pfe70] has a quantum phase transition [Sac07] and is exactly solveable using the Jordan-Wigner transformation in Eq. (5.3)-(5.5) [Pfe70]. Today, it is frequently used as a tool model to explain and study phenomena related to quantum phase transitions [Sac07].

5.2 One-dimensional fermionic quantum liquids

Many one-dimensional models belong to the Luttinger liquid class that describes metallic states with correlation functions that decay algebraically in space and time [Gia03]. The terminology Luttinger liquid goes back to a work by F. Duncan M. Haldane in 1981, in which the Luttinger liquid has been first proposed as a rather general class of one-dimensional models with certain characteristics [Hal81]. In the following, we go one step back in time and look at the origin of the concept. We hereby follow partially Ref. [Sch04].

Shin'ichirō Tomonaga predicted in 1950 that the low-energy physics of translational invariant one-dimensional electronic systems are dominated by bosonic excitations [Tom50]. He pointed out that an interacting one-dimensional fermionic system behaves similar to coupled harmonic oscillators. Thereupon, Joaquin M. Luttinger formulated an exactly solveable one-dimensional interacting fermionic model for which the momentum distribution of the ground state decays algebraically [Lut63]. The model itself was later solved exactly by Elliott H. Lieb and Daniel C. Mattis using a bosonization approach [ML65]. Let us in the following take a closer look at some of the technical details.

Therefore, we consider spinless interacting fermions along a one-dimensional chain with length L and periodic boundary conditions described by the Hamiltonian

$$H = H^0 + H_{\text{int}} = \sum_k \epsilon_k c^\dagger_k c_k + \sum_{k_i} V_{k_1,k_2,k_3,k_4} c^\dagger_{k_1} c_{k_2} c^\dagger_{k_3} c_{k_4}, \tag{5.8}$$

where we consider the dispersion $\epsilon_k = \frac{k^2}{2m}$ and interaction

$$V_{k_1,k_2,k_3,k_4} = \frac{1}{L}\tilde{v}(k_1 - k_3)\delta_{k_1+k_3,k_2+k_4}, \tag{5.9}$$

where $\tilde{v}(k)$ is a two-body interaction. Shin'ichirō Tomonaga focused on a long-range interaction that sets a momentum cutoff k_c much smaller than the Fermi momentum k_F above which the interaction is assumed to vanish, i.e. $\tilde{v}(k)$. Frequently, two interaction parameters $\{g_2, g_4\}$ for such intrabranch interactions are introduced (cf. Fig. 5.2 and 5.3 (a)). According to this, the low-energy physics is restricted around the two Fermi points such that a linear dispersion relation is assumed to be a reasonable approximation: $\epsilon_k = \epsilon_F \pm v_F[k \mp k_F]$ with Fermi velocity $v_F = k_F/m$. He realized that the Hamiltonian (5.8) is quadratic when written in the Fourier transform of the density operator $\rho_n = \sum_{n'} c^\dagger_{n'} c_{n'+n}$ with $k = \frac{2\pi}{L} n$, where $n \in \mathbb{Z}$. The Kronig identities [Voi95, Sch05] indeed show the deep relation between bosonic particles defined as

$$\sqrt{|n|} b_n = \rho_{n>0} = \rho_+, \tag{5.10}$$

$$\sqrt{|n|} b^\dagger_n = \rho_{n\leq 0} = \rho_-, \tag{5.11}$$

and the kinetic term of the fermionic system with linear dispersion

$$H^0_{\mathrm{B},+} = \sum_n v_F k_n c^\dagger_n c_n = v_F \frac{2\pi}{L}[\sum_{m>0} b^\dagger_m b_m + \frac{1}{2}\mathcal{N}_+(\mathcal{N}_+ + 1)], \tag{5.12}$$

where $k_n = \frac{2\pi}{L} n$ with $n \in \mathbb{Z}$ and $\mathcal{N}_+ = \sum_{n>0} c^\dagger_n c_n$. The overall Hamiltonian consists then of the following terms

$$H = \sum_{\eta=+,-} H^0_{\mathrm{B},\eta} + H_{\mathrm{int}} + \frac{\pi}{2L}[v_N \mathcal{N}^2 + v_J \mathcal{J}^2], \tag{5.13}$$

where we introduced the total particle operator $\mathcal{N} = \mathcal{N}_+ + \mathcal{N}_-$ and current operator $\mathcal{J} = \mathcal{N}_+ - \mathcal{N}_-$. The interaction term in (5.13) includes off-diagonal quadratic terms, $\propto b^\dagger_m b^\dagger_{-m}$ and $\propto b_m b_{-m}$. However, the Hamiltonian can be diagonalized using a Bogoliubov transformation. For further details on this transformation we refer to the literature [Gia03]. The velocities in Eq. (5.13) are given by $v_N = v_F + \frac{\tilde{v}(0)}{\pi}$ and $v_J = v_F$. In case the excitations are close to the Fermi points and the interaction $\tilde{v}(k)$ is smooth, the bosonic quasiparticles have a linear dispersion and propagate with charge velocity $v_c = \sqrt{v_J v_N}$. Besides, the stiffness constant $K = \sqrt{v_J/v_N}$ is a crucial parameter that describes the compressibility of the system [Gia03]. The stiffness constant is by definition $K = 1$ for a free fermionic system and $K > 1$ $(0 < K < 1)$ in case the fermions interact via an attractive (repulsive) interaction. In summary, the famous Tomonaga-Luttinger model is rooted in the works by Joaquin M. Luttinger and Shin'ichirō Tomonaga. In the subsequent years, it was shown to describe a large class of one-dimensional models.

As originally claimed and later verified by Elliot H. Lieb and Daniel C. Mattis [ML65], the momentum distribution of the Tomonaga-Luttinger model is smooth around the Fermi points:

$$\langle n_{k,+} \rangle - \frac{1}{2} \propto |\frac{k - k_F}{k_c}|^\alpha \,\mathrm{sign}(k_F - k), \tag{5.14}$$

where the critical exponent depends solely on the interaction strength, $\alpha = (K-1)^2/2K$. This confirms that Fermi liquid theory is not applicable in one-dimensional systems, since the occupation function has not a step proportional to the quasiparticle weight for a single fermionic excitation as in ordinary metals in higher dimensions. The inverse mapping of the fermionic field operator in bosons was developed shortly after [SS69] and simplified further calculations of fermionic single particle correlation functions [Hal81, VDS98]. The fermionic

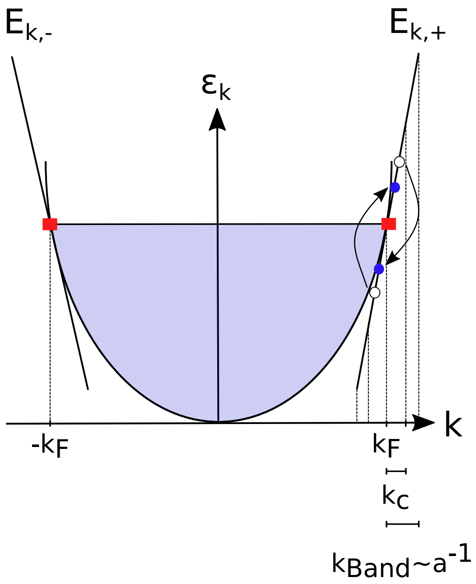

Figure 5.2 All states up to the Fermi points $\pm k_F$ are occupied. Usually, the dispersion in the low-energy regime is linearized around the Fermi points. This is an essential ingredient of the Tomonaga-Luttinger model. In the original works, both focused on long-range interaction with momentum cutoff k_c. Additionally, Shin'ichirō Tomonaga considered a finite band cutoff $k_{\text{band}} \approx a^{-1}$, below which the dispersion is assumed to be linear. The illustrated interaction g_4 conserves the individual particle numbers at each branch. Both particle-hole excitations are here assumed to be located at the positive branch. The fermions at this branch are right movers.

field operator (cf. also Eq. (5.17)-(5.18) below) is thereby represented as follows

$$\psi(x) = F(x)e^{i\varphi^\dagger(x)}e^{i\varphi(x)}. \tag{5.15}$$

Here, the Klein factor $F(x)$ is introduced, which connects electronic subspaces with different number of particles N. Each electronic state with a fixed particle number can then be created by applying a series of particle-hole excitations according to

$$\varphi(x) = \sum_{p>0} \frac{1}{\sqrt{p}} e^{-ipx} b_p e^{-ap}, \tag{5.16}$$

where a is a small positive cutoff (s. Fig. 5.2). The above representation (5.16) satisfies the fermionic anticommutation relations. In conclusion, the complete fermionic Hilbert space can be represented in a bosonic basis of particle-hole excitations. The physical fermions are usually separated into left and right moving particles as follows

$$\begin{aligned}\psi_{\text{phy}}(x) &= \left(\frac{2\pi}{L}\right)^{1/2} \sum_{k\leq k_F} [e^{-i(k_F+k)x} c_{-k_F-k} + e^{i(k_F+k)x} c_{k_F+k}] \\ &= e^{-ik_F x}\psi_-(x) + e^{ik_F x}\psi_+(x),\end{aligned} \tag{5.17}$$

where the fermions associated with each branch are defined as

$$\psi_\mp(x) = \left(\frac{2\pi}{L}\right)^{1/2} \sum_{k\leq k_F} e^{\mp ikx} c_{\mp(k_F+k)}. \tag{5.18}$$

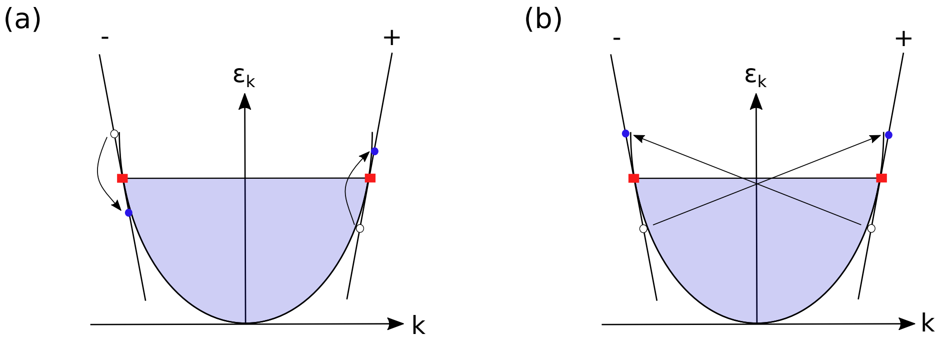

Figure 5.3 (a) The illustration shows a g_2 process, which conserves the particle number within each branch. However, the particle-hole excitations are located at different branches. (b) Such interbranch processes, usually called g_1 processes, have a momentum transfer of $p \approx 2k_F$.

The local spectral density $\rho(\omega)$ has been calculated using this bosonic representation of fermionic fields and shows a power law decay at zero temperature [LP74, Med99] (critical exponent cf. Eq. (5.14)) that reads as follows

$$\rho(\omega) \propto \theta(\omega)(-\omega)^{\alpha}. \tag{5.19}$$

At finite temperature spectral weight appears also at positive frequencies [SM93]. The calculation of the spectral function for a general momentum dependent interaction is rather difficult (except at the Fermi momentum). Here, the local density has in contrast to Fermi liquid theory no sharp peak in the spectrum, but contains a power law divergence.

Igor E. Dzyaloshinski and A. I. Larkin considered further spinful fermions and found the appearance of spin-charge separation [DL74]. The according Hamiltonian consists of two identical copies of Tomonaga-Luttinger Hamiltonians for the spin and charge degrees of freedom. Both commute with each other. The charge and spin degrees of freedom are thereby defined as follows

$$b_{n,c} = \frac{1}{\sqrt{2}}[b_{n,\uparrow} + b_{n,\downarrow}], \tag{5.20}$$

$$b_{n,s} = \frac{1}{\sqrt{2}}[b_{n,\uparrow} - b_{n,\downarrow}]. \tag{5.21}$$

This yields then also two copies of velocities and stiffness constants. The spectral function has been calculated for constant interactions within a certain momentum cutoff. It shows indeed two individual singularities associated with charge and spin [MS92, Voi93].

5.3 Luttinger liquid class

Early attemps have focused on long-range interactions such that the according particle-hole excitations are located within a single branch (s. Fig. 5.2 and 5.3 (a)). Later on, people started to consider processes that include a momentum transfer $\pm 2k_F$. Such local interactions are usually described by the parameter g_1 (s. Fig. 5.3 (b)). A renormalization group study of the model in Eq. (5.8) including also g_1 processes have shown that the fixed-point theory for repulsive interaction $g_1 > 0$ boils down to the Tomonaga-Luttinger Hamiltonian [Sól79]. In case of an attractive interaction $g_1 < 0$, the spectra for both spin and charge were calculated using a mixture of bosonization and refermionization techniques and revealed a finite gap in the spin sector. However, the elementary excitations still separate into spin and charge fractions [LE74].

In case an underlying lattice is considered, additional Umklapp processes occur. Here, the momentum conservation is just satisfied up to a integer multiple of $2k_F$. For spinless fermions at half-filling, Bethe calculations and renormalization group approaches confirmed that the system is for small repulsive interaction $U < t$ described by a Tomonaga-Luttinger liquid [Sha94]. However, the particles tend to localize on every other site with increasing U and charge-density wave order evolves. For long-range interaction the system turns out to be not a Luttinger liquid [Sch93]. When including spin, the Fermi-Hubbard model at half-filling has always a gap in the charge sector. For large repulsive interaction, the gap is of the order $\Delta \approx U$ [EFG+05] and is rather small when the particles have a comparable large finite kinetic energy. In the latter case, Umklapp processes are indeed not irrelevant. Away from half-filling, the Hubbard model is again a Luttinger liquid [Sch90]. In conclusion, the Tomonaga-Luttinger concept is applicable to a broad class of one-dimensional fermionic models. It has been studied with a variety of analytical methods including renormalization group analysis, Bethe ansatz and diagrammatic approaches [Gia03].

5.4 Signatures of Tomonaga-Luttinger theory in experiments

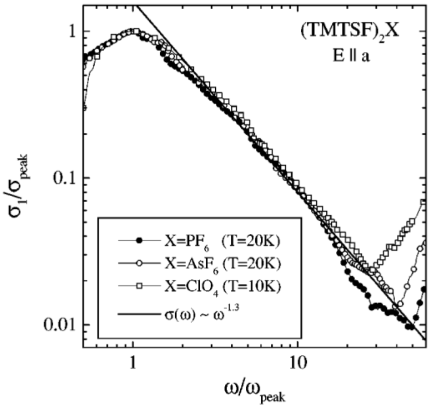

Figure 5.4 The measurement of the optical conductivity above the charge gap shows clear power law decay in accordance with Luttinger liquid theory, reprinted with permission from Ref. [SDG+98]. Copyright (1998) by the American Physical Society.

Several experiments were performed on (quasi-)one-dimensional systems in order to find clear signatures of Tomonaga-Luttinger theory. Early attempts have focused on organic conductors. The physics in such materials is given by an anisotropic tight-binding model with a dominant hopping along a certain direction [BJ08].

The optical conductivity has been measured in some of these materials and shows in accordance with predictions from Tomonaga-Luttinger theory (cf. Eq. (5.19)) a power law form above the charge gap [SDG+98] (cf. Fig. 5.4). Furthemore, charge transport measurements on such materials had also clear Tomonaga-Luttinger characteristics.

Later, carbon nanotubes, which are tightly rolled up sheets of graphene, were used as platfroms to study one-dimensional systems. The critical exponent of the density of states close to the Fermi surface shows the correct dependence on the interaction parameter in agreement with Tomonaga-Luttinger predictions [Egg07]. Also the temperature and differential conductance behaviour when exposing the system to a small bias voltage $V \ll k_B T/e$ by using metallic tunneling leads pointed in the same direction [BCL+99]. Carbon nanotubes were further investigated using a variety of other experiments, including for instance photoemission spectroscopy [IKS+03].

Third, optical lattice systems have been used to mimic one-dimensional systems of interacting fermions and bosons [BDZ08]. Indeed, many one-dimensional bosonic systems map in the low-energy regime onto a Luttinger model. We get back to this point in Sec. 5.6. Even though distinct parameter regimes of the Tomonaga-Luttinger model have been succesfully implemented in ultracold gas setups, the inhomogeneous trap in general leads to a suppression of the power law decay and thus prohibits the construction of a true translational invariant one-dimensional system. Meanwhile, experiments on atom chips are used to overcome this discrepancy and in fact lead to direct measurements of the Luttinger parameters [SHA+05, HLF+06, LSH+06, FKS+08].

So far we have mainly focused on experiments that try to find signatures of the Tomonaga-Luttinger theory in form of the power law decay of correlation functions. Another crucial aspect of Tomonaga-Luttinger states is the fractionalization of the spectrum in charge and spin degrees of freedom. The separation of magnons into two spinon excitations has been confirmed by the measurement of the Cloiseaux-Pearson spectrum in neutron scattering experiments on spin chains [TCNT95, SRB+03, TRR+09]. Furthermore, tunneling sepctroscopy measurements have partially led to the detection of the spinon spectrum [AYDP+02, THAY02]. Other than that, the detection of fractionalization has turned out to be rather difficult in conventional one-dimensional electronic systems.

Of course, many more setups exist, e.g. edge states in Hall sytems, which are frequently used to investigate one-dimensional systems. More details on one-dimensional experimental setups can be found in the literature [Gia03].

5.5 Inhomogeneous one-dimensional system

5.5.1 Overview

The bosonization formalism was succesfully applied to a variety of physical setups with translational invariant interactions among electrons [Gia03, GNT04]. Further directions that became relevant in the last years include the impact of scattering among bosonic quasiparticles originating from the band curvature (for bosonic system s. Sec. 5.6), boundary effects [MMS$^+$00, SE10, Ryl19] and the investigation of impurities in a one-dimensional fermionic system [MMSS02, HR14]. Our approach provides a complementary point of view on many of these subfields and is based on a higher-order bosonization approach from which the following scattering operators are constructed:

$$K^m_{q\eta} = \sum_k n^m_k :c^\dagger_{k-q} c_k :, \tag{5.22}$$

where $m \in \mathrm{N}_0$ and η is a flavor index. Such a representation is especially suited to describe inhomogeneous one-dimensional electronic systems with a position-dependent local interaction. Former studies on one-dimensional systems with local interactions considered for instance a local impurity and performed a renormalization group flow study to investigate in what regimes the system is splitted into two halves [KF92, Gia03]. In order to understand the motivation for our work, let us take a step back and consider again that F. Duncan M. Haldane formulated in 1981 the Tomonaga-Luttinger liquid concept for translatonal invariant interactions [Hal81]. Its validity goes beyond non-linear effects from the band curvature. It contains among other things two major aspects that are necessary to assign a system to the Tomonaga-Luttinger class:

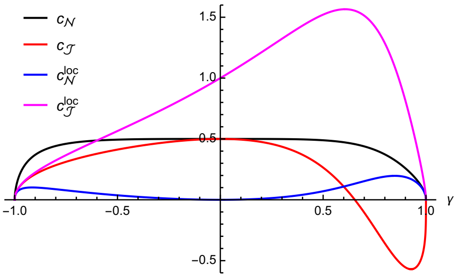

Figure 5.5 The coefficients in a linear relation between excitation velocities in the inhomogeneous Tomonaga-Luttinger model as a function of the interaction parameter γ. Fig. is adapted from our publication Ref. [HK19].

- The excitation spectrum is dominated by density fluctuation boson modes, charge and current excitations associated with the velocities v_S, v_N and v_J, wich are related as follows $v_S = \sqrt{v_N v_J}$.
- The correlation functions decay algebraically with a critical exponent given by a fixed relation between the excitation velocities (s. p. 9 in the article below 5.5.2).

We shed light onto the question how much of this original concept carries over to for inhomogeneous symmetric local interactions $V(x) = V(-x)$. Our model has a inter- and intrabranch local interaction with two flavors of electrons, namely right and left movers. In the first step, we use higher order bonoization identities to simplify the Hamiltonian represented by scattering operators (5.22). Next, we apply a combination of bosonization and refermionization transformations in order to calculate the single electron propagator at zero temperature. The final outcome bear the following conclusions:

- The Luttinger velocities (s. Fig. 5.5) are related according to a modified identity (s. p. 8 in the article below 5.5.2).
- For a symmetric interaction $V(x) = V(-x)$ and on a certain parameter submanifold, the analytic form of the electronic propagater decays algebraically, however with a modified critical exponent.

Thus, we claim a paradigm shift of the original Tomonaga-Luttinger concept [Hal81] towards inhomogeneous systems that manifests in our calculation in a new analytic form of the single electron propagator compared to the translational invariant case. In order to verify this rigorously, the robustness of the analytic form of the propagator against pertubrative corrections from the band curvature has to be confirmed in a subsequent works.

From Luttinger liquids to Luttinger droplets via higher-order bosonization identities

by

S. Huber[1], and M. Kollar[2]

[1]Theoretical Solid State Physics, Arnold Sommerfeld Center for Theoretical Physics, Center for NanoScience, and Munich Center for Quantum Science and Technology, Ludwig-Maximilians-University, Theresienstr. 37, 80333 Munich, Germany

[2]Theoretical Physics III, Center for Electronic Correlations and Magnetism, Institute of Physics, University of Augsburg, 86135 Augsburg, Germany

reprinted on pages 104–117

arXiv preprint: **arXiv:1911.03158** [**cond-mat.str-el**],

submitted to Phys. Rev. Research

From Luttinger liquids to Luttinger droplets via higher-order bosonization identities

Sebastian Huber[1] and Marcus Kollar[2]
[1] *Theoretical Solid State Physics, Arnold Sommerfeld Center for Theoretical Physics,*
Center for NanoScience, and Munich Center for Quantum Science and Technology,
Ludwig-Maximilians-University, Theresienstr. 37, 80333 Munich, Germany
[2] *Theoretical Physics III, Center for Electronic Correlations and Magnetism,*
Institute of Physics, University of Augsburg, 86135 Augsburg, Germany

(Dated: November 11, 2019)

We derive generalized Kronig identities expressing quadratic fermionic terms including momentum transfer to bosonic operators and use them to obtain the exact solution for one-dimensional fermionic models with linear dispersion in the presence of position-dependent interactions and scattering potential. In these Luttinger droplets, which correspond to Luttinger liquids with spatial variations or constraints, the position dependences of the couplings break the translational invariance of correlation functions and modify the Luttinger-liquid interrelations between excitation velocities.

I. INTRODUCTION

An important goal of condensed matter theory is a reliable description of the correlated behavior of electrons which is rooted in the Coulomb interaction between them. In one-dimensional geometries they exhibit a special coherence at low energies:[1,2] the dispersion can be approximately linearized in the vicinity of the Fermi points $\pm k_\mathrm{F}$ as $\epsilon_k \simeq \pm v_\mathrm{F}(k \pm k_\mathrm{F})$, so that the energy $\delta\epsilon = v_\mathrm{F}\delta k$ of a particle-hole excitation from k_1 to k_2 is a function only of the momentum transfer $\delta k = k_2 - k_1$. By contrast, in higher dimensions the magnitude and relative orientation of the two momenta usually enter into $\delta\epsilon$, leading to a continuum of excitation energies for a given momentum transfer. This coherence in one dimension is prominently featured in the Tomonaga-Luttinger model,[3,4] which is based on the approximation that one can regard a physical electron field operator $\Psi(x)$ for a wire of length L at low energies as a sum of two independent fields,

$$\Psi(x) = \sum_k \frac{e^{\mathrm{i}kx}}{\sqrt{L}}\mathcal{C}_k = \sum_{\substack{k>-k_\mathrm{F}\\ \lambda=\pm}} \frac{e^{\mathrm{i}\lambda(k_\mathrm{F}+k)x}}{\sqrt{L}}\mathcal{C}_{\lambda(k_\mathrm{F}+k)} \tag{1a}$$

$$\simeq \frac{e^{\mathrm{i}k_\mathrm{F}x}\psi_\mathrm{R}(x) + e^{-\mathrm{i}k_\mathrm{F}x}\psi_\mathrm{L}(x)}{\sqrt{2\pi}}\,, \tag{1b}$$

where the lower summations limits $-k_\mathrm{F}$ in (1a) were replaced by $-\infty$ (1b). Then $\psi_{\mathrm{R,L}}(x) = \psi_{1,2}(\mp x)$ and $\psi_\eta(x) = (2\pi/L)^{\frac{1}{2}} \sum_k \mathrm{e}^{-\mathrm{i}kx} c_{k\eta}$ are defined in terms of canonical fermions $c_{k\eta} = \mathcal{C}_{\pm(k_\mathrm{F}+k)}$ which correspond to the physical fermions $\mathcal{C}_k$ near the two Fermi points for $\eta = 1, 2$. In the Tomonaga-Luttinger model the dispersion is linearized near the Fermi points and only forward-scattering density interactions between left- and right-moving fermions are kept. The Tomonaga-Luttinger model can be solved by bosonization,[3–13] which expresses the above-mentioned coherence of excitations into an exact mapping to bosonic degrees of freedom (at the operator level[9,14–18] or in a path-integral formulation;[19–22] throughout we use Ref. 17's constructive finite-size bosonization approach, which is recapped below). Bosonization has led to such remarkable results and concepts as spin-charge separation of elementary excitations,[3,4] interaction-dependent exponents of correlation functions,[9,23–25] and the Luttinger-liquid paradigm[13,26] which states that the relations between excitation velocities and correlation exponents of the Tomonaga-Luttinger model remain valid even for weakly nonlinear dispersion. These topics are nowadays presented in many reviews[1,14,15,17,27–30] and textbooks.[2,31–36] Characteristic signatures of one-dimensional electron liquids have been observed in a variety of experiments.[37–50] The theory of nonlinear dispersion terms has been of particular further interest,[6,13,51–53] including refermionization techniques which use bosonization identities in reverse to map diagonalized bosonic systems back to free fermions.[52,54–58]

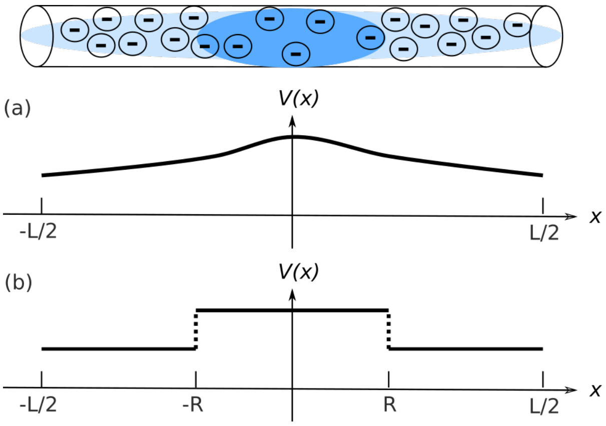

FIG. 1. Wire of length L with position-dependent interaction potential $V(x)$ in (4), with $V(x) = V(-x)$, sketched here for the repulsive case with larger $V(x)$ near $x = 0$ so that particles tend to keep a larger distance from each other there. An additional single-particle potential $W(x) = W(-x)$ may also be present. (a) A general smooth interaction potential. (b) A piecewise constant interaction potential, i.e., with piecewise constant value $V(0)$ inside and $V(L/2)$ outside a central region of width $2R$, as solved explicitly in Sec. IV D 4 for $L \to \infty$ and finite R.

For Luttinger liquids out of equilibrium[59–72] nonlinear dispersion effects are also essential.[73–75]

The technical hallmarks of bosonization are the following. On the one hand, a two-body density interaction term for fermions $c_{k\eta}$ becomes quadratic in terms of canonical bosons, defined for $q > 0$ as $b_{q\eta} = -\mathrm{i}\sum_k c^+_{k-q\eta} c_{k\eta}/\sqrt{n_q}$. Here the momentum sum runs over $k = \frac{2\pi}{L}(n_k - \frac{1}{2}\delta_\mathrm{b})$ with integer n_k, and the parameter $0 \leq \delta_\mathrm{b} < 2$ fixes the boundary conditions, $\psi_\eta(x + L/2) = \mathrm{e}^{i\pi\delta_\mathrm{b}}\ \psi_\eta(x - L/2)$. On the other hand the fermionic kinetic energy also translates into free bosons by means of the so-called Kronig identity,[28,76,77]

$$H^{(1)}_{0\eta} = \sum_k k\, {}^{*}_{*} c^+_{k\eta} c_{k\eta} {}^{*}_{*} \tag{2a}$$

$$= \sum_{q>0} q\, b^+_{q\eta} b_{q\eta} + \frac{\pi}{L}(\hat{N}_\eta + 1 - \delta_\mathrm{b})\hat{N}_\eta\,, \tag{2b}$$

where the fermionic number operator is given by[78] $\hat{N}_\eta = \sum_k {}^{*}_{*} c^+_{k\eta} c_{k\eta} {}^{*}_{*}$, which commutes with $b_{q\eta}$. The normal ordering ${}^{*}_{*}\cdots{}^{*}_{*}$ is defined with respect to the state $|\mathbf{0}\rangle_0$, where $|\boldsymbol{N}\rangle_0$ is an eigenstate of all $c^+_{k\eta} c_{k\eta}$ (with eigenvalue 1 if $n_k \leq N_\eta$ and 0 otherwise). Furthermore, real-space fermionic and bosonic fields are related by the celebrated bosonization identity,[7–9,17]

$$\psi_\eta(x) = \left(\tfrac{2\pi}{L}\right)^{\frac{1}{2}} F_\eta\, \mathrm{e}^{-\mathrm{i}\frac{2\pi}{L}(\hat{N}_\eta - \frac{1}{2}\delta_\mathrm{b})x}\, \mathrm{e}^{-\mathrm{i}\varphi^+_\eta(x)}\, \mathrm{e}^{-\mathrm{i}\varphi_\eta(x)}, \tag{3}$$

which allows the calculation of fermionic in terms of bosonic correlation functions.[9] Here the fermionic Klein factor F_η decreases the fermionic particle number $\hat{N}_\eta$ by one, and $\varphi_\eta(x) = -\sum_{q>0} b_{q\eta}\, \mathrm{e}^{-\mathrm{i}qx - aq}/\sqrt{n_q}$. The regularization parameter $a \to 0^+$ is needed to obtain a finite commutator,[17] $[\varphi_\eta(x), \varphi^+_\eta(x')] = -\ln\big(1 - \mathrm{e}^{-\frac{2\pi\mathrm{i}}{L}(x - x' - \mathrm{i}a)}\big)$. A final ingredient to the solution of the Tomonaga-Luttinger model is a Boguljubov transformation, which absorbs the interaction between left- and right-moving fermions into the free bosonic theory.[3]

In the present work we will study Luttinger liquids with additional spatial constraints, which we term *Luttinger droplets.* Namely, we consider a (spinless) fermionic Hamiltonian with linear dispersion, position-dependent interactions $V(x)$ and $U(x)$, and scattering potential $W(x)$ (all assumed to be real symmetric functions of x),

$$\begin{aligned} H = \int \frac{\mathrm{d}x}{L}\, {}^{*}_{*} v_\mathrm{F}[\psi^+_\mathrm{R}(x)\mathrm{i}\partial_x\psi_\mathrm{R}(x) - \psi^+_\mathrm{L}(x)\mathrm{i}\partial_x\psi_\mathrm{L}(x)] \\ + W(x)[n_\mathrm{L}(x) + n_\mathrm{R}(x)] + U(x)n_\mathrm{L}(x)n_\mathrm{R}(x) \\ + \frac{1}{2}V(x)[n_\mathrm{L}(x)^2 + n_\mathrm{R}(x)^2]{}^{*}_{*}\,, \end{aligned} \tag{4a}$$

in terms of densities $n_{\mathrm{R,L}}(x) = \psi^+_{\mathrm{R,L}}(x)\psi_{\mathrm{R,L}}(x)/(2\pi)$. Without $W(x)$ and with constant $V(x)$ and $U(x)$, H reduces to the usual translationally invariant Tomonaga-Luttinger model (with contact interactions). Below we will diagonalize (4a) exactly for the special case

$$U(x) = \gamma\,[2\pi v_\mathrm{F} + V(x)]\,, \qquad -1 < \gamma < 1\,, \tag{4b}$$

for otherwise arbitrary $V(x) > -2\pi v_\mathrm{F}$ and a constant γ. This means that real Fourier components $V_q = V_{-q}$ as well as $U_{q=0}$ can be chosen freely; then $\gamma = U_0/[2\pi v_\mathrm{F} + V_0]$ and $U_{q\neq 0} = \gamma V_q$. Thus γ characterizes the relative strength of interbranch interactions. Below we obtain the single-particle Green function for the ground state of this model, the exponents of which will reflect the spatial dependence of the couplings. We first derive generalized Kronig-type identities in Sec. II, which we then use to solve a single-flavor chiral version of (4) in Sec. III. We then proceed to the two-flavor case in Sec. IV, with a discussion of the similiarities and differences of the spectrum and Green function compared to the translationally invariant case. One representative choice of $V(x)$ to be discussed below involves a central region with stronger repulsion than at the edges of the system, as shown in Fig. 1a. An explicit evaluation is provided for a piecewise constant $V(x)$ as shown in Fig. 1b in Sec. IV D 4. Relations between the excitation velocities and Green function exponents are discussed in Sec. V, followed by a summary in Sec. VI.

Many results for inhomogeneous Luttinger liquids are of course known, e.g., with barriers,[79,80] impurities,[81,82] boundaries,[83–85] leads,[22,86] confinements[87] and so on. Models with (effective) position-dependent Luttinger liquid parameters or interaction potentials have also been investigated.[21,88–91] Our goal is to provide a complementary perspective on these setups with the exact solution of the rather flexible model (4), i.e., the Hamiltonian (4a) with parameters from the manifold (4b), and to possibly enable new applications, e.g., to ultradilute quantum droplets held together by weak cohesive forces.[92]

II. KRONIG-TYPE IDENTITIES WITH ARBITRARY MOMENTUM TRANSFER

A. Bosonic forms of bilinear fermionic terms

Consider a general bilinear fermionic term,

$$H^{(m)}_{q\eta} = \sum_k k^m\, {}^{*}_{*} c^+_{k-q\eta} c_{k\eta} {}^{*}_{*} \tag{5a}$$

$$= \int \frac{\mathrm{d}x}{2\pi}\, \mathrm{e}^{\mathrm{i}qx}\, {}^{*}_{*} \psi^+_\eta(x)(\mathrm{i}\partial_x)^m \psi_\eta(x) {}^{*}_{*}\,, \tag{5b}$$

for integer exponents $m \geq 0$ and momentum transfer $q = \frac{2\pi}{L}\, n_q$ with integer n_q; here and throughout real-space integrals without indicated endpoints extend over the interval $[-L/2, L/2]$. Arbitrary dispersion terms are included in (5a) for $q = 0$, such as (2a) for $m = 1$. Forming the product of (3) with its hermitian conjugate at different positions x and $x + \ell$, canceling the Klein factors ($F^+_\eta F_\eta = 1$), commuting the bosonic fields, taking a to zero, and combining exponentials, we obtain

$$\begin{aligned}&\frac{L}{2\pi}\,\psi^{+}_{\eta}(x)\psi_{\eta}(x+\ell) \qquad (6)\\ &= \mathrm{e}^{\pi\mathrm{i}(\delta_{\mathrm{b}}-2\hat{N}_{\eta})\ell/L}\,\mathrm{e}^{\mathrm{i}\varphi^{+}_{\eta}(x)}\,\mathrm{e}^{\mathrm{i}\varphi_{\eta}(x)}\,\mathrm{e}^{-\mathrm{i}\varphi^{+}_{\eta}(x+\ell)}\,\mathrm{e}^{-\mathrm{i}\varphi_{\eta}(x+\ell)}\\ &= \frac{\mathrm{e}^{\pi\mathrm{i}(\delta_{\mathrm{b}}-2\hat{N}_{\eta})\ell/L}}{1-\mathrm{e}^{2\pi\mathrm{i}\ell/L}}\,\mathrm{e}^{\mathrm{i}(\varphi^{+}_{\eta}(x)-\varphi^{+}_{\eta}(x+\ell))}\,\mathrm{e}^{\mathrm{i}(\varphi_{\eta}(x)-\varphi_{\eta}(x+\ell))}\,,\end{aligned}$$

A generating function of the terms in (5a) then reads

$$\begin{aligned}&\sum_{m=0}^{\infty}\frac{(-\mathrm{i}\ell)^m}{m!}\,H^{(m)}_{q\eta} = \sum_{k}\mathrm{e}^{-\mathrm{i}k\ell}\,{}^{*}_{*}c^{+}_{k-q\eta}c_{k\eta}{}^{*}_{*} \qquad (7)\\ &= \int\frac{\mathrm{d}x}{2\pi}\,\mathrm{e}^{\mathrm{i}qx}\,{}^{*}_{*}\psi^{+}_{\eta}(x)\psi_{\eta}(x+\ell)^{*}_{*} = \int\frac{\mathrm{d}x}{L}\,\frac{\mathrm{e}^{\pi\mathrm{i}\delta_{\mathrm{b}}\ell/L}\,\mathrm{e}^{\mathrm{i}qx}}{1-\mathrm{e}^{2\pi\mathrm{i}\ell/L}}\\ &\times\,\big(\mathrm{e}^{-2\pi\mathrm{i}\hat{N}_{\eta}\ell/L}\,\mathrm{e}^{\mathrm{i}\varphi^{+}_{\eta}(x)-\mathrm{i}\varphi^{+}_{\eta}(x+\ell)}\,\mathrm{e}^{\mathrm{i}\varphi_{\eta}(x)-\mathrm{i}\varphi_{\eta}(x+\ell)}-1\big)\,,\end{aligned}$$

where we summed the Taylor series of the terms (5b), inserted relation (6), and performed the normal ordering. Taylor expanding the exponentials and taking coefficients of ℓ^m on both sides of (7) now yields $H^{(m)}_{q\eta}$ in terms of bosonic operators, as discussed below. Relation (7) thus provides explicit bosonic representations of general bilinear fermionic operators, including (2).[93]

We also introduce operators which use the more convenient powers of the integer n_k instead of momentum k,

$$K_{q\eta}(\lambda) = \sum_{k}\mathrm{e}^{\lambda n_k}\,{}^{*}_{*}c^{+}_{k-q\eta}c_{k\eta}{}^{*}_{*} = \sum_{m=0}^{\infty}\frac{\lambda^m}{m!}\,K^{(m)}_{q\eta}\,, \qquad (8a)$$

$$K^{(m)}_{q\eta} = \sum_{k}n_k^{m}\,{}^{*}_{*}c^{+}_{k-q\eta}c_{k\eta}{}^{*}_{*}\,, \qquad (8b)$$

$$K^{(0)}_{q\eta} = \sum_{k}{}^{*}_{*}c^{+}_{k-q\eta}c_{k\eta}{}^{*}_{*} = \begin{cases}\hat{N}_{\eta} & \text{if}\, n_q=0,\\ \mathrm{i}\sqrt{n_q}\;\;b_{q\eta} & \text{if}\, n_q>0,\\ -\mathrm{i}\sqrt{n_{-q}}\,b^{+}_{-q\eta} & \text{if}\, n_q<0,\end{cases} \qquad (8c)$$

so that the terms (5a) are then given by $H^{(m)}_{q\eta} = (\pi/L)^m \sum_{n=0}^{m}\binom{m}{n}(-\delta_{\mathrm{b}})^{m-n}\,2^n\,K^{(n)}_{q\eta}$ and the bosonic commutation relations become $[K^{(0)}_{-q\eta}, K^{(0)}_{q'\eta'}] = -n_q\delta_{qq'}\delta_{\eta\eta'}$. The operators $K_{q\eta}(\lambda)$, which are operator-valued formal power series in the (complex) indeterminate λ with coefficients $K^{(m)}_{q\eta}$, obey the intriguing operator algebra

$$\begin{aligned}\Big[K_{-q\eta}(\lambda), K_{q'\eta'}(\lambda')\Big] &= \delta_{\eta\eta'}\Big[\delta_{qq'}\frac{\mathrm{e}^{-\lambda n_q}-\mathrm{e}^{\lambda' n_q}}{1-\mathrm{e}^{-\lambda-\lambda'}} \qquad (9)\\ &+(\mathrm{e}^{-\lambda n_{q'}}-\mathrm{e}^{\lambda' n_q})K_{q'-q\eta}(\lambda+\lambda')\Big],\end{aligned}$$

which is reminiscient of affine Lie algebras,[96] but not immediately recognizable. From (7), or alternatively from (9), the generating function (8a) becomes

$$K_{q\eta}(\lambda) = \frac{\mathrm{e}^{\lambda\hat{N}_{\eta}}Y_{q\eta}(\lambda)-\delta_{q0}}{1-\mathrm{e}^{-\lambda}}\,, \qquad (10a)$$

$$\begin{aligned}Y_{q\eta}(\lambda) &= \sum_{n,r=0}^{\infty}\frac{1}{n!r!}\sum_{\substack{p_1,\dots,p_n>0\\ p'_1,\dots,p'_r>0}}\delta_{p_1+\cdots p_n+q,p'_1+\cdots p'_r}\\ &\times\Big(\prod_{i=1}^{n}\frac{1-\mathrm{e}^{-\lambda n_{p_i}}}{n_{p_i}}K^{(0)}_{-p_i\eta}\Big)\Big(\prod_{j=1}^{r}\frac{\mathrm{e}^{\lambda n_{p'_j}}-1}{n_{p'_j}}K^{(0)}_{p'_j\eta}\Big)\\ &= \sum_{m=0}^{\infty}\frac{\lambda^m}{m!}Y^{(m)}_{q\eta}\,. \qquad (10b)\end{aligned}$$

The coefficients $K^{(m)}_{q\eta}$ and $Y^{(m)}_{q\eta}$ of λ^m in these expression are given by

$$\begin{aligned}K^{(m)}_{q\eta} &= \sum_{m=0}^{\infty}\frac{\lambda^m}{m!}\,K^{(m)}_{q\eta} = \frac{B_{m+1}(\hat{N}_{\eta}+1)-B_{m+1}(1)}{m+1}\delta_{q0}\\ &+\sum_{n=0}^{m}\binom{m}{n}\frac{(-1)^n}{m+1-n}B_n(-\hat{N}_{\eta})\,Y^{(m+1-n)}_{q\eta}\,, \qquad (11a)\end{aligned}$$

$$\begin{aligned}Y^{(m)}_{q\eta} &= \int\frac{\mathrm{d}x}{L}\,\mathrm{e}^{\mathrm{i}qx}\sum_{n=0}^{m}\binom{m}{n}\mathfrak{B}_m\big(K^{(1)}_{+,\eta}(x),...,K^{(m)}_{+,\eta}(x)\big)\\ &\times\mathfrak{B}_m\big(K^{(1)}_{-,\eta}(x),...,K^{(m)}_{-,\eta}(x)\big)\,, \qquad (11b)\end{aligned}$$

Here $K^{(m)}_{\pm,\eta}(x) = \sum_{\pm p>0}n^{m-1}_{-p}K^{(0)}_{-p\eta}\mathrm{e}^{\mathrm{i}px}$ and $B_n(x)$ and $\mathfrak{B}_m(x_1,\dots,x_m)$ are the Bernoulli and complete Bell polynomials, respectively, defined by[97]

$$\frac{\lambda\,\mathrm{e}^{\lambda x}}{\mathrm{e}^{\lambda}-1} = \sum_{m=0}^{\infty}\frac{\lambda^m}{m!}B_m(x)\,, \qquad (12a)$$

$$\exp\Big(\sum_{m=1}^{\infty}\frac{\lambda^m}{m!}\,x_m\Big) = \sum_{m=0}^{\infty}\frac{\lambda^m}{m!}\mathfrak{B}_m(x_1,\dots,x_m)\,. \qquad (12b)$$

A detailed derivation of (10)-(11) will be presented elsewhere.

B. Bosonic representation of a fermionic scattering term

Generalized Kronig identities for arbitrary order m follow from the equivalence of (8b) and (11a), with the latter involving only fermionic number operators and normal-ordered bosonic operators. As a special case, we obtain for $m=1$ and $q\neq 0$ the finite-q generalization of (2),

$$\begin{aligned}K^{(1)}_{q\eta} &= \sum_{k}n_k\,{}^{*}_{*}c^{+}_{k-q\eta}c_{k\eta}{}^{*}_{*}\\ &= \Big(\frac{n_q+1}{2}+\hat{N}_{\eta}\Big)K^{(0)}_{q\eta}+\frac{1}{2}\sum_{p(\neq 0,q)}K^{(0)}_{q-p\eta}K^{(0)}_{p\eta}\,, \qquad (13)\end{aligned}$$

which can also be expressed as

$$H^{(1)}_{q\eta} = \sum_k k\,{}^{*}_{*}c^{+}_{k-q\eta}c_{k\eta}{}^{*}_{*} = \frac{2\pi}{L}K^{(1)}_{q\eta} - \frac{\pi\delta_{\mathrm{b}}}{L}\hat{N}_\eta \tag{14a}$$

$$\begin{aligned} &= \Big(\frac{q}{2} + \frac{\pi}{L}(2\hat{N}_\eta + 1 - \delta_{\mathrm{b}})\Big)\,\mathrm{i}\sqrt{n_q}\,b_{q\eta} \\ &\quad - \frac{1}{2}\sum_{q>p>0}\sqrt{(q-p)p}\,b_{q-p\eta}b_{p\eta} \\ &\quad + \sum_{p>0}\sqrt{p(q+p)}\,b^{+}_{p\eta}b_{q+p\eta}\,, \qquad (q>0) \end{aligned} \tag{14b}$$

so as to make the modification of the momentum-diagonal identity (2) more apparent.

III. CHIRAL LUTTINGER DROPLETS

A. Droplet model with only right movers

As a simple application of (14) and for later reference we first consider a single species of spinless fermions with density

$$n(x) = \frac{1}{2\pi}\,\psi^{+}(x)\psi(x) = \frac{1}{L}\sum_q K^{(0)}_q e^{-iqx}\,, \tag{15}$$

subjected to a single-particle potential $w(x) = w(-x)$ and a position-dependent interaction $g(x) = g(-x)$, with Fourier transforms $w_q = \int w(x)\,\mathrm{e}^{-\mathrm{i}qx}\mathrm{d}x/L = w_{-q}$ and so on. For simplicity we choose antiperiodic boundary conditions ($\delta_{\mathrm{b}} = 1$). For a linear dispersion the Hamiltonian of such a 'chiral Luttinger droplet' is given by

$$\begin{aligned} H_{\mathrm{chiral}} &= v_{\mathrm{F}}\sum_k k\,{}^{*}_{*}c^{+}_{k}c_{k}{}^{*}_{*} + \int\frac{\mathrm{d}x}{L}\,w(x)\,{}^{*}_{*}n(x)^{*}_{*} \\ &\quad + \frac{1}{2}\int\frac{\mathrm{d}x}{L}\,g(x)\,{}^{*}_{*}n(x)^{2}{}^{*}_{*}\,. \end{aligned} \tag{16}$$

B. Diagonalization of the chiral model

On the one hand, we can now express the fermionic Hamiltonian H_{chiral} in terms of bosonic operators. We define

$$\begin{aligned} H^{\mathrm{bosonic}}_{[\tilde{\boldsymbol{g}},\hat{\tilde{\boldsymbol{w}}};\boldsymbol{K}]} &= \frac{\tilde{g}_0}{L}\sum_{q>0}K^{(0)}_{-q}K^{(0)}_{q} \\ &\quad + \frac{1}{L}\sum_{q\neq 0}\Bigg[\hat{\tilde{w}}_q K^{(0)}_q + \frac{\tilde{g}_q}{2}\sum_{p(\neq 0,q)}K^{(0)}_p K^{(0)}_{q-p}\Bigg]\,, \end{aligned} \tag{17}$$

with symmetric parameters $\hat{\tilde{w}}_q$ (that may contain $\hat{N}$) and $\tilde{g}_q$. For $\tilde{g}_q = 2\pi v_{\mathrm{F}}\delta_{q0} + g_q$ and $\hat{\tilde{w}}_q = w_q L + g_q\hat{N}$ we find that

$$H_{\mathrm{chiral}} = H^{\mathrm{bosonic}}_{[\tilde{\boldsymbol{g}},\hat{\tilde{\boldsymbol{w}}};\boldsymbol{K}]} + \frac{\tilde{g}_0}{2L}\hat{N}^2 + w_0\hat{N}\,. \tag{18}$$

On the other hand, the fermionic basis permits a full diagonalization as follows. Using (13) to eliminate the last term in (17) we arrive at a fermionic scattering Hamiltonian,

$$\begin{aligned} H_{\mathrm{chiral}} &= \sum_{kk'}T_{kk'}\,{}^{*}_{*}c^{+}_{k}c_{k'}{}^{*}_{*}\,, \\ T_{kk'} &= v_{\mathrm{F}}k\,\delta_{kk'} + w_{k'-k} + (k+k')\frac{g_{k'-k}}{4\pi}\,. \end{aligned} \tag{19}$$

We conclude that the four-fermion interaction terms in (16) cancel, as they do in the Kronig identity (2). In terms of field operators we obtain

$$H_{\mathrm{chiral}} = \int\mathrm{d}x\,{}^{*}_{*}\frac{\psi^{+}(x)h(x)\psi(x)}{2\pi}{}^{*}_{*}\,, \tag{20a}$$

$$h(x) = \tilde{g}(x)(-\mathrm{i}s\partial_x) - \frac{1}{2}\mathrm{i}s\tilde{g}'(x) + w(x)\,, \tag{20b}$$

where $\tilde{g}(x) = 2\pi v_{\mathrm{F}} + g(x)$ as above, and $s = -1/(2\pi)$.

Next we use the spectrum of the first-quantized Hamiltonian in (20b), $h = s[\tilde{g}(X)P + P\tilde{g}(X)]/2 + w(X)$ with $[X,P] = \mathrm{i}$. The eigenvalue equation $h(x)\xi_k(x) = E_k\xi_k(x)$ is separable because h is linear in P. For a constant real scale s and real functions $\tilde{g}(x)$, $w(x)$ on an interval $[x_1,x_2]$ with $\tilde{g}(x) > 0$ and $\tilde{g}(x_1) = \tilde{g}(x_2)$, and demanding $\xi_k(x_2) = \xi_k(x_1)\mathrm{e}^{\pi\mathrm{i}\delta_{\mathrm{b}}}$, we find $E_k = (S_1 - sLk)/S_0$, $\xi_k(x) = [\tilde{g}(x)S_0]^{-\frac{1}{2}}\exp(\mathrm{i}[s_0(x,0)E_k - s_1(x,0)]/s)$, where the momentum k takes on the same discrete values k_n as before. Here $S_j = s_j(x_2,x_1)$ with $s_j(x,x') = \int_{x'}^{x}\mathrm{d}y\,(\delta_{j0} + \delta_{j1}w(y))/\tilde{g}(y)$. These eigenstates correspond to plane waves subject to a local scale transformation induced by the interaction potential, reminiscient of eikonal wave equations or semiclassical Schrödinger equations. We note the eigenstate expectation values $\langle w(X)\rangle = S_1/S_0 = E_k - s\langle P\rangle$.

Setting $x_1 = -x_2 = L/2$ and $\delta_{\mathrm{b}} = 1$ and requiring $g_{q=0} > -2\pi v_{\mathrm{F}}$, we thus diagonalize (16), (19), (20) in terms of new canonical fermions, $\{\Xi_k, \Xi^{+}_{k'}\} = \delta_{kk'}$, as

$$\begin{aligned} H_{\mathrm{chiral}} &= \sum_k E_k\,{}^{*}_{*}\Xi^{+}_{k}\Xi_{k}{}^{*}_{*} \equiv H^{\mathrm{diagonal}}_{[\tilde{\boldsymbol{g}},\boldsymbol{w};\boldsymbol{\Xi}]}\,, \\ E_k &= \tilde{v}(k-\tilde{k})\,, \quad \hat{N} = \sum_k {}^{*}_{*}\Xi^{+}_{k}\Xi_{k}{}^{*}_{*} = \sum_k {}^{*}_{*}c^{+}_{k}c_{k}{}^{*}_{*}\,, \\ \Xi_k &= \int\frac{\mathrm{d}x}{\sqrt{2\pi}}\,\xi_k(x)\,\psi(x)\,, \quad \tilde{k} = -\int\frac{\mathrm{d}x}{L}\,\frac{2\pi w(x)}{\tilde{g}(x)}\,, \\ \xi_k(x) &= \frac{\sqrt{2\pi\tilde{v}}\;\mathrm{e}^{-\mathrm{i}[\tilde{r}_0(x)k - \tilde{r}_1(x)]}}{\sqrt{L\,\tilde{g}(x)}}\,,\ \tilde{r}_0(x) = \int_0^x\mathrm{d}y\,\frac{2\pi\tilde{v}}{\tilde{g}(y)}\,, \\ \tilde{r}_1(x) &= \tilde{k}\,\tilde{r}_0(x) + \int_0^x\mathrm{d}y\,\frac{2\pi w(y)}{\tilde{g}(y)},\ \tilde{v} = \left[\int\frac{\mathrm{d}x}{L}\,\frac{2\pi}{\tilde{g}(x)}\right]^{-1}. \end{aligned} \tag{21}$$

Note that the renormalized dressed Fermi velocity $\tilde{v}$ is given by the spatial harmonic average of the renormalized 'local' Fermi velocity $v_{\mathrm{F}} + g(x)/(2\pi) = \tilde{g}(x)/(2\pi)$.

C. Green function for the chiral model

From the above solution it is straightforward to obtain the time-ordered Green function for the Heisenberg operators of the chiral field,

$$
\begin{aligned}
G(x,x';t) &= \theta(t)G^{>}(x,x';t) - \theta(-t)G^{<}(x,x';t)\,, && (22)\\
G^{\gtrless}(x,x';t) &= \begin{cases} -\mathrm{i}\langle\psi(x,t)\,\psi^{+}(x',0)\rangle\,, \\ -\mathrm{i}\langle\psi^{+}(x',0)\,\psi(x,t)\rangle\,, \end{cases} && (23)
\end{aligned}
$$

with $\theta(\pm t) = (1 \pm \mathrm{sgn}(t))/2$. At zero temperature in a state with fixed particle number N we find

$$
\begin{aligned}
\mathrm{i}G(x,x';t) &= \frac{\tilde{v}}{\sqrt{\tilde{g}(x)\tilde{g}(x')}}\,\frac{\mathrm{e}^{\mathrm{i}S(x,x',t)}}{\frac{L}{\pi}\sinh\frac{\pi}{L}(\mathrm{i}R(x,x',t) + a\,\mathrm{sgn}\,t)}\,,\\
R(x,x',t) &= \tilde{r}_0(x) - \tilde{r}_0(x') - \tilde{v}t\,, && (24)\\
S(x,x',t) &= \tilde{r}_1(x) - \tilde{r}_1(x') + \tilde{v}\tilde{k}t - \frac{2\pi N}{L}R(x,x',t)\,,
\end{aligned}
$$

where $a \to 0^+$ stems from a convergence factor that was included in the momentum sum. For constant $g(x)$ and $w(x)$ we recover the translationally invariant case, $G(x,x';t) \propto 1/(x - x' + \tilde{v}t + a\,\mathrm{sgn}\,t)$, with renormalized Fermi velocity. Position-dependent couplings, on the other hand, may lead to a substantial redistribution of spectral weight. The critical behavior however remains unaffected, in the sense that the exponent of the denominator involving $R(x,x',t)$ remains unity for the chiral model.

IV. LUTTINGER DROPLETS

A. Droplet model with with right and left movers

We now study a generalization of the two-flavor Tomonaga-Luttinger model to position-dependent interactions and scattering potentials. Such a 'Luttinger droplet' involves right- and left-moving fermions, $\psi_{\mathrm{R}}(x) = \psi_1(-x)$ and $\psi_{\mathrm{L}}(x) = \psi_2(x)$ (see introduction) with linear dispersion in opposite directions, subject to the one-particle potential $W(x)$, as well as intrabranch and interbranch density interactions $V(x)$ and $U(x)$, respectively, as given in (4). In terms of fermions with flavor $\eta = 1, 2$ we have

$$
\begin{aligned}
H = {}^{*}_{*}\sum_{\eta}\Bigg[v_{\mathrm{F}}\sum_{k} k\,c^{+}_{k\eta}c_{k\eta} + \int\frac{\mathrm{d}x}{L}\,W(x)n_{\eta}(x)\\
+ \frac{1}{2}V(x)n_{\eta}(x)^2\Bigg] + \int\frac{\mathrm{d}x}{L}\,U(x)n_1(-x)n_2(x)^{*}_{*}\,, \quad (25)
\end{aligned}
$$

i.e., compared to (16) the couplings $g(x)$ and $w(x)$ were relabeled as $V(x)$ and $W(x)$, indices η were put on operators, and the interaction term with $U(x)$ was included.

B. Diagonalization of the Luttinger droplet model

1. Bosonic form of the Hamiltonian

Rewritten with bosonic operators this becomes

$$
\begin{aligned}
H &= H_{\mathrm{TL}} + H' + H''\,, && (26)\\
H_{\mathrm{TL}} &= \sum_{\eta}\left[\frac{2\pi v_{\mathrm{F}} + V_0}{L}\left(\frac{\hat{N}_{\eta}^2}{2} + \sum_{q>0} K^{(0)}_{-q\eta}K^{(0)}_{q\eta}\right)\right]\\
&\quad + \frac{U_0}{L}\left[\hat{N}_1\hat{N}_2 + \sum_{q>0}\left(K^{(0)}_{-q1}K^{(0)}_{-q2} + K^{(0)}_{q1}K^{(0)}_{q2}\right)\right],\\
H' &= \sum_{\eta}\left[W_0\hat{N}_{\eta} + \sum_{q\neq 0}\left(W_q + \frac{V_q}{L}\hat{N}_{\eta} + \frac{U_q}{2L}\hat{N}_{\bar{\eta}}\right)K^{(0)}_{q\eta}\right],\\
H'' &= \sum_{\eta}\sum_{q\neq 0}\sum_{p(\neq 0,q)} K^{(0)}_{p\eta}\left[\frac{V_q}{2L}K^{(0)}_{q-p\eta} + \frac{U_q}{2L}K^{(0)}_{p-q\bar{\eta}}\right].
\end{aligned}
$$

H contains a standard (i.e., translationally invariant) Tomonaga-Luttinger model H_{TL} involving only the zero-momentum (space-averaged) couplings, which by itself can be diagonalized by a Bogoljubov transformation. For position-dependent couplings, on the other hand, also H' (linear in bosons) and H'' (quadratic in bosons with momentum transfer) are present.

2. Specialization to common spatial dependence

For simplicity we set from now on

$$
\begin{pmatrix} V(x)\\ U(x)\end{pmatrix} = \begin{pmatrix} V_0\\ U_0\end{pmatrix} + \begin{pmatrix} V\\ U\end{pmatrix}\sum_{q\neq 0} f_q\cos(qx)\,, \qquad (27)
$$

with constant prefactors V and U and $f_q = V_q/V = U_q/U = f_{-q}$ for $q \neq 0$. We can then simplify the momentum-offdiagonal term H'' by a Bogoljubov transformation to $K^{(0)}_{q\sigma}$ (for $q \neq 0$, $\sigma = -\bar{\sigma} = \pm$, letting $\eta_\sigma = (3-\sigma)/2$, $\sigma_\eta = 3 - 2\eta$ for $\eta = 3 - \bar{\eta} = 1, 2$),

$$
\begin{aligned}
K^{(0)}_{q\sigma} &= u\,K^{(0)}_{q\eta_\sigma} + v\,K^{(0)}_{-q\bar{\eta}_\sigma}\,, && (28a)\\
K^{(0)}_{q\eta} &= u\,K^{(0)}_{q\sigma_\eta} - v\,K^{(0)}_{-q\bar{\sigma}_\eta}\,, && (28b)
\end{aligned}
$$

$u = \cosh\theta$, $v = \sinh\theta$, which preserves the bosonic algebra, $[K^{(0)}_{-q\sigma}, K^{(0)}_{q'\sigma'}] = -n_q\delta_{qq'}\delta_{\sigma\sigma'}$. The choice $U/V = \tanh 2\theta$, assuming $|U| < V$, yields

$$
\begin{aligned}
H &= \sum_{\sigma=\pm}\left(H^{(0)}_{\sigma} + H^{(1)}_{\sigma}\right) + H^{(2)} + \hat{H}_{\mathrm{N}} + E_0\,, && (29)\\
H^{(0)}_{\sigma} &= \frac{\bar{V}}{L}\sum_{q>0} K^{(0)}_{-q\sigma}K^{(0)}_{q\sigma} + \sum_{q\neq 0}\frac{\bar{U}f_q}{2L}\sum_{p(\neq 0,q)} K^{(0)}_{p\sigma}K^{(0)}_{q-p\sigma}\,,\\
H^{(1)}_{\sigma} &= \frac{1}{L}\sum_{q\neq 0}\hat{\bar{w}}_{q\sigma}K^{(0)}_{q\sigma}\,, \qquad H^{(2)} = \frac{\bar{V}'}{L}\sum_{q\neq 0} K^{(0)}_{q+}K^{(0)}_{q-}\,,\\
\hat{H}_{\mathrm{N}} &= \frac{2\pi v_{\mathrm{F}} + V_0}{2L}\sum_{\eta}\hat{N}_{\eta}^2 + \frac{U_0}{L}\hat{N}_1\hat{N}_2 + W_0\sum_{\eta}\hat{N}_{\eta} && (30)
\end{aligned}
$$

where E_0 is a constant energy shift, omitted from now on, which diverges due to the contact interactions in H. Here and below we use the following abbreviations and relations,

$$\begin{aligned}
\bar{V} &= \frac{(2\pi v_{\mathrm{F}} + V_0)V - U_0 U}{\bar{U}}\,, \quad \bar{U} = \bar{\gamma} V, && (31)\\
\bar{V}' &= \frac{U_0 V - (2\pi v_{\mathrm{F}} + V_0)U}{\bar{U}}\,,\\
\hat{\bar{w}}_{q\sigma} &= L W_q \mathrm{e}^{-\theta} + \bar{\gamma}\, V_q \big[u^3 \hat{N}_1 \delta_{\sigma +} - v^3 \hat{N}_2 \delta_{\sigma -}\big], \ (q \neq 0)\\
\gamma &= \frac{U}{V} = \tanh 2\theta\,, \ \bar{\gamma} = \sqrt{1-\gamma^2} = \mathrm{sech} 2\theta\,,\\
\gamma_3 &= u^3 - v^3 = (1 + \tfrac{1}{2}\gamma)(1-\gamma)^{-\frac{1}{4}}(1+\gamma)^{-\frac{3}{4}}\,,\\
\mathrm{e}^{-\theta} &= (V-U)^{\frac{1}{4}}(V+U)^{-\frac{1}{4}} = (1-\gamma)^{\frac{1}{4}}(1+\gamma)^{-\frac{1}{4}}\,,\\
2v^2 &= 2\sinh^2\theta = (1-\gamma^2)^{-\frac{1}{2}} - 1\,.
\end{aligned}$$

The Hamiltonian H has thus become diagonal in the new flavors σ except for the term $H^{(2)}$ in (29).

3. *Specialization to interrelated interaction strengths*

For simplicity we now assume that $\bar{V}' = 0$, i.e., that the bare Fermi velocity v_{F} and the strengths of the position-averaged (V_0 and U_0) and position-dependent interactions (V and U) combine so that $H^{(2)}$ is absent. This corresponds to the special case

$$\gamma = \frac{U}{V} = \frac{U_0}{2\pi v_{\mathrm{F}} + V_0}\,, \qquad (32)$$

which together with (27) is equivalent to (4b). From now on we will thus consider $v_{\mathrm{F}}, V_q, \gamma$ to be chosen freely (with $V_0 > -2\pi v_{\mathrm{F}}$), with the other parameters in H then being given by

$$\begin{aligned}
U_q &= \gamma\,(2\pi v_{\mathrm{F}} \delta_{q0} + V_q)\,, && (33\mathrm{a})\\
\bar{V} &= \bar{\gamma}\,(2\pi v_{\mathrm{F}} + V_0)\,,\ \bar{U} = \bar{\gamma} V\,,\ \bar{V}' = 0\,, && (33\mathrm{b})
\end{aligned}$$

i.e., $\bar{U} f_q = \bar{\gamma} V_q$ for $q \neq 0$. Then for $\sigma = \pm 1$ each decoupled Hamiltonian has precisely the form of the bosonic Hamiltonian (17) encountered in the chiral model,

$$\begin{aligned}
H &= \hat{H}_{\mathrm{N}} + \sum_{\sigma=\pm} H_\sigma\,, && (34)\\
H_\sigma &= H_\sigma^{(0)} + H_\sigma^{(1)} = H^{\mathrm{bosonic}}_{[\bar{\boldsymbol{g}}, \hat{\bar{\boldsymbol{w}}}_\sigma; \boldsymbol{K}_\sigma]}\,,
\end{aligned}$$

with effective interaction $\bar{g}_q = \bar{V}\delta_{q0} + (1-\delta_{q0})\bar{U} f_q$, i.e.,

$$\begin{aligned}
&\bar{g}_q = \bar{\gamma}\,[2\pi v_{\mathrm{F}} \delta_{q0} + V_q]\,,\ \ \bar{g}(x) = \bar{\gamma}\,[2\pi v_{\mathrm{F}} + V(x)]\,, && (35\mathrm{a})\\
&\bar{v} = \left[\int \frac{\mathrm{d}x}{L}\, \frac{2\pi}{\bar{g}(x)}\right]^{-1}, \ \ \bar{W} = \int \frac{\mathrm{d}x\, 2\pi\bar{v}}{L}\, \frac{W(x)}{\bar{g}(x)}\,, && (35\mathrm{b})
\end{aligned}$$

where we also introduced the renormalized Fermi velocity $\bar{v}$ and averaged one-particle potential $\bar{W}$ which will emerge below.

4. *Refermionization as separately diagonalizable chiral models*

We thus refermionize each H_σ, first in terms of new fermions $\psi_\sigma(x)$, with bosonic fields $\phi_\sigma(x) = \varphi_\sigma^+(x) + \varphi_\sigma(x)$ built from the $K_{q\sigma}^{(0)}$ analogously to (3),

$$\begin{aligned}
\psi_\sigma(x) &= \sqrt{\frac{2\pi}{L}}\, \sum_k \mathrm{e}^{-\mathrm{i}kx} c_{k\sigma}\\
&= \frac{F_\sigma}{\sqrt{a}}\, \mathrm{e}^{-\mathrm{i}\frac{2\pi}{L}(\hat{N}_\sigma - \frac{1}{2})x}\, \mathrm{e}^{-\mathrm{i}\phi_\sigma(x)}\,. && (36)
\end{aligned}$$

Below we will fix the connection between the fermionic number operators $\hat{N}_\sigma$ and their associated Klein factors F_σ to the original fermions $c_{k\eta}$, which is not determined by the purely bosonic Bogoljubov transformation (28).

Next each chiral-type Hamiltonian H_σ is diagonalized with fermions $\Xi_{k\sigma}$ according to (21),

$$\begin{aligned}
H_\sigma &= H^{\mathrm{bosonic}}_{[\bar{\boldsymbol{g}}, \hat{\bar{\boldsymbol{w}}}_\sigma; \boldsymbol{K}_\sigma]} = H^{\mathrm{diagonal}}_{[\bar{\boldsymbol{g}}, \hat{\bar{\boldsymbol{w}}}_\sigma; \boldsymbol{\Xi}_\sigma]} - \frac{\bar{g}_0}{2L}\hat{N}_\sigma^2\,, && (37)\\
H^{\mathrm{diagonal}}_{[\bar{\boldsymbol{g}}, \hat{\bar{\boldsymbol{w}}}_\sigma; \boldsymbol{\Xi}_\sigma]} &= \bar{v} \sum_k (k - \hat{\bar{k}}_\sigma) {}^*_* \Xi^+_{k\sigma} \Xi_{k\sigma} {}^*_*\,.
\end{aligned}$$

with the two types of fermions ψ_σ and Ξ_σ related by

$$\begin{aligned}
\Xi_{k\sigma} &= \int \frac{\mathrm{d}x}{\sqrt{2\pi}}\, \xi_{k\sigma}(x)\, \psi_\sigma(x)\,, && (38\mathrm{a})\\
\hat{N}_\sigma &= \sum_k {}^*_* \Xi^+_{k\sigma} \Xi_{k\sigma} {}^*_* = \sum_k {}^*_* c^+_{k\sigma} c_{k\sigma} {}^*_*\,, && (38\mathrm{b})
\end{aligned}$$

in terms of the following functions and parameters

$$\begin{aligned}
\xi_{k\sigma}(x) &= \frac{\sqrt{2\pi\bar{v}}\ \mathrm{e}^{-\mathrm{i}[r_0(x)k - \hat{r}_{1\sigma}(x)]}}{\sqrt{L\,\bar{g}(x)}}\,, && (39\mathrm{a})\\
r_0(x) &= \int_0^x \mathrm{d}y\, \frac{2\pi\bar{v}}{\bar{g}(y)} = -r_0(-x)\,, && (39\mathrm{b})\\
\hat{r}_{1\sigma}(x) &= \hat{\bar{k}}_\sigma\, r_0(x) + \int_0^x \mathrm{d}y\, \frac{2\pi \hat{\bar{w}}_\sigma(y)}{\bar{g}(y)}\,, && (39\mathrm{c})\\
\hat{\bar{k}}_\sigma &= -\int \frac{\mathrm{d}x}{L}\, \frac{2\pi}{\bar{g}(x)} \sum_{q\neq 0} \frac{\hat{\bar{w}}_{q\sigma}}{L} \mathrm{e}^{-\mathrm{i}qx}\,. && (39\mathrm{d})
\end{aligned}$$

5. *Rebosonization into canonical form with quadratic number operator terms*

Due to the linear dispersion we can rebosonize the $\Xi_{k\sigma}$ in terms of new canonical bosons $B_{q\sigma}$, which will also be needed for the calculation of Green functions below. The corresponding (re-)bosonization identity reads

$$\Xi_\sigma(x) = \frac{\mathcal{F}_\sigma}{\sqrt{a}} \mathrm{e}^{-\frac{2\pi\mathrm{i}}{L}(\hat{N}_\sigma - \frac{1}{2})x + \sum_{q>0} \frac{\mathrm{i}\mathrm{e}^{-a|q|}}{\sqrt{nq}}[B_{q\sigma}\mathrm{e}^{-\mathrm{i}qx} + B^+_{q\sigma}\mathrm{e}^{\mathrm{i}qx}]}\,, \qquad (40)$$

where $\mathcal{F}_\sigma$ is another Klein factor which lowers $\hat{N}_\sigma$ by one. We note that once we fix F_σ, then $\mathcal{F}_\sigma$ is determined by (36), (38a), (40), although its explicit form is not needed in the following. The transformation (40) yields

$$H = H_\Xi + H_\mathrm{N} - \sum_\sigma \left(\frac{\bar{g}_0}{2L} \hat{N}_\sigma^2 + \bar{v}\bar{k}_\sigma \hat{N}_\sigma \right), \tag{41}$$

$$H_\Xi = \sum_{\sigma;k} \bar{v}k \,{}^*_*\Xi^+_{k\sigma}\Xi_{k\sigma}{}^*_* = \sum_{\sigma;q>0} \bar{v}qB^+_{q\sigma}B_{q\sigma} + \frac{\pi}{2L}\sum_\sigma \hat{N}_\sigma^2,$$

We observe that even for position-dependent interactions, collective bosonic excitations with linear dispersion emerge.

To complete the diagonalization of H in (41), we must still define the new number operators $\hat{N}_\sigma$ (with integer eigenvalues) and Klein factors F_σ in terms of the original $\hat{N}_\eta$ and F_η (which also appear in H_N). We set

$$\hat{N}_\sigma = \hat{N}_1\delta_{\sigma-} + \hat{N}_2\delta_{\sigma+} \,, \tag{42}$$

which ensures that the ground state (without bosonic excitations $B^+_{q\sigma}$) remains in a sector with finite $\hat{N}_1 = \hat{N}_2$, because then only the density terms ($\hat{N}_1^2 + \hat{N}_2^2$) and $\hat{N}_1\hat{N}_2$ appear in the Hamiltonian. We note that no other form of $\hat{N}_\sigma$ that is linear in $\hat{N}_1$ and $\hat{N}_2$ has this feature The corresponding Klein factors are then given by

$$F_\sigma = F_1\delta_{\sigma-} + F_2\delta_{\sigma+} \,. \tag{43}$$

Collecting terms, the diagonalization of the Luttinger droplet Hamiltonian (4) is then finally complete,

$$H = \sum_{\sigma;q>0} \bar{v}qB^+_{q\sigma}B_{q\sigma} + \frac{\pi}{2L}\left[v_\mathcal{N}\hat{\mathcal{N}}^2 + v_\mathcal{J}\hat{\mathcal{J}}^2\right] + \epsilon\hat{\mathcal{N}}, \tag{44}$$

$$\hat{\mathcal{N}} = \hat{N}_1 + \hat{N}_2 \,, \quad \hat{\mathcal{J}} = \hat{N}_1 - \hat{N}_2 \,,$$

in which the following parameters appear,

$$\begin{aligned} v_\mathcal{N} &= v_1 + v_2 \,, & v_\mathcal{J} &= v_1 - v_2 \,, \\ v_1 &= \tilde{v}_\mathrm{F} + \Delta v \,, & \tilde{v}_\mathrm{F} &= v_\mathrm{F} + \tfrac{1}{2\pi}V_0 \,, \\ v_2 &= \gamma\tilde{v}_\mathrm{F} + \gamma_3\Delta v \,, & \Delta v &= \bar{v} - \bar{\gamma}\tilde{v}_\mathrm{F} \,, \\ \epsilon &= \bar{W}\mathrm{e}^{-\theta} + W_0(1 - \mathrm{e}^{-\theta}) \,, \end{aligned} \tag{45}$$

and $\bar{v}$ and $\bar{W}$ were defined in (35b). Here the total and relative fermionic number operators, $\hat{\mathcal{N}}$ and $\hat{\mathcal{J}}$, take on integer values and commute with the two flavors of bosonic operators. We note the ground-state value of $\hat{\mathcal{N}}$ may shift due to the one-particle potential $W(x)$ according to the value ϵ, which also depends on the interaction via $\bar{W}$.

We consider (44) to be the canonical form of the diagonalized Luttinger droplet Hamiltonian, as it is essentially the same as that of the bosonized translationally invariant Tomonaga-Luttinger model. Namely, both are characterized by the renormalized Fermi velocity $\bar{v}$ for collective bosonic particle-hole excitations with linear dispersion, as well as $v_{\mathcal{N},\mathcal{J}}$ for total and relative particle number changes. For the Luttinger droplet, however, spatial dependencies enter into the diagonalization and lead to qualitatively different behavior for the fermionic degrees of freedom, as discussed below.

C. Spectrum of the Luttinger droplet model

1. *Recovery of the translationally invariant case*

For position-independent potentials, the translationally invariant case is fully recovered by setting $f_{q\neq 0} = 0$, so that $\bar{v} = \bar{\gamma}\tilde{v}_\mathrm{F}$ and $\Delta v = 0$. We thus find that

$$W(x) = W_0 \,, \; V(x) = V_0 \,, \; U(x) = U_0$$

$$\Rightarrow \;\; H = H_\mathrm{TL} + W_0\hat{\mathcal{N}} \,, \; \gamma = \frac{U_0}{2\pi v_\mathrm{F} + V_0} \,, \tag{46a}$$

$$\begin{aligned} v_{\mathcal{N},\mathcal{J}} &= v_\mathrm{F} + \frac{V_0 \pm U_0}{2\pi} \\ &= \bar{v}\left[\frac{1+\gamma}{1-\gamma}\right]^{\pm\frac{1}{2}} \,, \end{aligned} \tag{46b}$$

$$\begin{aligned} \bar{v} &= \sqrt{\left(v_\mathrm{F} + \frac{V_0}{2\pi}\right)^2 - \left(\frac{U_0}{2\pi}\right)^2} \\ &= \bar{\gamma}\left(v_\mathrm{F} + \frac{V_0}{2\pi}\right) = \bar{\gamma}\tilde{v}_\mathrm{F} \,, \end{aligned} \tag{46c}$$

i.e., the parameter γ of (32) only relates v_F, V_0, U_0 to one another, as the interactions V and U are absent for the translationally invariant case. As before, γ characterizes the relative strength of (translationally invariant) interbranch interactions. It is one of the characteristic properties of a Luttinger liquid[13] that the relations

$$\bar{v} = \sqrt{v_\mathcal{N}v_\mathcal{J}} \,, \qquad \gamma = \frac{v_\mathcal{N} - v_\mathcal{J}}{v_\mathcal{N} + v_\mathcal{J}} \,, \tag{47}$$

remain valid even if the dispersion in H_TL is weakly nonlinear. This connects the excitation velocities $\bar{v}$, $v_\mathcal{N}$, $v_\mathcal{J}$ as well as the power-law exponents in the single-particle Green function, which contain the parameter γ, as discussed below.

2. *Excitation velocities for position-dependent interactions*

By contrast, for the Luttinger droplet (4) with position-dependent interactions, the renormalized Fermi velocity $\bar{v}$ depends on $V(x)$ according to (35b), so that $\bar{v}$ can be varied independently from the average interaction potential V_0. Namely if $\bar{v} \neq \bar{\gamma}\tilde{v}_\mathrm{F}$ in (45), i.e., if

$$\int \frac{\mathrm{d}x}{2\pi v_\mathrm{F} + V(x)} \neq \int \frac{\mathrm{d}x}{2\pi v_\mathrm{F} + V_0} \,, \tag{48}$$

the three velocities $\bar{v}$, $v_\mathcal{N}$, $v_\mathcal{J}$ are independent of each other (but together determine γ).

In the following, however, we will adopt a different perspective. We regard γ as given by the interactions as in (4b),

$$\gamma = \frac{U_0}{2\pi v_\mathrm{F} + V_0} = \frac{U(x)}{2\pi v_\mathrm{F} + V(x)} \,. \tag{49}$$

Then it follows from (45) that the velocities are related by

$$\bar{v} = \frac{\gamma - \bar{\gamma}\gamma_3 - (1-\bar{\gamma})}{2(\gamma - \gamma_3)} v_{\mathcal{N}} + \frac{\gamma - \bar{\gamma}\gamma_3 + (1-\bar{\gamma})}{2(\gamma - \gamma_3)} v_{\mathcal{J}} \,, \tag{50a}$$

$$\tilde{v}_{\mathrm{F}} = \frac{1-\gamma_3}{2(\gamma-\gamma_3)} v_{\mathcal{N}} - \frac{1+\gamma_3}{2(\gamma - \gamma_3)} v_{\mathcal{J}} \,, \tag{50b}$$

which replaces (47).

Hence we may already conclude that the Luttinger droplet (4) is strictly speaking *not* a Luttinger liquid, in the sense that $\bar{v} \neq \sqrt{v_{\mathcal{N}} v_{\mathcal{J}}}$ if (48) holds, so that the Luttinger liquid relation (47) is violated and the linear relations (50) between the velocities $\bar{v}$, $v_{\mathcal{N}}$, $v_{\mathcal{J}}$, $\tilde{v}_{\mathrm{F}}$ hold instead.

Note also that while the canonical form of the Hamiltonian (44) and its eigenvalues are very similar to the translationally invariant case, their relation to the original fermions is more complex since it was obtained from a position-dependent canonical transformation. As a result, the position dependence of the interaction appears in the Green function, which we calculate next.

D. Green function for Luttinger droplet model

1. Rebosonization route to the Green function

As in the translationally invariant case, the Green function is obtained from the bosonization identity (3) and the Bogoljubov transformation (28), but also makes use of the refermionization (36) and the rebosonization (40). Using $\phi_\eta(x) = \varphi^+_\eta(x) + \varphi_\eta(x) = u\phi_{\sigma_\eta}(x) + \phi_{\bar{\sigma}_\eta}(-x)$, we have

$$\psi_\eta(x) = \frac{1}{\sqrt{a}} F_\eta \, \mathrm{e}^{-\mathrm{i}\frac{2\pi}{L}(\hat{N}_\eta - \frac{1}{2})x} \, \mathrm{e}^{-\mathrm{i}[u\phi_{\sigma_\eta}(x) + v\phi_{\bar{\sigma}_\eta}(-x)]} \,. \tag{51}$$

To evaluate correlation functions of this field, we need to express it in the diagonalizing fermionic basis (38a). We define the auxiliary functions

$$\begin{aligned}
\lambda_q(x) &= \mathrm{i}\frac{\mathrm{e}^{-\mathrm{i}qx - a|q|/2}}{n_q} \,, \quad \tilde{\lambda}(x-x') = \sum_{q\neq 0} \lambda_q(x)\mathrm{e}^{\mathrm{i}qx'} \,, \\
\tilde{\lambda}(x) &= \mathrm{i}\sum_{q\neq 0} \frac{\mathrm{e}^{-\mathrm{i}qx - a|q|/2}}{n_q} = 2\sum_{n=1}^{\infty} \frac{1}{n} \sin\frac{2\pi n x}{L} \\
&= \pi \,\mathrm{sgn}(x) - \frac{2\pi x}{L} \,, \qquad (-L < x < L)
\end{aligned} \tag{52}$$

in terms of which we can express the bosonic fields as

$$\begin{aligned}
\phi_\sigma(x) &= \sum_{q\neq 0} \lambda_q(x) K^{(0)}_{q\sigma} = \sum_{q \neq 0, k} \lambda_q(x) c^+_{k-q\sigma} c_{k\sigma} \\
&= \int \frac{\mathrm{d}x'}{2\pi} \, \tilde{\lambda}(x-x') \, {}^{*}_{*}\psi^+_\sigma(x')\psi_\sigma(x')^{*}_{*} \\
&= \sum_{k,k'} \chi_{k-k'}(x) {}^{*}_{*}\Xi^+_{k\sigma}\Xi_{k'\sigma}{}^{*}_{*} \,.
\end{aligned} \tag{53}$$

Here further auxiliary functions were introduced,

$$\begin{aligned}
\chi_q(x) &= 2\pi\bar{v} \int \frac{\mathrm{d}y}{L} \, \frac{\tilde{\lambda}(x-y)}{\bar{g}(y)} \, \mathrm{e}^{-\mathrm{i}qr_0(y)} \\
&= \frac{2\pi\mathrm{i}}{qL}\big(\mathrm{e}^{-\mathrm{i}qr_0(x)} - \bar{R}_q\big) \,, \quad \chi_0(x) = \frac{2\pi}{L} r_0(x) \,,
\end{aligned} \tag{54}$$

$$\begin{aligned}
\bar{R}_q &= \frac{2}{L} \int_0^{L/2} \mathrm{d}x \, \cos(qr_0(x)) \\
&= \frac{2}{L} \int_0^{L/2} \mathrm{d}r \, x_0'(r) \cos(qr) \,, \; \bar{R}_0 = 1 \,,
\end{aligned} \tag{55}$$

$$x_0(r) = r + 2\sum_{q>0} \bar{R}_q \frac{\sin qr}{q} \,, \tag{56}$$

where $x_0(r)$ is the unique inverse function of $r_0(x)$, which was substituted in the integral in (55) and expressed in terms of $\bar{R}_q$ via Fourier transform in (56) for later reference. The rebosonization relation (40) then yields

$$\begin{aligned}
\phi_\sigma(x) &= \sum_q \chi_{-q}(x) \sum_{k'} {}^{*}_{*}\Xi^+_{k'-q\sigma}\Xi_{k'\sigma}{}^{*}_{*} \\
&= \chi_0(x)\hat{N}_\sigma + \mathrm{i}A_\sigma(x) \,,
\end{aligned} \tag{57}$$

$$A_\sigma(x) = \sum_{q>0} \chi_{-q}(x)\sqrt{n_q} B_{q\sigma} - \mathrm{h.c.} \,, \tag{58}$$

finally expressing the fermionic field (51) in the diagonal bosonic basis (44). For the Green function we also need the time dependence of the Klein factors, which originates from $H_{\mathrm{N}} + H'$ in (26) and (29). This leads to a sum over $K^{(0)}_{q\sigma_\eta}$ which we calculate from the inversion $K^{(0)}_{q\sigma} = \int \frac{\mathrm{d}x}{2\pi} \, \mathrm{e}^{-\mathrm{i}qx} \partial_x \phi_\sigma(x)$ $(q \neq 0)$, namely $\sum_{q\neq 0} V_q K^{(0)}_{q\sigma} = \bar{\kappa}_0 \hat{N}_\sigma / L + \mathrm{i}\bar{A}_\sigma$, where

$$\bar{A}_\sigma = \sum_{q>0} \bar{\kappa}_{-q} \sqrt{n_q} B_{q\sigma} - \mathrm{h.c.} \,, \tag{59}$$

$$\bar{\kappa}_q = \int \frac{\mathrm{d}x}{2\pi L} \, (V(x) - V_0)\chi_q'(x) = -\frac{2\pi\tilde{v}_{\mathrm{F}}}{L} \bar{R}_q \,. \tag{60}$$

Using the hyperbolic relation $\mathrm{e}^{\mp\theta}(1 \pm \gamma/2) = \bar{\gamma}(u^3 \mp v^3)$ and eliminating U_0 with (32), the time-dependent Klein factor then becomes

$$\begin{aligned}
F_\eta(t) &= \mathrm{e}^{\mathrm{i}(H_{\mathrm{N}} + H')t} F_\eta \, \mathrm{e}^{-\mathrm{i}(H_{\mathrm{N}} + H')t} \\
&= F_\eta \mathrm{e}^{-\mathrm{i}t[2\pi\tilde{v}_{\mathrm{F}}(\hat{N}_\eta + \gamma\hat{N}_{\bar{\eta}} - \frac{1}{2})/L + W_0 + \bar{\gamma}\bar{\kappa}_0(u^3\hat{N}_{\bar{\eta}} - v^3\hat{N}_\eta)]} \\
&\qquad \times \mathrm{e}^{\mathrm{i}\bar{\gamma}(u^3\bar{A}_{\sigma_\eta} - v^3\bar{A}_{\bar{\sigma}_\eta})} \,.
\end{aligned} \tag{61}$$

We evaluate the Green function in the ground state with $\hat{N}_\eta = \mathcal{N}/2 = \hat{N}_\sigma$ and $B^+_{q\sigma}B_{q\sigma} = 0$ for all $q > 0$, where $\mathcal{N}$ is the integer closest to $-\epsilon/(2v_{\mathcal{N}})$,

$$G_\eta(x,x';t) = \theta(t)G^>_{\eta\eta}(x,x';t) - \theta(-t)G^<_{\eta\eta}(x,x';t) \,, \tag{62}$$

with $\theta(\pm t) = (1 \pm \mathrm{sgn}(t))/2$. The greater and lesser Green functions,

$$\begin{aligned}
G^{\gtrless}_{\eta\eta'}(x,x';t) &= \begin{cases} -\mathrm{i}\langle\psi_\eta(x,t)\,\psi^+_{\eta'}(x',0)\rangle \,, \\ -\mathrm{i}\langle\psi^+_{\eta'}(x',0)\,\psi_\eta(x,t)\rangle \,, \end{cases} \\
&= \delta_{\eta\eta'} G^{\gtrless}_{\eta\eta}(x,x';t) \,,
\end{aligned} \tag{63}$$

are then flavor-diagonal. They are evaluated by first clearing the Klein factors, inserting the Bogoljubov-transformed bosonic fields, separate them according to the index σ, and then express them with $\hat{N}_\sigma$, $B_{q\sigma}$, $B^+_{q\sigma}$. This leads to

$$\mathrm{i}aG^{\gtrless}_\eta(x,x';t) = M^{\gtrless}_{x,x',t}\, M_{\sigma_\eta}(t\bar{\gamma}u^3, \pm u, x_{\gtrless}, t_{\gtrless}, x_{\lessgtr}, t_{\lessgtr}) \\ \times M_{\bar{\sigma}_\eta}(-t\bar{\gamma}v^3, \pm v, -x_{\gtrless}, t_{\gtrless}, -x_{\lessgtr}, t_{\lessgtr})\,, \tag{64}$$

with a phase factor and σ-diagonal exponential bosonic expectation values

$$M^{\gtrless}_{x,x',t} = \mathrm{e}^{-\frac{\mathrm{i}\pi}{L}[(\mathcal{N}\pm1)(x-x')+v_{\gtrless}t]-\mathrm{i}\mathrm{e}^{-\theta}[\chi_0(x)-\chi_0(x')]\frac{\mathcal{N}}{2}}, \\ M_\sigma(\tau,\nu,x,t,x',t') = \langle \mathrm{e}^{\tau\bar{A}_\sigma}\mathrm{e}^{\nu A_\sigma(x,t)}\mathrm{e}^{-\nu A_\sigma(x',t')}\rangle_\sigma, \tag{65}$$

with $x_> = x$, $x_< = x'$, $t_> = t$, $x_< = 0$, and a velocity parameter given by $v_{\gtrless} = (\tilde{v}_\mathrm{F} - \bar{\gamma}\kappa_0 v^3/(2\pi))(\mathcal{N} + 1 \pm 1) + (\tilde{v}_\mathrm{F}\gamma + \bar{\gamma}\kappa_0 u^3/(2\pi))\mathcal{N} + LW_0/\pi - \tilde{v}_\mathrm{F}$. To evaluate the remaining expectation value, we use the identity[17]

$$\langle \mathrm{e}^{A_1}\mathrm{e}^{A_2}\mathrm{e}^{A_3}\rangle = \mathrm{e}^{\langle A_1A_2+A_2A_3+A_1A_3+\frac{1}{2}(A_1^2+A_2^2+A_3^2)\rangle}\,, \tag{66}$$

valid for linear bosonic operators A_1, A_2, A_3 and eigenstates of the bosonic particle numbers. We obtain

$$M(\tau,\nu,x,t,x',t') = \mathrm{e}^{-\frac{1}{2}\tau^2\bar{S}_0^{[a]}-\tau\nu\left(\bar{S}_1^{[\bar{v}t,a]}(x)-\bar{S}_1^{[\bar{v}t',a]}(x')\right)} \\ \times \mathrm{e}^{\frac{1}{2}\nu^2\left(2\bar{S}_2^{[\bar{v}(t'-t),a]}(x,x')-\bar{S}_2^{[0,a]}(x,x)-\bar{S}_2^{[0,a]}(x',x')\right)}\,, \tag{67}$$

where the index σ was omitted because M_σ is independent of it, and we used the abbreviations

$$\bar{S}_0 = \sum_{q>0} n_q|\bar{\kappa}_q|^2\mathrm{e}^{iqs}\mathrm{e}^{-aq}\,, \tag{68a}$$

$$\bar{S}_1^{[s,a]}(y) = \sum_{q>0} n_q\bar{\kappa}_{-q}\chi_q(y)\mathrm{e}^{iqs}\mathrm{e}^{-aq}\,, \tag{68b}$$

$$\bar{S}_2^{[s,a]}(x,y) = \sum_{q>0} n_q\chi_{-q}(x)\chi_q(y)\mathrm{e}^{iqs}\mathrm{e}^{-aq}\,. \tag{68c}$$

Using the explicit wave functions and the definition (55), they evaluate to

$$\bar{S}_0 = \Big(\frac{2\pi\tilde{v}_\mathrm{F}}{L}\Big)^2\bar{R}^{[0,a]}_{1,2}\,, \tag{69a}$$

$$\bar{S}_1^{[s,a]}(y) = \frac{2\pi\tilde{v}_\mathrm{F}}{L}\mathrm{i}\Big(\bar{R}^{[s,a]}_{0,2} - \bar{R}^{[s-r_0(y),a]}_{0,1}\Big)\,, \tag{69b}$$

$$\bar{S}_2^{[s,a]}(x,y) = \bar{R}^{[s+r_0(x)-r_0(y),a]}_{-1,0} + \bar{R}^{[s,a]}_{-1,2} \\ - \bar{R}^{[s+r_0(x),a]}_{-1,1} - \bar{R}^{[s-r_0(y),a]}_{-1,1}\,. \tag{69c}$$

Here we introduced the functions

$$\bar{R}^{[s,a]}_{m,n} = \sum_{q>0} n_q^m\bar{R}_q^n\mathrm{e}^{\mathrm{i}qs}\mathrm{e}^{-aq}\,, \tag{70}$$

which for $n \neq 0$ depend on the position dependence of $V(x)$ through $\bar{R}_q$ of (55). Putting (65), (67), (69) into (64), the calculation of the Green function is complete, and can be summarized as

$$G^>_\eta(x,x';t) = M^>_{x,x',t} \tag{71a}$$
$$\times M(t\bar{\gamma}u^3, +u, x, t, x', 0)M(-t\bar{\gamma}v^3, +v, -x, t, -x', 0)\,,$$

$$G^<_\eta(x,x';t) = M^<_{x,x',t} \tag{71b}$$
$$\times M(t\bar{\gamma}u^3, -u, x', 0, x, t)M(-t\bar{\gamma}v^3, -v, -x', 0, -x, t)\,,$$

with the factors given by (65) and (67). We now discuss this result for different settings, referring for simplicity only to $G^>_\eta(x,x';t)$.

2. *Recovery of the translationally invariant case*

In the translationally invariant case (46) we have $r_0(x) = x$, due to the constant function $r_0'(x) = \bar{v}/(\bar{\gamma}\tilde{v}_\mathrm{F}) = 1$, cf. (39). Also $\bar{R}_q = \delta_{q0}$, so that all sums over $\bar{R}_q$ (with $q > 0$) vanish. In $\bar{S}_2^{[\bar{v}(t'-t),a]}(x,x')$ only the usual logarithmic sum

$$\bar{R}^{[s,a]}_{-1,0} = \sum_{q>0}\frac{\mathrm{e}^{\mathrm{i}qs}\mathrm{e}^{-aq}}{n_q} \tag{72}$$
$$= -\ln\Big(1-\mathrm{e}^{\frac{2\pi}{L}(\mathrm{i}s-a)}\Big) \overset{L\to\infty}{\longrightarrow} -\ln\Big(\frac{2\pi}{L}(a-\mathrm{i}s)\Big)$$

survives, so that the contributions to the Green function for $L \to \infty$ become

$$M(\tau,\nu,x,t,x',t') = \left[\frac{a}{\mathrm{i}[x-x'-\bar{v}(t-t')]+a}\right]^{\nu^2}. \tag{73}$$

The Green function then takes the familiar power-law form

$$G^>_\eta(x,x';t) = M^>_{x,x',t} \tag{74}$$
$$\times\left[\frac{-\mathrm{i}a}{x-x'-\bar{v}t-\mathrm{i}a}\right]^{1+v^2}\left[\frac{\mathrm{i}a}{x-x'+\bar{v}t+\mathrm{i}a}\right]^{v^2},$$

with dependence on only $x - x' \pm \mathrm{i}\bar{v}t$. The interaction-dependent exponent, $v^2 = (\sqrt{v_\mathcal{N}/v_\mathcal{J}} - \sqrt{v_\mathcal{J}/v_\mathcal{N}})^2/4$, depends only on the velocity ratio of $v_\mathcal{N}/v_\mathcal{J}$, which is a characteristic feature of the Luttinger liquid that remains valid even for weakly nonlinear dispersions.[13] Furthermore, in the translationally invariant case without interaction we have $\gamma = 0$ and hence $v = 0$, so that only the first factor with unit exponent correctly remains in (74).

3. *Weak quadratic position dependence of the interactions*

Next we consider position-dependent potentials that are regular at the origin, i.e., $V(x) = V(0) + V''(0)x^2/2 + O(x^4)$, which is sketched in Fig. 1a for the repulsive case. From (39) we find for the function $r_0(x)$ that

$$\begin{aligned} r_0(x) &= r_0'(0)\,x + \frac{1}{6}r_0'''(0)\,x^3 + O(x^5)\,, \qquad (75)\\ r_0'(0) &= \frac{2\pi\bar{v}}{\bar{\gamma}(2\pi v_{\mathrm{F}} + V(0))} \equiv \alpha\,,\ r_0''(0) = 0\,,\\ r_0'''(0) &= \frac{-2\pi\bar{v}V''(0)}{\bar{\gamma}(2\pi v_{\mathrm{F}} + V(0))^2} \equiv 6\beta\,. \end{aligned}$$

We will be interested in the asymptotic behavior of Green functions (rather than their periodicity in L) and thus will eventually take the limit $L \to \infty$. We therefore consider a weak correction to the linear behavior $r'(0)$, i.e.,

$$\begin{aligned} r_0(x) &= \alpha x + \beta x^3 + O(\beta^2 x^5)\,, \quad \beta = \frac{\mathrm{const}}{L^2}\,, \qquad (76)\\ x_0(r) &= \bar{\alpha} r - \bar{\beta} r^3 + O(\bar{\beta}^2 r^5)\,, \quad \bar{\alpha} = \frac{1}{\alpha}\,,\ \bar{\beta} = \frac{\beta}{\alpha^4}\,. \end{aligned}$$

For the potential this means

$$V(x) = V(0) - \frac{6\pi\tilde{v}_{\mathrm{F}}\beta}{\alpha}x^2 + O\Big(\frac{x^4 V_0}{L^4}\Big)\,. \qquad (77)$$

The following choice of coefficients $\bar{R}_q$ turn out to produce this behavior,

$$\bar{R}_q = e^{-c|q|L/\pi}\,, \qquad (78)$$

where c is positive dimensionless parameter, because from (56) we find

$$x_0(r) = r + \frac{L}{\pi}\arctan\frac{\sin\frac{2\pi r}{L}}{\mathrm{e}^{2c} - \cos\frac{2\pi r}{L}}\,, \qquad (79)$$

which for small $|x/L|$ corresponds to (76) with

$$\bar{\alpha} = \coth c\,, \qquad \bar{\beta} = \frac{\pi^2}{3}\frac{\cosh c}{\sinh^3 c}\Big(\frac{2}{L}\Big)^2, \qquad (80a)$$

$$\alpha = \tanh c\,, \qquad \beta = \frac{\pi^2}{3}\frac{\sinh c}{\cosh^3 c}\Big(\frac{2}{L}\Big)^2. \qquad (80b)$$

The functions (70) are evaluated from (78) as

$$\bar{R}^{[s,a]}_{-1,n} = -\ln\Big(1 - \mathrm{e}^{\frac{2\pi}{L}(\mathrm{i}s - a - ncL/\pi)}\Big)\,, \qquad (81a)$$

$$\bar{R}^{[s,a]}_{m,n} = \frac{\mathrm{e}^{(-\frac{2\pi}{L}(\mathrm{i}s-a)+2nc)m}}{[\mathrm{e}^{-\frac{2\pi}{L}(\mathrm{i}s-a)+2nc} - 1]^{m+1}}\,. \quad (m = 0, 1) \qquad (81b)$$

For large L, the last logarithmic term in the exponent of (67) then dominates, containing

$$\begin{aligned} \bar{S}^{[s,a]}_2(x,y) = -\ln\Bigg[&\frac{\sinh\frac{\pi}{L}(\mathrm{i}[s + r_0(x) - r_0(y)] - a)}{\sinh\frac{\pi}{L}(\mathrm{i}[s + r_0(x)] - a - cL/\pi)}\\ &\times\frac{\sinh\frac{\pi}{L}(\mathrm{i}s - a - cL/\pi)}{\sinh\frac{\pi}{L}(\mathrm{i}[s - r_0(y)] - a - cL/\pi)}\Bigg]\,. \qquad (82) \end{aligned}$$

To leading order in x/L, x'/L, the Green function then becomes

$$\begin{aligned} G^{>}_{\eta}(x,x';t) &= M^{>}_{x,x',t} \qquad (83)\\ &\times\left[\frac{-\mathrm{i}a}{\alpha(x-x') - \bar{v}t - \mathrm{i}a}\right]^{1+v^2}\left[\frac{\mathrm{i}a}{\alpha(x-x') + \bar{v}t + \mathrm{i}a}\right]^{v^2}, \end{aligned}$$

i.e., translational invariance is only broken in finite-size corrections.

Note that according to (83) a fermionic single-particle perturbation near $x = 0$, as measured by the Green function, propagates with velocity $\bar{v}/\alpha = \bar{v}/r_0'(0) = \bar{\gamma}(v_{\mathrm{F}} + V(0)/(2\pi)$. This which differs from the translationally invariant case (47) with corresponding velocity $\bar{\gamma}(v_{\mathrm{F}} + V_0/(2\pi)$ for which only the position-averaged interaction V_0 matters. For the Luttinger droplet, the position dependence of $V(x)$ is thus observable in the propagation velocity described by the Green function. This can be observed in more detail for a stronger position dependence of $V(x)$, as discussed in the next subsection.

We also note that the exponent v^2 (expressed in terms of γ in (31)) is no longer related only to the velocity ratio of $v_{\mathcal{N}}/v_{\mathcal{J}}$, hence this feature of the Luttinger liquid is also no longer present.

4. Piecewise constant interaction potential

As a minimal example which explicitly breaks the translational invariance of the Green function, we consider an interaction potential that is piecewise constant,

$$V(x) = \begin{cases} V(0) & \text{if } |x| < R\,,\\ V(\frac{L}{2}) & \text{if } |x| > R\,, \end{cases} \qquad (84)$$

i.e., the particles interact differently inside a central region and outside of it, as depicted in Fig. 1b for the repulsive case. The average of this function is given by

$$V_0 = r\,V(0) + (1-r)\,V(\tfrac{L}{2})\,, \quad r = \frac{2R}{L}\,. \qquad (85)$$

Here r is the fraction of the central region with interaction $V(0)$, which tends to zero if we consider a fixed finite central interval of width $2R$ but let L tend to infinity, see below. For the potential (84) we find

$$\bar{v} = \frac{\bar{\gamma}}{2\pi}\frac{1}{rs + (1-r)\tilde{s}}\,, \qquad (86a)$$

$$r_0(x) = \begin{cases} \alpha x & \text{if } |x| \le R\,,\\ \tilde{\alpha}x + \mathrm{sgn}(x)(\alpha - \tilde{\alpha})R & \text{if } |x| \ge R\,, \end{cases} \qquad (86b)$$

$$\bar{R}_q = r\,\frac{V(0) - V(\frac{L}{2})}{2\pi v_{\mathrm{F}} + V(0)}\,\frac{\sin n_q\pi r\alpha}{n_q\pi r\alpha}\,, \quad (q > 0)\,, \qquad (86c)$$

with the abbreviations

$$\begin{aligned} s &= \frac{1}{2\pi v_{\mathrm{F}} + V(0)}\,, \qquad \tilde{s} = \frac{1}{2\pi v_{\mathrm{F}} + V(\frac{L}{2})}\,, \qquad (87)\\ \alpha &= r_0'(0) = \frac{s}{\tilde{s} + (s - \tilde{s})r}\,, \quad \tilde{\alpha} = r_0'(\tfrac{L}{2}) = \frac{\tilde{s}}{\tilde{s} + (s - \tilde{s})r}\,. \end{aligned}$$

From now on we consider only fixed finite R and let $L \to \infty$, i.e., $r \to 0$. The second fraction in (86c) involving the sine function can then be replaced by unity. In this limit the summations (70) evaluate to

$$\bar{R}^{[s,a]}_{m,n} = \left[r\, \frac{V(0) - V(\frac{L}{2})}{2\pi v_{\mathrm{F}} + V(0)} \right]^{n} \bar{R}^{[s,a]}_{m,0}\,. \tag{88}$$

The logarithmic term in $\bar{S}_2^{[s,a]}(x,y)$ then again provides the leading term in (67) for $L \to \infty$,

$$\begin{aligned} &M(\tau,\nu,x,t,x',t') \\ &\quad = \left[\frac{a}{\mathrm{i}[r_0(x) - r_0(x') - \bar{v}(t-t')] + a} \right]^{\nu^2}. \end{aligned} \tag{89}$$

The Green function then takes a power-law form with piecewise linear argument

$$\begin{aligned} G^{>}_{\eta}(x,x';t) &= M^{>}_{x,x',t} \\ &\times \left[\frac{-\mathrm{i}a}{r_0(x) - r_0(x') - \bar{v}t - \mathrm{i}a} \right]^{1+v^2} \\ &\times \left[\frac{\mathrm{i}a}{r_0(x) - r_0(x') + \bar{v}t + \mathrm{i}a} \right]^{v^2}, \end{aligned} \tag{90}$$

with the exponent v^2 given in terms of γ in (31). As listed in (86b), in the present case $r_0(x)$ is piecewise linear in x with a change in slope at $|x| = R$. Hence if x and x' lie both inside or both outside the central region, the Green function is essentially the same as in the case of weak position dependence (83) or the translationally invariant case (74), respectively. However, if only one of x and x' is inside the central region, the two coordinates enter with different prefactors into the Green function, breaking its translational invariance. The Green function (90) and velocity relation (50) indicate that for the interaction potential (84) the Luttinger droplet (4) is distinguishable from the Luttinger liquid.

Moreover, the Green function (90) shows that a fermionic single-particle perturbation created at position x will initially propagate with velocity $\bar{v}/r_0'(x) = \bar{\gamma}(v_{\mathrm{F}} + V(x)/(2\pi)$, which is piecewise constant in the present case. As might have been expected, the position dependence of $V(x)$ thus translates into a position-dependent 'local' propagation velocity. Its relation to the other excitation velocitues of the Luttinger droplet model will be discussed the next section.

V. TOWARDS A LUTTINGER DROPLET PARADIGM

The translationally invariant Tomonaga-Luttinger model obeys the relations (46) between excitation velocities and Green function exponents, i.e., in our notation between $\bar{v}$, $v_{\mathcal{N}}$, $v_{\mathcal{J}}$, and γ. In particular, the dressed Fermi velocity $\bar{v}$ appears in the Green function (74) as the velocity with which a fermion $\psi^{+}_{\eta}(x)$ propagates when added to the Luttinger liquid ground state. For the Luttinger droplet model (4) (with linear dispersion) we found different relations between the excitation velocities and γ, as given in (50). Furthermore, the Green functions of Sec. IV D show that a fermion $\psi^{+}_{\eta}(x)$, inserted into the Luttinger droplet ground state at position x, initially propagates with velocity $\bar{v}/r_0'(x)$. This behavior was observed explicitly for a weak and piecewise constant position dependence of the interaction potential $V(x)$ in (83) and (90), respectively. It can be traced to (39), where a phase $r_0(x)k$ appears in the exponent of the eigenfunctions $\xi_k(x)$ of the refermionized model (36). We can therefore expect that a 'local' propagation velocity of fermionic perturbations,

$$v^{\mathrm{loc}}(x) = \frac{\bar{v}}{r_0'(x)} = \bar{\gamma} \left(v_{\mathrm{F}} + \frac{V(x)}{2\pi} \right), \tag{91}$$

will appear in the Green function also for more general $V(x)$. Compared to the translationally invariant case this is a new range of velocities, which we will now relate to the other excitation velocities of the Luttinger droplet.

For this purpose we first seek to characterize the scales of $v^{\mathrm{loc}}(x)$. One way to do this uses its arithmetic and harmonic averages over the entire system. For these we find

$$\overline{v^{\mathrm{loc}}} \equiv \langle\langle v^{\mathrm{loc}}(x) \rangle\rangle_{\mathrm{arith}} \equiv \int \frac{\mathrm{d}x}{L}\, v^{\mathrm{loc}}(x) = \bar{\gamma}\tilde{v}_{\mathrm{F}}\,, \tag{92a}$$

$$\langle\langle v^{\mathrm{loc}}(x) \rangle\rangle_{\mathrm{harm}} \equiv \left[\int \frac{\mathrm{d}x}{L}\, \frac{1}{v^{\mathrm{loc}}(x)} \right]^{-1} = \bar{v}\,, \tag{92b}$$

where, as above, $\tilde{v}_{\mathrm{F}} = v_{\mathrm{F}} + V_0/(2\pi)$. For general $V(x)$ these two averages are different, but coincide in the translationally invariant case. With the excitations of the Luttinger droplet characterized by the velocities $\bar{v}$, $\overline{v^{\mathrm{loc}}}$, $v_{\mathcal{N}}$, $v_{\mathcal{J}}$, we then obtain their interrelation from (50),

$$\bar{v} = c_{\mathcal{N}}(\gamma)\, v_{\mathcal{N}} + c_{\mathcal{J}}(\gamma)\, v_{\mathcal{J}}\,, \tag{93a}$$

$$\overline{v^{\mathrm{loc}}} = c^{\mathrm{loc}}_{\mathcal{N}}(\gamma)\, v_{\mathcal{N}} + c^{\mathrm{loc}}_{\mathcal{J}}(\gamma)\, v_{\mathcal{J}}\,, \tag{93b}$$

where the prefactors are given by

$$c_{\mathcal{N},\mathcal{J}}(\gamma) = \frac{(\gamma - \bar{\gamma}\gamma_3) \mp (1 - \bar{\gamma})}{2(\gamma - \gamma_3)}\,, \tag{94a}$$

$$c^{\mathrm{loc}}_{\mathcal{N},\mathcal{J}}(\gamma) = \bar{\gamma}\, \frac{(\pm 1 - \gamma_3)}{2(\gamma - \gamma_3)}\,, \tag{94b}$$

Furthermore γ, which characterizes the relative strength of interbranch interactions, determines the Green function exponent v^2 according to (31). The dependence of the coefficients (94) on γ is shown in Fig. 2. We note that for $\gamma = 0$, the two branches in the Hamiltonian do not mix; in this case $v_{\mathcal{N}}$ and $v_{\mathcal{J}}$ contribute equally to $\bar{v}$ and $\overline{v^{\mathrm{loc}}}$ equals $v_{\mathcal{N}}$. On the other hand, for only interbranch interactions ($\gamma \to \pm 1$), $\bar{\gamma}$ vanishes and hence so do $v_{\mathcal{N},\mathcal{J}}$.

A preliminary physical interpretation of the velocities (92) might be that $\bar{v}$ plays the role of group velocity, as $\bar{v}q$ is the energy of a bosonic excitation in (44) which involves a nonlocal and mixed-flavor superposition of original fermions. On the other hand, since $v^{\mathrm{loc}}(x)$

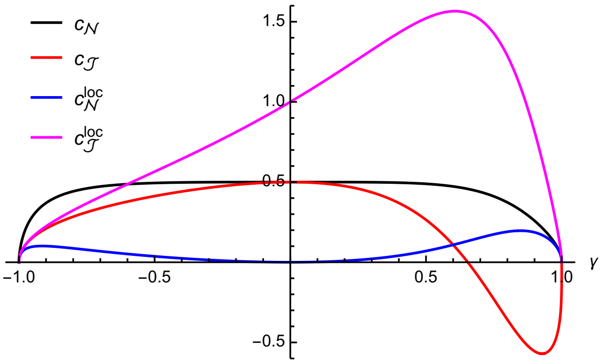

FIG. 2. Coefficients (94) in the linear relation (93) between excitation velocities in the Luttinger droplet model (4) as a function of the interaction parameter γ given by (32), (49).

plays the role of a local phase velocity, its scale is presumably captured by the arithmetic average $\overline{v^{\mathrm{loc}}}$. Note that for the translationally invariant case $\bar{v} = \bar{\gamma}\tilde{v}_{\mathrm{F}}$, and indeed the group velocity and (position-independent) phase velocity are both given by $\bar{v}$, cf. (44), (46), (74).

We conclude that for the Luttinger droplet model (4) the quantities $\bar{v}$, $\overline{v^{\mathrm{loc}}}$, $v_{\mathcal{N}}$, $v_{\mathcal{J}}$, and γ are related, extending the Luttinger liquid relations between $\bar{v}$, $v_{\mathcal{N}}$, $v_{\mathcal{J}}$, γ to the position-dependent case. However, it remains to clarify how the relations (93) evolve away from the special case (4b). Furthermore, in order to be regarded as a paradigm for one-dimensional electronic systems with position-dependent interactions, these relations would have to remain valid also for weak nonlinearites in the dispersion. Both of these questions would therefore be worthwhile to address, e.g., by perturbative methods.

VI. CONCLUSION

Using higher-order bosonization identities, i.e., Kronig-type relations with finite momentum transfer, we solved the Luttinger droplet model (4) for a large class of position-dependent interactions and arbitrary one-particle potentials. While the diagonalized Hamiltonian has the same operator expression as for the Luttinger liquid, the relation between its velocity parameters is not fulfilled in general, as the bosonic excitations and particle number changes involve different averages of the interaction potential over all positions. Similarly the Green functions retain their power-law form for weak position-dependence of the interaction potential, but their exponents also no longer depend only on the ratio of excitation velocities for particle-number changes. For weak position-dependent interactions the Luttinger-liquid characteristics are rather robust regarding their functional form, although the interrelation of the dressed scales and exponents is somewhat different. On the other hand, for an interaction potential with different (e.g., constant) values inside or outside a central region of finite width, not only are the Luttinger-liquid velocity relations modified, but also the Green function is no longer translationally invariant and exhibits a position-dependent propagation velocity of single-particle excitations. This may mean that the group velocity of such an excitation differs from its (position-dependent) phase velocity, in contrast to the Luttinger liquid. We conclude that the Luttinger droplet model has a ground state with different characteristics than the Luttinger liquid. It remains to be seen how the velocity relations obtained for (4) evolve for more general one-dimensional models with position-dependent interactions, and whether a Luttinger droplet paradigm emerges for them.

ACKNOWLEDGMENTS

The authors would like to thank Matthias Punk and Jan von Delft for valuable discussions. M.K. would also like to thank Sebastian Diehl, Erik Koch, Volker Meden, Lisa Markhof, Aditi Mitra, Herbert Schoeller, and Eva Pavarini for useful discussions. S.H. gratefully acknowledges support by the German Excellence Cluster Nanosystems Initiative Munich (NIM) and by the Deutsche Forschungsgemeinschaft under Germany's Excellence Strategy EXC-2111-390814868. M.K. was supported in part by Deutsche Forschungsgemeinschaft under Projektnummer 107745057 (TRR 80) and performed part of this work at the Aspen Center for Physics, which is supported by National Science Foundation grant PHY-1607611.

---

[1] D. Sénéchal, arXiv:cond-mat/9908262.
[2] T. Giamarchi, *Quantum Physics in One Dimension* (Clarendon Press, 2003).
[3] S.-I. Tomonaga, Prog. Theor. Phys. **5**, 544 (1950).
[4] J. M. Luttinger, J. Math. Phys. **4**, 1154 (1963).
[5] D. C. Mattis and E. H. Lieb, J. Math. Phys. **6**, 304 (1965).
[6] M. Schick, Phys. Rev. **166**, 404 (1968).
[7] K. D. Schotte and U. Schotte, Phys. Rev. **182**, 479 (1969).
[8] D. C. Mattis, J. Math. Phys. **15**, 609 (1974).
[9] A. Luther and I. Peschel, Phys. Rev. B **9**, 2911 (1974).
[10] S. Coleman, Phys. Rev. D **11**, 2088 (1975).
[11] S. Mandelstam, Phys. Rev. D **11**, 3026 (1975).
[12] R. Heidenreich, B. Schroer, R. Seiler, and D. Uhlenbrock, Phys. Lett. A **54**, 119 (1975).
[13] F. D. M. Haldane, J. Phys. C: Solid State Phys. **12**, 4791 (1979); J. Phys. C: Solid State Phys. **14**, 2585 (1981).
[14] V. J. Emery, in *Highly Conducting One-Dimensional Solids*, Physics of Solids and Liquids, edited by J. T. De-

vreese, R. P. Evrard, and V. E. v. Doren (Springer, 1979) p. 247.

[15] J. Voit, Rep. Prog. Phys. **58**, 977 (1995).

[16] G. Kotliar and Q. Si, Phys. Rev. B **53**, 12373 (1996).

[17] J. von Delft and H. Schoeller, Ann. Phys. **7**, 225 (1998).

[18] J. von Delft, G. Zaránd, and M. Fabrizio, Phys. Rev. Lett. **81**, 196 (1998); G. Zaránd and J. von Delft, Phys. Rev. B **61**, 6918 (2000).

[19] D. K. K. Lee and Y. Chen, J. Phys. A: Math. Gen. **21**, 4155 (1988).

[20] I. V. Yurkevich, in *Strongly Correlated Fermions and Bosons in Low-Dimensional Disordered Systems*, NATO Science Series (Springer, Dordrecht, 2002) pp. 69–80.

[21] A. Grishin, I. V. Yurkevich, and I. V. Lerner, Phys. Rev. B **69**, 165108 (2004); A. Galda, I. V. Yurkevich, and I. V. Lerner, Phys. Rev. B **83**, 041106 (2011).

[22] M. Filippone and P. W. Brouwer, Phys. Rev. B **94**, 235426 (2016).

[23] V. Meden and K. Schönhammer, Phys. Rev. B **46**, 15753 (1992); K. Schönhammer and V. Meden, Phys. Rev. B **47**, 16205 (1993); Phys. Rev. B **48**, 11521 (1993).

[24] V. Meden, Phys. Rev. B **60**, 4571 (1999).

[25] L. Markhof and V. Meden, Phys. Rev. B **93**, 085108 (2016).

[26] F. D. M. Haldane, Phys. Rev. Lett. **45**, 1358 (1980); Phys. Lett. A **81**, 153 (1981); Phys. Rev. Lett. **47**, 1840 (1981).

[27] J. Sólyom, Adv. Phys. **28**, 201 (1979).

[28] K. Schönhammer, arXiv:cond-mat/9710330; in *Strong interactions in low dimensions*, Physics and Chemistry of Materials with Low-Dimensional Structures, edited by D. Baeriswyl and L. Degiorgi (Springer Netherlands, 2004) p. 93; J. Phys.: Condens. Matter **25**, 014001 (2013).

[29] E. Miranda, Braz. J. Phys. **33**, 3 (2003).

[30] M. A. Cazalilla, R. Citro, T. Giamarchi, E. Orignac, and M. Rigol, Rev. Mod. Phys. **83**, 1405 (2011).

[31] P. Kopietz, *Bosonization of Interacting Fermions in Arbitrary Dimensions* (Springer, 1997).

[32] A. O. Gogolin, A. A. Nersesyan, and Alexei M. Tsvelik, *Bosonization and Strongly Correlated Systems* (Cambridge University Press, 2004).

[33] H. Bruus and K. Flensberg, *Many-Body Quantum Theory in Condensed Matter Physics: An Introduction* (Oxford University Press, 2004).

[34] G. Giuliani and G. Vignale, *Quantum Theory of the Electron Liquid* (Cambridge University Press, 2008).

[35] P. Phillips, *Advanced Solid State Physics*, 2nd ed. (Cambridge University Press, 2012).

[36] V. Mastropietro and D. C. Mattis, *Luttinger Model - The First 50 Years and Some New Directions*, Series on Directions in Condensed Matter Physics, Vol. 20 (World Scientific, 2013).

[37] F. P. Milliken, C. P. Umbach, and R. A. Webb, Sol. State Comm. **97**, 309 (1996).

[38] I. J. Maasilta and V. J. Goldman, Phys. Rev. B **55**, 4081 (1997).

[39] A. M. Chang, Rev. Mod. Phys. **75**, 1449 (2003).

[40] M. Bockrath, D. H. Cobden, J. Lu, A. G. Rinzler, R. E. Smalley, L. Balents, and P. L. McEuen, Nature **397**, 598 (1999).

[41] H. Ishii, H. Kataura, H. Shiozawa, H. Yoshioka, H. Otsubo, Y. Takayama, T. Miyahara, S. Suzuki, Y. Achiba, M. Nakatake, T. Narimura, M. Higashiguchi, K. Shimada, H. Namatame, and M. Taniguchi, Nature **426**, 540 (2003).

[42] A. N. Aleshin, H. J. Lee, Y. W. Park, and K. Akagi, Phys. Rev. Lett. **93**, 196601 (2004).

[43] M. Boninsegni, A. B. Kuklov, L. Pollet, N. V. Prokof'ev, B. V. Svistunov, and M. Troyer, Phys. Rev. Lett. **99**, 035301 (2007); A. Del Maestro, M. Boninsegni, and I. Affleck, Phys. Rev. Lett. **106**, 105303 (2011); P.-F. Duc, M. Savard, M. Petrescu, B. Rosenow, A. D. Maestro, and G. Gervais, Science Advances **1**, e1400222 (2015).

[44] Y. Jompol, C. J. B. Ford, J. P. Griffiths, I. Farrer, G. A. C. Jones, D. Anderson, D. A. Ritchie, T. W. Silk, and A. J. Schofield, Science **325**, 597 (2009).

[45] G. Barak, H. Steinberg, L. N. Pfeiffer, K. W. West, L. Glazman, F. von Oppen, and A. Yacoby, Nat. Phys. **6**, 489 (2010).

[46] C. Blumenstein, J. Schäfer, S. Mietke, S. Meyer, A. Dollinger, M. Lochner, X. Y. Cui, L. Patthey, R. Matzdorf, and R. Claessen, Nat. Phys. **7**, 776 (2011).

[47] H. T. Mebrahtu, I. V. Borzenets, D. E. Liu, H. Zheng, Y. V. Bomze, A. I. Smirnov, H. U. Baranger, and G. Finkelstein, Nature **488**, 61 (2012); H. T. Mebrahtu, I. V. Borzenets, H. Zheng, Y. V. Bomze, A. I. Smirnov, S. Florens, H. U. Baranger, and G. Finkelstein, Nature Physics **9**, 732 (2013).

[48] B. Yang, Y.-Y. Chen, Y.-G. Zheng, H. Sun, H.-N. Dai, X.-W. Guan, Z.-S. Yuan, and J.-W. Pan, Phys. Rev. Lett. **119**, 165701 (2017).

[49] K. Cedergren, R. Ackroyd, S. Kafanov, N. Vogt, A. Shnirman, and T. Duty, Phys. Rev. Lett. **119**, 167701 (2017).

[50] R. Stühler, F. Reis, T. Müller, T. Helbig, T. Schwemmer, R. Thomale, J. Schäfer, and R. Claessen, arXiv:1901.06170.

[51] T. Busche and P. Kopietz, Int. J. Mod. Phys. B **14**, 1481 (2000); P. Pirooznia, F. Schütz, and P. Kopietz, Phys. Rev. B **78**, 075111 (2008).

[52] S. Teber, Phys. Rev. B **76**, 045309 (2007).

[53] C. Karrasch, R. G. Pereira, and J. Sirker, New J. Phys. **17**, 103003 (2015).

[54] A. V. Rozhkov, Phys. Rev. B **68**, 115108 (2003); Eur. Phys. J. B **47**, 193 (2005); Phys. Rev. B **74**, 245123 (2006); Phys. Rev. B **77**, 125109 (2008); Phys. Rev. Lett. **112**, 106403 (2014).

[55] A. Imambekov and L. I. Glazman, Science **323**, 228 (2009); Phys. Rev. Lett. **102**, 126405 (2009); A. Imambekov, T. L. Schmidt, and L. I. Glazman, Rev. Mod. Phys. **84**, 1253 (2012).

[56] H. Maebashi and Y. Takada, Phys. Rev. B **89**, 201109 (2014).

[57] F. H. L. Essler, R. G. Pereira, and I. Schneider, Phys. Rev. B **91**, 245150 (2015).

[58] L. Markhof, M. Pletyukov, and V. Meden, SciPost Physics **7**, 047 (2019).

[59] M. A. Cazalilla, Phys. Rev. Lett. **97**, 156403 (2006); A. Iucci and M. A. Cazalilla, Phys. Rev. A **80**, 063619 (2009); N. Nessi and A. Iucci, Phys. Rev. B **87**, 085137 (2013).

[60] G. S. Uhrig, Phys. Rev. A **80**, 061602 (2009).

[61] M. S. Foster, E. A. Yuzbashyan, and B. L. Altshuler, Phys. Rev. Lett. **105**, 135701 (2010).

[62] E. Perfetto and G. Stefanucci, EPL **95**, 10006 (2011).

[63] J. Dziarmaga and M. Tylutki, Phys. Rev. B **84**, 214522 (2011).

[64] B. Dóra, M. Haque, and G. Zaránd, Phys. Rev. Lett. **106**, 156406 (2011); B. Dóra, Á. Bácsi, and G. Zaránd, Phys. Rev. B **86**, 161109 (2012); B. Dóra and F. Pollmann, Phys. Rev. Lett. **115**, 096403 (2015); B. Dóra, R. Lundgren, M. Selover, and F. Pollmann, Phys. Rev. Lett. **117**, 010603

(2016).

[65] C. Karrasch, J. Rentrop, D. Schuricht, and V. Meden, Phys. Rev. Lett. **109**, 126406 (2012); J. Rentrop, D. Schuricht, and V. Meden, New J. Phys. **14**, 075001 (2012).

[66] E. Coira, F. Becca, and A. Parola, Eur. Phys. J. B **86**, 1 (2013).

[67] S. Ngo Dinh, D. A. Bagrets, and A. D. Mirlin, Phys. Rev. B **88**, 245405 (2013).

[68] T. Sabetta and G. Misguich, Phys. Rev. B **88**, 245114 (2013).

[69] D. M. Kennes and V. Meden, Phys. Rev. B **88**, 165131 (2013); D. M. Kennes, C. Klöckner, and V. Meden, Phys. Rev. Lett. **113**, 116401 (2014).

[70] R. Sachdeva, T. Nag, A. Agarwal, and A. Dutta, Phys. Rev. B **90**, 045421 (2014).

[71] M. Schiró and A. Mitra, Phys. Rev. B **91**, 235126 (2015).

[72] V. Mastropietro and Z. Wang, Phys. Rev. B **91**, 085123 (2015).

[73] D. B. Gutman, Y. Gefen, and A. D. Mirlin, Phys. Rev. B **81**, 085436 (2010); I. V. Protopopov, D. B. Gutman, and A. D. Mirlin, J. Stat. Mech. **2011**, P11001 (2011); Phys. Rev. B **90**, 125113 (2014); I. V. Protopopov, D. B. Gutman, M. Oldenburg, and A. D. Mirlin, Phys. Rev. B **89**, 161104 (2014); I. V. Protopopov, D. B. Gutman, and A. D. Mirlin, Phys. Rev. B **91**, 195110 (2015).

[74] J. Lin, K. A. Matveev, and M. Pustilnik, Phys. Rev. Lett. **110**, 016401 (2013).

[75] M. Buchhold and S. Diehl, Phys. Rev. A **92**, 013603 (2015); Eur. Phys. J. D **69**, 1 (2015); M. Buchhold, M. Heyl, and S. Diehl, Phys. Rev. A **94**, 013601 (2016); S. Huber, M. Buchhold, J. Schmiedmayer, and S. Diehl, Phys. Rev. A **97**, 043611 (2018).

[76] R. D. Kronig, Physica **2**, 968 (1935).

[77] C. B. Dover, Ann. Phys. **50**, 500 (1968).

[78] Throughout, hats appear only on those operators which involve fermionic number operators.

[79] C. L. Kane and M. P. A. Fisher, Phys. Rev. Lett. **68**, 1220 (1992); Phys. Rev. B **46**, 15233 (1992); Phys. Rev. B **46**, 7268 (1992).

[80] C. Rylands and N. Andrei, Phys. Rev. B **94**, 115142 (2016); Phys. Rev. B **96**, 115424 (2017); Phys. Rev. B **97**, 155426 (2018).

[81] V. Meden, W. Metzner, U. Schollwöck, and K. Schönhammer, J. Low Temp. Phys. **126**, 1147 (2002).

[82] K. Hattori and A. Rosch, Phys. Rev. B **90**, 115103 (2014).

[83] V. Meden, W. Metzner, U. Schollwöck, O. Schneider, T. Stauber, and K. Schönhammer, Eur. Phys. J. B **16**, 631 (2000).

[84] I. Schneider and S. Eggert, Phys. Rev. Lett. **104**, 036402 (2010).

[85] C. Rylands, arXiv:1910.11221.

[86] S. Eggert, Phys. Rev. Lett. **84**, 4413 (2000).

[87] W. Wonneberger, Phys. Rev. A **63**, 063607 (2001).

[88] D. L. Maslov and M. Stone, Phys. Rev. B **52**, R5539 (1995).

[89] I. Safi and H. J. Schulz, Phys. Rev. B **52**, R17040 (1995).

[90] V. V. Ponomarenko, Phys. Rev. B **52**, R8666 (1995).

[91] J. Rech and K. A. Matveev, J. Phys.: Condens. Matter **20**, 164211 (2008); Phys. Rev. Lett. **100**, 066407 (2008).

[92] I. Ferrier-Barbut, Physics Today **72**, 46 (2019).

[93] We note that our derivation of (7) is similar in spirit to the procedure in Sec. 3.2 of Ref. 94, and also bears some resemblance to the analysis of higher-order dispersion terms in Ref. 95. However our approach is more general since we also allow finite momentum transfer q and work with exact operator identities. Note also that one may view (7) as a fermionic representation of certain properties of vertex operators,[17] i.e., exponentiated bosonic fields.

[94] R. G. Pereira, J. Sirker, J.-S. Caux, R. Hagemans, J. M. Maillet, S. R. White, and I. Affleck, J. Stat. Mech. **2007**, P08022 (2007).

[95] A. Enciso and A. P. Polychronakos, Nucl. Phys. B **751**, 376 (2006); D. Karabali and A. P. Polychronakos, Phys. Rev. D **90**, 025002 (2014).

[96] P. D. Francesco, P. Mathieu, and D. Sénéchal, *Conformal Field Theory* (Springer, 1997).

[97] L. Comtet, *Advanced Combinatorics* (Springer Netherlands, Dordrecht, 1974).

5.6 Thermalization of an interacting Luttinger liquid

5.6.1 Phase diagram of one-dimensional Bose-Hubbard model

The Tomonaga-Luttinger model stands for a universality class to which in certain regimes also bosonic models belong. Bosonic systems are usually described by the following one-dimensional Bose-Hubbard model [GK63]:

$$H_{\text{BHM}} = -J\sum_i [b_i^\dagger b_{i+1} + \text{h.c.}] - \mu\sum_i n_i + U\sum_i n_i[n_i-1],\ \ n_i = b_i^\dagger b_i, \tag{5.23}$$

where the creation of bosonic particles at site i is described by the operator $b_i^\dagger$. The nearest neighbor hopping matrix element is given by J and we assume a repulsive on-site interaction U. The average particle density per site is set by the chemical potential μ.

The Bose-Hubbard model became of particular interest since it captures the essence of a superfluid-insulator transition [MHL86, GS88]. The according phase diagram in the plane of chemical potential and hopping in units of the interaction strength is shown in Fig. 5.6 [FM94, KM98, Sch09].

At small hopping the bosonic particles are essentially localized and the system is in a incompressible Mott-insulating phase. Increasing the agility of the particles, the bosons form a superfluid state with coherent phase relation between distant sites. Already a simple mean-field calculations at zero temperature yields the following relation

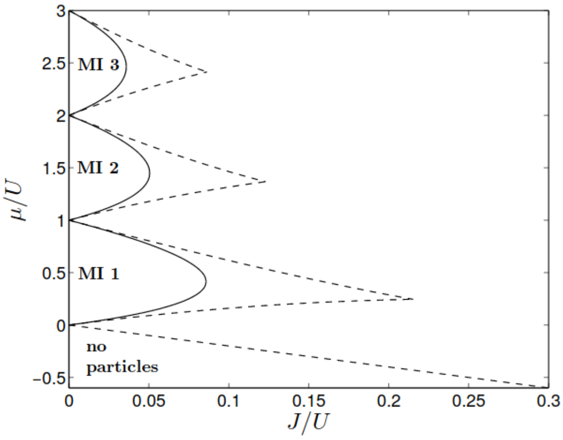

Figure 5.6 The phase boundary of the one-dimensional Bose-Hubbard model from mean-field theory (solid line) and third order perturbation theory (dashed line). Fig. adapted from Ref. [FM94] and [Sch09].

$$\frac{\mu}{U} = \left[2n-1-\frac{J}{U}\right] \pm \sqrt{1-2\frac{J}{U}(2n+1)+\left(\frac{J}{U}\right)^2}. \tag{5.24}$$

The according critical hopping of the phase boundary is underestimated in this mean-field approach, but this approach is in general already a good approximation of the phase diagram as shown in Fig. 5.6. More elaborate approaches including higher order perturbative expansions and numerical studies are available in the literature.

Within the superfluid regime, a finite momentum regime $p < p_L$ ($p_L \approx \sqrt{U\rho_0 m}$) exists, where the dispersion of the bosonic low-energy excitations is linear in momentum [AS10]. This liquid phase is however different to the superfluid phase occuring in higher dimensions, where the system has long-range order. In one dimensions the density fluctuations are gapless [Gia03, CCG$^+$11].

In this superfluid regime, the low-energy state is captured by a Tomonaga-Luttinger liquid Hamiltonian equivalent to Eq. (5.13). A phenomenological approach to the according concept was first formulated in the work of F. Duncan M. Haldane [Hal81]. We shortly summarize this formalism following Ref. [Gia03, CCG$^+$11]. Consider a one-dimensional chain of bosonic particles located at sites i with the density given by

$$\rho(x) = \sum_i \delta(x - x_i). \tag{5.25}$$

The bosonic operators in the continuum limit can be defined in this superfluid regime in a polar description as follows

$$b^\dagger(x) = \sqrt{\rho(x)}\ e^{-i\theta(x)}. \tag{5.26}$$

The phase and density operator fullfill the commutation relation as follows

$$[\rho(x), \theta(x')] = i\delta(x - x'). \tag{5.27}$$

In the low-energy regime, where the density operator just deviates weakly from its average $\rho_0 = \langle \rho(x) \rangle$, the bosonic operator yields

$$b^\dagger(x) \approx \sqrt{\rho_0 - \frac{1}{\pi}\partial_x \phi(x)} e^{-i\theta(x)}. \tag{5.28}$$

The one-dimensional Bose-Hubbard model in Eq. (5.23) reads for a small finite repulsive interaction in the continuum limit as follows

$$H = \frac{1}{2\pi} \int dx\ [\nu K (\partial_x \theta(x))^2 + \frac{\nu}{K} (\partial_x \phi(x))^2] + \kappa \int dx\ \partial_x \phi(x)\ (\partial_x \theta(x))^2, \tag{5.29}$$

where the Luttinger parameters are related to the microscopic parameters as follows: $\nu = \sqrt{\frac{\rho_0 U}{m}}$ and $K = \frac{\pi}{2}\sqrt{\frac{\rho_0}{Um}}$. The first two terms of this Hamiltonian are diagonalized in a phonon basis according to [Gia03]

$$\theta(x) = \frac{\pi x}{L\sqrt{K}}[N_+ - N_-] + \frac{i}{2L}\sum_{n\neq 0}\sqrt{\frac{1}{K|n|}} e^{-\frac{\pi}{L}a|n| - i\frac{2\pi}{L}nx}[b_n^\dagger - b_{-n}], \tag{5.30}$$

$$\phi(x) = -\frac{\pi x}{L\sqrt{K}}[N_+ + N_-] - \frac{i}{2L}\sum_{n\neq 0}\sqrt{\frac{K}{|n|}} e^{-\frac{\pi}{L}a|n| - i\frac{2\pi}{L}nx}[b_n^\dagger + b_{-n}]. \tag{5.31}$$

The corresponding dispersion relation of the gapless bosonic low-energy excitations is linear in momentum. The correlation functions have been frequently calculated and decay algebraically [Gia03, CCG$^+$11]. Furthermore, the last term describes cubic scattering processes among bosonic particles rooted in the band curvature of the dispersion in Eq. (5.23) [And80, BD15]. It is mediated by the parameter $\kappa = 1/m$. Such a cubic scattering term is negligible on large distances, however is frequency dependent and therefore influences the time evolution of the system. The purpose of our work is to study the long-time and relaxation dynamics of different initial states according to a setup proposed by one-dimensional Bose gas experiments [KISD11, GKL$^+$12, GLMS14].

5.6.2 Stages of relaxation

This section is devoted to explain the physical aspects of nonequilibrium dynamics initialized by a quench scenario, where the initial state evolves according to an instantanously manipulated Hamiltonian $H_0 \to H$ [CC06, RDYO07, Caz06, CK12, AA02, KSvDZ05, BL05]. The time evolution of the initial density operator $\rho_0 = \rho(t = 0)$, which is considered to be an equilibrium state of H_0 and has thus non-diagonal elements in the eigenstate basis of H, is usually rather complex and might include certain metastable states, so-called prethermal states (cf. Fig. 5.7) [BBW04, EKW09, MK09]. A finite number of observables at this metastable fixed point might already take their thermal steady state value. At this stage, former works have proposed that the system is described by a Gibbs ensemble based on the according integral of motions $\langle A_m \rangle$ [RDYO07, Caz06, CK12, Jay57]:

$$\rho = e^{-\sum_m \lambda_m A_m} / \mathcal{Z}, \tag{5.32}$$

where λ_m are Lagrange multipliers and $\mathcal{Z}$ is the partition sum. Especially, integrable models with an extensive number of integrals of motions have been in the focus of latest studies, where the system is strongly constrained in phase space such that thermalization is not possible by ergodicity. For instance, the bare Tomonaga-Luttinger model (5.29) for $\kappa = 0$ is an integrable model. It is diagonal in the phonon basis and each momentum distribution $n_p = b_p^\dagger b_p$ is a conserved observable. We continue this discussion in Sec. 5.7. A very famous concept within the field of thermalization is the eigenstate thermalization hypothesis for which there has been so far no rigorous proof, but a variety of different models that are well described [RDO08, RS12]. It states that in case of an isolated many-body system, which is completely decoupled from its environment and has a non-degenerate eigenenergy spectrum $\{E_\alpha\}$, the matrix elements of an observable $A_{\alpha\beta} = \langle E_\alpha | A | E_\beta \rangle$ evolve in time to a thermal state described by a microcanonical ensemble with just small fluctuations around the corresponding expectation value if the following two properties hold [RS12]:

- The diagonal matrix elements $A_{\alpha\alpha}$ are smoothly varying as functions of the eigenenergies and consecutive elements are exponentially small in the system size.
- The off-diagonal elements $A_{\alpha\beta}$ $(\alpha \neq \beta)$ also decay exponentially in the system size and are much smaller than the diagonal elements.

We refer for further details to literatures on thermalization [RDO08, THKS15] including also aspects of many-body localization in this context [AABS19].

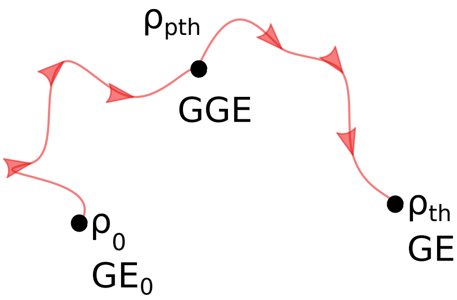

Figure 5.7 The time evolution of an initial density matrix ρ_0 described by a Gibbs ensemble (GE$_0$) of the initial Hamiltonian H_0. After a quench the density matrix is shifted out-of-equilibrium and evolves in the configuration space. It might reach a metastable fixed point, commonly called a prethermal state (ρ_{pth}), where the system is described by a generalized Gibbs ensemble (GGE). Finally, the system is considered to time evolve towards a final thermal state (ρ_{th}, GE).

5.6.3 Short review on the Keldysh formalism

A system out-of-equilibrium is commonly described using the Keldysh path integral formalism. The formalism has been explained to a large extend in the literature [AS10, Kam11, SBD16]. We thus describe in the following just the cornerstone of this approach. As usually in field integral formalisms, the generating function of the time evolution $\mathcal{Z}(t) = \mathrm{Tr}[\rho(t)]$ is mapped onto a field integral representation by separating the time line in single slices and introducing at each time step on the forward and backward branch a unity operator expressed by an appropriate basis set of the many-body system. The according action in the Keldysh framework consists then of four propagators, however with a certain redundancy that is utilized when rotating into a symmetric and antisymmetric superposition of forward and backward fields with respect to each branch. The latter is called Keldysh basis. In total, the system is then described by a retarded and advanced propagator that yield spectral information of the system and a Keldysh component that describes the occupation. At equilibrium all of these components are linked to each other in form of the fluctuation-dissipation theorem.

5.7 Relaxation dynamics of interacting Luttinger liquids

5.7.1 Overview

Lately, one-dimensional Bose gases have been realized on atom chips, which provide highly tunable platforms with long coherence time [SHA+05, HLF+06, LSH+06, FKS+08]. The experimental setup consists initially of a thermal one-dimensional Bose-Einstein condensate, which is then suddenly split into two halves [KISD11, GKL+12, GLMS14, LEG+15]. Of course, the subsequent state is highly entangled and usually non-thermal. Former studies concentrated on intermediate time-scales of the relaxation dynamics governed by the quadratic Luttinger liquid theory, which is described by a generalized Gibbs ensemble [HHM+10, GKL+12, GLMS14, LEG+15]. Our work provides a complementary approach for long times, where scattering among phonons needs to be included.

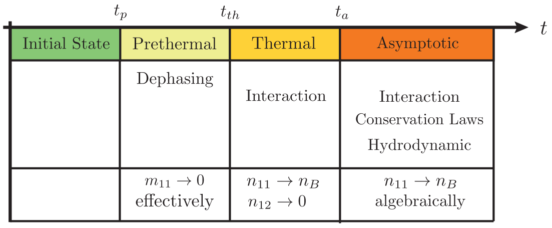

Figure 5.8 Illustration of the time regimes along which relaxation dynamics proceed, reprinted with permission from Ref. [HBSD18]. Copyright (2018) by the American Physical Society. On short time scales the annormal occupations $m_{\alpha\beta}$ $(\alpha, \beta \in \{1,2\})$ dephase, before interaction effects set in so that any inter-wire correlations $n_{\alpha\beta}$ $(\alpha \neq \beta)$ vanish and other occupations reach their thermal values. Finally, for very large times the systems is expected to be governed by slow hydrodynamic modes.

On the technical level, we map the Luttinger model with cubic scattering interaction among phonons on a Keldysh field integral representation. We then calculate the self-energies from a one-loop diagrammatic expansion using a self-consistent Born approximation. By applying kinetic theory and nonequilibrium Dyson-Schwinger equations similar to Ref. [BD15], we analyze the full relaxation dynamics beyond dephasing and include also thermalization effects.

After the split, the two one-dimensional Bose gases are usually released in the experiment and studied by their characteristic interference pattern [KISD11, GKL+12, GLMS14, LEG+15]. In our work below we study the integrated interference pattern from the experiment in comparison to our theoretical approach. Furthermore, the relative phase correlation function among the two-condensates is extracted from the experimental data and is also calculated within our analysis to monitor the time-dependent relaxation of the two-wire system.

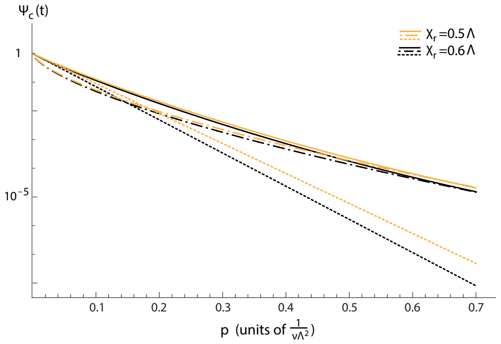

Figure 5.9 The coherence factor from the kinetic equation (bold line) shows for short times dephasing dynamics (dotted line) and afterwards clear signatures of collisions between phonons (dash-dotted line), reprinted with permission from Ref. [HBSD18]. Copyright (2018) by the American Physical Society. The two colors, bright and dark, represent two initial states.

Our analysis has led to the following conclusions

- We have established a quantitative tool for one-dimensional Bose gas experiments covering thermalization time scales.
- A crossover scale $x_t^{(c)} \sim t^{2/3}$ is determined that separates regimes with single-particle and many-body effects in agreement with the Andreev exponent (cf. article below 5.7.2).

We further propose an initial state for future experimental realizations, which oscillates on a certain momentum scale similar to Ref. [LEG+15], and that enables the clear distinction between dephasing and thermal regime. The oscillations are shown to be completely washed out solely by interactions among phonons.

Thermalization dynamics of two correlated bosonic quantum wires after a split

by

S. Huber[1], M. Buchhold[2,3], J. Schmiedmayer[4], and S. Diehl[2]

[1]Physics Department, Arnold Sommerfeld Center for Theoretical Physics and Center for NanoScience, Ludwig-Maximilians-University Munich, 80333 Munich, Germany

[2]Institute of Theoretical Physics, University Cologne, 50937 Cologne, Germany

[3]Department of Physics and Institute for Quantum Information and Matter, California Institute of Technology, Pasadena, California 91125, USA

[4]Vienna Center for Quantum Science and Technology, Atominstitut, TU Wien, Stadionallee 2, 1020 Vienna, Austria

reprinted on pages 125–143

with permission from

Phys. Rev. A **97(4), 043611 (2018)**,

DOI: 10.1103/PhysRevA.97.043611.

PHYSICAL REVIEW A **97**, 043611 (2018)

Thermalization dynamics of two correlated bosonic quantum wires after a split

Sebastian Huber,[1] Michael Buchhold,[2,3] Jörg Schmiedmayer,[4] and Sebastian Diehl[2]
[1] *Physics Department, Arnold Sommerfeld Center for Theoretical Physics and Center for NanoScience, Ludwig-Maximilians-University Munich, 80333 Munich, Germany*
[2] *Institute of Theoretical Physics, University Cologne, 50937 Cologne, Germany*
[3] *Department of Physics and Institute for Quantum Information and Matter, California Institute of Technology, Pasadena, California 91125, USA*
[4] *Vienna Center for Quantum Science and Technology, Atominstitut, TU Wien, Stadionallee 2, 1020 Vienna, Austria*

(Received 26 January 2018; published 11 April 2018; corrected 28 June 2018)

Coherently splitting a one-dimensional Bose gas provides an attractive, experimentally established platform to investigate many-body quantum dynamics. At short enough times, the dynamics is dominated by the dephasing of single quasiparticles, and well described by the relaxation towards a generalized Gibbs ensemble corresponding to the free Luttinger theory. At later times on the other hand, the approach to a thermal Gibbs ensemble is expected for a generic, interacting quantum system. Here, we go one step beyond the quadratic Luttinger theory and include the leading phonon-phonon interactions. By applying kinetic theory and nonequilibrium Dyson-Schwinger equations, we analyze the full relaxation dynamics beyond dephasing and determine the asymptotic thermalization process in the two-wire system for a symmetric splitting protocol. The major observables are the different phonon occupation functions and the experimentally accessible coherence factor, as well as the phase correlations between the two wires. We demonstrate that, depending on the splitting protocol, the presence of phonon collisions can have significant influence on the asymptotic evolution of these observables, which makes the corresponding thermalization dynamics experimentally accessible.

DOI: 10.1103/PhysRevA.97.043611

I. INTRODUCTION

In recent years, the field of ultracold atoms has produced tremendous progress in the experimental realization and observation of many-body quantum dynamics out of equilibrium [1–7]. Experiments have demonstrated that the purity of cold-atom systems in combination with their large degree of controllability allows one to precisely probe the fundamental processes in quantum many-body systems. This is exploited by a growing number of experiments, which study the relaxation dynamics of interacting quantum systems in a controlled environment, thereby fostering a more detailed understanding of paradigmatic single- and many-body effects, such as dephasing [1,8–10] and thermalization [4,11–15].

One-dimensional quantum systems play a special role in this context since the dynamics, especially that of collisions, is constrained to a reduced phase space. For many systems this leads to the emergence of an extensive number of quasiconserved charges, i.e., an extensive number of physical observables which are protected from fast relaxation by approximate conservation laws. The violation of these conservation laws becomes only visible for large timescales. Consequently, a large number of experiments with one-dimensional quantum gases has been described very well in terms of integrable models, for which the conservation laws become exact [2,7,16,17]. One general feature of these integrable models is the absence of thermalization, expressed by the fact that, due to the large number of conservation laws, they never relax towards a thermal Gibbs ensemble [2,7,13,16,18–23], but keep the information on their initial state for all times and evolve towards a so-called generalized Gibbs ensemble (GGE).

Realistic systems, however, are expected to behave generically, and to asymptotically approach a thermal state, although very slowly in one dimension [24,25]. The aim of this work is to study the full relaxation dynamics process, including thermalization, for a gas of ultracold bosons after initialization in an out-of-equilibrium state. The specific setup consists of an initial, one-dimensional Bose-Einstein condensate (BEC), which is suddenly split into two halves along its longitudinal axis, as it is performed experimentally in Vienna [2,7,16,26]. The system, now consisting of two initially strongly correlated condensates, evolves in time and relaxes towards a stationary state.

On short enough timescales, most of the relaxation dynamics has been described successfully in terms of the integrable Luttinger theory. It predicts the light-cone shaped dephasing of anomalous phonon modes, which leads to the transient relaxation of the system towards a GGE [18,22,24,27]. The GGE state is determined by the initial expectation value of the conserved charges of the integrable Luttinger theory. This description, however, neglects the effect of phonon-phonon collisions and the associated decay of the interwire correlations, as well as the energy redistribution between the modes within each individual wire. The processes, while very slow on experimental timescales, lead to the breakdown of the GGE on larger timescales, and the relaxation of the system towards a thermal Gibbs state.

The goal of this paper is to obtain a complete and quantitative picture of the thermalization dynamics of one-dimensional Bose gases, including the regime where nonlinear effects are important. In particular, we assess the observability of the associated physical effects in experiments. To this end, we study the time evolution of the two-wire system after the splitting in terms of a nonlinear Luttinger theory, which incorporates the leading order phonon scattering mechanisms for a gas of one-dimensional bosons. We focus on a regime with a large Luttinger parameter $K \gg 1$, i.e., weakly interacting bosons, for which diagrammatic methods are applicable [25,28–32]. The BEC is longitudinally trapped in a box potential of length L, which can be realized experimentally with high accuracy [33] and which allows us to approach the dynamics within a Luttinger framework with a physical infrared momentum cutoff $k_{\mathrm{IR}} = L^{-1}$. All analytical results will be discussed for $k_{\mathrm{IR}} = 0$, while the numerical simulations are carried out for $k_{\mathrm{IR}} = L^{-1}$. We determine the time evolution of temporally local correlators of the system, as these are the quantities accessible in current experiments.

Summary of main results. Our approach is based on a combination of Dyson-Schwinger and kinetic equations for the weakly interacting Bose gas. In this way, we are able to quantitatively capture all stages of the thermalization process, including the hydrodynamic relaxation enforced by global conservation laws on asymptotically large times [25].

At short times, dephasing of noninteracting phonon modes leads to a fast relaxation towards a generalized Gibbs ensemble. The physics can be understood on the single-phonon level, i.e., technically in the framework of the quadratic Luttinger theory. For intermediate and large times $t > t_{\mathrm{coll}}$, set by the typical phonon collision time t_{coll}, interactions become important and relaxation dynamics enters the realm of many-body physics. Collisions lead to energy redistribution between the phonons and to local equilibration, while on the other hand conservation laws do not yet play a dominant role. On the asymptotic timescales, however, conservation laws constrain the effects of many collisions and the dynamics enters a many-body hydrodynamic regime. This leads to algebraically slow relaxation of observables [25].

In addition to a quantitative description of the different dynamical regimes, we obtain as well a time-resolved estimate for the crossover scale $x_t^{(c)} \sim t^{2/3}$ between the single-particle and the many-particle regime. It grows in time with the typical Andreev exponent $1/\alpha = 2/3$ [29–32], confirming the picture that thermalization proceeds from high to low momentum modes, with crossover momentum $q^{(c)} \sim 1/x^{(c)}$. Collisions also lead to a stronger decay of coherence, which modifies the decay of the relative phase correlation function $\ln C_r \sim -t^{4/3}$ to faster than linear in time on large distances.

Our formulation allows us to address direct experimental observables, such as the relative phase correlation function and the coherence factor. We find that a careful choice of observables is necessary to quantitatively certify thermalization in the experiment. In more detail, our results indicate that for the standard splitting procedure both the relative phase correlation function as well as the coherence factor are only weakly modified by phonon collisions beyond the quadratic Luttinger model. Thermalization, while definitely present, is therefore hard to observe in common observables. This is caused by the form of the initial phonon distribution function, which follows a thermal Rayleigh-Jeans divergence $n_{p,t} \sim T_r/|p|$, with typical temperature T_r, at low momenta. While this temperature increases through the thermalization process towards an absolute temperature T_a, the form of the distribution remains untouched and thus no qualitative change in observables can be measured.

In order to overcome the difficulty in resolving thermalization, we propose to initialize the condensate in a modified far-from-equilibrium state, for which the phonon densities are different from a thermal distribution. Inspired by the recent realization of one such nonthermal state [16], we investigate initial states for which the phonon distribution oscillates on momentum scales ξ^{-1}. These oscillations remain preserved under dephasing but are washed out by the redistribution of energy in the thermalization process, leading to a strongly increased signal of thermalization at distances $x = 2\xi$, which could be detected in experiments and which would lead to a clear observation of t_{coll}.

This paper is organized as follows. We start by introducing the interacting Luttinger model and discussing the relevant physical observables in Sec. II. In Sec. III, we derive the kinetic equation approach for the correlated two-wire system. This section can be skipped by a reader more interested in the physics results. The formalism is then applied in Sec. IV to study the relaxation dynamics of an initial state which has nearly thermal form, corresponding to Refs. [2,7]. A discussion of the various stages of the relaxation process is provided in Sec. IV B. In Sec. V, a class of initial states is considered, which differ more strongly from a thermal state, and a representative of which has been implemented in recent experiments [16]. We conclude in Sec. VI.

II. MODEL

The present work analyzes the longitudinal splitting of a one-dimensional Bose-Einstein condensate at time $t = 0$, and the subsequent time evolution of the two resulting, identical and initially correlated BECs [2,7,26]. Each individual wire represents a one-dimensional gas of interacting bosons, whose long-wavelength dynamics will be described in the following in terms of an interacting Luttinger liquid theory. For a sufficiently strong separation of the two wires, all interwire couplings in the Hamiltonian vanish and the only correlations between the two gases result from the correlations in the initial state for $t < 0$.

A. Hamiltonian

Labeling the two subsystems with bosonic creation and annihilation operators $b^\dagger_{\alpha,x}, b_{\alpha,x}, \alpha \in \{1,2\}$, where $b_{\alpha,x}$ annihilates a boson at coordinate x in wire α, the Hamiltonian of the joint system for times $t > 0$ is

$$H = H_{1,\mathrm{IB}} \otimes \mathbb{1}_2 + \mathbb{1}_1 \otimes H_{2,\mathrm{IB}}. \tag{2.1}$$

Here, $H_{\alpha,\mathrm{IB}}$ describes a generic system of short-range interacting bosons with mass m,

$$\begin{aligned} H_{\alpha,\mathrm{IB}} = &\int_x b^\dagger_{\alpha,x}\left[V(x) - \frac{\hbar^2}{2m}\nabla^2\right]b_{\alpha,x} \\ &+ \int_{x,x'} b^\dagger_{\alpha,x} b_{\alpha,x} u(x-x') b^\dagger_{\alpha,x'} b_{\alpha,x'}, \end{aligned} \tag{2.2}$$

with a two-body interaction potential u, which is short-ranged in space, and an external potential V, which we consider flat enough to justify a local density approximation (LDA).

The creation and annihilation operators are conveniently expressed in terms of conjugate phase and amplitude fields, $b_{\alpha,x} = \sqrt{\rho_{\alpha,x}}e^{i\theta_{\alpha,x}}$, with $\rho_{\alpha,x} = \rho_0 - \frac{1}{\pi}\nabla\phi_{\alpha,x}$, where ρ_0 is the average particle density in both wires [34,35]. Phase and amplitude are conjugate variables:

$$[\phi_{\alpha,x},\nabla\theta_{\beta,x'}] = -i\delta(x-x')\delta_{\alpha,\beta}. \tag{2.3}$$

In phase-amplitude representation, the leading order terms of the Hamiltonian (2.2) correspond to an interacting Luttinger liquid (ILL) [28–30] and read

$$\begin{aligned} H_{\alpha,\mathrm{ILL}} = \frac{\hbar}{2\pi}\int_x \bigg[& \nu K(\partial_x\theta_{\alpha,x})^2 + \frac{\nu}{K}(\partial_x\phi_{\alpha,x})^2 \\ & + \kappa(\partial_x\phi_{\alpha,x})(\partial_x\theta_{\alpha,x})^2\bigg]. \end{aligned} \tag{2.4}$$

The first line of this equation is quadratic in the fields and represents the noninteracting Luttinger liquid, which describes noninteracting elementary excitations, i.e., phonons, propagating with sound velocity $\nu = \sqrt{\frac{\rho_0 u(0)}{m}}$ and Luttinger parameter $K = \frac{\pi\hbar}{2}\sqrt{\frac{\rho_0}{u(0)m}}$. This quadratic part is integrable and governs the transient dynamics after the splitting. It leads to the evolution of the system towards a quasistationary state, a so-called generalized ensemble (GGE) [18,22,24,27].

The second line of Eq. (2.4) instead is a nonlinear coupling, which represents the leading order deviation from an integrable model and makes the ILL generic; i.e., it enables true thermalization on large and asymptotic timescales [28–30]. The vertex κ describes the deviation from a perfectly linear dispersion and can be estimated to be $\kappa = \hbar/m$, where m is the mass of an atom. The major contribution of this work is to include the effect of nonzero κ, and to study the asymptotic thermalization after two different, experimentally relevant splitting procedures. This extends the understanding of the relaxation dynamics after the splitting to timescales beyond prethermalization.

The Hamiltonian of the entire system after the splitting is again the sum of the two individual wires:

$$H = H_{1,\mathrm{ILL}} \otimes \mathbb{1}_2 + \mathbb{1}_1 \otimes H_{2,\mathrm{ILL}}. \tag{2.5}$$

Since the considered splitting protocol is symmetric with respect to the wires, both will be identical in geometry and average particle density after the splitting. Thus, they are described by the same set of Luttinger parameters $\{\nu,K,\kappa\}$.

In order to diagonalize the quadratic part of the Hamiltonian $H_{\alpha,\mathrm{ILL}}$, one applies the canonical Bogoliubov transformation [34,35] to the phonon operators $a^\dagger_{\alpha,x},a_{\alpha,x}$,

$$\theta_{\alpha,x} = \Theta_\alpha + i\int_p' \sqrt{\frac{\pi}{2K|p|}}e^{-ipx-\frac{|p|}{\Lambda}}(a^\dagger_{\alpha,p} - a_{\alpha,-p}), \tag{2.6}$$

$$\phi_{\alpha,x} = \Phi_\alpha - i\int_p' \sqrt{\frac{\pi K}{2|p|}}\mathrm{sgn}(p)e^{-ipx-\frac{|p|}{\Lambda}}(a^\dagger_{\alpha,p} + a_{\alpha,-p}), \tag{2.7}$$

where $\Lambda = \sqrt{4mu(0)\rho_0}/\hbar$ is the short-distance cutoff, $a_{\alpha,p} = \int_x e^{ipx}a_{\alpha,x}$, and the integral $\int_p'$ runs over all momenta except $p = 0$. The global, zero-momentum modes $\Theta_\alpha,\Phi_\alpha$ contribute only to the global dephasing of the wires [33], which is not considered here, and are therefore neglected in the following.

In this basis, the quadratic part of the Hamiltonian [first line of Eq. (2.4)] is diagonal and describes phonons with a linear dispersion $\epsilon_p = \nu|p|$. The nonlinear part of the Hamiltonian describes cubic phonon scattering processes. It can be decomposed into a resonant part, which conserves the phonon energies, and an off-resonant part, which does not conserve the phonon energy during a single scattering process. The latter processes induce only virtual transitions between the many-body states and represent irrelevant contributions for the forward time evolution, in contrast to the resonant ones [36]. The common procedure is thus to neglect the off-resonant scattering processes in a rotating wave approximation for the kinetics at large times, and only consider resonant processes. In the resonant approximation, the Hamiltonian is

$$\begin{aligned} H_{\alpha,\mathrm{ILL}} = \int_p \nu|p|a^\dagger_{\alpha,p}a_{\alpha,p} + v\int_{p,q}'' & \sqrt{|pq(q+p)|} \\ & \times (a^\dagger_{\alpha,p+q}a_{\alpha,p}a_{\alpha,q} + \mathrm{H.c.}), \end{aligned} \tag{2.8}$$

with $v = \kappa\sqrt{\frac{9\pi}{2K}}$. The integral $\int_{q,p}''$ only considers resonant processes, i.e., those processes with $|p+q| = |p| + |q|$ (for more details on the resonant approximation, see [28,29,36]). From now on, we set $\hbar = 1$ within the analytic expressions.

The Hamiltonian, Eqs. (2.5) and (2.8), describes the time evolution of the two wires after they have been split initially at $t = 0$. Each wire thereby represents an independent, interacting Luttinger liquid and the Hamiltonian generates no additional interwire correlations. The latter are, however, generated by the splitting procedure itself and the analysis of the interwire and intrawire correlations' time evolution under (2.5) is the purpose of this article.

B. Phonon correlation functions

In the following sections, the dynamics of the two wires is analyzed in terms of the single-particle phonon Green's functions, which in turn determine a set of relevant physical observables. These are for instance the so-called phase correlation function $C(x,t) = \langle e^{i(\theta_{1,x,t}-\theta_{2,x,t})}e^{-i(\theta_{1,0,t}-\theta_{2,0,t})}\rangle$ between the two wires and the coherence factor $\Psi_c(t)$, which we will introduce in this section. The basic notation and relations for the nonequilibrium Green's functions will be discussed below.

In the Heisenberg picture, with operators $a_{\alpha,p,t} = e^{iHt}a_{\alpha,p}e^{-iHt}$, the retarded Nambu response function is defined as

$$iG^R_{\alpha,\beta,p,t,t'} = \Theta(t-t')\begin{pmatrix} \langle[a_{\alpha,p,t},a^\dagger_{\beta,p,t'}]\rangle & \langle[a_{\alpha,p,t},a_{\beta,-p,t'}]\rangle \\ \langle[a^\dagger_{\alpha,-p,t},a^\dagger_{\beta,p,t'}]\rangle & \langle[a^\dagger_{\alpha,p,t},a_{\beta,p,t'}]\rangle \end{pmatrix}, \tag{2.9}$$

while the Nambu correlation function (or Keldysh Green's function) is defined as

$$iG^K_{\alpha,\beta,p,t,t'} = \begin{pmatrix} \langle\{a_{\alpha,p,t},a^\dagger_{\beta,p,t'}\}\rangle & \langle\{a_{\alpha,p,t},a_{\beta,p,t'}\}\rangle \\ \langle\{a^\dagger_{\alpha,p,t},a^\dagger_{\beta,p,t'}\}\rangle & \langle\{a^\dagger_{\alpha,p,t},a_{\beta,p,t'}\}\rangle \end{pmatrix}. \tag{2.10}$$

Here, $[\cdot,\cdot]$ labels the commutator and $\{\cdot,\cdot\}$ the anticommutator.

The retarded Green's function can immediately be simplified by noticing that the Hamiltonian (2.5) does not introduce any interwire coupling and therefore states with $\alpha \neq \beta$ in Eq. (2.9) commute at all times. Furthermore, within a single wire, $H_{\alpha,\mathrm{ILL}}$ in (2.8) does not couple states with opposite momenta $a_{\alpha,q,t}, a_{\alpha,-q,t'}$. Consequently, the off-diagonal elements of G^R vanish exactly for all times t,t'. The advanced Green's function is the Hermitian conjugate of the retarded Green's function, $G^A = (G^R)^\dagger$.

A special emphasis will be put on the equal-time Green's functions, relevant for current experiments, which determine the time evolution of static, i.e., frequency-independent, observables. For the retarded and advanced Green's functions, one finds

$$\left(G^R_{\alpha,\beta,q,t,t} - G^A_{\alpha,\beta,q,t,t}\right) = -i\delta_{\alpha,\beta}\sigma_z, \tag{2.11}$$

$$\left(G^R_{\alpha,\beta,q,t,t} + G^A_{\alpha,\beta,q,t,t}\right) = 0 \tag{2.12}$$

for all times, while

$$iG^K_{\alpha,\beta,p,t,t} = \begin{pmatrix} 2n_{\alpha,\beta,p,t} + \delta_{\alpha,\beta} & 2m_{\alpha,\beta,p,t}e^{2i\nu|p|t} \\ 2m_{\alpha,\beta,p,t}e^{-2i\nu|p|t} & 2n_{\beta,\alpha,p,t} + \delta_{\alpha,\beta} \end{pmatrix}. \tag{2.13}$$

It describes the time evolution of intra- $(\alpha = \beta)$ and interwire $(\alpha \neq \beta)$ phonon densities, both diagonal $n_{\alpha,\beta,p,t} = \langle a^\dagger_{\alpha,p,t} a_{\beta,p,t}\rangle$ and off-diagonal $m_{\alpha,\beta,p,t} = |\langle a_{\alpha,p,t} a_{\beta,p,t}\rangle|$. Here we made the time-dependent complex phase of the off-diagonal modes explicit such that $m_{\alpha,p,t}$ is real and positive for all times.

Both wires are exactly identical and therefore the system is symmetric under the exchange of the wire index; this yields

$$G^{R/A/K}_{11,p,t,t'} = G^{R/A/K}_{22,p,t,t'} \quad \text{and} \quad G^{R/A/K}_{12,p,t,t'} = G^{R/A/K}_{21,p,t,t'}. \tag{2.14}$$

The same holds for the phonon densities in the wire basis

$$n_{11,p,t} = \langle a^\dagger_{1,p,t} a_{1,p,t}\rangle = \langle a^\dagger_{2,p,t} a_{2,p,t}\rangle = n_{22,p,t}, \tag{2.15}$$

$$n_{12,p,t} = \langle a^\dagger_{1,p,t} a_{2,p,t}\rangle = \langle a^\dagger_{2,p,t} a_{1,p,t}\rangle = n_{21,p,t}, \tag{2.16}$$

$$m_{12,p,t} = |\langle a_{1,p,t} a_{2,p,t}\rangle| = |\langle a_{2,p,t} a_{1,p,t}\rangle| = m_{21,p,t}. \tag{2.17}$$

C. Relative and absolute mode and experimental observables

Due to the symmetry of the system under exchange of the wires, i.e., $1 \leftrightarrow 2$, the Green's functions in the wire basis $G^{R/A/K}_{\alpha,\beta}$ show some redundancy. It can be removed by switching from the basis of individual wires to a basis of relative and absolute degrees of freedom for the two wires. These latter degrees of freedom give a more compact description and are directly related to the relevant experimental observables such as the relative phase correlation function and the coherence factor of the bosons.

The relative $(a_{r,p,t})$ and absolute $(a_{a,p,t})$ degrees of freedom are introduced by the unitary transformation of the Heisenberg operators

$$\begin{pmatrix} a_{a,p,t} \\ a_{r,p,t} \end{pmatrix} = \frac{1}{\sqrt{2}} \begin{pmatrix} 1 & 1 \\ 1 & -1 \end{pmatrix} \begin{pmatrix} a_{1,p,t} \\ a_{2,p,t} \end{pmatrix}. \tag{2.18}$$

Using Eq. (2.14), one can directly see that correlations between the absolute and relative modes vanish, and that only two independent Nambu Green's functions are required, namely the absolute and the relative Green's functions

$$G^\lambda_{a,p,t,t'} = G^\lambda_{11,p,t,t'} + G^\lambda_{12,p,t,t'}, \tag{2.19}$$

$$G^\lambda_{r,p,t,t'} = G^\lambda_{11,p,t,t'} - G^\lambda_{12,p,t,t'}, \tag{2.20}$$

with $\lambda = R,A,K$. We note that this does not require any specific form of the interactions but only the fact that the Hamiltonian as well as the initial conditions are invariant under exchange of the wire indexes.

The dynamics of $G^\lambda_{r/a,p,t,t'}$ is uniquely determined by $G^\lambda_{11,p,t,t'}$ and $G^\lambda_{12,p,t,t'}$. It is equivalent to work in the relative and absolute basis or in the basis of individual wires. The Hamiltonian, however, and the corresponding time evolution take a simpler form in the individual-wire basis. On the other hand, experimental signatures and the initial state of the system are determined in the relative-absolute basis. In the following, the most convenient of both representations is used, depending on the individual computation.

The major experimental observable for the present system is the relative phase between the two wires, from which the relative coherence between the wires is extracted. This observable can be measured with high precision in matter-wave interferometry measurements [9,31,37]. This is done by releasing the two condensates from the wires, and then letting them expand freely in space. When the two condensates start to overlap, they form a characteristic interference pattern. The integrated interference pattern is described by the coherence factor of the two condensates

$$\Psi_c(t) = L^{-1}\int_x \langle b^\dagger_{1,x,t} b_{2,x,t}\rangle = \frac{\rho_0}{L}\int_x \langle e^{i(\theta_{r,x,t})}\rangle = \rho_0 e^{-g(t)}, \tag{2.21}$$

where the integral runs over the entire length L of the wire and $\theta_{r,x,t} = \theta_{1,x,t} - \theta_{2,x,t}$ is the relative phase of the two condensates. The subleading effect of density fluctuations has been neglected in the definition of $\Psi_c(t)$.

According to the linked cluster theorem, the coherence factor up to fourth-order vertex corrections [25,38] is

$$\begin{aligned} g(t) &= \int_p \frac{\pi e^{-\frac{|p|}{\Lambda}}}{8K|p|}\mathrm{Tr}\left[iG^K_{r,p,t}(\mathbb{1} + \sigma^x)\right] \qquad (2.22) \\ &= \int_p \frac{\pi e^{-\frac{|p|}{\Lambda}}}{8K|p|}[2n_{r,p,t} + 1 - 2\cos(2\nu|p|t)m_{r,p,t}]. \end{aligned}$$

It is fully determined by the time evolution of the relative phonon densities $n_{r,p,t}, m_{r,p,t}$. For the present analysis, we approximate the system as being spatially homogenous. This approximation applies very well for current experiments, which are governed by the dynamics in the longitudinal center of the wires [2,7,26].

A further tool to get experimental access to the correlations between the two wires is to measure the relative phase between the two wires for different positions in space. The observed interference pattern of this measurement is proportional to the phase correlation function

$$C(x,t) = e^{-\frac{1}{2}\Delta\theta_{r,x,t}}, \tag{2.23}$$

where $x = x_1 - x_2$ and $\Delta\theta_{r,x,t} = \langle[\theta_{r,x,t} - \theta_{r,0,t}]^2\rangle$. The relative phase fluctuation $\Delta\theta_{r,x,t}$ is determined along the lines of Eq. (2.21),

$$\Delta\theta_{r,x,t} = \int_p \left\{ \frac{\pi e^{-\frac{|p|}{\Lambda}}}{4Kp}[1-\cos(px)] \right. \\ \left. \times [2n_{r,p,t} + 1 - 2\cos(2\nu|p|t)m_{r,p,t}] \right\}. \tag{2.24}$$

It reveals the time-dependent spatial spread (or decay) of correlations and has served as the major experimental observable to monitor the time-dependent relaxation of the two-wire system. In order to shorten notation in the following, we will refer to $\Delta\theta_{r,x,t}$ simply as the relative phase.

In order to make theoretical predictions on the dynamics of the phase correlation function and the coherence factor of the system after the split, we thus need to determine the time evolution of the relative phonon densities $n_{r,p,t}, m_{r,p,t}$. In the major body of previous works, this has been performed in terms of the quadratic Luttinger theory, which neglects collisions between phonons, as described by the cubic part of Eq. (2.8). This is well justified for short and intermediate times, which are smaller that the typical, inverse collision rate, and describes the so-called prethermalization dynamics. The present work goes beyond the former, noninteracting approaches and takes into account the effect of phonon-phonon scattering, which leads to an energy redistribution between the phonon modes and enables thermalization on large timescales. The time evolution of the phonon densities is determined via a kinetic equation approach, which is set up in the following section.

III. KINETIC EQUATION FOR THE PHONON DENSITIES

The time evolution of the phonon densities in the present system is determined by a modified version of the common kinetic equation approach [29,36]. It has been established in previous works in order to deal with the resonant phonon interactions, for which perturbative approaches display fatal on-shell divergencies. The kinetic equation approach here is based on Dyson-Schwinger equations [39,40], resulting in regular expressions for the time evolution of the phonon densities. The Dyson-Schwinger equations will be truncated at the level of the cubic vertex (to be precise, including the cubic vertex correction) and solved self-consistently. This approach has been outlined in detail in [28,29] and will be briefly discussed below, including the extension to the bosonic two-wire system.

The kinetic equation is expressed in temporal Wigner coordinates, which describe the time evolution of any two-time function, depending on time variables t_1, t_2, as a function of the average forward time $t = \frac{t_1+t_2}{2}$ and the relative time $\delta_t = t_1 - t_2$. Fourier-transforming the relative time coordinate introduces the frequency ω, i.e., $G_{t,\omega} = \int_{\delta_t} e^{i\omega\delta_t} G_{t,\delta_t}$ for an arbitrary Green's function. Frequency integration thus produces equal-time functions in Wigner representation. The Dyson equation [38] in the individual-wire basis and in Wigner coordinates reads

$$G^{-1}_{\alpha\beta,p,\omega,t} = \begin{pmatrix} 0 & P^A_{\alpha\beta,p,\omega,t} - \Sigma^A_{\alpha\beta,p,\omega,t} \\ P^R_{\alpha\beta,p,\omega,t} - \Sigma^R_{\alpha\beta,p,\omega,t} & -\Sigma^K_{\alpha\beta,p,\omega,t} \end{pmatrix}, \tag{3.1}$$

with the self-energies $\Sigma^{R,A,K}_{\alpha\beta,p,\omega,t}$, and the bare propagators of the noninteracting system $P^{R,A}_{\alpha\beta,p,\omega,t} = [\sigma_z(\omega \pm i\eta) - \nu|p|\mathbb{1}]\delta_{\alpha,\beta}$. The retarded and advanced Green's functions are modified in the presence of interactions due to nonzero self-energies $\Sigma^{R,A}_{\alpha\beta,p,\omega,t}$. As pointed out above, however, the Hamiltonian neither mixes different wires $\alpha \neq \beta$ nor opposite momenta $p, -p$ and thus the retarded and advanced self-energies are diagonal in the wire index and in Nambu space.

Considering a spectral function that has support only in the close vicinity of the dispersion, the relevant self-energy contributions for the kinetic equation are the ones which are on-shell, i.e., which fulfill $\omega = \nu|p|$ [36]. Here, these contributions are purely imaginary and the on-shell self-energy can be parametrized as [29] [see also Appendix A, Eq. (A10), with $\Phi^R_{\alpha\beta,p,\omega,t} = 0$]

$$\Sigma^R_{\alpha\beta,p,\omega=\nu|p|,t} = -i\delta_{\alpha\beta}\begin{pmatrix} \sigma^R_{p,t} & 0 \\ 0 & \sigma^A_{p,t} \end{pmatrix}. \tag{3.2}$$

Here, $\sigma^{R,A}_{p,t}$ are positive functions of momentum p and forward time t. For $\sigma^{R,A}_{p,t} \ll \nu|p|$, the self-energy is interpreted as the inverse lifetime $\tau^{-1}_{p,t} = \sigma^R_{p,t}$ of the phonon modes, which remain well-defined quasiparticles in this case.

The on-shell Keldysh self-energy is, by definition, anti-Hermitian and, due to the symmetry of the system with respect to exchange of the wires, conveniently parametrized as

$$\Sigma^K_{\alpha\beta,p,\omega=\nu|p|,t} = -i2\begin{pmatrix} \sigma^K_{\alpha\beta,p,t} & \Phi^K_{\alpha\beta,p,t} \\ \Phi^K_{\alpha\beta,p,t} & \sigma^K_{\alpha\beta,p,t} \end{pmatrix}. \tag{3.3}$$

In contrast to the retarded self-energy, the off-diagonal elements of the Keldysh self-energy both in Nambu space and in the wire index are generally nonvanishing. This is a consequence of the initial splitting protocol, which generates correlations between the wires but also occupies anomalous phonon modes. We have, however, again factored out the complex phase of the off-diagonal modes, as in Eq. (2.13). As a consequence, Φ^K is purely real for all times.

The kinetic equation for the phonon occupations is determined by parametrizing the anti-Hermitian Keldysh Green's function in terms of the retarded, advanced Green's functions and the Hermitian occupation function F, i.e.,

$$G^K_{p,\omega,t} = (G^R \circ \Sigma_z F - F\Sigma_z \circ G^A)_{p,\omega,t}, \tag{3.4}$$

where $\circ$ denotes the convolution with respect to times and frequencies and matrix multiplication with respect to momentum, Nambu, and wire index. The matrix $\Sigma_z = \sigma_z \otimes \mathbb{1}$ ensures the symplectic structure of bosonic Nambu space. Inserting Eq. (3.4) into (3.1), one finds

$$(P^R \circ \Sigma_z F - F\Sigma_z \circ P^A)_{p,\omega,t} = I^{\text{coll}}_{p,\omega,t}, \tag{3.5}$$

with the collision integral

$$I^{\text{coll}}_{p,\omega,t} = \Sigma^K_{p,\omega,t} - (\Sigma^R \circ \Sigma_z F - F\Sigma_z \circ \Sigma^A)_{p,\omega,t}. \tag{3.6}$$

In order to bring Eqs. (3.5) and (3.6) into a convenient form, several steps have to be performed, which are outlined in Appendix A. First, the Green's functions and the occupation function have to be expressed in the Dirac interaction picture. This guarantees that the left-hand side of (3.5) becomes proportional to the temporal derivative of F. Second, one has to apply the Wigner approximation to the second term of the collision integral (3.6). The latter approximates convolution with respect to frequency and time in Wigner representation by the product

$$I^{\text{coll}}_{p,\omega,t} \approx \Sigma^K_{p,\omega,t} - \left(\Sigma^R_{p,\omega,t}\Sigma_z F_{p,\omega,t} - F_{p,\omega,t}\Sigma_z\Sigma^A_{p,\omega,t}\right). \tag{3.7}$$

As detailed in Appendix A and Refs. [25,28,29], this is justified as long as the condition

$$\frac{|\partial_t F_{\alpha\beta,q,\omega,t}|\left|\partial_\omega \Sigma^R_{\alpha\beta,q,\omega,t}\right|}{|F_{\alpha\beta,q,\omega,t}|\left|\Sigma^R_{\alpha\beta,q,\omega,t}\right|} \ll 1 \tag{3.8}$$

is fulfilled. Physically, Eq. (3.8) requires that the characteristic timescale of the global system's time evolution is much larger than the characteristic timescale of a single scattering event. This is justified for splitting protocols, at sufficiently low energies, for which (see Ref. [29])

$$\epsilon v \ll v^2, \tag{3.9}$$

where ϵ is the average energy per momentum mode in the system.

Multiplying both sides of the kinetic equation (3.5) with the system's spectral functions

$$\mathcal{A}_{p,\omega,t} = \frac{i}{2\pi}\left(G^R_{p,\omega,t} - G^A_{p,\omega,t}\right) \tag{3.10}$$

projects the kinetic equation onto the region where $\mathcal{A}_{p,\omega,t}$ has nonzero support, i.e., onto the physical quasiparticle states. For a given momentum and energy p,ϵ_p the width of the spectral function can be estimated to be $\sim\sigma^R_p \ll \epsilon_p$ in the relevant regime of low momenta and small energy density [29,32]. The corresponding criterion in the present setting is identical to the criterion for Luttinger theory to be applicable, i.e., to have a sufficiently low excitation energy density $n_q < \Lambda/q$ (cf. [28]). The kinetic equation is thus projected on-shell and one can make use of Eqs. (3.2) and (3.3) to simplify the collision integral I^{coll}. On the other hand (for $\alpha,\beta = 1,2$) (2.15),

$$\int_\omega (\mathcal{A}\Sigma_z F\Sigma_z)_{\alpha\beta,p,\omega,t} \approx \begin{pmatrix} 2n_{\alpha\beta,p,t} + \delta_{\alpha,\beta} & -2m_{\alpha\beta,p,t} \\ -2m_{\alpha\beta,p,t} & 2n_{\alpha\beta,p,t} + \delta_{\alpha,\beta} \end{pmatrix}, \tag{3.11}$$

which finally leads to

$$\partial_t n_{11,p,t} = \sigma^K_{11,p,t} - \sigma^R_{p,t}(2n_{11,p,t} + 1), \tag{3.12}$$

$$\partial_t n_{12,p,t} = \sigma^K_{12,p,t} - 2\sigma^R_{p,t} n_{12,p,t}, \tag{3.13}$$

$$\partial_t m_{11,p,t} = \Phi^K_{11,p,t} - 2\sigma^R_{p,t} m_{11,p,t}. \tag{3.14}$$

The anomalous densities $m_{12,p,t}$ never deviate from zero and their time evolution is not considered here.

The self-energies are evaluated in the self-consistent Born approximation; see Appendix B. An additional rescaling of time $\tilde{t} = vt$ and the retarded self-energy $\tilde{\sigma}^R_{p,t} = v^{-1}\sigma^R_{p,\tilde{t}}$ removes the explicit dependence of $\tilde{\sigma}^R_{p,\tilde{t}}$ and $n_{p,\tilde{t}},m_{p,\tilde{t}}$ on the nonlinearity v completely. This yields the equations of motion for the phonon densities

$$\partial_{\tilde{t}} n_{11,p} = \int_{0<q<p} \gamma^-_{p,q}[n_{11,p-q}n_{11,q} - n_{11,p}(n_{11,p-q} + n_{11,q} + 1)] + 2\int_{0<q} \gamma^+_{p,q}[n_{11,p+q}(1 + n_{11,q} + n_{11,p}) - n_{11,q}n_{11,p}], \tag{3.15}$$

$$\partial_{\tilde{t}} n_{12,p} = \int_{0<q<p} \gamma^-_{p,q}[n_{12,p-q}n_{12,q} - n_{12,p}(n_{11,p-q} + n_{11,q} + 1)] + 2\int_{0<q} \gamma^+_{p,q}[(n_{11,p+q} - n_{11,q})n_{12,p} - n_{12,p+q}n_{12,q}], \tag{3.16}$$

$$\partial_{\tilde{t}} m_{11,p} = \int_{0<q<p} \gamma^-_{p,q}[m_{11,p-q}m_{11,q} - m_{11,p}(n_{11,p-q} + n_{11,q} + 1)] + 2\int_{0<q} \gamma^+_{p,q}[(n_{11,p+q} - n_{11,q})m_{11,p} - m_{11,p+q}m_{11,q}], \tag{3.17}$$

with the effective scattering vertex

$$\gamma^\pm_{p,q} = \frac{qp(p \pm q)}{\tilde{\sigma}^R_p + \tilde{\sigma}^R_q + \tilde{\sigma}^R_{p\pm q}}. \tag{3.18}$$

At each time step, the retarded self-energy has to be determined self-consistently. It is determined by the equation (see Appendix B)

$$\tilde{\sigma}^R_p = 2\int_q \left\{\left[\frac{\partial_{\tilde{t}}\, n_{11,q}}{\tilde{\sigma}^R_q} + (2n_{11,q} + 1)\right] \times \left[\frac{qp(p-q)}{\tilde{\sigma}^R_q + \tilde{\sigma}^R_{p-q}} + \frac{qp(p+q)}{\tilde{\sigma}^R_q + \tilde{\sigma}^R_{p+q}}\right]\right\}. \tag{3.19}$$

The system of equations (3.15)–(3.19) is solved iteratively according to the scheme shown in Fig. 1. The initial state at $\tilde{t} = 0$ is determined by the individual splitting procedure. At each time step $\tilde{t}$, one has to compute the self-energy $\tilde{\sigma}^R_{p,\tilde{t}}$ which then enables the next infinitesimal time step $\tilde{t} + \delta$ via the equations of motion. The procedure is repeated until the steady state has been reached.

To obtain the closed set of equations (3.15)–(3.19), the Dyson-Schwinger equations for the interacting Luttinger liquid have been truncated at the quadratic order; i.e., we neglect any vertex correction to Eq. (3.18) from higher order loops. In principle it is possible to include these corrections within the present formalism as was discussed in Ref. [29]. This work shows, however, that higher order vertex corrections are generally very small, which is in agreement with numerical test simulations of the vertex correction for the present setup, and can thus be safely neglected. At this order, the

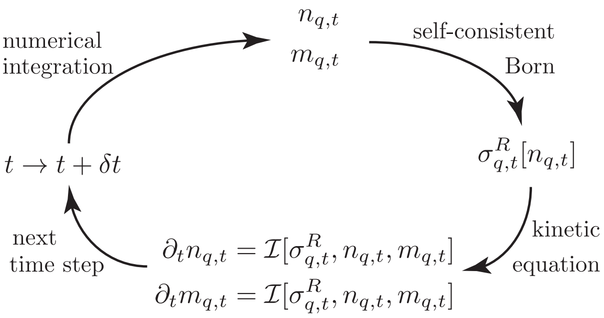

FIG. 1. Schematic illustration of the numerical routine for solving the kinetic equations. For a given occupation $n_{q,t}, m_{q,t}$, the self-energies are computed within the self-consistent Born approximation. Inserting the self-energies into the collision integral determines the evolution of $n_{q,t}, m_{q,t}$ via the kinetic equation. Numerical integration yields the occupations at the next time step $t \to t + \delta t$.

Dyson-Schwinger equations are identical to the self-consistent Born approximation.

IV. SPLITTING TO A NEARLY THERMAL STATE

The splitting experiments in the Vienna group have been performed via two different splitting protocols. In this section, we will investigate a set of splitting experiments, in which the bosonic wires were split in such a way that the resulting state of the system remained close to a thermal state. We demonstrate that, as a consequence, the prethermalized state and the asymptotic thermal state are hard to distinguish and the asymptotic thermalization dynamics is difficult to track experimentally. We will discuss the different stages of thermalization for this splitting procedure and numerically investigate the behavior of observables in the corresponding stages. This serves as a preparation for the discussion of the second set of splitting procedures in the subsequent section.

A. Initial state

The initial state in the two wires is prepared by coherently splitting a phase-fluctuating one-dimensional quasicondensate in the longitudinal direction. The splitting is performed on a fast timescale such that the longitudinal phase profiles in the newly generated quantum wires are nearly identical $\theta_1(x) \approx \theta_2(x)$ [2,7,26], while the uncertainty in the local density is maximal.

We label the phase and density $\theta_\alpha, \rho_\alpha$ of the two wires with $\alpha = 1,2$ and introduce the relative $\theta_r = \theta_1 - \theta_2$ and absolute phase $\theta_a = \frac{\theta_1+\theta_2}{2}$ and analogously relative and absolute density ρ_r, ρ_a. The absolute phase and density remain unchanged by a sudden splitting and correspond to the initial quasicondensate. The relative phase and density instead are generated only by the splitting. Their initial variance can be expressed via the initial average density in the wires ρ_0 and per unit volume reads as [2,7,26]

$$\langle \rho_r(x)\rho_r(x)\rangle \approx \frac{\rho_0}{2}, \tag{4.1}$$

$$\langle \theta_r(x)\theta_r(x)\rangle \approx \frac{1}{2\rho_0}. \tag{4.2}$$

The quasiparticle densities in the relative mode can be determined from Eqs. (4.1) and (4.2) in combination with Eqs. (2.6) and (2.7),

$$n_{r,p} = \langle a_r^\dagger(p)a_r(p)\rangle = \frac{T_r}{\nu|p|} + \chi_r|p| - \frac{1}{2}, \tag{4.3}$$

$$m_{r,p} = \langle a_r(p)a_r(-p)\rangle = \frac{T_r}{\nu|p|} - \chi_r|p|. \tag{4.4}$$

At low momenta $|p| < \sqrt{\frac{T_r}{\nu\chi_r}}$ the normal density adopts thermal behavior $n_{r,p} \sim |p|^{-1}$ with an effective relative temperature $T_r = \frac{\rho_0\pi}{4}\frac{\nu}{K}$, which depends on the state before the splitting via ρ_0, and on the Hamiltonian via the Luttinger parameters. For intermediate momenta $\sqrt{\frac{T_r}{\nu\chi_r}} < |p| < \Lambda$, on the other hand, it increases linearly in momentum with a splitting-dependent slope $\chi_r = \frac{1}{4\pi\rho_0}K$. On the largest momenta $|p| > \Lambda$ the quasiparticle density is suppressed exponentially. Analogous behavior is found for the anomalous density $m_{r,p}$, which must, however, be zero for a thermal ensemble. This should be contrasted with the thermal occupation of the absolute quasiparticle mode [2,7,26]

$$n_{a,p} = \langle a_r^\dagger(p)a_r(p)\rangle = \frac{\cosh(\nu|p|/T_a) - 1}{2} \approx \frac{T_a}{\nu|p|}, \tag{4.5}$$

$$m_{a,p} = \langle a_a(p)a_a(-p)\rangle = 0, \tag{4.6}$$

which is described by the initial temperature T_a of the quasicondensate before the splitting.

The low-momentum effective temperature of the relative mode $T_r \sim \rho_0/K$ can be initialized at rather small values, depending on the ratio of the initial density and the Luttinger parameter. On the other hand, decreasing T_r increases the slope $\chi_r \sim K/\rho_0$ and shifts the splitting energy from lower to larger momenta. The larger χ_r, the more $n_{r,p}$ deviates from a thermal distribution and the larger will be the impact of energy redistributing collisions at large times. In previous experiments, the linear increase of the occupation has not been detected in any of the observables, indicating that the crossover momentum $\sqrt{\frac{T_r}{\chi_r\nu}}$ is large, i.e., of the order of the ultraviolet cutoff and thus χ_r is small. While this still implies an energy transfer from the high-momentum to the low-momentum regime on times of the order of the collision time, our results show that the initial, thermal form of the low-momentum distribution makes such transfer hard to detect. This is discussed in detail in Secs. IV B and IV B 2. An illustration of the relative and absolute densities is shown in Figs. 2 and 3 (see also Fig. 4) for two different sets of splitting parameters.

As pointed out in the previous section, the kinetics of the quasiparticles is most conveniently expressed in the basis of individual wires. Inserting the definition of the relative and absolute mode $a_{r,a} = \frac{1}{\sqrt{2}}(a_1 \mp a_2)$ into the densities one finds immediately

$$n_{r,p} = n_{11,p} - n_{12,p}, \tag{4.7}$$

$$m_{r,p} = m_{11,p}, \tag{4.8}$$

$$n_{a,p} = n_{11,p} + n_{12,p}, \tag{4.9}$$

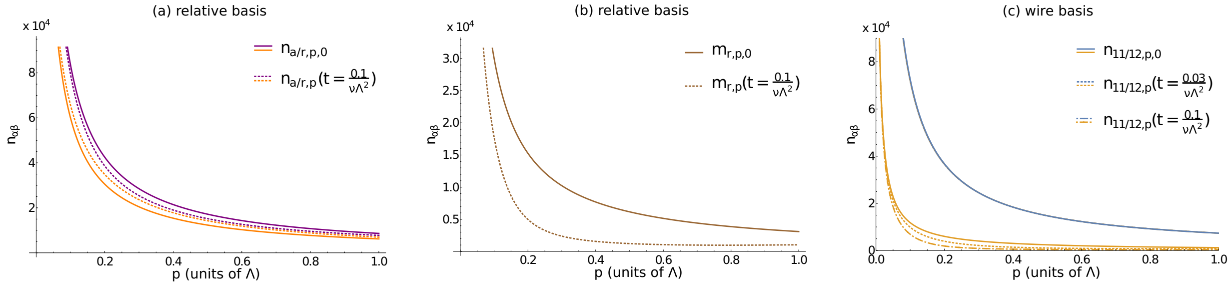

FIG. 2. Parameters as in Table I but $\chi_r = 0$: (a) The relative and absolute phonon densities, $n_{i,p}$ with $i \in \{r,a\}$, with an initial thermal distribution (bold lines) as shown in Fig. 4 approach each other as time evolves. Both occupations converge against a final thermal state characterized by a single temperature T_{f}. (b) The anomalous density $m_{r,p,t}$ decays in time and approaches zero. (c) In this case, $\chi_r \approx 0$ is negligible and the evolution is governed by the slow decay of $n_{12,p,t}$ in time, while $n_{11,p,t}$ remains constant in time [all blue (dark) lines coincide].

where we used the symmetry $n_{22,p} = n_{11,p}$ and $n_{12,p} = n_{21,p}$ between the two subsystems and $m_{a,p} = 0 \Leftrightarrow m_{11} = -m_{12}$. The initial values can be read off directly from Eqs. (4.3)–(4.6).

B. Prethermalization and thermalization: Time regimes in the double-wire dynamics

The splitting procedure initializes the two-wire system in a nonthermal, out-of-equilibrium state, which will start to relax immediately after the splitting. This relaxation process undergoes the typical, stepwise process towards equilibration, which we will discuss in the following. We start with a qualitative discussion of the different relaxation processes based on the Hamiltonian (2.8) and the initial-state properties, expressed via n_{11},n_{12},m_{11}. This scenario is then confirmed quantitatively by simulations of the kinetic equations (3.15)–(3.17) and discussed on the basis of experimentally relevant observables. The relaxation of a generic, weakly interacting quantum system is expected to happen in a sequence of steps connecting the initial nonequilibrium state with the asymptotic state of the system [24,25,43]. We will review this typical scenario briefly, adapted to the present system.

Straight after the initialization of the out-of-equilibrium state, the time evolution of the system is dominated by the fastest process captured by the Hamiltonian (2.8) with $v = 0$, which is the formation of well-defined, weakly interacting quasiparticles. Typical for this first process is the dephasing of anomalous correlations

$$\langle a_{\alpha,p} a_{\beta,-p} \rangle_t \approx e^{i2v|p|t} \langle a_{\alpha,p} a_{\beta,-p} \rangle_{t=0}, \tag{4.10}$$

caused by the quadratic part of the Hamiltonian. The spatiotemporal regime, which is influenced by the dephasing, is spanned by a pair of counterpropagating quasiparticles, leading to a light cone whose shape is set by the phonon velocity. Outside this light cone, correlations are still determined by the initial state at $t = 0$. We term this regime the "initial-state regime." Inside the light cone quasiparticles have formed and observables are dominated by the time-dependent quasiparticle densities $n_{11,p,t}$,$n_{12,p,t}$, whereas the off-diagonal part $m_{11,p,t}$, due to the dephasing, is effectively zero.

As long as both wires are described by the same microscopic parameters, the densities $n_{11,p,t}$,$n_{12,p,t}$ are constants of motion of the quadratic Luttinger Hamiltonian. Their time evolution is solely set by energy redistributing collisions as described in the nonlinear part of H_{ILL}. Since the quasiparticle interactions are weak and display subleading scaling behavior in momentum space, the typical timescale for long-wavelength collisions is much larger than for the dephasing; i.e., for a momentum mode q, $t_{\mathrm{coll}} = [v|q|^{\frac{3}{2}}(T_r/v)^{\frac{1}{2}}]^{-1} \gg (v|q|)^{-1} = t_{\mathrm{deph}}$ [25,28]. Consequently, there exists an extended spatiotemporal regime for which dephasing has lead to the formation of quasiparticles, which have, however, not experienced a substantial number of

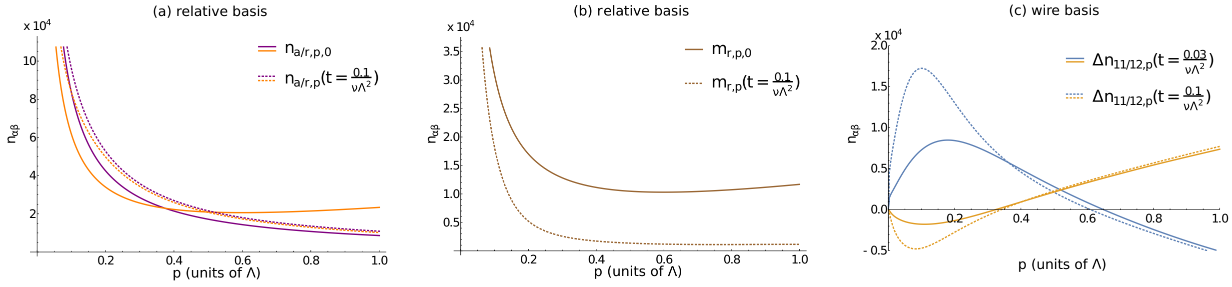

FIG. 3. Parameters as in Table I with $\chi_r = \frac{1}{4\pi\rho_0}K$: (a) The initial diagonal relative phonon density $n_{r,p}$ (bright, bold) has a linear tail (see Fig. 4) and energy stored at larger momenta. During the time evolution, $n_{r,p,t}$ and $n_{a,p,t}$ converge towards an identical final distribution, which corresponds to a larger temperature. Energy is distributed from larger to small momenta. (b) The off-diagonal occupation decays to zero exponentially in time. (c) Time evolution of the difference $\Delta n_{\alpha,p}(t) = n_{\alpha,p}(t) - n_{\alpha,p}(0)$. The crossover momentum $p_t^{(c)}$ separating fast, thermal-like evolution at $p > p_t^{(c)}$ from a slow nonequilibrium relaxation at $p < p_t^{(c)}$ leads to a bump in $\Delta n_{\alpha,p}(t)$ as discussed in the main text.

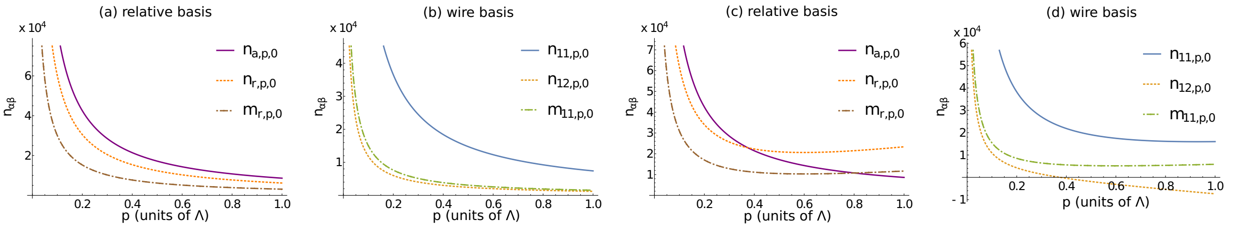

FIG. 4. For parameters as in Table I but χ_r set to zero $\chi_r = 0$ by hand: (a) initial distribution in the absolute n_a and relative n_r, m_r modes; (b) initial distribution in the single-wire basis. We focus in this analysis on the low-energy dynamics of the system below a certain cutoff $p < \Lambda$. Due to Eqs. (4.3) and (4.4), the initial distributions are almost thermal for all momenta. For parameters as in Table I but $\chi_r = \frac{1}{4\pi\rho_0}K$: (c) and (d) the presence of $\sqrt{T_r/(\nu\chi_r)} \approx 0.5\Lambda < \infty$ distinguishes two momentum regimes: small momenta $|p| < \sqrt{T_r/(\nu\chi_r)}$ with a thermal relative density $n_r = T_r/(\nu|p|) < n_a$ and large momenta $|p| > \sqrt{T_r/(\nu\chi_r)}$ with a linear increasing density $n_r = \chi_r|p| > n_a$.

collisions. In this regime, the densities $n_{11,p,t}, n_{12,p,t}$ are pinned to their initial values and are not yet evolving in time. The corresponding state is commonly termed prethermal.

For times $t > t_{\text{coll}}$, typically only a few collisions ($\sim$3) are necessary to redistribute energy and establish a local thermal equilibrium. By local, we refer to a local region in momentum space $p \in [q-\delta, q+\delta]$, which is very well described by thermal quasiparticle densities $n_{12,p,t} = 0, n_{11,p,t} = n_B(\nu|p|/T_{\text{loc}})$ and a joint, local effective temperature T_{loc}. This effective thermalization timescale is of the order of few collision timescales $t_{\text{therm}} = O(t_{\text{coll}})$ and therefore, together with T_{loc}, momentum-dependent.

On asymptotic timescales, the locally thermalized regions have to adjust their temperature and relax towards the global thermal equilibrium. At this stage of the relaxation, conserved quantities like energy and momentum have to be transferred over large distances in momentum space. This transport involves many subsequent collisions and belongs to the regime of hydrodynamics, which is governed by the global conservation laws of the system. This regime makes a clear distinction between the interwire coherences $n_{12,p,t}$, which are not part of any conservation law and thus decay exponentially towards their thermal value, and the intrawire density $n_{11,p,t}$, whose evolution is constrained by total energy and momentum conservation. As a consequence, $n_{11,p,t}$ will relax algebraically slowly towards its thermal value in this asymptotic regime.

TABLE I. Left column: Microscopic parameters, which are used throughout this work in order to perform the numerical simulations. They represent a set of experimentally realizable conditions and can be found, e.g., in Refs. [2,3,26,41,42]. m_{Rb} is the mass of a ^{87}Rb atom, which is used in the experiment, and $u = 1.66 \times 10^{-27}$ kg is the atomic mass unit. For typical experiments, the relative and absolute temperature vary between 10 nK $\leqslant T_a \leqslant$ 100 nK and 5 nK $\leqslant T_r \leqslant$ 25 nK. Right column: Luttinger liquid parameters inferred from the microscopic parameters.

Experimental parameters	Luttinger liquid parameters
$m_{\text{Rb}} = 87u$	$K = 25.4$
$\rho_0 = 30 \times 10^6\ \text{m}^{-1}$	$\nu = 1.3 \times 10^{-3}\ \frac{\text{m}}{\text{s}}$
$T_a = 30$ nK	$\upsilon = 5.4 \times 10^{-10}\ \frac{\text{m}^2}{\text{s}}$
$u(0) \approx 8.8 \times 10^{-39}$ J m	$T_r = 21.5$ nK
	$\Lambda = 2.5 \times 10^6\ \text{m}^{-1}$

In the following, the time evolution of the densities $n_{11,p,t}, n_{12,p,t}, m_{11,p,t}$ is determined on the basis of the kinetic equations (3.15)–(3.17) and the emergence of the different relaxation regimes is discussed on the basis of several observables.

1. Time evolution of the phonon densities

The kinetic equations (3.15)–(3.17) determine the relaxation of the densities $n_{11,p,t}, n_{12,p,t}$, and $m_{11,p,t}$ towards a thermal ensemble. The Hamiltonian (2.5) contains no interactions between the two wires and between states of opposite momentum, such that the off-diagonal terms are expected to decay to zero $n_{12,p,t\to\infty} = m_{11,p,t\to\infty} = 0$ for a thermal state. The different stages of relaxation are as follows.

For times $t < t_{\text{therm}}$, the normal densities $n_{11,p}, n_{12,p}$ are nearly constant and the only relaxation is caused by the dephasing of $m_{11,p}$. This time regime is adequately described and understood in terms of the quadratic Hamiltonian alone. On the other hand, for times $t > t_{\text{therm}}$, the dephasing of the anomalous modes has already eliminated all the influence of $m_{11,p}$ on physical observables, although its absolute value remains nonzero. As it turns out, the dynamics for $t > t_{\text{therm}}$ can be understood completely on the basis of the relaxation of the normal occupations, and we will thus restrict the following discussion to the time evolution of $n_{11,p,t}, n_{12,p,t}$. The simulated relaxation of $m_{11,p,t}$ is, however, shown for completeness.

The diagonal density $n_{11,p,t\to\infty} = n_{\text{B}}(\epsilon_p/T_{\text{f}})$ evolves towards a Bose-Einstein distribution n_{B} with asymptotic temperature T_{f}. In the basis of relative and absolute modes, both normal occupations approach each other during the evolution and converge towards an identical, thermal distribution $n_{r,p,t\to\infty} = n_{a,p,t\to\infty} = n_{\text{B}}(\epsilon_p/T_{\text{f}})$, as can be inferred from Eqs. (4.7)–(4.9). The anomalous occupation $m_{r,p,t\to\infty} = 0$ instead decays to zero.

The asymptotic value of the temperature of the diagonal, normal phonon distribution $n_{11,p,t\to\infty} = n_{\text{B}}(\nu|p|/T_{\text{f}})$ can be determined by the initial state due to energy conservation. The quadratic part of the Hamiltonian, i.e., the kinetic energy density, commutes with the resonant collision terms in Eq. (2.8). The kinetic energy density is thus an integral of motion and its final and initial value must coincide $\epsilon_{t=0} = \epsilon_{t=\infty}$, i.e.,

$$\int_p \nu|p|n_{11,p,t=0} \overset{!}{=} \int_p \nu|p|n_{11,p,t=\infty} = \frac{\pi^2 T_{\text{f}}^2}{3\nu}. \qquad (4.11)$$

This determines the asymptotic temperatures $T_{\mathrm{f}} = \sqrt{3\nu\epsilon_{t=0}}/\pi$.

For initial states of the form given in Eq. (4.3), one can distinguish between two experimentally relevant limiting cases, namely $K \ll \rho_0 \Leftrightarrow \chi_r \approx 0$, where $\chi_r\Lambda$ is negligibly small, and $\chi_r\Lambda \approx T_r/(\nu\Lambda)$, for which the linear tail $\sim\chi_r p$ cannot be neglected.

In the former case, the relative and absolute mode are both described by an approximate high-temperature distribution $n_{\alpha,p} \approx T_\alpha/(\nu|p|)$, where $\alpha = a,r$. The time evolution then lets both distributions approach each other slowly, merging at a joint temperature $T_{\mathrm{f}} = (T_r + T_a)/2$. In the basis of $n_{11,p}, n_{12,p}$, such initial states lead to an almost time-independent diagonal occupation $n_{11,p,t} = n_{11,p,0}$ and only $n_{12,p,t}$ is decaying to zero. The results of a corresponding kinetic equation simulation are shown in Fig. 2.

In the case of $\chi_r \neq 0$ or generally for a relative distribution $n_{r,p,t}$ deviating from a thermal one, not only $n_{12,p,t}$ decays in time, but also $n_{11,p,t}$ will evolve in a nontrivial way. Since the Hamiltonian conserves the energy within a single wire, $n_{11,p,t}$ is not simply decaying but energy is redistributed within this mode. For an initial distribution of the form (4.3) with $\chi_r \neq 0$, energy is initially stored at large momenta $\sqrt{T_r/(\nu\chi_r)} < q < \Lambda$ and will be transferred to lower momenta via phonon-phonon collisions in order to reach a thermal state. In Fig. 3, the phonon distributions for such a scenario are shown. One can clearly observe the time evolution of the diagonal density $n_{11,p,t}$ and its effect on $n_{r,p,t}, n_{a,p,t}$, which are both evolving towards an increased temperature state with $T_{\mathrm{f}} > (T_r + T_a)/2$.

Due to the structure of the interaction vertex $V(p,q,p \pm q) = \nu\sqrt{|pq(p \pm q)|}$ the collision rate decreases with the momentum of the contributing phonon modes. The modification of $n_{\alpha,p,t}$ due to collisions sets in at large momenta and approaches lower and lower momenta as time proceeds. In Fig. 3(c), the deviation $\Delta n_{\alpha,p,t} = n_{\alpha,p,t} - n_{\alpha,p,0}$ of the densities $\alpha = 11,12$ from their initial values is shown for different time steps. It has been observed previously [25,28] that this deviation displays two characteristic momentum regimes, a low-momentum regime $p < p_t^{(c)}$ with linear deviation $\Delta n_{\alpha,p,t} \sim |p|$ and a large-momentum regime $p > p_t^{(c)}$ with a Rayleigh-Jeans type deviation $\Delta n_{\alpha,p,t} \sim 1/|p|$. In this large-momentum regime, the phonon modes have reached a local, nearly thermal equilibrium and $\Delta n_{\alpha,p,t}$ evolves very slowly in time. In the vicinity of the crossover momentum $p_t^{(c)}$, however, the redistribution of energy is fast and $\Delta n_{\alpha,p,t}$ undergoes a strong evolution. The time evolution of $p_t^{(c)} \sim t^{-\alpha}$ is algebraic in time with $1/2 \leqslant \alpha < 1$ depending on the initial state [25]. For a nearly thermal initial state $\alpha \approx 2/3$, which is consistent with the typical collision time $t_{\mathrm{coll}} = [\nu|q|^{\frac{3}{2}}(T_r/\nu)^{\frac{1}{2}}]^{-1}$. Tracking the evolution of the crossover momentum $p_t^{(c)}$ in the experiment can thus be used to detect the thermal relaxation exponent $\alpha = 2/3$ predicted for the one-dimensional Bose gas [25,28,30,32].

2. Dynamics of the relative phase correlation function

The phase correlation function $C(x,t) \sim \exp(-\Delta\theta_{r,x,t}/2)$ defined in Eqs. (2.23), (2.24) is an experimentally accessible measure to monitor the time evolution of the two quantum wires [2,7,16,26]. It has been discussed extensively on the level of the quadratic Luttinger model without phonon collisions, which describes very well the dynamics of the initial and the prethermal state. Below, we will discuss in which way the phase correlation function is modified by phonon-phonon collisions. We show that C is dominated by the thermal part of the phonon distribution and that it is quite insensitive towards a modification of $n_{r,p,t}$ of the form $\Delta_p = \chi_r|p|$. As a consequence, the thermalization dynamics of C for an initial state of the form (4.3) does not display any pronounced additional features compared to a collisionless evolution. The latter signals the evolution of the system towards a GGE state caused by the dephasing of $m_{p,t}$. The only resolvable effect of the collisions is an effective temperature in the relative mode $T_{\mathrm{eff}} > T_r$, slightly larger than the initial state T_r.

Dynamics without collisions. In the absence of collisions, the time evolution of the relative phase is determined solely by the dephasing of the anomalous modes $m_{r,p}$. Eliminating constant terms, which vanish upon normalization of C, the time-dependent relative phase is

$$\begin{aligned}\Delta\theta_{r,x,t} &= \int_p \frac{e^{-\frac{|p|}{\Lambda}}}{2K|p|}[1-\cos(px)][2n_{r,p,0}\\&\quad+1-2m_{r,p,0}\cos(2\nu|p|t)]\\&\approx \begin{cases}\frac{\pi T_r}{2K\nu}x, & x<2\nu t,\\ \frac{\pi T_r}{K}t, & 2\nu t<x,\end{cases}\end{aligned} \tag{4.12}$$

where $m_{r,p,0} = \frac{T_r}{\nu|p|} - \chi_r|p|$ and $n_{r,p,0} = \frac{T_r}{\nu|p|} + \chi_r|p| - \frac{1}{2}$. The approximation on the right of (4.12) is valid for $x \gg a$, i.e., distances larger than the short-distance cutoff. It shows two characteristic properties: First, there is no functional dependence on χ_r, which modifies only the short-distance modes at larger momenta $p > \sqrt{T_r/(\nu\chi_r)}$. The linear tail $\sim\chi_r|p|$ appears only as a global shift of $\Delta\theta_{r,x,t}$, which is not resolved in experiments. Second, the light cone $x = 2\nu t$ clearly separates the initial-state regime $x > 2\nu t$ from the prethermal regime $x < 2\nu t$. This feature of the relative phase has been exploited in order to experimentally measure the spreading of prethermal correlations and the value the sound velocity in the quantum wires [2,3,7]. It also determines the ratio T_r/K, which depends both on the initial state via T_r and the Hamiltonian via the Luttinger parameter K. In Fig. 5, the time evolution of $C, \Delta\theta_r$ in the absence of collisions [orange (bright) lines] is plotted for two distinct initial states with either $\chi_r = 0$ or $\chi_r \neq 0$.

Dynamics in the presence of collisions. In the presence of collisions energy is redistributed from the absolute to the relative mode via the decay of the interwire coherence $n_{12,p,t} \to 0$. For nonzero initial χ_r, there will be an additional transfer of energy from larger to lower momenta in order to establish a thermal phonon distribution within each wire. This process is monitored by a nonvanishing deviation $\Delta n_{r,p,t} = n_{r,p,t} - n_{r,p,0}$, which is building up in time. Following the discussion of the time evolution of $n_{r,p,t}$ above, $\Delta n_{r,p,t}$ can be decomposed into two distinct regimes. For momenta lower than the crossover momentum $p < p_t^{(c)}$, $\Delta n_{r,p,t} \sim |p|$, while for larger momenta $p > p_t^{(c)}$ it is that $\Delta n_{r,p,t} \sim 1/|p|$.

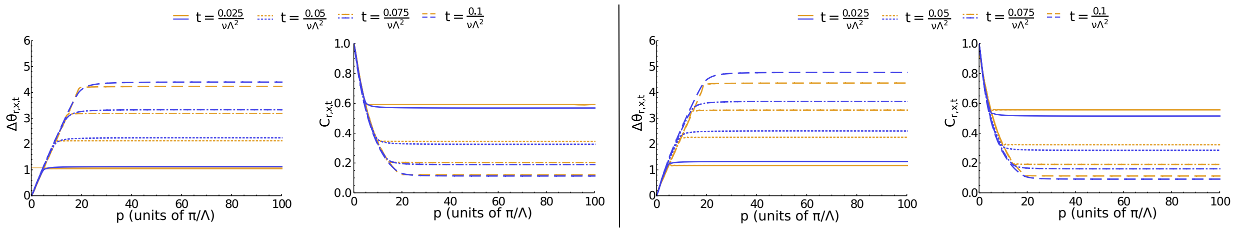

FIG. 5. Relative phase fluctuation $\Delta\theta_r$ and phase correlation function C for a nearly thermal initial state with $\chi_r \approx 0$ (left column, corresponding to data as in Fig. 2) and for an initial state with non-negligible linear tail $\chi_r \neq 0$ (right column, corresponding to data as in Fig. 3). The evolution in the absence (orange (bright) lines; see Ref. [3]) and in the presence [blue (dark) lines] of phonon-phonon collisions is compared for increasing times $t = (1,2,3,4)/(40\nu\Lambda^2)$.

On distances $x > 2\nu t$, the anomalous contributions $\sim m_{r,p,t}$ have already dephased and the relative phase can be approximated as

$$\Delta\theta_{r,x,t} = \int_p \frac{e^{-\frac{|p|}{\Lambda}}}{2Kp}[1-\cos(px)][2n_{r,p,0}+1+2\Delta n_{r,p,t}]$$

$$\approx \begin{cases} \frac{\pi x}{2K\nu} T_{\mathrm{f}}, & \text{for } p_t^{(c)}x < 1, \\ \frac{\pi x}{2K\nu}\left[T_r + (T_{\mathrm{f}} - T_r)p_t^{(c)}x\right], & \text{for } p_t^{(c)}x > 1, \end{cases} \tag{4.13}$$

where T_{f} is again the final temperature in the relative mode, determined via Eq. (4.11), and T_r depends on the initial condition. The crossover distance in Eq. (4.13) can be estimated with $x_t^{(c)} = 1/p_t^{(c)} \approx (T_r v^2/\nu)^{-1/3}t^{2/3}$. For $x_t^{(c)} > a$ larger than the short-distance cutoff, it spreads slower than the prethermal distance $x_{\mathrm{pre}} = 2\nu t$ and thus the decomposition of Fig. 6 applies.

Along the same lines, one can determine the relative phase for distances $x > 2\nu t$, which yields after some algebra

$$\Delta\theta_{r,x,t} \overset{x>2\nu t}{\approx} \frac{\pi t}{K}\left[T_r + 2\nu(T_{\mathrm{f}} - T_r)p_t^{(c)}t\right]. \tag{4.14}$$

The additional term in this equation compared to the collisionless case in Eq. (4.12) grows in time $\sim(T_{\mathrm{f}} - T_r)t^2 p_t^{(c)} = (T_{\mathrm{f}} - T_r)t^{4/3}$ for $p_t^{(c)} \sim t^{-2/3}$; i.e., it is proportional to the difference of initial and final temperature and grows faster than linear in time, witnessing interaction effects.

As for the collisionless case, Eqs. (4.13), (4.14) do not contain any explicit dependence on χ_r. A nonzero χ_r in the initial state only enters the final temperature T_{f} since the energy stored in the linear tail is redistributed over the whole momentum range. In total, the phase correlation function C can hardly distinguish between a thermal state $\chi_r = 0$ where the only increase in the relative temperature results from the equilibration with the absolute mode or a nonthermal state $\chi_r > 0$, for which in addition to the equilibration with the absolute mode, energy is redistributed within the relative mode as well. Only significantly large $\chi_r\Lambda \gg T_r/(\nu\Lambda)$ would change this observation, by drastically increasing T_f, which would, however, as well prohibit working in the low-energy Luttinger framework. Furthermore, the spatial structures of $\Delta\theta_{r,x,t}$ in the thermal ($xp_t^{(c)} < 1$) and prethermal regime ($xp_t^{(c)} > 1$) are almost indistinguishable within a real-time evolution of $\Delta\theta_{r,x,t}$ and C_r as shown in Fig. 5.

From this analysis, we must conclude that the thermalization dynamics of the two-wire system can hardly be investigated on the basis of initial states of the form (4.3) and (4.4). One possible, minor witness for the presence or absence of thermalization could be the additional, nonlinear growth of $\Delta\theta_{r,x,t}$ in time in the regime $x > 2\nu t$ as expressed in Eq. (4.14). Despite that $T_f - T_r$ may be substantial in experiments, however, the nonlinear dependence of the relative phase would be hard to resolve in practice; cf. Fig. 5.

3. Time evolution of the coherence factor

The coherence factor $\Psi_c(t) = \rho_0 e^{-g(t)}$ as defined in Eqs. (2.21), (2.22) measures the integrated coherence between the two wires. It only depends on the absolute forward time and is expected to decay as time evolves since the coherence between the two uncoupled wires decays due to dephasing and collisions. The decay of the coherence factor has been investigated in previous works, which found different asymptotic behavior, depending on the relevant decay mechanism. In Ref. [9], a linear time dependence $g(t) = g_0 t$ of the exponent has been predicted by the analysis of the collisionless model, while in Ref. [31], a stretched exponential $g(t) \sim g_1 t^{2/3}$ has been found by assuming energy exchange via collisions of the relative mode phonons from a thermal bath. Here, we will consider the most general case, which combines dephasing

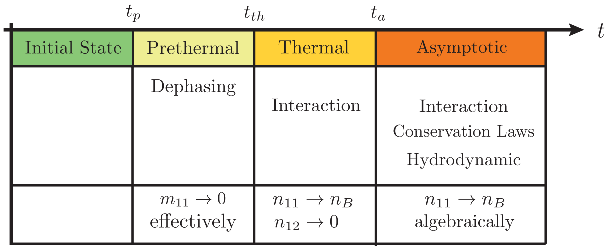

FIG. 6. Illustration of the various stages of thermalization for an arbitrary but fixed patch in momentum space centered around momentum q. After an initial state dominated time interval $0 \leqslant t < t_{\mathrm{deph}} = (\nu|q|)^{-1}$, the dephasing of the anomalous modes $m_{11,q}$ becomes significant, introducing a prethermal regime. Collisions between the phonon modes modify the normal densities $n_{11,q}, n_{12,q}$ on timescales $t = t_{\mathrm{coll}} = [v|q|^{\frac{3}{2}}(T_r/\nu)^{\frac{1}{2}}]^{-1}$ and bring the system into a thermalizing regime for times $t > t_{\mathrm{therm}} = O(t_{\mathrm{coll}})$. The thermalizing regime is separated into an initial stage, governed by a fast evolution of the normal densities due to few, local collisions and an asymptotic stage, governed by energy and momentum transport over many distinct momentum patches. This stage involves many collisions, captured by slow, hydrodynamic modes.

as well as phonon-phonon collisions as possible decoherence mechanisms and whose results do not rely on a particular initial state. We begin the discussion with a nearly thermal initial state, $\chi_r = 0$, and then extend the scenario to initial states with $\chi_r \neq 0$.

Nearly thermal initial state. For initial states with $\chi_r = 0$, the diagonal phonon density $n_{11,p,0} = \frac{T_r + T_a}{2\nu|p|}$ and the retarded self-energy σ_q^R in Eq. (3.19) can be solved analytically. The self-energy takes the thermal form [29–32] and reads as

$$\sigma_q^R = 0.789\nu\sqrt{\frac{\pi(T_r + T_a)}{\nu}}|q|^{\frac{3}{2}} = \gamma|q|^{\frac{3}{2}}, \qquad (4.15)$$

where we have absorbed all momentum-independent terms in the prefactor γ. The dynamics of the anomalous and the interwire phonon mode $m_{11,q,t}$,$n_{12,q,t}$ is not constrained by any conservation laws and they decay in this case as $m_{11,q,t} = \exp(-\gamma|q|^{3/2}t)m_{11,q,t=0}$ and $n_{12,q,t} = \exp(-\gamma|q|^{3/2}t)n_{12,q,t=0}$. The diagonal phonon mode $n_{11,q,t}$ on the other hand is thermally occupied and does not evolve in time.

The exponent of the coherence factor in this case can be computed analytically:

$$\begin{aligned} g(t) &= \int_p \frac{e^{-\frac{|p|}{\Lambda}}}{8K|p|}[2n_{r,p,t} + 1 - 2\cos(2\nu|p|t)m_{r,p,t}] \\ &\approx \int_p \frac{e^{-\frac{|p|}{\Lambda}}}{4K\nu p^2}\{T_{\mathrm{f}} + e^{-\gamma|p|^{\frac{3}{2}}t}[T_r - T_{\mathrm{f}} - \cos(2\nu|p|t)T_r]\} \\ &= \frac{T_{\mathrm{f}}}{2K\nu}(\gamma t)^{\frac{2}{3}} f_{y,T_r/T_{\mathrm{f}}}. \end{aligned} \qquad (4.16)$$

The shape of the dimensionless function $f_{y,T_r/T_{\mathrm{f}}}$ is determined by the value of the dimensionless parameter $y = t\nu^3\gamma^{-2}$. It has the general asymptotic behavior

$$f_{y,\tau} = \begin{cases} \Gamma\left(\frac{1}{3}\right), & \text{for } y \ll 1, \\ \pi y^{\frac{1}{3}}\tau, & \text{for } y \gg 1. \end{cases} \qquad (4.17)$$

Thus it is dominated by thermal collisions for small times $t < \frac{\gamma^2}{\nu^3} = 0.789^2\pi T_{\mathrm{f}}$ and dominated by dephasing for larger times $t > 0.789^2\pi T_{\mathrm{f}}$ depending on T_f and therefore, via Eq. (4.11), implicitly on the initial state. This behavior is counterintuitive since one expects quantum effects to influence the short-time rather than the long-time behavior. It can, however, be explained by a proper decomposition of the integral into high- and low-momentum modes and is supported by the numerical evaluation of the coherence factor in Fig. 7. The latter starts with a $\ln\psi_c \sim t^{2/3}$ curvature for small times and becomes less curved at large times in a logarithmic representation.

A nonlinear initial decay of the coherence factor could be observed in experiments, as suggested in previous works [31], where the absolute modes $n_{a,p,t}$ have been treated as a bath for the relative modes, which does not relax at all. For short times, where the distribution of $n_{a,p,t}$ has not yet been modified by collisions, this is a reasonable assumption and thus coincides with our short-time prediction. Compared to the behavior of $g(t)$ in the noninteracting case $g(t) = \frac{\pi T_r t}{2K}$ for all $t > 0$ is a signature of collisions and goes beyond the quadratic Luttinger model.

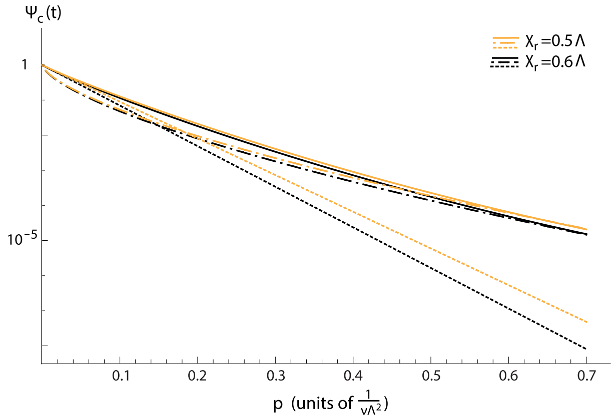

FIG. 7. Time evolution of the coherence factor $\Psi_c(t)$ from the kinetic equations (bold line) compared to an exponential decay $\sim\exp(-t/t_0)$ (dashed line), as predicted from pure dephasing, and a stretched exponential $\sim\exp[-(t/t_0)^{2/3}]$ (dash-dotted line), as predicted from phonon collisions; see Eqs. (4.16), (4.17). The colors (bright and dark) represent two different initial states with $\chi_r = 0.5\Lambda^{-1}$ and $\chi_r = 0.6\Lambda^{-1}$.

Nonthermal initial state. For initial states with $\chi_r \neq 0$, the major difference compared to the previous case of $\chi_r = 0$ is the redistribution of energy within the diagonal mode, which leads to a nontrivial $\Delta n_{11,p,t} = n_{11,p,t} - n_{11,p,t=0} \neq 0$. Since the exponential decay of the anomalous and interwire modes is dominated by the Rayleigh-Jeans divergence in the diagonal density, it is not expected to be crucially modified. Performing the decomposition $n_{11,p,t} = n_{11,p,t=0} + \Delta n_{11,p,t}$ and inserting this into the definition of $g(t)$, Eq. (2.22), we find $g(t) = g_0(t) + \Delta g(t)$ with

$$\begin{aligned} \Delta g(t) &= \int_p \frac{e^{-\frac{|p|}{\Lambda}}}{4K|p|}\Delta n_{11,p,t} \approx \frac{3T_{\mathrm{f}}}{4K\nu p_t^{(c)}} \\ &\approx \frac{3}{4K}\left(\frac{T_{\mathrm{f}}^4 v^2}{\nu^4}\right)^{\frac{1}{3}} t^{\frac{2}{3}}. \end{aligned} \qquad (4.18)$$

Due to energy redistribution within a single wire, the coherence factor thus shows again a stretched exponential decay with an exponent $\sim t^{2/3}$ even at the largest times. This stretched exponential decay of the coherence factor at the shortest and the longest timescales represents a clear sign of phonon-phonon collisions, either leading to a decay of the interwire correlations $\sim n_{12,p,t}$ or the redistribution of energy in the intrawire density $n_{11,p,t}$. In Fig. 7, the time evolution of the numerically simulated coherence factor is shown to significantly deviate from a linear exponential decay at all times. For short and intermediate times, it is faster than the analytically predicted $\exp[-(t/t_0)^{2/3}]$ but it approaches this behavior in the limit $t \to \infty$, as predicted from the simplified analysis above.

V. SPLITTING TO A NONTHERMAL INITIAL STATE

In order to observe the thermalization dynamics in the two-wire system much more clearly than in the previous section, it is most promising to design the splitting protocol in such a way

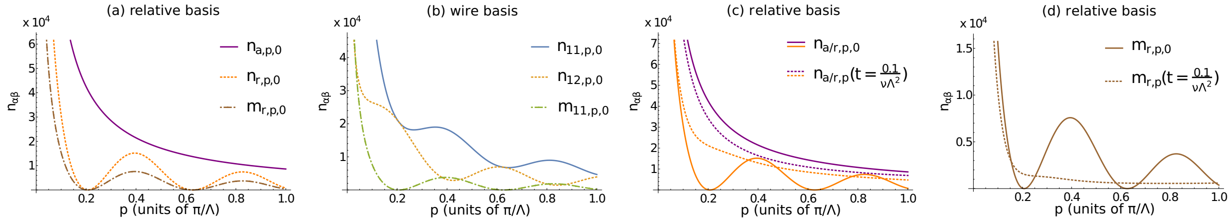

FIG. 8. Distribution for a nonthermal initial state with parameters as in Table I and an oscillation length $\xi = 7.5/\Lambda$: (a) The initial relative and absolute occupations and (b) the intra- and interwire occupations. (c) and (d) Time evolution of the relative and absolute density occupations in the presence of phonon-phonon collisions. The collisions lead to an adjustment of $n_{r,p,t}$ and $n_{a,p,t}$ as time evolves, which is accompanied with the temporal fade-out of the scale ξ.

that the initial state is no longer close to an effective thermal state but rather shows a clear structure of an out-of-equilibrium state in the normal, relative mode density $n_{r,q,t=0}$. Such a state will then relax very differently depending on whether phonon-phonon collisions are present or absent, making their influence on the dynamics clearly observable. Here, we are inspired by the latest experiments in Vienna, where the initial state has been prepared in such a way that the occupations of the quantized phonon modes with odd momentum index were much smaller than the occupations of the even modes. The latter could be described by an effective thermal distribution [16]. Within the short-time evolution probed in the experiment, the two-wire system entered the prethermal regime and relaxed towards a nonthermal, generalized Gibbs ensemble (GGE) [18,22,24,27]. Below, we explore the complete time evolution of such an initial state in the presence of phonon-phonon collisions and discuss in which way the thermalization dynamics can be made experimentally accessible by tuning the initial state of the system.

A. Initial state and relaxation of the phonon densities

The above-mentioned, experimentally observed initial state was realized in a wire of length L for which the low-momentum modes were approximately quantized to integer multiples of π/L. By modifying the splitting protocol, only the even modes were considerably populated, while the odd-momentum modes remained empty [16]. Here we generalize this state by going to the continuum of momentum modes and introducing a flexible length scale ξ for the oscillations of the phonon occupations. The phonon occupation shall be maximal for momenta $p = 2\alpha\pi/\xi$ and minimal for $p = (2\alpha + 1)\pi/\xi$, where n is an integer. Thus, for $\xi = L/2$ the experimentally observed state is recovered. Motivated by this observation, we consider an initial phonon distribution of the form (see Fig. 8)

$$n_{r,p,t=0} = \frac{T_r}{\nu|p|}\cos^2(p\xi) - \frac{1}{2}, \tag{5.1}$$

$$n_{a,p,t=0} = n_B(\nu|p|/T_a), \tag{5.2}$$

$$m_{r,p,t=0} = \frac{T_r}{\nu|p|}\cos^2(p\xi). \tag{5.3}$$

Here, T_r is the effective temperature of the envelope function $\sim\frac{T_r}{\nu|p|}$, as in the previous section. We will consider, however, a more general oscillation length scale $0 \leqslant \xi \leqslant L/2$, which interpolates continuously between the GGE state in Ref. [16] for $\xi = L/2$ and the previously discussed, nearly thermal state [2,4,7,16,26], obtained for $\xi = 0$.

An initial relative density of the form (5.1) with $\xi = L/2$ has been inferred from the experimental data in Ref. [16] after splitting one wire within a single, relatively fast splitting operation. The corresponding initial anomalous phonon density $m_{r,p,t}$ is much more difficult to detect in the experiment. It must, however, be of the form (5.3) in order to guarantee a vanishing initial relative phase difference $\Delta\theta_{r,p,t} = 0$ between the two wires.

The nearly thermal relative density (4.3) with $\xi = 0$, on the other hand, has been observed experimentally after performing a two-staged splitting protocol, which consists of a slow initial and a much faster final splitting operation [16]. It is therefore reasonable to assume that a general ξ between these two limiting cases can be obtained by continuously modifying the corresponding splitting procedure.

In the absence of phonon collisions, the dynamics is governed by the dephasing of $m_{r,p,t}$, which drives the system into the prethermal regime. The corresponding steady state is described by a GGE, respecting the initial structure of the normal relative density $n_{r,p,t}$, which in the absence of collisions is an integral of motion. In the presence of phonon collisions, on the other hand, the relative and the absolute phonon density both relax towards a thermal distribution with a uniform temperature T_f.

As in the previous section, the temperature T_f can be determined from the initial state by exploiting the conservation of the total kinetic energy. Analogously to Eq. (4.11) this yields the final temperature

$$T_\mathrm{f} = \frac{T_r + T_a}{2} - \frac{T_r(\xi\Lambda)^2}{1 + 4(\xi\Lambda)^2}. \tag{5.4}$$

It reduces to the previously discussed expression $T_\mathrm{f} = (T_r + T_a)/2$ in the limit of vanishing oscillation scale and to $T_\mathrm{f} = (T_r/2 + T_a)/2$ in the limit $\xi = L \gg \Lambda$. The time evolution of $n_{r,p,t}$,$n_{a,p,t}$ and the corresponding adjustment of both distributions is shown in Fig. 8.

One way of experimentally tracing the thermalization dynamics is to detect the time evolution of the phonon densities. The latter can be inferred from the experimental data in the limit of $m_{r,p,t} = 0$, i.e., after the complete dephasing of the anomalous densities, when prethermalization has been reached. In this limit, the relative phase is determined by the normal distribution alone. This has been demonstrated successfully in Ref. [16]. For an initial state considered here,

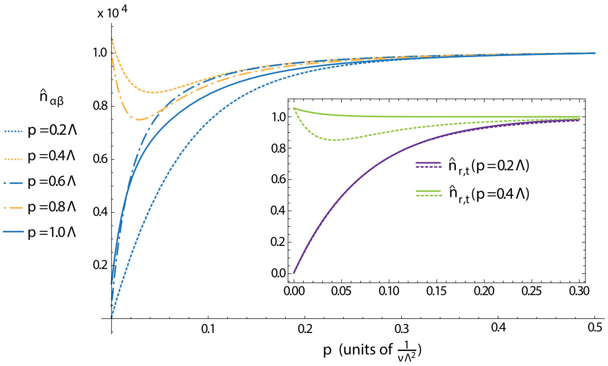

FIG. 9. Long-time relaxation of the phonon densities $n_{r,p,t}$ for momenta $p = \frac{l\pi}{2\xi} \approx 0.2l\Lambda$ for $\xi = 7.5/\Lambda$ and $l = 1,2,\ldots,5$, as in Fig. 8 ($l = 2,4$ correspond to even modes in the experiment [16]). For better visualization, the phonon densities are normalized to their asymptotic, thermal value $\hat{n}_{r,t}(p) = n_{r,p,t}\nu|p|/T_{\mathrm{f}}$. The relaxation can be described in terms of a two-stage process. In the first stage, the relative modes try to approach one common temperature $\sim T_r < T_{\mathrm{f}}$ in order to remove the oscillating structure in $n_{r,p,t}$; i.e., energy is redistributed within the relative modes. This can be achieved already by local scattering processes with momenta $\sim\xi^{-1}$. In the second, slower stage, the temperature between the relative and the absolute mode are adjusted via energy transfer from the absolute to the relative mode. The two stages are most prominently visible in the evolution for the momenta $p = 0.4, 0.8\ \Lambda$, which first decrease below their asymptotic value and then, together with the other modes, increase again towards T_{f}. The inset shows comparison of a bare exponential decay (bold lines) corresponding to a single-stage relaxation process with the numerical data (dotted lines) for $p = 0.2\Lambda$ (lower graphs) and $p = 0.4\Lambda$ (upper graphs). For the latter, the deviation is very pronounced.

the time evolution of $n_{r,p,t}$ is most pronounced at the local extrema of the initial phonon density at momenta $p = \frac{l\pi}{2\xi}$, with integer l. The corresponding evolution is shown in Fig. 9 for parameters as in Fig. 8. In the inset, we compare this evolution with the analytical prediction

$$n_{r,p,t} = n_{r,p,t=0} + (n_{r,p,t=\infty} - n_{r,p,t=0})e^{-\sigma_p^R t} \qquad (5.5)$$

for a self-energy $\sigma_p^R = 0.789\nu\sqrt{2\pi T_{\mathrm{f}}/\nu}$ [cf. Eqs. (4.15), (5.4)] which we approximate to be time-independent and uniform.

This comparison demonstrates that the thermalization of the phonon modes for this particular initial state is a two-stage process. This is pronouncedly visible in the maximally occupied modes ($p = \frac{2l\pi}{2\xi}$), corresponding to the even modes in the experiment [16]. In the first stage, the oscillatory behavior of $n_{r,p,t}$ is smoothened via local collisions of momenta $\sim\xi^{-1}$. This corresponds to energy exchange between the relative modes. In the second stage, global thermalization is achieved by energy redistribution between the relative and the absolute mode; see Fig. 9.

B. Relaxation of the phase correlation function

The oscillatory behavior of the phonon densities introduces an additional length scale, the oscillation length ξ, which will be visible in experimental observables that depend on $n_{r,q,t}$, such as the phase correlation function $C(x,t)$ discussed above. The thermalization dynamics due to collisions will, however, lead to a uniform, nonoscillating temperature and erase the effect of ξ in the asymptotic evolution. In the following, we discuss in which way this behavior can be monitored in terms of the phase correlation function.

Relaxation in the absence of phonon collisions. In the absence of collisions, the dynamics of $\theta_{r,x,t}$ is completely governed by the dephasing of the anomalous contributions and the relative phase is determined by the middle part of Eq. (4.12) and the initial densities (5.1)–(5.3), leading to

$$\Delta\theta_{r,x,t} = \int_p \frac{T_r e^{-\frac{|p|}{\Lambda}}}{K\nu p^2}[1-\cos(px)][1-\cos(2\nu|p|t)]\cos^2(p\xi). \qquad (5.6)$$

This equation can be solved analytically but contains quite a number of different temporal and spatial regimes. Since we are generally interested in the thermalization dynamics at distances $x \sim \xi$, we assume $\nu t \gg \xi$ in the following. In this limit, we find

$$\Delta\theta_{r,x,t} = \frac{\pi T_r}{4K\nu} \times \begin{cases} x, & \text{for } x < 2\xi, \\ 2x - 2\xi, & \text{for } 2\xi < x < 2\nu t, \\ 4\nu t - 2\xi, & \text{for } 2\nu t < x, \end{cases} \qquad (5.7)$$

and recognize a change in the slope of $\Delta\theta_{r,x,t}$ at distances $x = 2\xi$. For smaller distances $x < 2\xi$, the slope is only half as steep as for larger distances $x > 2\xi$.

This leads to a clearly observable cusp in the spatial dependence of $\Delta\theta_{r,x,t}$ as well as in $C(x,t)$ at $x = 2\xi$, as one can see from Fig. 10 [orange (bright) lines]. This cusp is observable in the prethermal regime $t_{\mathrm{ther}} > t > t_{\mathrm{preth}}$, for which $m_{r,p,t}$ is dephased but $n_{r,p,t}$ remains still pinned to its initial value $n_{r,p,t=0}$. One does, however, not expect such behavior in the thermal regime for times $t > t_{\mathrm{therm}}$ and thus to serve as an indicator of thermalization on distances $x \sim 2\xi$.

Relaxation in the presence of collisions. In the presence of collisions, the normal relative density $n_{r,p,t}$ is no longer prevented from relaxation and acquires the shape of a thermal Rayleigh-Jeans distribution, $n_{r,p,t\to\infty} = T_{\mathrm{f}}/(\nu|p|)$. The thermalized momentum regime, i.e., the momentum regime $p > p_t^{(c)}$, for which the relative density is well described by this distribution, is established at larger momenta and spreads to lower momenta as time evolves. As soon as the thermalized regime reaches the inverse oscillation scale, $2p_t^{(c)} = \xi^{-1}$, the effect of collisions becomes visible on the length scale of the oscillations. Consequently, the relative phase on smaller distances $x < 2\xi$ is thermal $\Delta\theta_{r,x,t} = \frac{\pi T_{\mathrm{f}} x}{2K\nu}$. In Fig. 10(a), the time-evolved relative phase $\Delta\theta_{r,x,t}$ in the presence of phonon collisions is compared to the $\Delta\theta_{r,x,t}$ in the absence of collisions and the difference is clearly visible at $x = 2\xi = 15\Lambda^{-1}$.

In the limit of $t \to \infty$, one can evaluate the ratio of the thermal coherence factor $C^{(\mathrm{therm})}$ over the coherence factor in the absence of collisions $C^{(\mathrm{preth})}$:

$$c_\xi = \frac{C^{(\mathrm{therm})}(2\xi,t)}{C^{(\mathrm{preth})}(2\xi,t)} = e^{\frac{\pi\xi}{4K\nu}(T_r - 2T_{\mathrm{f}})} = e^{\frac{\pi\xi}{4K\nu}\left(\frac{2T_r(\xi\Lambda)^2}{1+4(\xi\Lambda)^2} - T_a\right)}. \qquad (5.8)$$

For the choice of a moderate oscillation length $\xi \approx 7.5\Lambda^{-1}$ and the parameters from Table I, $c_\xi \approx 0.83$, which is clearly within the experimental resolution of the coherence factor.

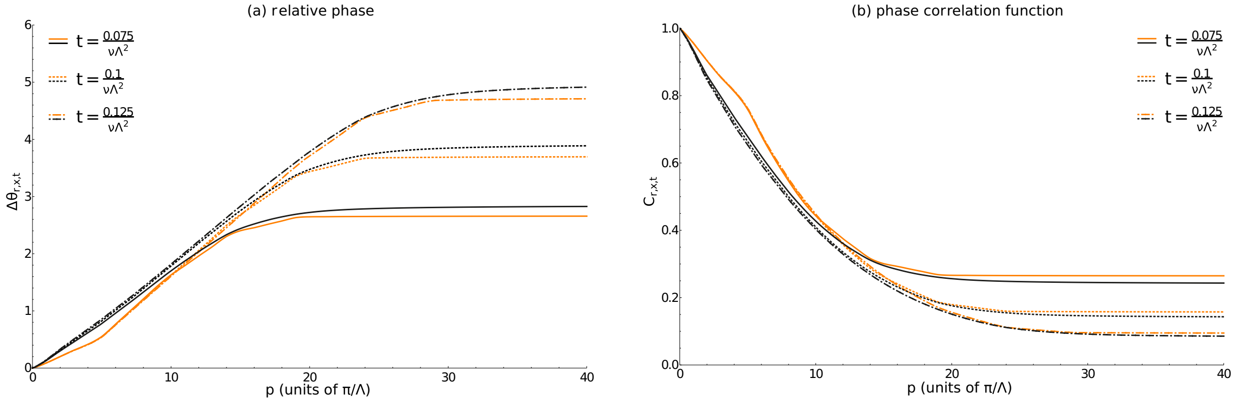

FIG. 10. Initial parameters as in Table I and an oscillation length $\xi = 7.5\Lambda^{-1}$: (a) Comparison of the evolution of the relative phase $\Delta\theta_{r,x,t}$ in the presence [black (dark) lines] and absence [orange (bright) lines] of phonon collisions. (b) The same comparison for the coherence factor $C(x,t)$. The difference between a thermal and a nonthermalized state becomes quite significant at distances on the order of twice the oscillation length, $x = 2\xi$.

The typical timescale at which the coherence factor of the thermalizing system starts to deviate from the prethermal coherence factor at $x = 2\xi$ is given by the collision time at momentum $p = \xi$, $t_{\text{coll}} = (\nu/T_r v^2)^{1/2}\xi^{\frac{3}{2}}$. For a set of initial states with different oscillation lengths ξ this would also allow the measurement of the exponent $\alpha = 3/2$ for the self-energy, validating the picture of resonantly interacting phonons in one dimension.

In Fig. 10(b), the evolution of the coherence factor for a thermalizing system with an oscillating initial distribution is compared to its evolution in the absence of collisions. For the chosen evolution times t, the evolution at the distance $x = 2\xi$ has taken place and both graphs are static but well separable. This demonstrates the clear difference between the prethermal state of the system (corresponding to an evolution in the absence of collisions) and the asymptotic thermal state for this class of initial states and thus c_ξ can serve as a tool for the experimental observation of thermalization in the two-wire system. In contrast to the evolution starting from a nearly thermal state, where asymptotic thermalization is hardly observable in the long-distance behavior of the coherence factor (cf. Fig. 7), the evolution of an oscillating initial density features a clear, short-distance ($x \approx 2\xi$) signature of thermalization. Given the experimental realizability of such out-of-equilibrium states, which is motivated here based on previous experiments, they may serve as good candidates for the observation of thermalization in atomic interferometers.

VI. CONCLUSION

In this article, we have investigated the relaxation of two initially correlated quantum wires after an initial split in the presence of intrawire phonon collisions. We put an emphasis on comparing this dynamics to the previously studied collisionless Luttinger liquid theory and on the analysis of the experimental observability of the asymptotic thermalization in the interacting model. While the effect of collisions is clearly visible in terms of the temporal decay of interwire correlations $\langle a^\dagger_{1,x,t} a_{2,x,t}\rangle \overset{t\to\infty}{\to} 0$ and the redistribution of energy between the intrawire modes, it is less pronounced in typical experimental observables like the coherence factor $\Psi_c(t)$ or the relative phase correlation function $C(x,t)$. This sheds light on the experimental observation that, even for relatively large times, a deviation of the dynamics from the quadratic Luttinger theory prediction is hardly observable. The latter relies on the fact that for the common splitting procedure the resulting initial state is very close to a thermal state, which features a discrepancy in the temperatures between the relative and the absolute mode. We demonstrate, however, that indications for thermalization can become more pronounced if the initial state is prepared farther away from a thermal state, for instance by modifying the splitting procedure. By tuning the initial state such that it becomes clearly nonthermal, the effect of collisions and the dynamics beyond single-particle dephasing can be clearly observed in experiments. This lays out a potential route for further experiments in order to reveal the asymptotic thermalization dynamics of nearly integrable models.

ACKNOWLEDGMENTS

We thank B. Rauer for fruitful discussions. S.H. was supported by the German Excellence Initiative via the Nanosystems Initiative Munich (NIM). M.B. and S.D. acknowledge support by the German Research Foundation (DFG) through the Institutional Strategy of the University of Cologne within the German Excellence Initiative (ZUK 81), and S.D. support by the DFG within the CRC 1238 (project C04) and the European Research Council via ERC Grant Agreement No. 647434 (DOQS). M.B. acknowledges support from the Alexander von Humboldt foundation. J.S. acknowledges support by the European Research Council, ERC-AdG *QuantumRelax* (320975).

APPENDIX A: KINETIC EQUATION FROM THE KELDYSH FORMALISM

We give a short overview on the central concepts and formulas of the Keldysh field integral formalism that are used in the main work. The first section is devoted to the description of the Green's function in Nambu basis for the coupled two-wire system. Then we go on and introduce the Wigner transformation and finally discuss the derivation of the kinetic equations.

1. Nambu space representation

In the presence of anomalous modes, the Green's functions and correlations are conveniently expressed in terms of Nambu spinors of complex bosonic fields in Keldysh space [36]

$$\begin{aligned} A_{\alpha,p,t} &= (A_{cl,\alpha,p,t}, A_{q,\alpha,p,t}) \\ &= (a_{cl,\alpha,p,t}, a^{*}_{cl,\alpha,-p,t}, a_{q,\alpha,p,t}, a^{*}_{q,\alpha,-p,t})^{T}, \end{aligned} \tag{A1}$$

where (cl,q) label classical and quantum fields and α is either the wire index $\alpha = 1,2$ or labels the relative and absolute modes $\alpha = a,r$. The total Nambu Green's function in the wire basis is defined as

$$iG_{p,t,t'} = \left\langle \begin{pmatrix} A_{1,p,t} \\ A_{2,p,t} \end{pmatrix} (A^{\dagger}_{1,p,t'}, \quad A^{\dagger}_{2,p,t'}) \right\rangle. \tag{A2}$$

It consists of 4 sectors α,β whereas each sector consists of advanced or retarded and Keldysh (correlation) Green's function

$$\begin{aligned} iG_{\alpha\beta,p,t,t'} &= \langle A_{\alpha,p,t} A^{\dagger}_{\beta,p,t'} \rangle \\ &= \begin{pmatrix} G^{K}_{\alpha\beta,p,t,t'} & G^{R}_{\alpha\beta,p,t,t'} \\ G^{A}_{\alpha\beta,p,t,t'} & 0 \end{pmatrix}, \end{aligned} \tag{A3}$$

where, again, α,β are wire indexes. The retarded Green's function in operator representation reads ([,] the commutator)

$$\begin{aligned} &iG^{R}_{\alpha\beta,p,t,t'} \\ &= \Theta(t-t') \begin{pmatrix} \langle [a_{\alpha,p,t}, a^{\dagger}_{\beta,p,t'}] \rangle & \langle [a_{\alpha,p,t}, a_{\beta,-p,t'}] \rangle \\ \langle [a^{\dagger}_{\beta,p,t'}, a^{\dagger}_{\alpha,-p,t}] \rangle & \langle [a^{\dagger}_{\beta,-p,t'}, a_{\alpha,-p,t}] \rangle \end{pmatrix} \\ &= i \begin{pmatrix} d^{R}_{\alpha\beta,p,t,t'} & o^{R}_{\alpha\beta,p,t,t'} \\ o^{A}_{\alpha\beta,-p,t,t'} & d^{A}_{\alpha\beta,-p,t,t'} \end{pmatrix}. \end{aligned} \tag{A4}$$

Advanced and retarded propagators are Hermitian conjugate to each other $G^{A}_{\alpha\beta,p,t,t'} = [G^{R}_{\alpha\beta,p,t,t'}]^{\dagger}$. Since the Hamiltonian does not couple the two different wires, annihilation and creation operators of different wires commute at all times, i.e., $[a_{\alpha,p}, a^{\dagger}_{\beta,p'}] = \delta_{\alpha,\beta}\delta_{p,p'}$, and thus the retarded Green's function is diagonal in the wire index.

The Keldysh Green's function in the wire basis has the operator representation ({,} the anticommutator)

$$\begin{aligned} iG^{K}_{\alpha\beta,p,t,t'} &= \begin{pmatrix} \langle \{a_{\alpha,p,t}, a^{\dagger}_{\beta,p,t'}\} \rangle & \langle \{a_{\alpha,p,t}, a_{\beta,p,t'}\} \rangle \\ \langle \{a^{\dagger}_{\alpha,p,t}, a^{\dagger}_{\beta,p,t'}\} \rangle & \langle \{a_{\alpha,p,t}, a^{\dagger}_{\beta,p,t'}\} \rangle \end{pmatrix} \\ &= i \begin{pmatrix} d^{K}_{\alpha\beta,p,t,t'} & o^{K}_{\alpha\beta,p,t,t'} \\ o^{K}_{\alpha\beta,-p,t,t'} & d^{K}_{\alpha\beta,-p,t,t'} \end{pmatrix}. \end{aligned} \tag{A5}$$

It is anti-Hermitian $G^{K}_{\alpha\beta,p,t,t'} = -[G^{K}_{\alpha\beta,p,t,t'}]^{\dagger}$, which allows us to parametrize it in terms of the Hermitian distribution function $F_{p,t,t'}$ and the retarded or advanced Green's function, as well as the matrix $\Sigma_z = \sigma_z \otimes \mathbb{1}$ via

$$G^{K}_{p,t,t'} = (G^{R} \circ \Sigma_z \circ F - F \circ \Sigma_z \circ G^{A})_{p,t,t'}. \tag{A6}$$

The matrix Σ_z thereby preserves the symplectic structure of the bosonic Nambu space and $\circ$ represents a convolution in time and a product in momentum space.

2. Wigner approximation and Dyson equation

The two-point functions in this work are represented in Wigner coordinates in time. It is a convenient representation for non-time-translationally-invariant systems and for two different times t_1,t_2 introduces a forward (or absolute) time $t = (t_1+t_2)/2$ and a relative time $\delta_t = t_1 - t_2$ [36]. The Wigner transform $\mathcal{WT}$ is the Fourier transform with respect to the relative time argument; we denote the corresponding Green's function as

$$G_{p,t,\omega} = \mathcal{WT}\{G_{p,t_1,t_2}\} = \int_{\delta_t} e^{-i\omega\delta_t} G_{p,\, t+\frac{\delta_t}{2},\, t-\frac{\delta_t}{2}}. \tag{A7}$$

In order to determine the time evolution of the distribution function F, which contains the phonon densities, one makes use of the Dyson equation

$$G^{-1} = P - \Sigma, \tag{A8}$$

where G is the full propagator and P is the inverse, bare propagator, and Σ is the self-energy. It has the structure

$$\Sigma_{\alpha\beta,p,\omega,t} = \begin{pmatrix} 0 & \Sigma^{A}_{\alpha\beta,p,\omega,t} \\ \Sigma^{R}_{\alpha\beta,p,\omega,t} & \Sigma^{K}_{\alpha\beta,p,\omega,t} \end{pmatrix}. \tag{A9}$$

As discussed in Sec. II, the resonant interactions couple only phonons that travel in the same direction and thus no pairs $p, -p$, which excludes anomalous retarded self-energies. Furthermore, the Hamiltonian contains no interwire coupling, such that the retarded self-energy must be also diagonal in the wire basis (please note that both of these statements do not hold for the Keldysh self-energy). It thus reads as

$$\Sigma^{R}_{\alpha\beta,p,\omega,t} = -i\delta_{\alpha,\beta} \begin{pmatrix} \sigma^{R}_{\alpha\beta,p,\omega,t} & 0 \\ 0 & \sigma^{A}_{\alpha\beta,-p,-\omega,t} \end{pmatrix}. \tag{A10}$$

The anti-Hermitian Keldysh self-energy is

$$\Sigma^{K}_{\alpha\beta,p,\omega,t} = -i2 \begin{pmatrix} \sigma^{K}_{\alpha\beta,p,\omega,t} & \Phi^{K}_{\alpha\beta,p,\omega,t} \\ (\Phi^{K}_{\alpha\beta,p,\omega,t})^{*} & \sigma^{K}_{\alpha\beta,p,\omega,t} \end{pmatrix}. \tag{A11}$$

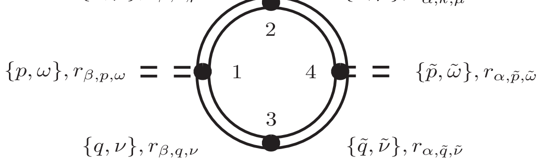

FIG. 11. One-loop diagram for the self-energy Σ. Each line has momentum and frequency $\{k,\omega\}$ and a direction $r_{\alpha,k,\mu} = \pm 1$ for outgoing, ingoing lines, which depends also on the wire index α. Momentum conservation, energy conservation, and the resonance condition have to be applied at each connecting element {1,2,3,4}, which requires that normal (anomalous) self-energies are generated exclusively by normal (anomalous) Green's functions.

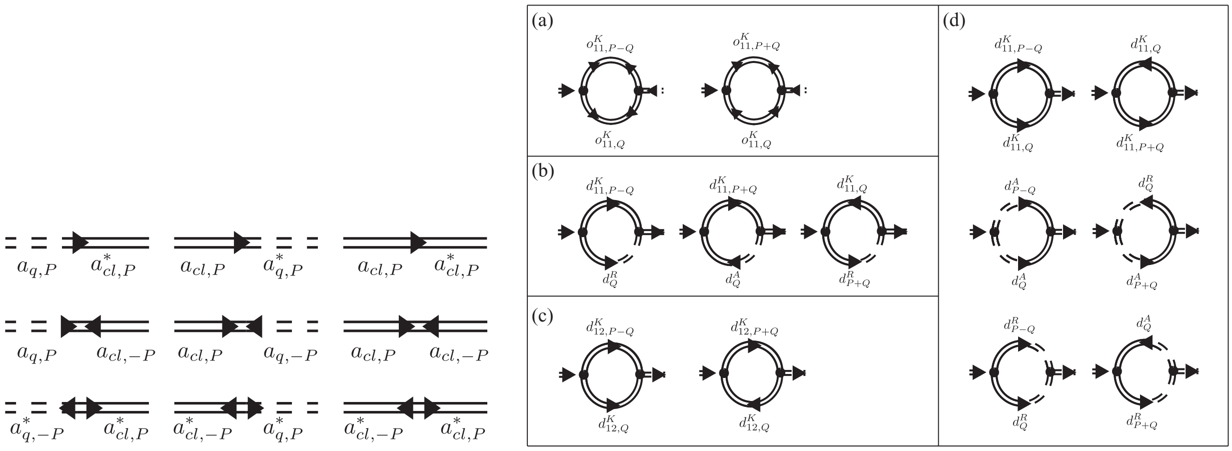

FIG. 12. Left column: Illustration of the diagrammatic lines for the propagators in Keldysh space. Dashed lines correspond to quantum fields and bold lines to classical fields. Arrows indicate the momentum and energy transfer direction, going from annihilation to creation operators. Right column: Diagrammatic representation of the self-energy diagrams. (a) Anomalous intrawire Keldysh self-energy. (b) Retarded self-energy. (c) Normal interwire Keldysh self-energy. (d) Normal intrawire Keldysh self-energy.

The kinetic equation (3.5) is now determined by substituting Eq. (A8) into (A6) and rearranging it to

$$(P^R \circ \Sigma_z \circ F - F \circ \Sigma_z \circ P^A)_{p,\omega,t} = I^{\text{coll}}_{p,\omega,t}. \tag{A12}$$

The collision integral on the right side is defined as

$$I^{\text{coll}}_{p,\omega,t} = \Sigma^K_{p,\omega,t} - (\Sigma^R \circ \Sigma_z \circ F - F \circ \Sigma_z \circ \Sigma^A)_{p,\omega,t}. \tag{A13}$$

The Wigner transform of a convolution $A = B \circ C$ in time is not simply the product of the Wigner transforms of B,C. Instead one finds

$$\begin{aligned} A_{\omega,t} &= \mathcal{WT}\{A\} = \mathcal{WT}\{B \circ C\} \qquad \text{(A14)} \\ &= \mathcal{WT}\{B\} e^{\frac{i}{2}(\overleftarrow{\partial}_t \overrightarrow{\partial}_\omega - \overleftarrow{\partial}_\omega \overrightarrow{\partial}_t)} \mathcal{WT}\{C\} \\ &= B_{\omega,t} e^{\frac{i}{2}(\overleftarrow{\partial}_t \overrightarrow{\partial}_\omega - \overleftarrow{\partial}_\omega \overrightarrow{\partial}_t)} C_{\omega,t}. \end{aligned}$$

Partial derivatives pointing to the left act on B, while those pointing on the right act on C. Thus approximating $A_{\omega,t} = B_{\omega,t} C_{\omega,t}$ by the product of Wigner transforms is satisfactory, if the corrections to the zeroth-order term in the exponential in Eq. (A14) are sufficiently small.

The expansion of the kinetic equation in zeroth order is

$$i\partial_t \tilde{F}_{p,\omega,t} \approx \Sigma^R_{p,\omega,t} \tilde{F}_{p,\omega,t} \Sigma_z - \Sigma_z \tilde{F}_{p,\omega,t} \Sigma^A_{p,\omega,t} + \Sigma^K_{p,\omega,t}, \tag{A15}$$

where $\tilde{F}_{p,\omega,t} = \Sigma_z F_{p,\omega,t} \Sigma_z$ and Eq. (A15) contains only matrix multiplications. This is the Wigner approximation for the kinetic equation and it is valid in the case of negligible higher order corrections, i.e.,

$$\frac{|\partial_t F_{\alpha\beta,q,\omega,t}| \left|\partial_\omega \Sigma^R_{\alpha\beta,q,\omega,t}\right|}{|F_{\alpha\beta,q,\omega,t}| \left|\Sigma^R_{\alpha\beta,q,\omega,t}\right|} \ll 1. \tag{A16}$$

This criterion is discussed in Eq. (3.8).

APPENDIX B: DIAGRAMMATIC ANALYSIS OF THE SELF-ENERGIES

We give a brief summary of the diagrammatic approach for the computation of the self-energies and refer to Ref. [29] for a detailed analysis. We use the shorthand notation $P = (p,\omega,t)$ and $-P = (-p,-\omega,t)$.

1. Selection rules for the diagrammatic representation of the self-energies

The combination of resonant interactions, momentum conservation, and energy conservation restricts the contributions to the self-energies to a certain subclass of diagrams [29]. A general one-loop diagram is depicted in Fig. 11. We identify each leg with a label for momentum, frequency, and subsystem $\alpha,\beta \in \{1,2\}$. In addition, we explicitly label the direction of momentum and energy transfer with $r_{\alpha/\beta} \in \{\pm 1\}$ for outgoing and incoming.

The resonance condition yields an additional constraint to this class of diagrams, which, after some algebra, requires $r_{\beta,k,\mu}\, r_{\alpha,\tilde{k},\tilde{\mu}} = r_{\beta,q,\nu}\, r_{\alpha,\tilde{q},\tilde{\nu}} = r_{\beta,p,\omega}\, r_{\alpha,\tilde{p},\tilde{\omega}}$, in addition to momentum and energy conservation at each vertex. This very helpful condition implies that normal propagators contribute exclusively to the normal self-energy, while anomalous propagators contribute exclusively to the anomalous self-energy.

2. Self-energies

The self-energies are determined via the canonical Dyson-Schwinger approach [29]. The corresponding diagrams are summarized in Fig. 12. The analytic expressions for the self-energies contain the diagonal Green's functions $d^{R,A,K}$ and the off-diagonal Green's functions o^K as defined in Eqs. (A4), (A5), as well as the vertex $V_{p,q,p\pm q}$. The Dyson-Schwinger equations for the latter can be found in Ref. [29]. Using their bare value (which corresponds to the Born approximation) yields

$V(p,q,p\pm q)=\sqrt{|pq(p\pm q)|}$. The Dyson-Schwinger equations for the self-energies are (all retarded and advanced functions are diagonal in wire-index and Nambu space)

$$\sigma^R_P = \frac{i}{4\pi^2}\int_q\int_\nu \left(2V^2_{p,q,p-q}\left[d^K_{11,P-Q}d^R_Q\right] + 2V^2_{p,q,p+q}\left[d^K_{11,P+Q}d^A_Q\right] + 2V^2_{p,q,p+q}\left[d^R_{P+Q}d^K_{11,Q}\right]\right), \tag{B1}$$

$$\begin{aligned}\sigma^K_{11,P} = -\frac{1}{4\pi^2}\int_q\int_\nu \Big(&V^2_{p,q,p-q}\left[d^R_{P-Q}d^R_Q\right] + V^2_{p,q,p-q}\left[d^A_{P-Q}d^A_Q\right] + V^2_{p,q,p-q}\left[d^K_{11,P-Q}d^K_{11,Q}\right]\\ &+2V^2_{p,q,p+q}\left[d^R_{P+Q}d^A_Q\right] + 2V^2_{p,q,p+q}\left[d^A_{P+Q}d^R_Q\right] + 2V^2_{p,q,p+q}\left[d^K_{11,P+Q}d^K_{11,Q}\right]\Big),\end{aligned} \tag{B2}$$

$$\sigma^K_{12,P} = -\frac{1}{4\pi^2}\int_q\int_\nu \left(V^2_{p,q,p-q}\left[d^K_{12,P-Q}d^K_{12,Q}\right] + 2V^2_{p,q,p+q}\left[d^K_{12,P+Q}d^K_{12,Q}\right]\right), \tag{B3}$$

$$\Phi^K_{11,P} = -\frac{1}{4\pi^2}\int_q\int_\nu \left(V^2_{p,q,p-q}\left[o^K_{11,P-Q}o^K_{11,Q}\right] + 2V^2_{p,q,p+q}\left[o^K_{11,P+Q}o^K_{11,Q}\right]\right). \tag{B4}$$

In the quasiparticle approximation, all the spectral weight is located on-shell. As a consequence, the spectral function $\mathcal{A}_P$, defined in Eq. (3.10), is sharply peaked at frequencies equal to the dispersion. Then the retarded, advanced, and Keldysh Green's function can be expressed via the spectral function and the phonon densities, as in Eqs (3.10), (3.11). This yields

$$\sigma^R_{p,t} = \int_q\int_{\omega,\nu} \left(V^2_{p,q,p-q}[2n_{1,1,p-q,t} + 2n_{1,1,q,t} + 2]\mathcal{A}_{P-Q}\mathcal{A}_Q + 2V^2_{p,q,p+q}[2n_{1,1,q,t} - 2n_{1,1,p+q,t}]\mathcal{A}_{P+Q}\mathcal{A}_Q\right), \tag{B5}$$

$$\begin{aligned}\sigma^K_{11,p,t} = \int_q\int_{\omega,\nu} \Big(&V^2_{p,q,p-q}[4n_{1,1,p-q,t}n_{1,1,q,t} + 2n_{1,1,p-q,t} + 2n_{1,1,q,t} + 2]\mathcal{A}_{P-Q}\mathcal{A}_Q\\ &+2V^2_{p,q,p+q}[4n_{1,1,p+q,t}n_{1,1,q,t} + 2n_{1,1,p+q,t} + 2n_{1,1,q,t}]\mathcal{A}_{P+Q}\mathcal{A}_Q\Big),\end{aligned} \tag{B6}$$

$$\sigma^K_{12,p,t} = \int_q\int_{\omega,\nu} \left(V^2_{p,q,p-q}[4n_{1,2,p-q,t}n_{1,2,q,t}]\mathcal{A}_{P-Q}\mathcal{A}_Q + 2V^2_{p,q,p+q}[4n_{1,2,p+q,t}n_{1,2,q,t}]\mathcal{A}_{P+Q}\mathcal{A}_Q\right), \tag{B7}$$

$$\Phi^K_{11,p,t} = \int_q\int_{\omega,\nu} \left(V^2_{p,q,p-q}[4m_{1,1,p-q,t}m_{1,1,q,t}]\mathcal{A}_{P-Q}\mathcal{A}_Q + 2V^2_{p,q,p+q}[4m_{1,1,p+q,t}m_{1,1,q,t}]\mathcal{A}_{P+Q}\mathcal{A}_Q\right). \tag{B8}$$

This eliminates the frequency integrals from the expression and leads to Eqs. (3.15)–(3.17).

[1] T. Kinoshita, T. Wenger, and D. S. Weiss, Nature (London) **440**, 900 (2006).

[2] M. Gring, M. Kuhnert, T. Langen, T. Kitagawa, B. Rauer, M. Schreitl, I. Mazets, D. A. Smith, E. Demler, and J. Schmiedmayer, Science **337**, 1318 (2012).

[3] T. Langen, R. Geiger, M. Kuhnert, B. Rauer, and J. Schmiedmayer, Nat. Phys. **9**, 640 (2013).

[4] S. Hofferberth, I. Lesanovsky, B. Fischer, T. Schumm, and J. Schmiedmayer, Nature (London) **449**, 324 (2007).

[5] S. Trotzky, Y.-A. Chen, A. Flesch, I. P. McCulloch, U. Schollwöck, J. Eisert, and I. Bloch, Nat. Phys. **8**, 325 (2012).

[6] F. Meinert, M. J. Mark, E. Kirilov, K. Lauber, P. Weinmann, A. J. Daley, and H.-C. Nägerl, Phys. Rev. Lett. **111**, 053003 (2013).

[7] R. Geiger, T. Langen, I. Mazets, and J. Schmiedmayer, New J. Phys. **16**, 053034 (2014).

[8] M. Andrews, C. Townsend, H.-J. Miesner, D. Durfee, D. Kurn, and W. Ketterle, Science **275**, 637 (1997).

[9] R. Bistritzer and E. Altman, Proc. Natl. Acad. Sci. USA **104**, 9955 (2007).

[10] N. K. Whitlock and I. Bouchoule, Phys. Rev. A **68**, 053609 (2003).

[11] J. Schachenmayer, L. Pollet, M. Troyer, and A. J. Daley, Phys. Rev. A **89**, 011601 (2014).

[12] N. Strohmaier, D. Greif, R. Jördens, L. Tarruell, H. Moritz, T. Esslinger, R. Sensarma, D. Pekker, E. Altman, and E. Demler, Phys. Rev. Lett. **104**, 080401 (2010).

[13] M. Rigol, V. Dunjko, and M. Olshanii, Nature (London) **452**, 854 (2008).

[14] L. M. Sieberer, M. Buchhold, and S. Diehl, Rep. Prog. Phys. **79**, 096001 (2016).

[15] L. Foini and T. Giamarchi, Phys. Rev. A **91**, 023627 (2015).

[16] T. Langen, S. Erne, R. Geiger, B. Rauer, T. Schweigler, M. Kuhnert, W. Rohringer, I. E. Mazets, T. Gasenzer, and J. Schmiedmayer, Science **348**, 207 (2015).

[17] E. Haller, R. Hart, M. J. Mark, J. G. Danzl, L. Reichsöllner, M. Gustavsson, M. Dalmonte, G. Pupillo, and H.-C. Nägerl, Nature (London) **466**, 597 (2010).

[18] E. T. Jaynes, Phys. Rev. **106**, 620 (1957).

[19] J. M. Deutsch, Phys. Rev. A **43**, 2046 (1991).

[20] M. Srednicki, Phys. Rev. E **50**, 888 (1994).

[21] M. Srednicki, J. Phys. A: Math. Gen. **32**, 1163 (1999).

[22] M. Rigol, V. Dunjko, V. Yurovsky, and M. Olshanii, Phys. Rev. Lett. **98**, 050405 (2007).

[23] J. Berges, S. Borsányi, and C. Wetterich, Phys. Rev. Lett. **93**, 142002 (2004).

[24] M. Kollar, F. A. Wolf, and M. Eckstein, Phys. Rev. B **84**, 054304 (2011).
[25] M. Buchhold, M. Heyl, and S. Diehl, Phys. Rev. A **94**, 013601 (2016).
[26] T. Kitagawa, A. Imambekov, J. Schmiedmayer, and E. Demler, New J. Phys. **13**, 073018 (2011).
[27] A. Polkovnikov, K. Sengupta, A. Silva, and M. Vengalattore, Rev. Mod. Phys. **83**, 863 (2011).
[28] M. Buchhold and S. Diehl, Phys. Rev. A **92**, 013603 (2015).
[29] M. Buchhold and S. Diehl, Eur. Phys. J. D **69**, 224 (2015).
[30] A. Andreev, Sov. Phys. JETP **51**, 1038 (1980).
[31] A. A. Burkov, M. D. Lukin, and E. Demler, Phys. Rev. Lett. **98**, 200404 (2007).
[32] M. Punk and W. Zwerger, New J. Phys. **8**, 168 (2006).
[33] B. Rauer, S. Erne, T. Schweigler, F. Cataldini, M. Tajik, and J. Schmiedmayer, Science, eaan7938 (2018), doi:10.1126/science.aan7938.
[34] T. Giamarchi, *Quantum Physics in One Dimension* (Oxford University Press, Oxford, 2004).
[35] F. D. M. Haldane, Phys. Rev. Lett. **47**, 1840 (1981).
[36] A. Kamenev, *Field Theory of Non-Equilibrium Systems* (Cambridge University Press, Cambridge, 2011).
[37] A. Polkovnikov, E. Altman, and E. Demler, Proc. Natl. Acad. Sci. USA **103**, 6125 (2006).
[38] G. D. Mahan, *Many-Particle Physics* (Springer Science & Business Media, New York, 2013).
[39] D. J. Amit and V. Martin-Mayor, *Field Theory, the Renormalization Group, and Critical Phenomena: Graphs to Computers* (World Scientific Publishing Co., Inc., Singapore, 2005).
[40] M. E. Peskin, *An Introduction to Quantum Field Theory* (Westview Press, Oxford, 1995).
[41] H. Monien, M. Linn, and N. Elstner, Phys. Rev. A **58**, R3395 (1998).
[42] M. Olshanii, Phys. Rev. Lett. **81**, 938 (1998).
[43] M. Moeckel and S. Kehrein, Phys. Rev. Lett. **100**, 175702 (2008).

Correction: A misspelling introduced in the abstract during the production process has been fixed.

6 Conclusion and outlook

In this thesis, two famous examples of non-Fermi liquids were studied in a combination of numerical and analytical methods.

Within the first four chapters, the concept of fractionalized Fermi liquids was used and investigated in form of the spinon-dopon approach and the quantum dimer Hamiltonian. We picked up the latest developments in the field of microscopy in ultracold quantum gas systems [GPM$^+$16, CNL$^+$16, CMD$^+$16, MCJ$^+$17] and proposed a sensitive and suitable technique to distinguish long- and short-range magnetically ordered states. Here, future progress in experimental techniques could open the path to realize interesting concepts in a microscopic and clean environment such as pseudogap formation and charge density wave order. Further work in this field could include an experimental proposal on how to implement the quantum dimer model in such systems similar to Ref. [NCA$^+$12]. This may shed light onto the question wether the concept of a resonating valence bond state stands in direct relation to such phenomena. Next, we also succesfully started to set up a cluster analysis of the two-dimensional Fermi-Hubbard model using a real-frequency impurity solver, the numerical renormalization group technique, to circumvent any uncontrolled analytic continuation. It is also applicable down to zero temperature. In our approach we considered spin-polarized baths due to numerical limitations. We verified the existence of a Mott gap at half-filling and further observed a momentum-selective Mott gap at small doping. However, the particle density on the cluster suddenly jumps when further doping the system away from half-filling. This is an artefact from the spin-polarized baths. According to the resolved doping regimes, the Fermi surface undergoes a topological transition (cf. Ref. in Sec. 4.4). The spectral weight at the Fermi level indicates that the main physics happens within three momentum patches $K \in \{(0,0),(0,\pi),(\pi,0)\}$. Thus, we are currently studying the Fermi-Hubbard model with three SU(2) symmetric baths coupled exactly to these patches. Due to this approach, the numerical cost is considerably reduced and SU(2) symmetry is restored. In this case we expect no artificial jump in the occupation number of the cluster. The implementation of the original quantum dimer Hamiltonian in a dimer Hilbert space with orthonormal dimer configurations would be a puzzeling task for the future in order to see wether both models show similar dynamical and static behavior in the relevant doping regime around $p \approx 0.1$ [PAS15].

In the second part of this thesis, we proposed a new construcive bosonization technique based on scattering operators, which are especially suited to inhomogeneous system. An exact solution for a rather general two-flavor model was derived. The impact of the dispersion band curvature along similar technical approaches as in Ref. [PGM14, PGOM14] could provide further insight into the nature of one-dimensional systems and could confirm the proposed paradigm shift towards inhomogeneous one-dimensional systems [Hal81]. Last, we showed that cubic interactions among low-energy bosonic excitations in one-dimensional systems break integrability of the quadratic Luttinger model and cause thermalization. We derived the kinetic equation for two uncoupled one-dimensional quantum wire after a sudden quench (s. Ref. in Sec. 5.7). As proposed in our analysis, the thermalization process could be monitored in future experiments by choosing a special initial state.

List of Figures

Bibliography

[AA88a] D. P. Arovas and A. Auerbach, *Functional integral theories of low-dimensional quantum Heisenberg models*, Phys. Rev. B **38** (1988), no. 1, 316. See page: 17

[AA88b] A. Auerbach and D. P. Arovas, *Spin dynamics in the square-lattice antiferromagnet*, Phys. Rev. Lett. **61** (1988), no. 5, 617. See page: 42

[AA02] E. Altman and A. Auerbach, *Oscillating superfluidity of bosons in optical lattices*, Phys. Rev. Lett. **89** (2002), no. 25, 250404. See page: 119

[AABS19] D. A. Abanin, E. Altman, I. Bloch, and M. Serbyn, *Colloquium: Many-body localization, thermalization, and entanglement*, Rev. Mod. Phys. **91** (2019), no. 2, 021001. See page: 120

[ABM$^+$10] M. Aichhorn, S. Biermann, T. Miyake, A. Georges, and M. Imada, *Theoretical evidence for strong correlations and incoherent metallic state in FeSe*, Phys. Rev. B **82** (2010), no. 6, 064504. See page: 7

[AJAB$^+$07] M. Abdel-Jawad, J. G. Analytis, L. Balicas, A. Carrington, J. P. H. Charmant, M. M. J. French, and N. E. Hussey, *Correlation between T_c and anisotropic quasiparticle scattering in $Tl_2Ba_2CuO_{6+\delta}$*, Phys. Rev. Lett. **99** (2007), no. 10, 107002. See page: 14

[ALR$^+$04] P. W. Anderson, P. A. Lee, M. Randeria, T. M. Rice, N. Trivedi, and F. C. Zhang, *The physics behind high-temperature superconducting cuprates: the 'plain vanilla' version of RVB*, J. Phys.: Cond. Matter **16** (2004), no. 24, R755. See page: 17

[AM88] I. Affleck and J. B. Marston, *Large-n limit of the heisenberg-hubbard model: Implications for high-T_c superconductors*, Phys. Rev. B **37** (1988), no. 7, 3774. See page: 17

[AM12] N. W. Ashcroft and D. N. Mermin, *Festkörperphysik*, Oldenbourg Verlag, 2012. See pages: 1, 3, 7, 19, and 93

[And73] P. W. Anderson, *Resonating valence bonds: A new kind of insulator?*, Materials Research Bulletin **8** (1973), no. 2, 153–160. See page: 39

[And80] A. F. Andreev, *The hydrodynamics of two-and one-dimensional liquids*, Sov. J. Exp. and Theor. Phys. **51** (1980), 1038. See page: 119

[AOM89] H. Alloul, T. Ohno, and P. Mendels, *^{89}Y NMR evidence for a fermi-liquid behavior in $YBa_2Cu_3O_{6+x}$*, Phys. Rev. Lett. **63** (1989), no. 16, 1700. See page: 13

[AS05] F. B. Anders and A. Schiller, *Real-time dynamics in quantum-impurity systems: A time-dependent numerical renormalization-group approach*, Phys. Rev. Lett. **95** (2005), no. 19, 196801. See page: 82

[AS10] A. Altland and B. D. Simons, *Condensed matter field theory*, Cambridge University Press, 2010. See pages: 7, 50, 93, 118, and 120

[ASJL96] O. K. Andersen, S. Y. Savrasov, O. Jepsen, and A. I. Liechtenstein, *Out-of-plane instability and electron-phonon contribution to s-and d-wave pairing in high-temperature superconductors; LDA linear-response calculation for doped $CaCuO_2$ and a generic tight-binding model*, J. Low Temp. Phys. **105** (1996), no. 3-4, 285–304. See page: 11

[Aue12] A. Auerbach, *Interacting electrons and quantum magnetism*, Springer Science & Business Media, 2012. See page: 50

[AYDP+02] O. M. Auslaender, A. Yacoby, R. De Picciotto, K. W. Baldwin, L. N. Pfeiffer, and K. W. West, *Tunneling spectroscopy of the elementary excitations in a one-dimensional wire*, Science **295** (2002), no. 5556, 825–828. See page: 100

[AZHA88] I. Affleck, Z. Zou, T. Hsu, and P. W. Anderson, *SU(2) gauge symmetry of the large-U limit of the Hubbard model*, Phys. Rev. B **38** (1988), no. 1, 745. See page: 17

[BA88] G. Baskaran and P. W. Anderson, *Gauge theory of high-temperature superconductors and strongly correlated Fermi systems*, Phys. Rev. B **37** (1988), no. 1, 580. See page: 17

[BAK+96] G. Blumberg, P. Abbamonte, M. V. Klein, W. C. Lee, D. M. Ginsberg, L. L. Miller, and A. Zibold, *Resonant two-magnon Raman scattering in cuprate antiferromagnetic insulators*, Phys. Rev. B **53** (1996), no. 18, R11930. See pages: 10 and 12

[Bar76] S. E. Barnes, *New method for the Anderson model*, Journal of Physics F: Metal Physics **6** (1976), no. 7, 1375. See page: 17

[BB97] K. B. Blagoev and K. S. Bedell, *Luttinger theorem in one dimensional metals*, Phys. Rev. Lett. **79** (1997), no. 6, 1106. See page: 6

[BBM+10] A. F. Bangura, T. M. Benseman, M. Matusiak, J. R. Cooper, N. E. Hussey, and A. Carrington, *Fermi surface and electronic homogeneity of the overdoped cuprate superconductor $Tl_2Ba_2CuO_{6+\delta}$ as revealed by quantum oscillations*, Phys. Rev. B **82** (2010), no. 14, 140501. See page: 14

[BBW04] J. Berges, Sz. Borsányi, and C. Wetterich, *Prethermalization*, Phys. Rev. Lett. **93** (2004), no. 14, 142002. See page: 120

[BCDS+87] A. Bianconi, A. C. Castellano, M. De Santis, P. Rudolf, P. Lagarde, A. M. Flank, and A. Marcelli, *L2, 3 xanes of the high T_c superconductor $YBa_2Cu_3O{\approx}7$ with variable oxygen content*, Solid State Commun. **63** (1987), no. 11, 1009–1013. See page: 9

[BCIP97] P. Bourges, H. Casalta, A. S. Ivanov, and D. Petitgrand, *Superexchange coupling and spin susceptibility spectral weight in undoped monolayer cuprates*, Phys. Rev. Lett. **79** (1997), no. 24, 4906. See page: 12

[BCJ+19] A. Bohrdt, C. S. Chiu, G. Ji, M. Xu, D. Greif, M. Greiner, E. Demler, F. Grusdt, and M. Knap, *Classifying snapshots of the doped Hubbard model with machine learning*, Nature Physics **15** (2019), no. 9, 921–924. See page: 20

[BCL$^+$99] M. Bockrath, D. H. Cobden, J. Lu, A. G. Rinzler, R. E. Smalley, L. Balents, and P. L. McEuen, *Luttinger-liquid behaviour in carbon nanotubes*, Nature **397** (1999), no. 6720, 598. See page: 99

[BCP08] R. Bulla, T. A. Costi, and T. Pruschke, *Numerical renormalization group method for quantum impurity systems*, Rev. Mod. Phys. **80** (2008), no. 2, 395. See pages: 78, 80, 82, and 87

[BCS57a] J. Bardeen, L. N. Cooper, and J. R. Schrieffer, *Microscopic theory of superconductivity*, Phys. Rev. **106** (1957), no. 1, 162. See pages: 7, 17, and 93

[BCS57b] ———, *Theory of superconductivity*, Phys. Rev. **108** (1957), no. 5, 1175. See pages: 7 and 93

[BD15] M. Buchhold and S. Diehl, *Kinetic theory for interacting Luttinger liquids*, Eur. Phys. J. D **69** (2015), no. 10, 224. See pages: 119 and 122

[BDZ08] I. Bloch, J. Dalibard, and W. Zwerger, *Many-body physics with ultracold gases*, Rev. Mod. Phys. **80** (2008), no. 3, 885. See pages: 19, 20, 21, and 99

[Bet31] H. Bethe, *Zur Theorie der Metalle*, Zeitschrift für Physik **71** (1931), no. 3-4, 205–226. See page: 94

[BF33] J. D. Bernal and R. H. Fowler, *A theory of water and ionic solution, with particular reference to hydrogen and hydroxyl ions*, J. Chem. Phys. **1** (1933), no. 8, 515–548. See page: 40

[BGK$^+$99] R. J. Birgeneau, M. Greven, M. A. Kastner, Y. S. Lee, B. O. Wells, Y. Endoh, K. Yamada, and G. Shirane, *Instantaneous spin correlations in* La_2CuO_4, Phys. Rev. B **59** (1999), no. 21, 13788. See page: 9

[BHS$^+$16] M. Boll, T. A. Hilker, G. Salomon, A. Omran, J. Nespolo, L. Pollet, I. Bloch, and C. Gross, *Spin and charge resolved quantum gas microscopy of antiferromagnetic order in Hubbard chains*, arXiv: 1605.05661 (2016). See page: 20

[BJ08] C. Bourbonnais and D. Jérome, *Interacting electrons in quasi-one-dimensional organic superconductors*, The Physics of Organic Superconductors and Conductors, Springer, 2008, pp. 357–412. See page: 99

[BK01] G. Biroli and G. Kotliar, *A note on cluster methods for strongly correlated electron systems*, arXiv cond-mat/0107108 (2001). See page: 73

[BK02] ———, *Cluster methods for strongly correlated electron systems*, Phys. Rev. B **65** (2002), no. 15, 155112. See page: 78

[BKG$^+$09] J.-S. Bernier, C. Kollath, A. Georges, L. De Leo, F. Gerbier, C. Salomon, and M. Köhl, *Cooling fermionic atoms in optical lattices by shaping the confinement*, Phys. Rev. A **79** (2009), no. 6, 061601. See page: 20

[BKK$^+$97] G. Blumberg, M. Kang, M. V. Klein, K. Kadowaki, and C. Kendziora, *Evolution of magnetic and superconducting fluctuations with doping of high-*T_c *superconductors*, Science **278** (1997), no. 5342, 1427–1432. See pages: 10 and 12

[BL05] R. A. Barankov and L. S. Levitov, *Dynamical projection of atoms to Feshbach molecules at strong coupling*, arXiv cond-mat/0506323 (2005). See page: 119

[BM86] J. G. Bednorz and K. A. Müller, *Possible high-T_c superconductivity in the Ba-La-Cu-O system*, Zeitschrift für Physik B Condensed Matter **64** (1986), no. 2, 189–193. See pages: 6 and 7

[BMGS$^+$19] P. T. Brown, D. Mitra, E. Guardado-Sanchez, R. Nourafkan, A. Reymbaut, C.-D. Hébert, S. Bergeron, A.-M. S. Tremblay, J. Kokalj, D. A. Huse, P. Schauß, and W. S. Bakr, *Bad metallic transport in a cold atom Fermi-Hubbard system*, Science **363** (2019), no. 6425, 379–382. See page: 20

[BPT$^+$10] W. S. Bakr, A. Peng, M. E. Tai, R. Ma, J. Simon, J. I. Gillen, S. Foelling, L. Pollet, and M. Greiner, *Probing the superfluid-to-Mott insulator transition at the single-atom level*, Science **329** (2010), no. 5991, 547–550. See page: 19

[BR70] W. F. Brinkman and T. M. Rice, *Application of Gutzwiller's variational method to the metal-insulator transition*, Phys. Rev. B **2** (1970), no. 10, 4302. See page: 16

[BTL$^+$16] S. Badoux, W. Tabis, F. Laliberté, G. Grissonnanche, B. Vignolle, D. Vignolles, J. Béard, D. A. Bonn, W. N. Hardy, R. Liang, N. Doiron-Leyraud, Louis Taillefer, and Cyril Proust, *Change of carrier density at the pseudogap critical point of a cuprate superconductor*, Nature **531** (2016), no. 7593, 210–214. See pages: 13, 14, and 147

[BTM87] J. G. Bednorz, M. Takashige, and K. A. Müller, *Susceptibility measurements support high-T_c superconductivity in the Ba-La-Cu-o system*, EPL **3** (1987), no. 3, 379. See page: 6

[BZA87] G. Baskaran, Z. Zou, and P. W. Anderson, *The resonating valence bond state and high-T_c superconductivity—a mean field theory*, Solid State Commun. **63** (1987), no. 11, 973–976. See page: 39

[Caz06] MA Cazalilla, *The Luttinger model following a sudden interaction switch-on*, arXiv cond-mat/0606236 (2006). See pages: 119 and 120

[CC06] P. Calabrese and J. Cardy, *Time dependence of correlation functions following a quantum quench*, Phys. Rev. Lett. **96** (2006), no. 13, 136801. See page: 119

[CCG$^+$11] M. A. Cazalilla, R. Citro, T. Giamarchi, E. Orignac, and M. Rigol, *One dimensional bosons: From condensed matter systems to ultracold gases*, Rev. Mod. Phys. **83** (2011), no. 4, 1405. See pages: 118 and 119

[CDMT$^+$16] M. K. Chan, C. J. Dorow, L. Mangin-Thro, Y. Tang, Y. Ge, M. J. Veit, G. Yu, X. Zhao, A. D. Christianson, J. T. Park, Y. Sidis, P. Steffens, D. L. Abernathy, P. Bourges, and M. Greven, *Commensurate antiferromagnetic excitations as a signature of the pseudogap in the tetragonal high-T_c cuprate $HgBa_2CuO_{(4+\delta)}$*, Nature communications **7** (2016), 10819. See page: 12

[CHA$^+$01] R. Coldea, S. M. Hayden, G. Aeppli, T. G. Perring, C. D. Frost, T. E. Mason, S.-W. Cheong, and Z. Fisk, *Spin waves and electronic interactions in La_2CuO_4*, Phys. Rev. Lett. **86** (2001), no. 23, 5377. See page: 10

[CISD97] N. J. Curro, T. Imai, C. P. Slichter, and B. Dabrowski, *High-temperature* ^{63}*Cu(2) nuclear quadrupole and magnetic resonance measurements of* $YBa_2Cu_4O_8$, Phys. Rev. B **56** (1997), no. 2, 877. See page: 13

[CK12] J.-S. Caux and R. M. Konik, *Constructing the generalized Gibbs ensemble after a quantum quench*, Phys. Rev. Lett. **109** (2012), no. 17, 175301. See pages: 119 and 120

[CMD$^+$16] E. Cocchi, L. A. Miller, J. H. Drewes, M. Koschorreck, D. Pertot, F. Brennecke, and M. Köhl, *Equation of state of the two-dimensional Hubbard model*, Phys. Rev. Lett. **116** (2016), no. 17, 175301. See pages: 20 and 145

[CNL$^+$16] L. W. Cheuk, M. A. Nichols, K. R. Lawrence, M. Okan, H. Zhang, and M. W. Zwierlein, *Observation of 2D fermionic Mott insulators of* ^{40}K *with single-site resolution*, Phys. Rev. Lett. **116** (2016), no. 23, 235301. See pages: 20 and 145

[Col84] P. Coleman, *New approach to the mixed-valence problem*, Phys. Rev. B **29** (1984), no. 6, 3035. See page: 17

[Col07] ———, *Heavy fermions: Electrons at the edge of magnetism*, Handbook of Magnetism and Advanced Magnetic Materials (2007). See page: 6

[CRK$^+$93] S. L. Cooper, D. Reznik, A. Kotz, M. A. Karlow, R. Liu, M. V. Klein, W. C. Lee, J. Giapintzakis, D. M. Ginsberg, B. W. Veal, and A. P. Paulikas, *Optical studies of the a-, b-, and c-axis charge dynamics in* $YBa_2Cu_3o_{6+x}$, Phys. Rev. B **47** (1993), no. 13, 8233–8248. See page: 14

[CRKL90] B. Chakraborty, N. Read, C. Kane, and P. A. Lee, *Spiral phases and time-reversal-violating resonating-valence-bond states of doped antiferromagnets*, Phys. Rev. B **42** (1990), no. 7, 4819. See page: 17

[CVD$^+$14] M. K. Chan, M. J. Veit, C. J. Dorow, Y. Ge, Y. Li, W. Tabis, Y. Tang, X. Zhao, N. Barišić, and M. Greven, *In-plane magnetoresistance obeys Kohler's rule in the pseudogap phase of cuprate superconductors*, Phys. Rev. Lett. **113** (2014), no. 17, 177005. See page: 13

[CWV$^+$09] R. A. Cooper, Y. Wang, B. Vignolle, O. J. Lipscombe, S. M. Hayden, Y. Tanabe, T. Adachi, Y. Koike, M. Nohara, H. Takagi, C. Proust, and N. E. Hussey, *Anomalous criticality in the electrical resistivity of* $La_{2-x}Sr_xCuO_4$, Science **323** (2009), no. 5914, 603–607. See pages: 14, 15, and 147

[DFM88] E. Dagotto, E. Fradkin, and A. Moreo, *SU(2) gauge invariance and order parameters in strongly coupled electronic systems*, Phys. Rev. B **38** (1988), no. 4, 2926. See page: 17

[DHS03] A. Damascelli, Z. Hussain, and Z.-X. Shen, *Angle-resolved photoemission studies of the cuprate superconductors*, Rev. Mod. Phys. **75** (2003), no. 2, 473–541. See pages: 13, 14, and 48

[DL74] IE Dzyaloshinskii and AI Larkin, *Correlation functions for a one-dimensional Fermi system with long-range interaction (Tomonaga model)*, Sov. Phys. JETP **38** (1974), 202. See page: 98

[DNC+96] H. Ding, M. R. Norman, J. C. Campuzano, M. Randeria, A. F. Bellman, T. Yokoya, T. Takahashi, T. Mochiku, and K. Kadowaki, *Angle-resolved photoemission spectroscopy study of the superconducting gap anisotropy in* $Bi_2Sr_2CaCu_2o_{8+x}$, Phys. Rev. B **54** (1996), no. 14, R9678–R9681. See pages: 13 and 48

[DNM95] Elbio Dagotto, Alexander Nazarenko, and Adriana Moreo, *Antiferromagnetic and van Hove scenarios for the cuprates: taking the best of both worlds*, Phys. Rev. Lett. **74** (1995), no. 2, 310. See page: 18

[DPK13] K. B. Dave, P. W. Phillips, and C. L. Kane, *Absence of Luttinger's theorem due to zeros in the single-particle Green function*, Phys. Rev. Lett. **110** (2013), no. 9, 090403. See page: 6

[EFG+05] Fabian HL Essler, Holger Frahm, Frank Göhmann, Andreas Klümper, and Vladimir E Korepin, *The one-dimensional Hubbard model*, Cambridge University Press, 2005. See pages: 93, 94, and 99

[Egg07] S. Eggert, *One-dimensional quantum wires: A pedestrian approach to bosonization*, arXiv: 0708.0003 (2007). See page: 99

[EKW09] M. Eckstein, M. Kollar, and P. Werner, *Thermalization after an interaction quench in the Hubbard model*, Phys. Rev. Lett. **103** (2009), no. 5, 056403. See page: 120

[Eme87] V. J. Emery, *Theory of high-T_c superconductivity in oxides*, Phys. Rev. Lett. **58** (1987), no. 26, 2794. See page: 10

[Eme89] ______, *Electron doping tests theories*, Nature **337** (1989), no. 6205, 306. See page: 10

[Ess10] T. Esslinger, *Fermi-Hubbard physics with atoms in an optical lattice*, Annu. Rev. Condens. Matter Phys. **1** (2010), no. 1, 129–152. See page: 19

[ESY93] N. Elstner, R. R. P. Singh, and A. P. Young, *Finite temperature properties of the spin-1/2 Heisenberg antiferromagnet on the triangular lattice*, Phys. Rev. Lett. **71** (1993), no. 10, 1629. See page: 40

[ETS90] H. Eskes, L. H. Tjeng, and G. A. Sawatzky, *Cluster-model calculation of the electronic structure of CuO: A model material for the high-T_c superconductors*, Phys. Rev. B **41** (1990), no. 1, 288. See page: 9

[FCDL+09] M. Ferrero, P. S. Cornaglia, L. De Leo, O. Parcollet, G. Kotliar, and A. Georges, *Pseudogap opening and formation of Fermi arcs as an orbital-selective Mott transition in momentum space*, Phys. Rev. B **80** (2009), no. 6, 064501. See pages: 46, 73, 78, 83, and 89

[FCR+15] J. Fink, A. Charnukha, E. D. L. Rienks, Z. H. Liu, S. Thirupathaiah, I. Avigo, F. Roth, H. S. Jeevan, P. Gegenwart, M. Roslova, I. Morozov, S. Wurmehl, U. Bovensiepen, S. Borisenko, M. Vojta, and B. Büchner, *Non-fermi-liquid scattering rates and anomalous band dispersion in ferropnictides*, Phys. Rev. B **92** (2015), no. 20, 201106. See page: 7

[FHP18] J. Feldmeier, S. Huber, and M. Punk, *Exact solution of a two-species quantum dimer model for pseudogap metals*, Phys. Rev. Let. **120** (2018), no. 18, 187001. See pages: 64 and 149

[Fis61] M. E. Fisher, *Statistical mechanics of dimers on a plane lattice*, Phys. Rev. **124** (1961), no. 6, 1664. See pages: 40, 45, and 64

[FKS⁺08] R. Folman, P. Kruger, J. Schmiedmayer, J. Denschlag, and C. Henkel, *Microscopic atom optics: from wires to an atom chip*, arXiv: 0805.2613 (2008). See pages: 21, 100, and 122

[FM94] J. K. Freericks and H. Monien, *Phase diagram of the Bose-Hubbard model*, EPL **26** (1994), no. 7, 545. See pages: 118 and 151

[FMS02] P. Fendley, R. Moessner, and S. L. Sondhi, *Classical dimers on the triangular lattice*, Phys. Rev. B **66** (2002), no. 21, 214513. See page: 45

[FP11] T. Faulkner and J. Polchinski, *Semi-holographic Fermi liquids*, J. High Energ. Phys. **2011** (2011), no. 6, 12. See page: 3

[Fra13] E. Fradkin, *Field theories of condensed matter physics*, Cambridge University Press, 2013. See pages: 43 and 93

[FS63] M. E. Fisher and J. Stephenson, *Statistical mechanics of dimers on a plane lattice. ii. Dimer correlations and monomers*, Phys. Rev. **132** (1963), no. 4, 1411. See pages: 45 and 50

[FSE⁺13] T. Fukuhara, P. Schauß, M. Endres, S. Hild, M. Cheneau, I. Bloch, and C. Gross, *Microscopic observation of magnon bound states and their dynamics*, Nature **502** (2013), no. 7469, 76. See page: 19

[FTMUO87] A. Fujimori, E. Takayama-Muromachi, Y. Uchida, and B. Okai, *Spectroscopic evidence for strongly correlated electronic states in La-Sr-Cu and Y-Ba-Cu oxides*, Phys. Rev. B **35** (1987), no. 16, 8814. See page: 9

[FWM⁺06] S. Fölling, A. Widera, T. Müller, F. Gerbier, and I. Bloch, *Formation of spatial shell structure in the superfluid to Mott insulator transition*, Phys. Rev. Lett. **97** (2006), no. 6, 060403. See page: 19

[Gau83] Michel Gaudin, *La fonction d'onde de Bethe*, Masson, 1983. See page: 94

[GB17] C. Gross and I. Bloch, *Quantum simulations with ultracold atoms in optical lattices*, Science **357** (2017), no. 6355, 995–1001. See page: 19

[GCC17] G. Goldstein, C. Chamon, and C. Castelnovo, *d-wave superconductivity in boson+fermion dimer models*, Phys. Rev. B **95** (2017), no. 17, 174511. See page: 50

[Geo07] A. Georges, *Condensed matter physics with light and atoms: Strongly correlated cold fermions in optical lattices*, arXiv cond-mat/0702122 (2007). See page: 19

[GFP⁺10] E. Gull, M. Ferrero, O. Parcollet, A. Georges, and A. J. Millis, *Momentum-space anisotropy and pseudogaps: A comparative cluster dynamical mean-field analysis of the doping-driven metal-insulator transition in the two-dimensional Hubbard model*, Phys. Rev. B **82** (2010), no. 15, 155101. See pages: 73, 83, 84, and 89

[Gia03] T. Giamarchi, *Quantum physics in one dimension*, vol. 121, Clarendon Press, 2003. See pages: 3, 93, 94, 95, 96, 99, 100, 101, 118, and 119

[GK63] H. A. Gersch and G. C. Knollman, *Quantum cell model for bosons*, Phys. Rev. **129** (1963), no. 2, 959. See page: 118

[GK92] A. Georges and G. Kotliar, *Hubbard model in infinite dimensions*, Phys. Rev. B **45** (1992), no. 12, 6479. See page: 75

[GKKR96] A. Georges, G. Kotliar, W. Krauth, and M. J. Rozenberg, *Dynamical mean-field theory of strongly correlated fermion systems and the limit of infinite dimensions*, Rev. Mod. Phys. **68** (1996), no. 1, 13. See pages: 73, 74, 76, and 79

[GKL+12] M. Gring, M. Kuhnert, T. Langen, Ta. Kitagawa, B. Rauer, M. Schreitl, I. Mazets, D. A. Smith, E. Demler, and J. Schmiedmayer, *Relaxation and prethermalization in an isolated quantum system*, Science **337** (2012), no. 6100, 1318–1322. See pages: 119 and 122

[GLMS14] R. Geiger, T. Langen, I. E. Mazets, and J. Schmiedmayer, *Local relaxation and light-cone-like propagation of correlations in a trapped one-dimensional Bose gas*, New J. Phys. **16** (2014), no. 5, 053034. See pages: 119 and 122

[GMHB02] M. Greiner, O. Mandel, T. W. Hänsch, and I. Bloch, *Collapse and revival of the matter wave field of a Bose-Einstein condensate*, Nature **419** (2002), no. 6902, 51. See page: 19

[GNT04] A. O. Gogolin, A. A. Nersesyan, and A. M. Tsvelik, *Bosonization and strongly correlated systems*, Cambridge University pPress, 2004. See pages: 93 and 101

[GPM13] E. Gull, O. Parcollet, and A. J. Millis, *Superconductivity and the Pseudogap in the two-dimensional Hubbard model*, Phys. Rev. Lett. **110** (2013), no. 21, 216405. See pages: 73, 83, and 89

[GPM+16] D. Greif, M. F. Parsons, A. Mazurenko, C. S. Chiu, S. Blatt, F. Huber, G. Ji, and M. Greiner, *Site-resolved imaging of a fermionic Mott insulator*, Science **351** (2016), no. 6276, 953–957. See pages: 20 and 145

[GS88] Th. Giamarchi and H. J. Schulz, *Anderson localization and interactions in one-dimensional metals*, Phys. Rev. B **37** (1988), no. 1, 325. See page: 118

[Gut63] M. C. Gutzwiller, *Effect of correlation on the ferromagnetism of transition metals*, Phys. Rev. Lett. **10** (1963), no. 5, 159. See page: 16

[GVL94] R. J. Gooding, K. J. E. Vos, and P. W. Leung, *Theory of electron-hole asymmetry in doped CuO_2 planes*, Phys. Rev. B **50** (1994), no. 17, 12866. See pages: 11 and 18

[GZHC09] N. Gemelke, X. Zhang, C.-L. Hung, and C. Chin, *In situ observation of incompressible Mott-insulating domains in ultracold atomic gases*, Nature **460** (2009), no. 7258, 995. See page: 19

[HAJC+03] N. E. Hussey, M. Abdel-Jawad, A. Carrington, A. P. Mackenzie, and L. Balicas, *A coherent three-dimensional Fermi surface in a high-transition-temperature superconductor*, Nature **425** (2003), no. 6960, 814. See page: 14

[Hal81] F. D. M. Haldane, *'Luttinger liquid theory' of one-dimensional quantum fluids. i. Properties of the Luttinger model and their extension to the general 1D interacting spinless Fermi gas*, J. Phys. C: Solid State Physics **14** (1981), no. 19, 2585–2919. See pages: 95, 96, 101, 102, 118, and 145

[HBA+13] F. Hardy, A. E. Böhmer, D. Aoki, P. Burger, T. Wolf, P. Schweiss, R. Heid, P. Adelmann, Y. X. Yao, G. Kotliar, J. Schmalian, and C. Meingast, *Evidence of strong correlations and coherence-incoherence crossover in the iron pnictide superconductor KFe_2As_2*, Phys. Rev. Lett. **111** (2013), no. 2, 027002. See page: 7

[HBSD18] S. Huber, M. Buchhold, J. Schmiedmayer, and S. Diehl, *Thermalization dynamics of two correlated bosonic quantum wires after a split*, Phys. Rev. A **97** (2018), no. 4, 043611. See pages: 122 and 151

[Hen97] C. L. Henley, *Relaxation time for a dimer covering with height representation*, J. Stat. Phys. **89** (1997), no. 3-4, 483–507. See pages: 45, 46, and 64

[HFB04] M. Hermele, M. P. A. Fisher, and L. Balents, *Pyrochlore photons: The U(1) spin liquid in a s=1/2 three-dimensional frustrated magnet*, Phys. Rev. B **69** (2004), no. 6, 064404. See pages: 45 and 46

[HFP18] S. Huber, J. Feldmeier, and M. Punk, *Electron spectral functions in a quantum dimer model for topological metals*, Phys. Rev. B **97** (2018), no. 7, 075144. See pages: 43, 49, 148, and 149

[HFS+14] S. Hild, T. Fukuhara, P. Schauß, J. Zeiher, M. Knap, E. Demler, I. Bloch, and C. Gross, *Far-from-equilibrium spin transport in Heisenberg quantum magnets*, Phys. Rev. Lett. **113** (2014), no. 14, 147205. See page: 19

[HGP19] S. Huber, F. Grusdt, and M. Punk, *Signatures of correlated magnetic phases in the two-spin density matrix*, Phys. Rev. A **99** (2019), no. 2, 023617. See pages: 21 and 148

[HHM+10] E. Haller, R. Hart, M. J. Mark, J. G. Danzl, L. Reichsöllner, M. Gustavsson, M. Dalmonte, G. Pupillo, and H.-C. Nägerl, *Pinning quantum phase transition for a Luttinger liquid of strongly interacting bosons*, Nature **466** (2010), no. 7306, 597. See page: 122

[HHP53] D. G. Henshaw, D. G. Hurst, and N. K. Pope, *Structure of Liquid Nitrogen, Oxygen, and Argon by Neutron Diffraction*, Phys. Rev. **92** (1953), no. 5, 1229. See page: 7

[HK09] K. Haule and G. Kotliar, *Coherence-incoherence crossover in the normal state of iron oxypnictides and importance of hund's rule coupling*, New J. Phys. **11** (2009), no. 2, 025021. See page: 7

[HK19] S. Huber and M. Kollar, *From Luttinger liquids to Luttinger droplets via higher-order bosonization identities*, arXiv:1911.03158 (2019). See pages: 101 and 151

[HKMS03] D. A. Huse, W. Krauth, R. Moessner, and S. L. Sondhi, *Coulomb and liquid dimer models in three dimensions*, Phys. Rev. Lett. **91** (2003), no. 16, 167004. See pages: 45 and 46

[HLF+06] S. Hofferberth, I. Lesanovsky, B. Fischer, J. Verdu, and J. Schmiedmayer, *Radiofrequency-dressed-state potentials for neutral atoms*, Nature Physics **2** (2006), no. 10, 710. See pages: 21, 100, and 122

[HLS+08] S. Hofferberth, I. Lesanovsky, T. Schumm, A. Imambekov, V. Gritsev, E. Demler, and J. Schmiedmayer, *Probing quantum and thermal noise in an interacting many-body system*, Nature Physics **4** (2008), no. 6, 489. See page: 21

[HMA91] T. C. Hsu, J. B. Marston, and I. Affleck, *Two observable features of the staggered-flux phase at nonzero doping*, Phys. Rev. B **43** (1991), no. 4, 2866. See page: 17

[HMJK00] M. H. Hettler, M. Mukherjee, M. Jarrell, and H. R. Krishnamurthy, *Dynamical cluster approximation: Nonlocal dynamics of correlated electron systems*, Phys. Rev. B **61** (2000), no. 19, 12739. See pages: 73, 75, and 76

[HNUM10] M. Horikoshi, S. Nakajima, M. Ueda, and T. Mukaiyama, *Measurement of universal thermodynamic functions for a unitary Fermi gas*, Science **327** (2010), no. 5964, 442–445. See page: 19

[HR14] K. Hattori and A. Rosch, *Quantum impurity in a Tomonaga-Luttinger liquid: continuous-time quantum Monte Carlo approach*, Phys. Rev. B **90** (2014), no. 11, 115103. See page: 101

[HSG+17] T. A. Hilker, G. Salomon, F. Grusdt, A. Omran, M. Boll, E. Demler, I. Bloch, and C. Gross, *Revealing hidden antiferromagnetic correlations in doped Hubbard chains via string correlators*, Science **357** (2017), no. 6350, 484–487. See page: 20

[Hsu90] T. C. Hsu, *Spin waves in the flux-phase description of the S=1/2 Heisenberg antiferromagnet*, Phys. Rev. B **41** (1990), no. 16, 11379. See pages: 16 and 17

[HTL+93] C. C. Homes, T. Timusk, R. Liang, D. A. Bonn, and W. N. Hardy, *Optical conductivity of c axis oriented $YBa_2Cu_3O_{6.70}$: Evidence for a pseudogap*, Phys. Rev. Lett. **71** (1993), no. 10, 1645. See page: 13

[HTZJ+98] M. H. Hettler, A. N. Tahvildar-Zadeh, M. Jarrell, Th. Pruschke, and H. R. Krishnamurthy, *Nonlocal dynamical correlations of strongly interacting electron systems*, Phys. Rev. B **58** (1998), no. 12, R7475. See pages: 73 and 76

[Hub63] J. Hubbard, *Electron correlations in narrow energy bands*, Proc. R. Soc. Lond.. Series A. Mathematical and Physical Sciences **276** (1963), no. 1365, 238–257. See page: 73

[HVH+14a] M. Hashimoto, I. M. Vishik, R.-H. He, T. P. Devereaux, and Z.-X. Shen, *Energy gaps in high-transition-temperature cuprate superconductors*, Nature Physics **10** (2014), no. 7, 483–495. See pages: 13 and 48

[HVH+14b] ———, *Energy gaps in high-transition-temperature cuprate superconductors*, Nature Physics **10** (2014), no. 7, 483–495. See page: 48

[HZ09a] T.-L. Ho and Q. Zhou, *Squeezing out the entropy of fermions in optical lattices*, Proc. Natl. Acad. Sci. U.S.A. **106** (2009), no. 17, 6916–6920. See page: 20

[HZ09b] ———, *Universal cooling scheme for quantum simulation*, arXiv: 0911.5506 (2009). See page: 20

[IKS+03] H. Ishii, H. Kataura, H. Shiozawa, H. Yoshioka, H. Otsubo, Y. Takayama, T. Miyahara, S. Suzuki, Y. Achiba, M. Nakatake, T. Narimura, M. Higashiguchi, K. Shimada, H. Namatame, and M. Taniguchi, *Direct observation of Tomonaga-Luttinger-liquid state in carbon nanotubes at low temperatures*, Nature **426** (2003), no. 6966, 540. See page: 99

[IYS12] T. Ishiguro, K. Yamaji, and G. Saito, *Organic superconductors*, vol. 88, Springer Science & Business Media, 2012. See page: 6

[Jay57] E. T. Jaynes, *Information theory and statistical mechanics. ii*, Phys. Rev. **108** (1957), no. 2, 171. See page: 120

[JMHM01] M. Jarrell, Th. Maier, C. Huscroft, and S. Moukouri, *Quantum Monte Carlo algorithm for nonlocal corrections to the dynamical mean-field approximation*, Phys. Rev. B **64** (2001), no. 19, 195130. See pages: 73, 75, and 76

[JMRB80] D. Jérome, A. Mazaud, M. Ribault, and K. Bechgaard, *Superconductivity in a synthetic organic conductor (TMTSF)$_2$PF$_6$*, J. Phys. Lett. **41** (1980), no. 4, 95–98. See page: 6

[JS91] R. A. Jalabert and S. Sachdev, *Spontaneous alignment of frustrated bonds in an anisotropic, three-dimensional Ising model*, Phys. Rev. B **44** (1991), no. 2, 686. See pages: 44 and 45

[JW28] P. Jordan and E. Wigner, *Über das Paulische Äquivalenzverbot*, Zeitschrift für Physik **47** (1928), 631–651. See page: 94

[JXY15] P. D. Johnson, G. Xu, and W.-G. Yin, *Iron-based superconductivity*, vol. 211, Springer, 2015. See page: 7

[JYB12] H.-C. Jiang, H. Yao, and L. Balents, *Spin liquid ground state of the spin-1/2 square J_1-J_2 Heisenberg model*, Phys. Rev. B **86** (2012), no. 2, 024424. See page: 40

[Kam11] Alex Kamenev, *Field theory of non-equilibrium systems*, Cambridge University Press, 2011. See page: 120

[Kas61] P. W. Kasteleyn, *The statistics of dimers on a lattice: I. The number of dimer arrangements on a quadratic lattice*, Phys. **27** (1961), no. 12, 1209–1225. See pages: 40, 45, and 64

[KBSE98] M. A. Kastner, R. J. Birgeneau, G. Shirane, and Y. Endoh, *Magnetic, transport, and optical properties of monolayer copper oxides*, Rev. Mod. Phys. **70** (1998), no. 3, 897. See page: 12

[KF92] C. L. Kane and Matthew P. A. Fisher, *Transmission through barriers and resonant tunneling in an interacting one-dimensional electron gas*, Phys. Rev. B **46** (1992), no. 23, 15233. See page: 101

[KHH+06] Y. Kamihara, H. Hiramatsu, M. Hirano, R. Kawamura, H. Yanagi, T. Kamiya, and H. Hosono, *Iron-based layered superconductor: LaOFeP*, J. Am. Chem. Soc. **128** (2006), no. 31, 10012–10013. See page: 7

[KISD11] T. Kitagawa, A. Imambekov, J. Schmiedmayer, and E. Demler, *The dynamics and prethermalization of one-dimensional quantum systems probed through the full distributions of quantum noise*, New J. Phys. **13** (2011), no. 7, 073018. See pages: 119 and 122

[Kit06] A. Kitaev, *Anyons in an exactly solved model and beyond*, Ann. Phys. **321** (2006), no. 1, 2–111. See page: 64

[KKS$^+$06] B. Kyung, S. S. Kancharla, D. Sénéchal, A.-M. S. Tremblay, M. Civelli, and G. Kotliar, *Pseudogap induced by short-range spin correlations in a doped mott insulator*, Phys. Rev. B **73** (2006), no. 16, 165114. See page: 78

[KL88] G. Kotliar and J. Liu, *Superexchange mechanism and d-wave superconductivity*, Phys. Rev. B **38** (1988), no. 7, 5142. See page: 17

[KLFO02] S. A. Kivelson, D.-H. Lee, E. Fradkin, and V. Oganesyan, *Competing order in the mixed state of high-temperature superconductors*, Phys. Rev. B **66** (2002), no. 14, 144516. See page: 12

[KM98] T. D. Kühner and H. Monien, *Phases of the one-dimensional Bose-Hubbard model*, Phys. Rev. B **58** (1998), no. 22, R14741. See page: 118

[KMWW80] H. R. Krishna-Murthy, J. W. Wilkins, and K. G. Wilson, *Renormalization-group approach to the anderson model of dilute magnetic alloys. I. Static properties for the symmetric case*, Phys. Rev. B **21** (1980), no. 3, 1003. See page: 82

[Koc11] E. Koch, *8 The Lanczos Method*, The LDA+DMFT approach to strongly correlated materials (2011). See page: 48

[Kog79] J. B. Kogut, *An introduction to lattice gauge theory and spin systems*, Rev. Mod. Phys. **51** (1979), no. 4, 659. See page: 40

[KR86] G. Kotliar and A. E. Ruckenstein, *New functional integral approach to strongly correlated fermi systems: The gutzwiller approximation as a saddle point*, Phys. Rev. Lett. **57** (1986), no. 11, 1362. See page: 17

[KRS87] S. A. Kivelson, D. S. Rokhsar, and J. P. Sethna, *Topology of the resonating valence-bond state: Solitons and high-T_c superconductivity*, Phys. Rev. B **35** (1987), no. 16, 8865. See pages: 39 and 40

[KSPB01] G. Kotliar, S. Y. Savrasov, G. Pálsson, and G. Biroli, *Cellular dynamical mean field approach to strongly correlated systems*, Phys. Rev. Lett. **87** (2001), no. 18, 186401. See pages: 73, 74, and 75

[KSvDZ05] C. Kollath, U. Schollwöck, J. von Delft, and W. Zwerger, *One-dimensional density waves of ultracold bosons in an optical lattice*, Phys. Rev. A **71** (2005), no. 5, 053606. See page: 119

[KWHH08] Y. Kamihara, T. Watanabe, M. Hirano, and H. Hosono, *Iron-based layered superconductor $La[O_{1-x}F_x]$ FeAs (x= 0.05-0.12) with T_c=26 K*, J. Am. Chem. Soc. **130** (2008), no. 11, 3296–3297. See page: 7

[Lan50] C. Lanczos, *An iteration method for the solution of the eigenvalue problem of linear differential and integral operators*, J. Res. Nat. Bur. Stand. **49** (1950), no. 255. See page: 48

[Lau81] Robert B Laughlin, *Quantized hall conductivity in two dimensions*, Phy. Rev. B **23** (1981), no. 10, 5632. See page: 5

[LCR96] P. W. Leung, K. C. Chiu, and K. J. Runge, *Columnar dimer and plaquette resonating-valence-bond orders in the quantum dimer model*, Phys. Rev. B **54** (1996), no. 18, 12938. See page: 45

[LDA88] S. Liang, B. Doucot, and P. W. Anderson, *Some new variational resonating-valence-bond-type wave functions for the spin-*$1/2$ *antiferromagnetic heisenberg model on a square lattice*, Phys. Rev. Lett. **61** (1988), no. 3, 365. See pages: 39 and 40

[LE74] A. Luther and V. J. Emery, *Backward scattering in the one-dimensional electron gas*, Phys. Rev. Lett. **33** (1974), no. 10, 589. See page: 98

[LE93] P. W. Leung and V. Elser, *Numerical studies of a 36-site kagome antiferromagnet*, Phys. Rev. B **47** (1993), no. 9, 5459. See page: 40

[LEG$^+$15] T. Langen, S. Erne, R. Geiger, B. Rauer, T. Schweigler, M. Kuhnert, W. Rohringer, I. E. Mazets, T. Gasenzer, and J. Schmiedmayer, *Experimental observation of a generalized Gibbs ensemble*, Science **348** (2015), no. 6231, 207–211. See pages: 122 and 123

[LFA$^+$01] D. H. Lu, D. L. Feng, N. P. Armitage, K. M. Shen, A. Damascelli, C. Kim, F. Ronning, Z.-X. Shen, D. A. Bonn, R. Liang, W. N. hardy, A. I. Rykov, and S. Tajima, *Superconducting gap and strong in-plane anisotropy in untwinned* $YBa_2Cu_3o_{7-\delta}$, Phys. Rev. Lett. **86** (2001), no. 19, 4370. See page: 12

[LFSW88] K. B. Lyons, P. A. Fleury, L. F. Schneemeyer, and J. V. Waszczak, *Spin fluctuations and superconductivity in* $Ba_2YCu_3O_{6+\delta}$, Phys. Rev. Lett. **60** (1988), no. 8, 732. See pages: 10 and 12

[LI10] A. Liebsch and H. Ishida, *Correlation-induced spin freezing transition in FeSe: A dynamical mean field study*, Phys. Rev. B **82** (2010), no. 15, 155106. See page: 7

[LK00] A. I. Lichtenstein and M. I. Katsnelson, *Antiferromagnetism and d-wave superconductivity in cuprates: A cluster dynamical mean-field theory*, Phy. Rev. B **62** (2000), no. 14, R9283. See page: 73

[LKJBH10] J. Liang, R. N. Kohn Jr, M. F. Becker, and D. J. Heinzen, *High-precision laser beam shaping using a binary-amplitude spatial light modulator*, Applied optics **49** (2010), no. 8, 1323–1330. See page: 20

[LLC$^+$01] JW Loram, J Luo, JR Cooper, WY Liang, and JL Tallon, *Evidence on the pseudogap and condensate from the electronic specific heat*, J. Phys. Chem. Solids **62** (2001), no. 1-2, 59–64. See page: 13

[LLM$^+$88] W. H. Li, J. W. Lynn, H. A. Mook, B. C. Sales, and Z. Fisk, *Long-range antiferromagnetic order of the Cu in oxygen-deficient* $RBa_2Cu_3o_{6+x}$, Phys. Rev. B **37** (1988), no. 16, 9844. See page: 12

[LMCL93] J. W. Loram, K. A. Mirza, J. R. Cooper, and W. Y. Liang, *Electronic specific heat of* $YBa_2Cu_3O_{6+x}$ *from 1.8 to 300 K*, Phys. Rev. Lett. **71** (1993), no. 11, 1740. See page: 13

[LMM11] C. Lacroix, P. Mendels, and F. Mila, *Introduction to frustrated magnetism: materials, experiments, theory*, vol. 164, Springer Science & Business Media, 2011. See pages: 41, 42, and 45

[LNW06] P. A. Lee, N. Nagaosa, and X.-G. Wen, *Doping a Mott insulator: Physics of high-temperature superconductivity*, Rev. Mod. Phys. **78** (2006), no. 1, 17. See pages: 11, 12, 13, 14, 15, 17, 21, 39, and 42

[LP74] A. Luther and I. Peschel, *Single-particle states, Kohn anomaly, and pairing fluctuations in one dimension*, Phys. Rev. B **9** (1974), no. 7, 2911. See page: 98

[LSGB95] M. Langer, J. Schmalian, S. Grabowski, and K. H. Bennemann, *Theory for the excitation spectrum of high-T_c superconductors: quasiparticle dispersion and shadows of the Fermi surface*, Phys. Rev. Lett. **75** (1995), no. 24, 4508. See page: 6

[LSH$^+$06] I. Lesanovsky, T. Schumm, S. Hofferberth, L. M. Andersson, P. Krüger, and J. Schmiedmayer, *Adiabatic radio-frequency potentials for the coherent manipulation of matter waves*, Phys. Rev. A **73** (2006), no. 3, 033619. See pages: 21, 100, and 122

[LSM61] E. Lieb, T. Schultz, and D. Mattis, *Two soluble models of an antiferromagnetic chain*, Ann. Phys. **16** (1961), no. 3, 407–466. See page: 94

[Lut60] J. M. Luttinger, *Fermi surface and some simple equilibrium properties of a system of interacting fermions*, Phys. Rev. **119** (1960), no. 4, 1153. See page: 5

[Lut63] ———, *An exactly soluble model of a many-fermion system*, J. Math. Phys. **4** (1963), no. 9, 1154–1162. See pages: 64 and 95

[LVDW18] S.-S. B. Lee, J. Von Delft, and A. Weichselbaum, *Filling-driven Mott transition in SU(N) Hubbard models*, Phys. Rev. B **97** (2018), no. 16, 165143. See page: 82

[LVT$^+$07] W. S. Lee, I. M. Vishik, K. Tanaka, D. H. Lu, T. Sasagawa, N. Nagaosa, T. P. Devereaux, Z. Hussain, and Z.-X. Shen, *Abrupt onset of a second energy gap at the superconducting transition of underdoped Bi2212*, Nature **450** (2007), no. 7166, 81–84. See pages: 13, 48, and 49

[LW16] S.-S. B. Lee and A. Weichselbaum, *Adaptive broadening to improve spectral resolution in the numerical renormalization group*, Phys. Rev. B **94** (2016), no. 23, 235127. See page: 83

[Mah13] G. D. Mahan, *Many-particle physics*, Springer Science & Business Media, 2013. See pages: 1 and 50

[MCJ$^+$17] A. Mazurenko, C. S. Chiu, G. Ji, M. F. Parsons, M. Kanász-Nagy, R. Schmidt, F. Grusdt, E. Demler, D. Greif, and M. Greiner, *A cold-atom Fermi-Hubbard antiferromagnet*, Nature **545** (2017), no. 7655, 462. See pages: 17, 18, 20, 21, 145, and 148

[Med99] V. Meden, *Nonuniversality of the one-particle Green's function of a Luttinger liquid*, Phys. Rev. B **60** (1999), no. 7, 4571. See page: 98

[Mer68] N. D. Mermin, *Crystalline order in two dimensions*, Phys. Rev. **176** (1968), no. 1, 250. See page: 9

[MF94] C. Mudry and E. Fradkin, *Separation of spin and charge quantum numbers in strongly correlated systems*, Phys. Rev. B **49** (1994), no. 8, 5200. See page: 40

[MGWF+14] A. K. Mitchell, M. R. Galpin, S. Wilson-Fletcher, D. E. Logan, and R. Bulla, *Generalized Wilson chain for solving multichannel quantum impurity problems*, Phys. Rev. B **89** (2014), no. 12, 121105. See page: 83

[MH89] E. Müller-Hartmann, *Correlated fermions on a lattice in high dimensions*, Zeitschrift für Physik B Condensed Matter **74** (1989), no. 4, 507–512. See page: 79

[MHL86] M. Ma, B. I. Halperin, and P. A. Lee, *Strongly disordered superfluids: Quantum fluctuations and critical behavior*, Phys. Rev. B **34** (1986), no. 5, 3136. See page: 118

[MJP05] T. Maier, M. Jarrell, and T. Pruschke, *Quantum cluster theories*, Rev. Mod. Phys. **77** (2005), no. 3, 1027. See pages: 73, 74, 75, 76, 78, and 83

[MK09] M. Moeckel and S. Kehrein, *Real-time evolution for weak interaction quenches in quantum systems*, Ann. Phys. **324** (2009), no. 10, 2146–2178. See page: 120

[MKS92] T. Manako, Y. Kubo, and Y. Shimakawa, *Transport and structural study of* $Tl_2Ba_2CuO_{6+\delta}$ *single crystals prepared by the KCl flux method*, Phys. Rev. B **46** (1992), no. 17, 11019. See page: 14

[ML65] D. C. Mattis and E. H. Lieb, *Exact solution of a many-fermion system and its associated boson field*, J. Math. Phys. **2** (1965), no. 6, 304–312. See pages: 64, 95, and 96

[MMS+00] V. Meden, W. Metzner, U. Schollwöck, O. Schneider, T. Stauber, and K. Schönhammer, *Luttinger liquids with boundaries: Power-laws and energy scales*, Eur. Phys. J. B **16** (2000), no. 4, 631–646. See page: 101

[MMSS02] V. Meden, W. Metzner, U. Schollwöck, and K. Schönhammer, *A single impurity in a Luttinger liquid: How it "cuts" the chain*, Journal of low temperature physics **126** (2002), no. 3-4, 1147–1163. See page: 101

[MPJ02] Th. A. Maier, Th. Pruschke, and M. Jarrell, *Angle-resolved photoemission spectra of the Hubbard model*, Phys. Rev. B **66** (2002), no. 7, 075102. See pages: 73, 78, and 83

[MS92] V Meden and K Schönhammer, *Spectral functions for the Tomonaga-Luttinger model*, Phys. Rev. B **46** (1992), no. 24, 15753. See page: 98

[MS01a] R. Moessner and S. L. Sondhi, *Ising models of quantum frustration*, Phys. Rev. B **63** (2001), no. 22, 224401. See page: 42

[MS01b] ———, *Resonating valence bond phase in the triangular lattice quantum dimer model*, Phys. Rev. Lett. **86** (2001), no. 9, 1881. See pages: 42, 44, and 45

[MS03] ______, *Three-dimensional resonating-valence-bond liquids and their excitations*, Phys. Rev. B **68** (2003), no. 18, 184512. See pages: 45 and 46

[MTS04] R. Moessner, O. Tchernyshyov, and S. L. Sondhi, *Planar pyrochlore, quantum ice and sliding ice*, J. Stat. Phys. **116** (2004), no. 1-4, 755–772. See page: 46

[MV87] W. Metzner and D. Vollhardt, *Ground-state properties of correlated fermions: Exact analytic results for the Gutzwiller wave function*, Phys. Rev. Lett. **59** (1987), no. 1, 121. See page: 16

[MV89] ______, *Correlated lattice fermions in $d = \infty$ dimensions*, Phys. Rev. Lett. **62** (1989), no. 3, 324. See pages: 75 and 79

[MW66] N. D. Mermin and H. Wagner, *Absence of ferromagnetism or antiferromagnetism in one-or two-dimensional isotropic Heisenberg models*, Phys. Rev. Lett. **17** (1966), no. 22, 1133. See page: 9

[NBB$^+$98] Ch. Niedermayer, C. Bernhard, T. Blasius, A. Golnik, A. Moodenbaugh, and J. I. Budnick, *Common Phase Diagram for Antiferromagnetism in $La_{2x}Sr_xCuO_4$ and $Y_{1x}Ca_xBa_2Cu_3O_6$ as Seen by Muon Spin Rotation*, Phys. Rev. Lett. **80** (1998), no. 17, 3843–3846. See page: 12

[NBM$^+$03] S. Nakamae, K. Behnia, N. Mangkorntong, M. Nohara, H. Takagi, S. J. C. Yates, and N. E. Hussey, *Electronic ground state of heavily overdoped nonsuperconducting $La_{2-x}Sr_xCuO_4$*, Phys. Rev. B **68** (2003), no. 10, 100502. See page: 14

[NCA$^+$12] S. Nascimbène, Y.-A. Chen, M. Atala, M. Aidelsburger, S. Trotzky, B. Paredes, and I. Bloch, *Experimental realization of plaquette resonating valence-bond states with ultracold atoms in optical superlattices*, Phys. Rev. Lett. **108** (2012), no. 20, 205301. See page: 145

[NVH$^+$95] A Nazarenko, KJE Vos, S Haas, E Dagotto, and RJ Gooding, *Photoemission spectra of $Sr_2CuO_2Cl_2$: A theoretical analysis*, Phys. Rev. B. **51** (1995), no. 13, 8676. See page: 18

[OF08] M. Ogata and H. Fukuyama, *The t-J model for the oxide high-T_c superconductors*, Rep. Prog. Phys. **71** (2008), no. 3, 036501. See page: 10

[OLFY91] L. N. Oliveira, V. L. Libero, H. O. Frota, and M. Yoshida, *Renormalization-group calculation of dynamical properties for impurity models*, Physica B: Condensed Matter **171** (1991), no. 1-4, 61–68. See page: 82

[Ons44] L. Onsager, *Crystal statistics. i. A two-dimensional model with an order-disorder transition*, Phys. Rev. **65** (1944), no. 3-4, 117. See page: 95

[OO94] W. C. Oliveira and L. N. Oliveira, *Generalized numerical renormalization-group method to calculate the thermodynamical properties of impurities in metals*, Phys. Rev. B **49** (1994), no. 17, 11986. See page: 82

[Osh00a] M. Oshikawa, *Commensurability, excitation gap, and topology in quantum many-particle systems on a periodic lattice*, Phys. Rev. Lett. **84** (2000), no. 7, 1535. See page: 5

[Osh00b] ———, *Topological approach to Luttinger's theorem and the Fermi surface of a Kondo lattice*, Phys. Rev. Lett. **84** (2000), no. 15, 3370. See page: 5

[OTM$^+$90] Joseph Orenstein, G. A. Thomas, A. J. Millis, S. L. Cooper, D. H. Rapkine, T. Timusk, L. F. Schneemeyer, and J. V. Waszczak, *Frequency- and temperature-dependent conductivity in* $YBa_2Cu_3O_{6+x}$ *crystals*, Phys. Rev. B **42** (1990), no. 10, 6342–6362. See page: 14

[PAS15] M. Punk, A. Allais, and S. Sachdev, *Quantum dimer model for the pseudogap metal*, Proc. Natl. Acad. Sci. U.S.A. **112** (2015), no. 31, 9552–9557. See pages: 39, 45, 46, 47, 48, and 145

[PBH$^+$02] C. Proust, E. Boaknin, R. W. Hill, L. Taillefer, and A. P. Mackenzie, *Heat transport in a strongly overdoped cuprate: Fermi liquid and a pure d-wave BCS superconductor*, Phys. Rev. Lett. **89** (2002), no. 14, 147003. See page: 14

[PDSD$^+$01] E. Pavarini, I. Dasgupta, T. Saha-Dasgupta, O. Jepsen, and O. K. Andersen, *Band-structure trend in hole-doped cuprates and correlation with* T_{cmax}, Phys. Rev. Lett. **87** (2001), no. 4, 047003. See page: 11

[Pfe70] P. Pfeuty, *The one-dimensional Ising model with a transverse field*, Ann. Phys. **57** (1970), no. 1, 79–90. See page: 95

[PGM14] I. V. Protopopov, D. B. Gutman, and A. D. Mirlin, *Relaxation in Luttinger liquids: Bose-Fermi duality*, Phys. Rev. B **90** (2014), no. 12, 125113. See page: 145

[PGOM14] I. V. Protopopov, D. B. Gutman, M. Oldenburg, and A. D. Mirlin, *Dissipationless kinetics of one-dimensional interacting fermions*, Phys. Rev. B **89** (2014), no. 16, 161104. See page: 145

[Pla10] N. Plakida, *High-Temperature Cuprate Superconductors: Experiment, Theory, and Applications*, vol. 166, Springer Science & Business Media, 2010. See pages: 8, 9, 12, 14, and 15

[PLD$^+$05] W. J. Padilla, Y. S. Lee, M. Dumm, G. Blumberg, S. Ono, Kouji Segawa, Seiki Komiya, Yoichi Ando, and D. N. Basov, *Constant effective mass across the phase diagram of high-*T_c *cuprates*, Phys. Rev. B **72** (2005), no. 6, 060511. See page: 14

[PLS98] W. O. Putikka, M. U. Luchini, and R. R. P. Singh, *Violation of Luttinger's Theorem in the Two-Dimensional t-J Model*, Phys. Rev. Lett. **81** (1998), no. 14, 2966. See page: 6

[PMC$^+$16] M. F. Parsons, A. Mazurenko, C. S. Chiu, G. Ji, D. Greif, and M. Greiner, *Site-resolved measurement of the spin-correlation function in the Fermi-Hubbard model*, Science **353** (2016), no. 6305, 1253–1256. See page: 20

[PMT$^+$15] P. M. Preiss, R. Ma, M. E. Tai, A. Lukin, M. Rispoli, P. Zupancic, Y. Lahini, R. Islam, and M. Greiner, *Strongly correlated quantum walks in optical lattices*, Science **347** (2015), no. 6227, 1229–1233. See page: 19

[Pot04] M. Potthoff, *Non-perturbative construction of the Luttinger-Ward functional*, arXiv cond-mat/0406671 (2004). See page: 75

[PS12] M. Punk and S. Sachdev, *Fermi surface reconstruction in hole-doped t-J models without long-range antiferromagnetic order*, Phys. Rev. B **85** (2012), no. 19, 195123. See pages: 19 and 48

[PT19] C. Proust and L. Taillefer, *The remarkable underlying ground states of cuprate superconductors*, Annu. Rev. Cond. Mat. Phys. **10** (2019), 409–429. See pages: 12, 13, and 14

[RCD$^+$08] Z.-A. Ren, G.-C. Che, X.-L. Dong, J. Yang, W. Lu, W. Yi, X.-L. Shen, Z.-C. Li, L.-L. Sun, F. Zhou, and Z.-X. Zhao, *Superconductivity and phase diagram in iron-based arsenic-oxides $ReFeAsO_{1-\delta}$ (Re= rare-earth metal) without fluorine doping*, EPL **83** (2008), no. 1, 17002. See page: 7

[RDO08] M. Rigol, V. Dunjko, and M. Olshanii, *Thermalization and its mechanism for generic isolated quantum systems*, Nature **452** (2008), no. 7189, 854. See page: 120

[RDYO07] M. Rigol, V. Dunjko, V. Yurovsky, and M. Olshanii, *Relaxation in a completely integrable many-body quantum system: an ab initio study of the dynamics of the highly excited states of 1D lattice hard-core bosons*, Phys. Rev. Lett. **98** (2007), no. 5, 050405. See pages: 119 and 120

[RFB$^+$05] A. Ralko, M. Ferrero, F. Becca, D. Ivanov, and F. Mila, *Zero-temperature properties of the quantum dimer model on the triangular lattice*, Phys. Rev. B **71** (2005), no. 22, 224109. See pages: 45 and 46

[RK88] D. S. Rokhsar and S. A. Kivelson, *Superconductivity and the quantum hard-core dimer gas*, Phys. Rev. Lett. **61** (1988), no. 20, 2376. See pages: 39, 40, 41, 44, 45, 50, and 64

[RM04] M. Rigol and A. Muramatsu, *Confinement control by optical lattices*, Phys. Rev. A **70** (2004), no. 4, 043627. See page: 19

[RMS05] K. S. Raman, R. Moessner, and S. L. Sondhi, *SU(2)-invariant spin-1/2 Hamiltonians with resonating and other valence bond phases*, Phys. Rev. B **72** (2005), no. 6, 064413. See pages: 41 and 42

[Ros07] A. Rosch, *Breakdown of Luttinger's theorem in two-orbital Mott insulators*, Europ. Phys. J. B **59** (2007), no. 4, 495–502. See page: 6

[RRG$^+$98] Ch. Renner, B. Revaz, J.-Y. Genoud, K. Kadowaki, and Ø. Fischer, *Pseudogap precursor of the superconducting gap in under-and overdoped $Bi_2Sr_2CaCu_2O_{8+\delta}$*, Phys. Rev. Lett. **80** (1998), no. 1, 149. See page: 13

[RS89] N. Read and S. Sachdev, *Some features of the phase diagram of the square lattice SU(N) antiferromagnet*, Nuc. Phys. B **316** (1989), no. 3, 609–640. See page: 42

[RS90] ———, *Spin-peierls, valence-bond solid, and Néel ground states of low-dimensional quantum antiferromagnets*, Phys. Rev. B **42** (1990), no. 7, 4568. See page: 17

[RS91] ———, *Large-N expansion for frustrated quantum antiferromagnets*, Phys. Rev. Lett. **66** (1991), no. 13, 1773. See page: 17

[RS12] M. Rigol and M. Srednicki, *Alternatives to eigenstate thermalization*, Phys. Rev. Lett. **108** (2012), no. 11, 110601. See page: 120

[RW06] T. C. Ribeiro and X.-G. Wen, *Doped carrier formulation and mean-field theory of the tttJ model*, Phys. Rev. B **74** (2006), no. 15, 155113. See page: 18

[RYL$^+$08] Z.-A. Ren, J. Yang, W. Lu, W. Yi, G.-C. Che, X.-L. Dong, L.-L. Sun, and Z.-X. Zhao, *Superconductivity at 52 K in iron based F doped layered quaternary compound Pr [$O_{1-x}F_x$] FeAs*, Mater. Res. Innov. **12** (2008), no. 3, 105–106. See page: 7

[Ryl19] C. Rylands, *Exact Boundary Modes in an Interacting Quantum Wire*, arXiv: 1910.11221 (2019). See page: 101

[Sac07] S. Sachdev, *Quantum phase transitions*, Handbook of Magnetism and Advanced Magnetic Materials (2007). See pages: 6 and 95

[Sac10] ———, *Quantum criticality and the phase diagram of the cuprates*, Phys. C: Superconductivity and its applications **470** (2010), S4–S6. See page: 6

[Sam80] S. Samuel, *The use of anticommuting variable integrals in statistical mechanics. i. The computation of partition functions*, J. Math. Phys. **21** (1980), no. 12, 2806–2814. See page: 50

[SBD16] L. M. Sieberer, M. Buchhold, and S. Diehl, *Keldysh field theory for driven open quantum systems*, Rep. Prog. Phys. **79** (2016), no. 9, 096001. See page: 120

[SC16] S. Sachdev and D. Chowdhury, *The novel metallic states of the cuprates: Topological Fermi liquids and strange metals*, Prog. Theor. Exp. Phys. **2016** (2016), no. 12, 12C102. See pages: 5 and 43

[Sca95] D. J. Scalapino, *The case for $d_{x_2-y_2}$ pairing in the cuprate superconductors*, Phys. Rep. **250** (1995), no. 6, 329–365. See page: 48

[Sch90] H. J. Schulz, *Correlation exponents and the metal-insulator transition in the one-dimensional Hubbard model*, Phys. Rev. Lett. **64** (1990), no. 23, 2831. See page: 99

[Sch93] ———, *Wigner crystal in one dimension*, Phys. Rev. Lett. **71** (1993), no. 12, 1864. See page: 99

[Sch04] K. Schönhammer, *Luttinger liquids: the basic concepts*, Strong interactions in low dimensions, Springer, 2004, pp. 93–136. See page: 95

[Sch05] ———, *Interacting electrons in low dimensions*. See page: 96

[Sch09] B. Schmidt, *Exact numerical simulations of strongly interacting atoms in 1D trap potentials and optical lattices*, Ph.D. thesis, Technische Universität Kaiserslautern, 2009. See pages: 118 and 151

[SCHK06] T. D. Stanescu, M. Civelli, K. Haule, and G. Kotliar, *A cellular dynamical mean field theory approach to Mottness*, Ann. Phys. (New York City) **321** (2006), no. 7, 1682–1715. See page: 78

[SCW$^+$18] M. S. Scheurer, S. Chatterjee, W. Wu, M. Ferrero, A. Georges, and S. Sachdev, *Topological order in the pseudogap metal*, Proc. Natl. Acad. Sci. U.S.A **115** (2018), no. 16, E3665–E3672. See pages: 73 and 83

[SDG$^+$98] A. Schwartz, M. Dressel, G. Grüner, V. Vescoli, L. Degiorgi, and T. Giamarchi, *On-chain electrodynamics of metallic* $(TMTSF)_2X$ *salts: Observation of Tomonaga-Luttinger liquid response*, Phys. Rev. B **58** (1998), no. 3, 1261. See pages: 99 and 151

[SDW$^+$93] Z.-X. Shen, D. S. Dessau, B. O. Wells, D. M. King, W. E. Spicer, A. J. Arko, D. Marshall, L. W. Lombardo, A. Kapitulnik, P. Dickinson, S. Doniach, J. DiCarlo, T. Loeser, and C. H. Park, *Anomalously large gap anisotropy in the a-b plane of* $Bi_2Sr_2CaCu_2O_{8+\delta}$, Phys. Rev. Lett. **70** (1993), no. 10, 1553–1556. See pages: 12, 13, and 48

[SE10] I. Schneider and S. Eggert, *Recursive method for the density of states in one dimension*, Phys. Rev. Let. **104** (2010), no. 3, 036402. See page: 101

[SEB$^+$87] G. Shirane, Y. Endoh, R. J. Birgeneau, M. A. Kastner, Y. Hidaka, M. Oda, M. Suzuki, and T. Murakami, *Two-dimensional antiferromagnetic quantum spin-fluid state in* La_2CuO_4, Phys. Rev. Lett. **59** (1987), no. 14, 1613. See page: 9

[Sen08] T. Senthil, *Critical Fermi surfaces and non-Fermi liquid metals*, Phys. Rev. B **78** (2008), no. 3, 035103. See page: 3

[SH92] R. R. P. Singh and D. A. Huse, *Three-sublattice order in triangular-and kagomé-lattice spin-half antiferromagnets*, Phys. Rev. Lett. **68** (1992), no. 11, 1766. See page: 40

[Sha94] R. Shankar, *Renormalization-group approach to interacting fermions*, Rev. Mod. Phys. **66** (1994), no. 1, 129. See page: 99

[SHA$^+$05] T. Schumm, S. Hofferberth, L. M. Andersson, S. Wildermuth, S. Groth, I. Bar-Joseph, J. Schmiedmayer, and P. Krüger, *Matter-wave interferometry in a double well on an atom chip*, Nature Physics **1** (2005), no. 1, 57. See pages: 21, 100, and 122

[Shv03] A. M. Shvaika, *Dynamical mean-field theory of correlated hopping: A rigorous local approach*, Phys. Rev. B **67** (2003), no. 7, 075101. See page: 78

[SI95] A. Schiller and K. Ingersent, *Systematic 1/d corrections to the infinite-dimensional limit of correlated lattice electron models*, Phys. Rev. Let. **75** (1995), no. 1, 113. See page: 75

[SK04] T. D. Stanescu and G. Kotliar, *Strong coupling theory for interacting lattice models*, Phys. Rev. B **70** (2004), no. 20, 205112. See page: 78

[SK06] ———, *Fermi arcs and hidden zeros of the green function in the pseudogap state*, Phys. Rev. B **74** (2006), no. 12, 125110. See page: 78

[SM93] K. Schönhammer and V. Meden, *Correlation effects in photoemission from low dimensional metals*, Journal of electron spectroscopy and related phenomena **62** (1993), no. 1-2, 225–236. See page: 98

[SMB+02] S. Sorella, G. B. Martins, F. Becca, C. Gazza, L. Capriotti, A. Parola, and E. Dagotto, *Superconductivity in the two-dimensional t-J model*, Phys. Rev. Lett. **88** (2002), no. 11, 117002. See page: 18

[SMP04] N. Shannon, G. Misguich, and K. Penc, *Cyclic exchange, isolated states, and spinon deconfinement in an X X Z Heisenberg model on the checkerboard lattice*, Phys. Rev. B **69** (2004), no. 22, 220403. See page: 46

[SMvDW16] K. M. Stadler, A. K. Mitchell, J. von Delft, and A. Weichselbaum, *Interleaved numerical renormalization group as an efficient multiband impurity solver*, Phys. Rev. B **93** (2016), no. 23, 235101. See page: 83

[Sól79] J. Sólyom, *The Fermi gas model of one-dimensional conductors*, Advances in Physics **28** (1979), no. 2, 201–303. See page: 98

[Spa07] J. Spalek, *tJ model then and now: a personal perspective from the pioneering times*, arXiv: 0706.4236 (2007). See page: 40

[SPOT09] V. W. Scarola, L. Pollet, J. Oitmaa, and M. Troyer, *Discerning incompressible and compressible phases of cold atoms in optical lattices*, Phys. Rev. Lett. **102** (2009), no. 13, 135302. See page: 19

[SRB+03] M. B. Stone, D. H. Reich, C. Broholm, K. Lefmann, C. Rischel, C. P. Landee, and M. M. Turnbull, *Extended quantum critical phase in a magnetized spin-1/2 antiferromagnetic chain*, Phys. Rev. Lett. **91** (2003), no. 3, 037205. See page: 100

[SRL+05] K. M. Shen, F. Ronning, D. H. Lu, F. Baumberger, N. J. C. Ingle, W. S. Lee, W. Meevasana, Y. Kohsaka, M. Azuma, M. Takano, H. Takagi, and Z.-X. Shen, *Nodal quasiparticles and antinodal charge ordering in* $Ca_{2-x}Na_xCuO_2Cl_2$, Science **307** (2005), no. 5711, 901–4. See pages: 13 and 48

[SRVR88] S. Schmitt-Rink, C. M. Varma, and A. E. Ruckenstein, *Spectral function of holes in a quantum antiferromagnet*, Phys. Rev. Lett. **60** (1988), no. 26, 2793. See page: 18

[SS69] K. D. Schotte and U. Schotte, *Tomonaga's model and the threshold singularity of X-ray spectra of metals*, Phys. Rev. **182** (1969), no. 2, 479. See page: 96

[SSS88] S. Sugai, S. Shamoto, and M. Sato, *Two-magnon raman scattering in* $(La_{1-x}Sr_x)_2CuO_4$, Phys. Rev. B **38** (1988), no. 10, 6436. See pages: 10 and 12

[SSV03] T. Senthil, S. Sachdev, and M. Vojta, *Fractionalized fermi liquids*, Phys. Rev. Lett. **90** (2003), no. 21, 216403. See page: 15

[SSV05] ———, *Quantum phase transitions out of the heavy Fermi liquid*, Phys. B: Cond. Mat. **359** (2005), 9–16. See page: 6

[Sut88] B. Sutherland, *Systems with resonating-valence-bond ground states: Correlations and excitations*, Phys. Rev. B **37** (1988), no. 7, 3786. See page: 41

[SWE$^+$10] J. F. Sherson, C. Weitenberg, M. Endres, M. Cheneau, I. Bloch, and S. Kuhr, *Single-atom-resolved fluorescence imaging of an atomic Mott insulator*, Nature **467** (2010), no. 7311, 68. See page: 19

[SYvD$^+$15] K. M. Stadler, Z. P. Yin, J. von Delft, G. Kotliar, and A. Weichselbaum, *Dynamical mean-field theory plus numerical renormalization-group study of spin-orbital separation in a three-band hund metal*, Phys. Rev. Lett. **115** (2015), no. 13, 136401. See page: 82

[TCNT95] D. A. Tennant, R. A. Cowley, S. E. Nagler, and A. M. Tsvelik, *Measurement of the spin-excitation continuum in one-dimensional $KCuF_3$ using neutron scattering*, Phys. Rev. B **52** (1995), no. 18, 13368. See page: 100

[THAY02] Y. Tserkovnyak, B. I. Halperin, O. M. Auslaender, and A. Yacoby, *Finite-size effects in tunneling between parallel quantum wires*, Phys. Rev. Lett. **89** (2002), no. 13, 136805. See page: 100

[THH$^+$89] M. Takigawa, P. C. Hammel, R. H. Heffner, Z. Fisk, K. C. Ott, and J. D. Thompson, *O 17 nmr study of local spin susceptibility in aligned yba 2 cu 3 o 7 powder*, Phys. Rev. Lett. **63** (1989), no. 17, 1865. See page: 10

[THHF89] M Takigawa, PC Hammel, RH Heffner, and Z Fisk, *Spin susceptibility in superconducting $YBa_2Cu_3O_7$ from ^{63}Cu Knight shift*, Physical Review B **39** (1989), no. 10, 7371. See pages: 8 and 12

[THKS15] E. J. Torres-Herrera, D. Kollmar, and L. F. Santos, *Relaxation and thermalization of isolated many-body quantum systems*, Phys. Scr. **2015** (2015), no. T165, 014018. See page: 120

[Tin04] M. Tinkham, *Introduction to superconductivity*, Courier Corporation, 2004. See page: 7

[TKA$^+$90] Y. Tokura, S. Koshihara, T. Arima, H. Takagi, S. Ishibashi, T. Ido, and S. Uchida, *Cu-O network dependence of optical charge-transfer gaps and spin-pair excitations in single-CuO_2-layer compounds*, Phys. Rev. B **41** (1990), no. 16, 11657. See page: 9

[TL01] J. L. Tallon and J. W. Loram, *The doping dependence of T^* – what is the real high-T_c phase diagram?*, Physica C: Superconductivity **349** (2001), no. 1-2, 53–68. See page: 12

[TM94] T. Tohyama and S. Maekawa, *Role of next-nearest-neighbor hopping in the t-t'-J model*, Phys. Rev. B **49** (1994), no. 5, 3596. See page: 11

[TMKY$^+$88] T. Takahashi, H. Matsuyama, H. Katayama-Yoshida, Y. Okabe, S. Hosoya, K. Seki, H. Fujimoto, M. Sato, and H. Inokuchi, *Evidence from angle-resolved resonant photoemission for oxygen-2 p nature of the fermi-liquid states in bi 2 casr 2 cu 2 o 8*, Nature **334** (1988), no. 6184, 691–692. See page: 10

[Toh04] T. Tohyama, *Asymmetry of the electronic states in hole-and electron-doped cuprates: exact diagonalization study of the t-t-t-J model*, Phys. Rev. B **70** (2004), no. 17, 174517. See pages: 11 and 18

[Tom50] S. Tomonaga, *Remarks on Bloch's method of sound waves applied to many-fermion problems*, Prog. Theor. Phys. **5** (1950), no. 4, 544–569. See pages: 64 and 95

[TRR+09] B. Thielemann, Ch. Rüegg, H. M. Rønnow, A. M. Läuchli, J.-S. Caux, B. Normand, D. Biner, K. W. Krämer, H.-U. Güdel, J. Stahn, K. Habicht, K. Kiefer, M. Boehm, D. F. McMorrow, and J. Mesot, *Direct observation of magnon fractionalization in the quantum spin ladder*, Phys. Rev. Lett. **102** (2009), no. 10, 107204. See page: 100

[TSA+95] J. M. Tranquada, B. J. Sternlieb, J. D. Axe, Y. Nakamura, and S. Uchida, *Evidence for stripe correlations of spins and holes in copper oxide superconductors*, Nature **375** (1995), no. 6532, 561. See page: 12

[Uch97] S. Uchida, *Spin gap effects on the c-axis and in-plane charge dynamics of high-T_c cuprates*, Physica C: Superconductivity **282** (1997), 12–18. See page: 13

[UIT+91] S. Uchida, T. Ido, H. Takagi, T. Arima, Y. Tokura, and S. Tajima, *Optical spectra of $La_{2x}Sr_xCuO_4$: Effect of carrier doping on the electronic structure of the CuO_2 plane*, Phys. Rev. B **43** (1991), no. 10, 7942–7954. See page: 14

[VD94] P. G. J. Van Dongen, *Extended Hubbard model at weak coupling*, Phys. Rev. B **50** (1994), no. 19, 14016. See page: 75

[VDK10] D. Van Delft and P. Kes, *The discovery of superconductivity*, Phys. Tod. **63** (2010), no. 9, 38–43. See page: 7

[VDMVESH88] D. Van Der Marel, J. Van Elp, G. A. Sawatzky, and D. Heitmann, *X-ray photoemission, bremsstrahlung isochromat, Auger-electron, and optical spectroscopy studies of Y-Ba-Cu-O thin films*, Phys. Rev. B **37** (1988), no. 10, 5136. See page: 9

[VDS98] J. Von Delft and H. Schoeller, *Bosonization for beginners — refermionization for experts*, Ann. Phys. **7** (1998), no. 4, 225–305. See page: 96

[VHH+12] I. M. Vishik, M. Hashimoto, R.-H. He, W.-S. Lee, F. Schmitt, D. Lu, R G Moore, C. Zhang, W. Meevasana, T. Sasagawa, S. Uchida, K. Fujita, S. Ishida, M. Ishikado, Y. Yoshida, H. Eisaki, Z. Hussain, T. P. Devereaux, and Z.-X. Shen, *Phase competition in trisected superconducting dome*, Proc. Natl. Acad. Sci. U.S.A. **109** (2012), no. 45, 18332–7. See pages: 13 and 48

[Vis13] I. Vishik, *Low energy excitations in cuprate high temperature superconductors: Angle-resolved photoemission spectroscopy studies*, Ph.D. thesis, Stanford University, 2013. See pages: 9, 10, and 147

[VLH+10] I. M. Vishik, W. S. Lee, R.-H. He, M. Hashimoto, Z. Hussain, T. P. Devereaux, and Z.-X. Shen, *ARPES studies of cuprate Fermiology: superconductivity, pseudogap and quasiparticle dynamics*, New J. Phys. **12** (2010), no. 10, 105008. See pages: 13, 48, and 49

[Voi93] J. Voit, *Charge-spin separation and the spectral properties of Luttinger liquids*, J. Phys.: Condensed Matter **5** (1993), no. 44, 8305. See page: 98

[Voi95] ———, *One-dimensional Fermi liquids*, Rep. Prog. Phys. **58** (1995), no. 9, 977. See page: 96

[Vol84] D. Vollhardt, *Normal He_3: an almost localized Fermi liquid*, Rev. of Mod. Phys. **56** (1984), no. 1, 99. See page: 16

[Wag66] H. Wagner, *Long-wavelength excitations and the Goldstone theorem in many-particle systems with "broken symmetries"*, Zeitschrift für Physik **195** (1966), no. 3, 273–299. See page: 9

[WAT$^+$87] M.-K. Wu, J. R. Ashburn, C. J. Torng, P. H. Hor, R. L. Meng, L. Gao, Z. J. Huang, Y. Q. Wang, and C. W. Chu, *Superconductivity at 93 K in a new mixed-phase Y-Ba-Cu-o compound system at ambient pressure*, Phys. Rev. Lett. **58** (1987), no. 9, 908. See page: 6

[Wei12a] A. Weichselbaum, *Non-abelian symmetries in tensor networks: A quantum symmetry space approach*, Ann. Phys. (New York City) **327** (2012), no. 12, 2972–3047. See pages: 82 and 87

[Wei12b] ———, *Tensor networks and the numerical renormalization group*, Phys. Rev. B **86** (2012), no. 24, 245124. See page: 82

[Wen04] X.-G. Wen, *Quantum field theory of many-body systems: from the origin of sound to an origin of light and electrons*, Oxford University Press on Demand, 2004. See pages: 18, 43, and 46

[WGVW16] L. Wang, Z.-C. Gu, F. Verstraete, and X.-G. Wen, *Tensor-product state approach to spin-1/2 square J_1-J_2 antiferromagnetic Heisenberg model: Evidence for deconfined quantum criticality*, Phys. Rev. B **94** (2016), no. 7, 075143. See page: 40

[Wil75] K. G. Wilson, *The renormalization group: Critical phenomena and the Kondo problem*, Rev. Mod. Phys. **47** (1975), no. 4, 773. See page: 78

[WJWB$^+$89] W. W. Warren Jr., R. E. Walstedt, G. F. Brennert, R. J. Cava, R. Tycko, R. F. Bell, and G. Dabbagh, *Cu spin dynamics and superconducting precursor effects in planes above T_c in $YBa_2Cu_3O_{6.7}$*, Phys. Rev. Lett. **62** (1989), no. 10, 1193. See page: 13

[WSC$^+$18] W. Wu, M. S. Scheurer, S. Chatterjee, S. Sachdev, A. Georges, and M. Ferrero, *Pseudogap and Fermi-surface topology in the two-dimensional Hubbard model*, Phys. Rev. X **8** (2018), no. 2, 021048. See pages: 73 and 83

[WSFG19] W. Wu, M. S. Scheurer, M. Ferrero, and A. Georges, *Not all doped mott insulators have a pseudogap: key role of van hove singularities*, arXiv: 2001.00019 (2019). See pages: 83 and 84

[WvD07] A. Weichselbaum and J. von Delft, *Sum-rule conserving spectral functions from the numerical renormalization group*, Phys. Rev. Lett. **99** (2007), no. 7, 076402. See page: 82

[WVHL$^+$93] D. A. Wollman, D. J. Van Harlingen, W. C. Lee, D. M. Ginsberg, and A. J. Leggett, *Experimental determination of the superconducting pairing state in YBCO from the phase coherence of YBCO-Pb dc SQUIDs*, Phys. Rev. Lett. **71** (1993), no. 13, 2134. See page: 12

[YOA97] M. Yamanaka, M. Oshikawa, and I.n Affleck, *Nonperturbative approach to Luttinger's theorem in one dimension*, Phys. Rev. Lett. **79** (1997), no. 6, 1110. See page: 6

[Yos89] D. Yoshioka, *Slave-fermion mean field theory of the hubbard model*, Strong Correlation and Superconductivity, Springer, 1989, pp. 124–131. See page: 17

[ZGRS88] F.-C. Zhang, C. Gros, T. M. Rice, and H. Shiba, *A renormalised Hamiltonian approach to a resonant valence bond wavefunction*, Supercond. Sci. Technol. **1** (1988), no. 1, 36. See page: 16

[Zit09a] R. Zitko, *Convergence acceleration and stabilization for dynamical-mean-field-theory calculations*, arXiv: 0908.0613 (2009). See page: 86

[Žit09b] Rok Žitko, *Adaptive logarithmic discretization for numerical renormalization group methods*, Comput. Phys. Commun. **180** (2009), no. 8, 1271–1276. See page: 82

[ŽP09] R. Žitko and T. Pruschke, *Energy resolution and discretization artifacts in the numerical renormalization group*, Phys. rev. B **79** (2009), no. 8, 085106. See page: 82

[ZR88] F. C. Zhang and T. M. Rice, *Effective Hamiltonian for the superconducting Cu oxides*, Phys. Rev. B **37** (1988), no. 7, 3759. See page: 10

[ZSA85] J. Zaanen, G. A. Sawatzky, and J. W. Allen, *Band gaps and electronic structure of transition-metal compounds*, Phys. Rev. Lett. **55** (1985), no. 4, 418. See page: 9